
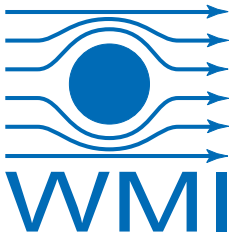

Nematic Fluctuations, Fermiology and the Pairing Potential in Iron-Based Superconductors

Dissertation

Florian Kretzschmar

Juli 2015

Fakultät für Physik
Technische Universität München

TECHNISCHE UNIVERSITÄT MÜNCHEN

Fakultät für Physik
Lehrstuhl E23 für Technische Physik

Walther-Meißner-Institut für Tieftemperaturforschung
der Bayerischen Akademie der Wissenschaften

Nematic Fluctuations, Fermiology and the Pairing Potential in Iron-Based Superconductors

Florian Kretzschmar

Vollständiger Abdruck der von der Fakultät für Physik der Technischen Universität München zur Erlangung des akademischen Grades eines

Doktors der Naturwissenschaften

genehmigten Dissertation.

Vorsitzender:		Univ.-Prof. Dr. J. L. van Hemmen (i.R.)
Prüfer der Dissertation:	1.	Univ.-Prof. Dr. R. Gross
	2.	Univ.-Prof. Chr. Pfleiderer, Ph.D.

Die Dissertation wurde am 27.07.2015 bei der
Technischen Universität München eingereicht und durch
die Fakultät für Physik am 18.08.2015 angenommen.

Abstract

This thesis comprises a systematic study on the doping, temperature and momentum dependent electron dynamics in iron-based superconductors using inelastic light scattering. The observation of Bardasis-Schrieffer modes in the excitation spectrum of superconducting $Ba_{0.6}K_{0.4}Fe_2As_2$ is reported and the energy and symmetry dependence of the modes is analyzed. The analysis yields the identification of a strong subdominant component of the interaction potential $V(\mathbf{k}, \mathbf{k}')$ in this material. Strong nematic fluctuations are investigated in $Ba(Fe_{1-x}Co_x)_2As_2$. The variation of the fluctuation contribution to the Raman susceptibility with temperature and polarization geometry is investigated and a theory is presented which accounts for the observations. The nature of the fluctuations and the origin of nematicity in $Ba(Fe_{1-x}Co_x)_2As_2$ are identified.

Kurzzusammenfassung

Diese Arbeit enthält eine systematische Studie der Ladungsträgerdynamik in Eisenbasierten Supraleitern mittels inelastischer Lichtstreuung unter Veränderung von Dotierung, Temperatur und Polarisationsgeometrie. Die experimentelle Methodik erlaubt dabei die Untersuchung impulsabhängiger Eigenschaften des Elektronensystems. Im Anregungsspektrum von $Ba_{0.6}K_{0.4}Fe_2As_2$ werden Bardasis-Schrieffer Moden beobachtet und deren Energie- und Symmetrieeigenschaften werden analysiert. Die Untersuchung zeigt, dass die Paarwechselwirkung $V(\mathbf{k}, \mathbf{k}')$ eine starke subdominante Komponente aufweist. In $Ba(Fe_{1-x}Co_x)_2As_2$ werden dagegen starke nematische Fluktuationen beobachtet. Die Abhängigkeiten dieser Fluktuationen von Temperatur und Polarisationsgeometrie werden studiert und eine Theorie wird vorgestellt, welche diese erklärt. Sowohl die Natur der Fluktuationen als auch der Ursprung der nematischen Phase in diesem Material können aufgeklärt werden.

Contents

1 Introduction **1**

2 The iron-based superconductors **5**
2.1 Basic properties . . . 5
2.1.1 Crystal structure . . . 6
2.1.2 Electronic structure . . . 7
2.1.3 Magnetic structure . . . 10
2.1.4 Phase diagram . . . 12
2.2 Pairing symmetry . . . 14
2.2.1 The BCS interaction potential . . . 15
2.2.2 Gap structure in the FeSCs . . . 17
2.2.3 Pairing via magnetic interactions . . . 19
2.2.4 Residual interactions and collective modes . . . 22
2.3 Nematic phase . . . 25
2.3.1 Nematicity and its relation to the pairing mechanism . . . 25
2.3.2 Spin-driven electronic nematicity . . . 27
2.3.3 Orbital-driven electronic nematicity . . . 30

3 Theory of electronic Raman scattering **33**
3.1 The Raman effect . . . 33
3.2 Coupling to light via electrons . . . 34
3.3 Single-particle excitations and weak correlations . . . 37
3.4 Selection rules . . . 39
3.5 Finite correlations . . . 42
3.5.1 Normal state: particle-hole excitations . . . 42
3.5.2 Normal state: higher order diagrams . . . 44
3.5.3 Superconducting state . . . 45

4 Experiment **47**
4.1 Incident light path . . . 47
4.2 Cryogenic environment . . . 49
4.3 Detection of scattered photons . . . 50
4.4 Samples . . . 52

5 Evidence of near-degenerate pairing channels in FeSCs **55**
5.1 Experimental results . . . 55
5.1.1 Experimental results: $Ba_{0.6}K_{0.4}Fe_2As_2$ . . . 55
5.1.2 Experimental results: $Rb_{0.8}Fe_{1.6}Se_2$ . . . 60
5.2 Discussion . . . 62
5.2.1 Bardasis-Schrieffer modes in $Ba_{0.6}K_{0.4}Fe_2As_2$ . . . 62
5.2.2 Gap distribution in $Ba_{0.6}K_{0.4}Fe_2As_2$ . . . 65
5.2.3 Doping dependent gap symmetry in $Ba(Fe_{1-x}Co_x)_2As_2$ . . . 69

6 Spin-driven nematic order in $Ba(Fe_{1-x}Co_x)_2As_2$ **75**
6.1 Experimental results . . . 75
6.1.1 Experimental results: $BaFe_2As_2$ . . . 75
6.1.2 Experimental results: $Ba(Fe_{0.975}Co_{0.025})_2As_2$ . . . 78
6.1.3 Experimental results: $Ba(Fe_{0.949}Co_{0.051})_2As_2$ . . . 79
6.2 Discussion . . . 81
6.2.1 Relaxation rate analysis . . . 81
6.2.2 Aslamazov-Larkin fluctuations . . . 86
6.2.3 Aslamazov-Larkin selection rules . . . 91
6.2.4 Considering spin-fluctuations with finite interactions . . . 95
6.2.5 Doping dependence . . . 103

7 Summary **105**

8 Appendices **109**
8.A Gap structure and magnitude in FeSCs . . . 109
8.B Nematic suscebtibility: Errorbar determination . . . 115
8.C Dynamic relaxation rates of $x=0$ and $x=0.051$ samples . . . 118
8.D Approximation of the p-h continua for $x=0$ and $x=0.051$ samples . . . 120
8.E AL fit parameters . . . 121

Bibliography **123**

List of publications **153**

Acknowledgment **155**

Chapter 1

Introduction

Superconductivity, the resistance-free flow of electrical charges, is one of the most thoroughly studied phenomena in solid-state physics. Even though the phenomenon was discovered more than a century ago [1], many questions remain unanswered, in particular those concerning the physics of superconductivity in the 100 K range. The celebrated BCS (Bardeen-Cooper-Schrieffer) theory [2, 3] gave a microscopic explanation of the phenomenon in terms of a condensate of paired electrons (Cooper-pairs) being responsible for the formation of the superconducting state. The theory requires an attractive effective interaction between the electrons which is provided by the exchange of phonons. However, the upper limit for the critical transition temperature T_c in the case of phonon exchange is believed to be of order 40 K [4]. Consequently, the discovery of the cuprates in 1986 by Bednorz and Müller [5] with transition temperatures that were quickly pushed beyond the temperature of liquid nitrogen [6] challenged the conventional BCS theory. The highest T_c was discovered in 1993 in mercury-based cuprates and reaches 135 K under ambient conditions and approximately 160 K with applied pressure [7]. The following 15 years brought little progress towards a further increase of T_c, and no new high-T_c materials were found.

In 2008, however, superconductivity with $T_c = 26$ K was found in the iron-based layered superconductor $La(O_{1-x}F_x)FeAs$ in the group of Hideo Hosono [8]. The discovery, arguably the most important breakthrough in this field for almost two decades, triggered a wave of research into this "pnictide" family of superconductors that quickly pushed the transition temperature to 56 K [9]. Even if T_c could not be boosted anywhere near to the one of the cuprates, it is hoped that the iron-based superconductors (FeSCs) will be instrumental in deciphering the 29-year-old mystery behind high-T_c superconductivity. Questions of vital importance are referring to the nature of the pairing mechanism and the puzzling normal-state properties which

are observed in both the cuprates and FeSCs. These two important issues will be scrutinized here for the FeSCs.

To this end the interaction potential $V(\mathbf{k},\mathbf{k}')$ of FeSCs needs to be analyzed since any type of interaction between the electrons such as phonons, spin fluctuations, Coulomb and exchange interaction leave imprints on $V(\mathbf{k},\mathbf{k}')$. In conventional superconductors with an isotropic gap Δ, the interaction potential $V(\mathbf{k},\mathbf{k}')$ can be derived by and large from the spectrum of lattice excitations $\hbar\omega_{\mathbf{q}}$ [10]. These excitations appear as prominent structures in many spectroscopies at $\hbar\omega_{\mathbf{q}}+\Delta$. However, this access is hampered in systems with the gap $\Delta_{\mathbf{k}}$ varying strongly with the electronic momentum $\hbar\mathbf{k}$.

In the case of anisotropic gaps the FeSCs [8,11] open up new vistas. They have quasi-2-dimensional Fermi surfaces with hole- and electron-like pockets which can be tuned by substitution. Therefore, they are considered model systems for studying the pairing interaction in anisotropic multi-band systems [12–14]. Yet, the question about the nature of the pairing interaction is still not settled. Repulsive spin [15] and attractive orbital [16] fluctuations were suggested to provide appreciable interaction potentials $V(\mathbf{k},\mathbf{k}')$. In the spin channel, the interactions between either the central hole-like and the peripheral electron-like Fermi surfaces V_s [15] or the electron bands alone V_d are nearly degenerate [13,17] and entail a sign change of the energy gap $\Delta_{\mathbf{k}}$.

Raman scattering offers an opportunity to scrutinize competing superconducting instabilities and derive essential properties of $V(\mathbf{k},\mathbf{k}')$. The electronic response provides direct access to the energy gap and its momentum dependence [18,19] reflecting the dominant channel responsible for Cooper-pairing. In addition, residual interactions resulting from anisotropies of the pairing potential $V(\mathbf{k},\mathbf{k}')$ may lead the formation of bound states of the two electrons of a broken Cooper-pair [17,20–23] similar to electron-hole excitons in semiconductors. In a Raman spectrum the bound-states appear as sharp modes below the gap-edge in superconductors having nodeless gaps or they may be damped considerably due to the existence of quasiparticles below the gap-maximum in the presence of gap nodes [24]. The energy and the symmetry properties of the bound-states provide insight into the momentum dependence of $V(\mathbf{k},\mathbf{k}')$ or decompositions thereof in terms of orthonormal functions ϕ_i such as $V(\mathbf{k},\mathbf{k}')=\phi_s^2V_s+\phi_d^2V_d+\ldots$ and, consequently, the type of interaction. $Ba_{0.6}K_{0.4}Fe_2As_2$ turns out to be an ideal system for these studies since the nearly isotropic and nodeless gaps [25–28] facilitate the search for dominant and subdominant pairing channels and address the question as to the type of interaction between

electrons.

The analysis of the superconducting state here and various other studies show that fluctuations of the charge or spin degrees of freedom play a similarly important role in the FeSCs as the phonons in conventional systems. This raises the question as to whether or nor the related fluctuations can be visualized directly. This question can in fact be addressed in the underdoped range between the spin density wave (SDW) parent state and composition exhibiting the highest T_c. This range is characterized by a decreasing transition temperature into the SDW state and eventually coexisting magnetism and superconductivity [29]. In addition, a new type of nematic order and the related fluctuations are observed [30]. In the nematic phase, the rotational symmetry (C_4) of the underlying lattice is spontaneously broken while the translational symmetry is preserved. It is characterized by a large nematic susceptibility, that is, the electronic ground state has a strong tendency to deform in response to a small symmetry-breaking perturbation. Observations of a nematic state have been reported for many iron-based [31–35] and copper-oxide high-temperature superconductors [36–39]. Whether nematicity plays an equally important role in these two systems is highly controversial. Similarly as magnetism, it is regularly found in close proximity to superconductivity in these compounds and it might support or hamper the formation of the superconducting state [30].

For these studies $Ba(Fe_{1-x}Co_x)_2As_2$ is preferable as it shows strong nematicity and enables the investigation of the doping dependence of the phase transition lines which border the nematic phase. This region of the phase diagram is located above the critical temperature T_m where magnetic long-range order vanishes, but below the temperature T_s where the system's crystal structure changes from tetragonal to orthorhombic. As doping increases, the T_s line tracks the T_m line across the phase diagram, approaching the superconducting dome (see Fig. 2.6). The term "strong nematicity" means that while the a and b lattice constants in this regime differ by only a few tenths of a per cent, the anisotropies in several electronic properties are found to be much larger. For instance the difference in the resistivities measured in two directions can be as large as 30% [34].

An important question is whether the phase transition at T_s is a regular structural transition driven by phonons [40], or whether electronic degrees of freedom play the key role [41–43]. Currently, experimental evidence strongly points to an electronic mechanism of nematicity [30,44]. In case of a regular structural phase transition, the crystal structure above T_s is tetragonal, and there should be no symmetry-breaking field to drive a nematic response. Nevertheless, high-temperature persistence of

symmetry breaking of the *electronic* structure and the measurement of a nematic response that ranges up to temperatures twice as high as T_s have been reported [32, 45–47]. These findings suggest that the structural phase transition at T_s is triggered by electronic degrees of freedom rather than lattice vibrations.

If electrons drive nematicity, it still has to be clarified which of their collective degrees of freedom are most relevant. Both spin [30, 48, 49] and charge/orbital [50] fluctuations have been considered candidates. Yet, this fundamental question could not be settled as some results argue in favor of a spin character of the nematic fluctuations [45, 51] whereas others support a charge/orbital driven fluctuation mechanism [52]. Answering this question might prove crucial for uncovering the origin of superconductivity in the iron-based systems, as charge/orbital fluctuations favor a sign-preserving s-wave state (s_{++}) whereas spin fluctuations favor a sign-changing s-wave ($s_{\pm}$) or a d-wave state [30].

The thesis is organized as follows: It starts with an overview of the basic properties such as the crystal and electronic structure of FeSCs in Ch. 2. In addition, the pairing symmetry and the nematic phase in FeSCs receive special attention. In Ch. 3 the theoretical aspects of electronic Raman scattering (ERS) are summarized, including scattering from collective excitations. Ch. 4 is devoted to the description of the Raman setup. The main body of the thesis in Chs. 5 and 6, comprises experimental results and discussions.

Chapter 2

The iron-based superconductors

In terms of transition temperature, the iron-based superconductors (FeSCs) [8, 11] with bulk T_c up to 55 K in $SmFeAsO_{1-x}F_x$ hold the second place behind the cuprates [5]. Both families share many properties, but also show prominent differences. Cuprates and FeSCs have 2D lattices of $3d$ transition metal ions as building blocks and in both cases orthorhombic distortions can be present at small doping. The phase diagrams of cuprates and many FeSCs are also quite similar. Superconductivity emerges as a result of doping an antiferromagnetic parent compound. The parent compound, however, is a Mott-insulator in case of the cuprates, while superconductivity in the Fe-based systems emerges from a metallic state showing itinerant antiferromagnetism. Moreover, cuprates are effective one-band systems while FeSCs exhibit multiple bands which cross the Fermi level. Nevertheless, it is considered possible that the ultimate source of the pairing interaction in both systems is fundamentally similar, although essential details such as pairing symmetry and gap structure in FeSCs depend on the topology of the Fermi surface (FS) and the orbital character of the bands [12]. Now the properties essential for the thesis will be summarized.

2.1 Basic properties

In the following, crystal, magnetic and electronic structure of FeSCs are briefly reviewed. Subsequently, the phase diagram is discussed.

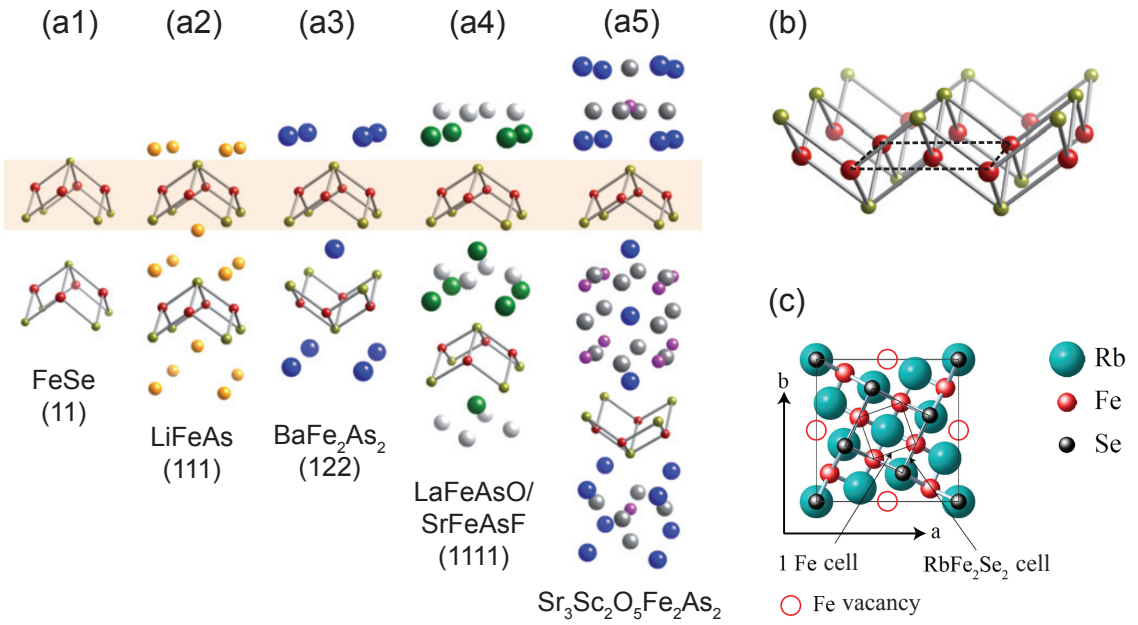

Figure 2.1: Crystallographic and magnetic structures of the iron-based superconductors. (a) Tetragonal structures (D_{4h} symmetry) known to support superconductivity. (b) Active planar iron layer common to all iron-based compounds, with iron ions shown in red and pnictogen/chalcogen anions shown in gold. (c) Alkali metal iron selenide structure with iron vacancies (view parallel to the crystallographic c axis). Adopted from Refs. [53] and [54].

2.1.1 Crystal structure

The family of Fe-based materials comprises over 50 different compounds, identified within just two years after the discovery of LaFeAsO ($T_c = 26\,\mathrm{K}$) in 2008 [8]. Early on, five unique crystallographic structures were shown to support superconductivity. As depicted in Fig. 2.1 (a), these structures all have tetragonal (D_{4h}) symmetry at room temperature, while their composition ranges from the simplest α-PbO-type binary element structure to more complicated quinternary structures composed of elements that span the entire periodic table [53].

The key ingredient is a quasi-two-dimensional layer consisting of iron atoms with tedrahedrally coordinated bonds to either P, As, Se or Te anions that are located above and below the iron lattice to form a checkerboard pattern that doubles the unit-cell size, as shown in Fig. 2.1 (b). These layers are either stacked together, as in FeSe, or are separated by spacer layers using alkali (e.g., Li) alkaline-earth (e.g., Ba), rare-earth oxide/fluoride (e.g., LaO or SrF) or more complicated perovskite-type combinations (e.g., $Sr_3Sc_2O_5$). These so-called blocking layers provide a quasi-two-dimensional character to the crystal because they form atomic bonds of more ionic

character with the FeAs layer, whereas the FeAs-type layer itself is held together by a combination of covalent (Fe-As) and metallic (Fe-Fe) bonds [53].

In 2010, the "alkali metal iron selenides" with the generic chemical formula $A_xFe_{2-y}Se_2$ (A = alkali element) joined the FeSCs family [55]. Here, the alkali elements serve as separating elements between the FeSe layers. One of the motivations for the use of alkali-elements as spacers derives from the observation that the T_c of the FeSCs appears to be controlled by the "anion height", i.e., the distance of the anion above the iron square-planes. Then T_c could be further enhanced via chemical substitution since that process can possibly optimize the local structure. This new family of compounds shows superconductivity at temperatures comparable to those of the pnictides [56].

Nominally, alkali metal iron selenides have $A_{0.8}Fe_{1.6}Se_2$ stoichiometry. They are characterized by a $\sqrt{5}\times\sqrt{5}$ order of Fe vacancies which assigns the crystal nominally to the lower C_{4h} symmetry class [Fig. 2.1 (c)]. Nevertheless, scanning tunneling microscopy experiments have shown that these compounds show microscopic phase separation into an insulating phase with well defined vacancy order and a superconducting AFe_2Se_2 phase (122 stoichiometry) without vacancies [57].

The experimental results presented in this thesis were acquired through the investigation of either cobalt or potassium doped $BaFe_2As_2$ crystals which belong to the 122 family of FeSCs [Fig. 2.1 (a3)] or $Rb_{0.8}Fe_{1.6}Se_2$ [Fig. 2.1 (c)], which belongs to the family of alkali metal iron selenides.

2.1.2 Electronic structure

The band structure of FeSCs was calculated using first-principles DFT, showing good general agreement with experimental measurements [15, 60]. The calculations showed that the electronic properties are dominated by five bands close to the Fermi level which are composed of Fe d-orbitals. Angular resolved photoemission spectra of the $BaFe_2As_2$ band dispersion close to the Fermi level are shown in Fig. 2.2 (d). Three out of five bands are observed, where two of them appear as almost parabolic hole bands crossing the Fermi level at the Γ point and an electron band centered around the X point. The hole-band, carrying the majority of the spectral weight, does never cross the Fermi level at the X point, irrespective of the amount of doping [58]. The quasi-two-dimensional character of the crystal structure results in the quasi-two-dimensional topology of the FS, depicted in Fig. 2.2 (b). The 1 Fe Brillouin-zone (BZ) is shown along with the hole-pockets encircling the Γ point, whereas the electron pockets are centered at the X and Y points. The 1 Fe BZ cor-

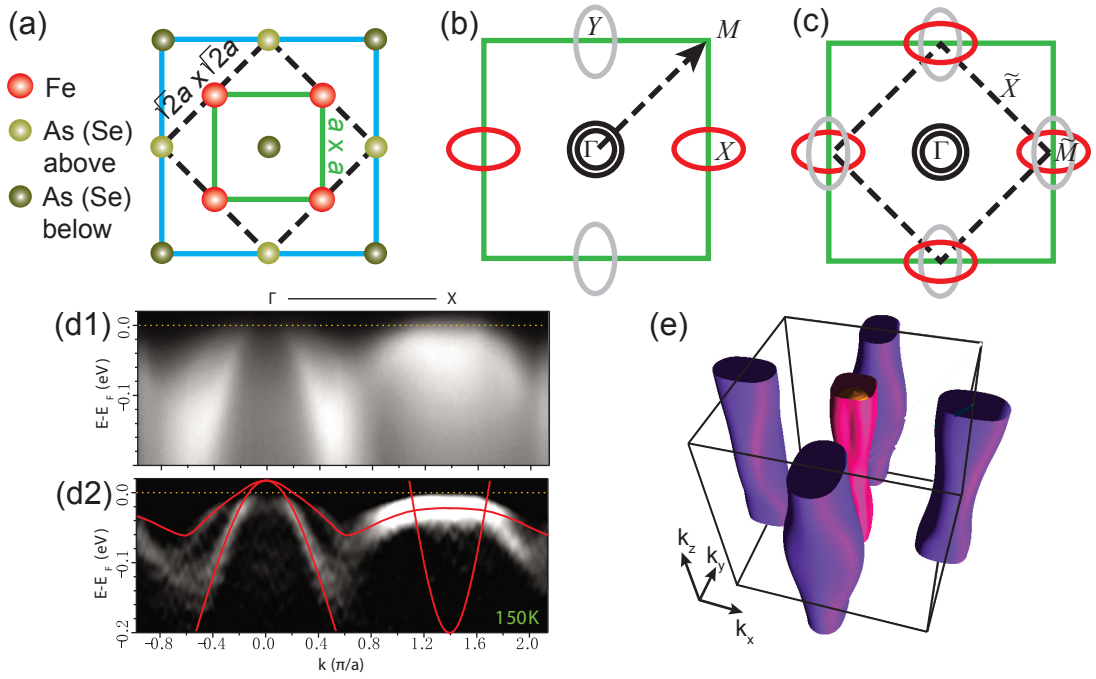

Figure 2.2: Crystallographic and electronic structure of FeSCs. (a) 2D FeAs (FeSe) lattice indicating As (Se) above and below the Fe plane. Green and dashed black squares indicate 1- and 2 Fe unit cells, respectively. The blue square indicates the magnetic unit cell, which is relevant in the magnetically ordered state, see Sec. 2.1.3. (b) Schematic 2D FS in the 1 Fe BZ whose boundaries are indicated by a green solid square. The arrow indicates folding wave vector (π, π). (c) Fermi sheets in the folded BZ whose boundaries are now shown by a dashed black square. (d1) Angular resolved photoemission spectra and (d2) second derivative image of the $BaFe_2As_2$ band dispersion along Γ-X close to the Fermi level, as adopted from [58]. The electron band at the X point is hardly visible due to the choice of the polarization geometry in the experiment. (e) FS based on a tight-binding band structure of $BaFe_2As_2$ in three dimensions, from [59]. Hole bands at the corners are not shown for simplicity.

responds to the 1 Fe unit cell of the crystal, which requires some explanation: The basic crystallographic element of all FeSCs is the FeAs (FeSe) plane [Fig. 2.2 (a)] with an $a \times a$ square plane of Fe atoms that are coordinated tetrahedrally with As (Se) ions above and below the Fe plane. The minimal unit cell of the entire FeAs plane is thus $\tilde{a} \times \tilde{a}$ where $\tilde{a} = a\sqrt{2}$, includes two formula units and is hence called the 2 Fe unit cell. In most cases the low-energy part of the electronic structure can be unfolded into a BZ which is twice as large, corresponding to the $a \times a$ unit cell which contains only one Fe-ion. This is possible in most cases, because the bands which cross the Fermi level are composed of Fe d-orbitals and therefore the unfolding does not alter the low-energy physics [12]. Therefore, regarding the symmetry assignment, the 1 Fe unit cell will be used as reference throughout this thesis.

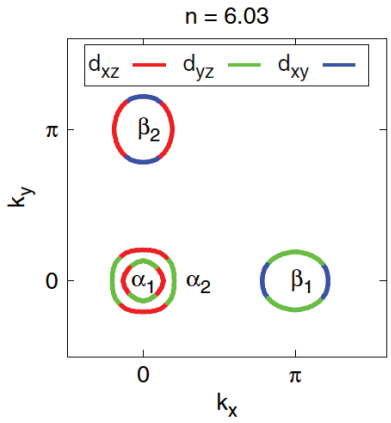

Figure 2.3: Fermi sheets of a five-band model of 1111 FeSCs in the unfolded BZ for a filling of $n = 6.03$. Shown is a quarter of the unfolded BZ. β_1 and β_2, indicating the $(\pi, 0)$ and $(0, \pi)$ electron pocket, respectively, are not composed from the same Fe-orbitals. The majority orbital character is as indicated by the colors (red = d_{xz}, green = d_{yz}, blue = d_{xy}). Taken from [12].

However, if the hopping of the Fe d electrons via the As is taken into account, the 2 Fe cell is used, which introduces a backfolding of the band structure by a vector (π, π) [see Fig. 2.2 (b)], thus electron pockets encircling the X point are folded on top of the electron pockets enclosing Y and vice versa. The result of the effect is shown in Fig. 2.2 (c). While the backfolding via (π, π) has in general only small impact on the low-energy physics of most FeSCs, it can cause the hybridization of the electron pockets. Depending on the hybridization strength, this may lead to portions of the FS exhibiting strong curvature. These regions, called "hot spots", are strongly highlighted in the Raman response and thus need sometimes to be considered in the interpretation of Raman spectra [61].

Fig. 2.2 (e) shows the FSs based on a tight-binding band structure of $BaFe_2As_2$ in three dimensions, revealing that the term "quasi-two-dimensional" has to be treated with care when used in the context of Fe-based materials. Hole and electron sheets are not purely cylindrical but show a weak k_z dispersion. The two-dimensionality of the FS varies within the whole material class. It is more pronounced in the 1111-compounds than in the 122-family [60, 62]. Finally, it has been found theoretically [62, 63] and verified experimentally [64–68] that the main effect of doping on the FS topology is a change in size of the electron and hole pockets. Upon hole doping (for instance by the substitution of Ba by K in $BaFe_2As_2$), electron pockets shrink and hole pockets grow in size, while electron doping (achieved, for instance, by the substitution of Fe by Co in $BaFe_2As_2$)[1] causes the inverse development.

According to models in which the band structure of FeSCs close to Fermi level is

[1] Despite the expansion of electron pockets and the shrinking of hole pockets as observed in angular resolved photoemission experiments [69], it is still being debated if Co-doping really adds electrons to the FeAs plane because the extra d electron of the Co is thought of being located within the muffin-tin sphere of the substituted site. Then, the main effect of Co doping is to add impurities to the FeAs plane [70, 71].

composed of all five Fe *d*-orbitals [72, 73], the electron sheets residing at $(\pi, 0)$ and $(0, \pi)$ are not composed from the same Fe-orbitals. As illustrated in Fig. 2.3, the β_1 electron pocket has predominantly d_{xy} and d_{yz} character, while the β_2 sheet is composed of d_{xy} and d_{xz} orbitals. The orbital character of the bands is supposed to play an important role in the formation of nodes in the superconducting order parameter [12], as well as the phenomenon of orbital ordering observed at the structural phase transition which will be discussed in Sec. 2.3.

Fig. 2.2 (b) reveals that hole- and electron-pockets are nested via the vector $(\pi, 0)$. As a consequence, many FeSCs exhibit a SDW ground state, as discussed in the following.

2.1.3 Magnetic structure

The nature of magnetism in FeSCs is still being debated. Antiferromagnetic (AFM) order in all FeAs based systems is found to have a wave vector $(\pi, 0)$ in the tetragonal (1 Fe) unit cell with a real-space spin arrangement consisting of AFM stripes. Fig. 2.4 (a) shows a projection of the FeAs square lattice with the magnetically ordered Fe sublattice having the spins ferromagnetically arranged along one chain of nearest neighbors within the iron plane, and antiferromagnetically arranged along the other direction. The magnitude of the ordered moment is typically smaller than $1\,\mu_B$ (Bohr magneton) [74, 75], which is much smaller than that of metallic Fe. Early on, theoretical calculations found these materials as being close to a Stoner instability [76], suggesting itinerant magnetism, potentially explaining the consistent overestimates of the ordered moment size by local-moment models. From this viewpoint the most prominent scenario is a SDW instability of the FS, arising from the nesting of two FS pockets by a large $\mathbf{Q} = (\pi, 0)$ vector that is commensurate with the structure. Strong support for $(\pi, 0)$ nesting across the whole material class comes from angular resolved photoemission spectroscopy (ARPES) [64, 66, 77, 78], quantum oscillation [79, 80] and neutron scattering experiments [81]. Moreover, the nesting vector corresponds to the magnetic ordering vector measured throughout the FeAs parent compounds as well as to that of magnetic fluctuations in the superconducting compounds [74, 75].

The magnetic unit cell corresponds to the blue square in Fig. 2.2 (a). The magnetic superstructure leads to a folding of the electron pockets at X on top of the hole pockets encircling the Γ point. Considering this within the 2 Fe unit cell [Fig. 2.2 (c)] leads to a very large number of bands close to the Fermi level, making the theoretical treatment of the system very challenging. Therefore, backfolding via the

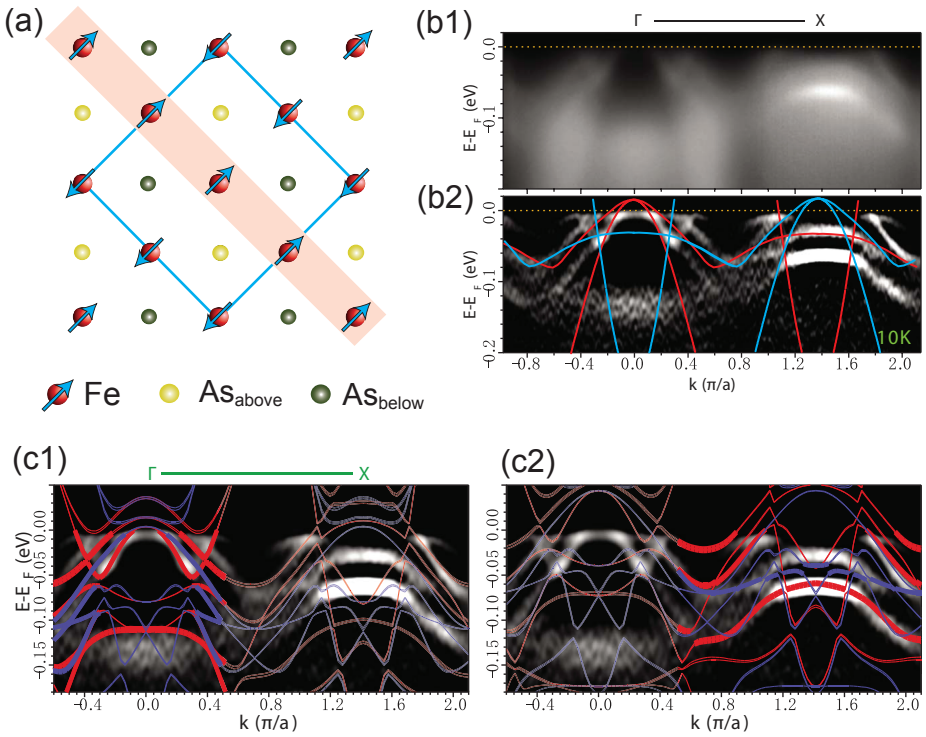

Figure 2.4: (a) Ordered spin arrangement for FeAs-based materials indicated by blue arrows. The blue square indicates the magnetic unit cell. (b) Direct $(\pi, 0)$ folding of the paramagnetic (1 Fe) BZ into the SDW BZ. (c) The best match (LDA with $M = 0.5\mu_B$) overlaid on the band dispersion along the Γ-X cut, with different renormalization for bands residing at the Γ point (c1) and the X point (c2). Adopted from Refs. [53, 58].

SDW vector is often considered only within the 1 Fe unit cell [Fig. 2.2 (b)], which, in principle, should be justified by the Fe $3d$ character of the bands near the Fermi level [12]. The effect on the band structure is shown in Fig. 2.4 (b). The ARPES spectra measured at 10 K show considerable reconstruction in the SDW phase [58]. A simple folding scenario, meaning a shift of the LDA band structure (red) by $(\pi, 0)$ as indicated in Fig. 2.4 (b2) cannot reproduce the measurement. To get a better match between theory and experiment, one has to consider the 2 Fe cell and artificially suppress the ordered magnetic moment in the LDA calculation, that otherwise overestimates its magnitude. The best result, achieved for $0.5\,\mu_B$ and slightly different renormalization for bands encircling Γ and X, is depicted in Fig 2.4 (c1) and (c2).

The magnetic structure is shown in Fig. 2.4 (a). The small orthorhombic distortion preceding or coinciding with the magnetic order is too small to be visible. In the orthorhombic state, the distance between iron atoms with ferromagnetically aligned nearest-neighbor spins shortens by approximately 1% with respect to the

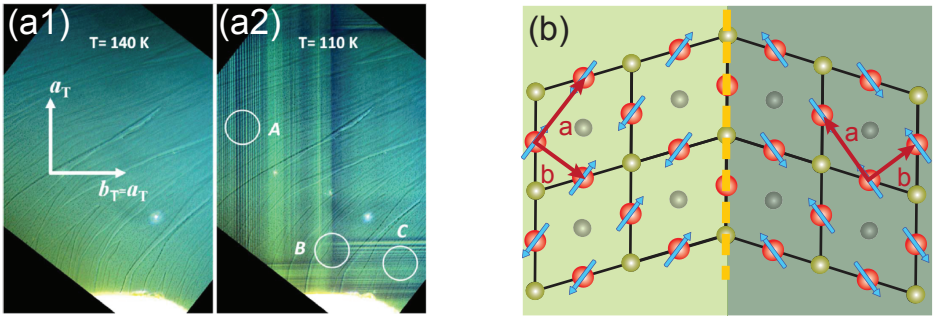

Figure 2.5: Twin formation in underdoped FeAs superconductors. (a) Optical images of a single crystal of $BaFe_2As_2$ above (a1) and below (a2) the coupled structural/magnetic transition at $T_{s/m} = 135\,K$, as adopted from [82]. a_T denotes the crystallographic a axis of the crystal. (b) Illustration of the FeAs plane in the orthorhombic state, with the crystal axes labeled. The structural phase transition corresponds to a stretching/contraction of the Fe-Fe distance along the orthorhombic a and b axes, respectively. Twin boundaries separate regions for which the a and b crystal axes are interchanged. The actual difference in the a and b lattice parameters is much less than illustrated in the diagram [83].

perpendicular direction [53]. The structural transition leads to twin formation, corresponding to an alternation of the orthorhombic a and b axes [82], as shown in Fig. 2.5. Even more importantly, large anisotropies in the in-plane electronic properties of FeSCs are found to develop at the same temperature, which cannot be explained by the structural distortion alone [83]. Measurements of the electronic anisotropy are hampered by twin formation. For probes which cannot distinguish the a and b orthorhombic directions, this effect obscures any in-plane anisotropy measured on length scales greater than the average twin dimension, which can be as small as a few micrometers. Therefore, several groups detwinned single crystals *in situ*, which was achieved by the application of uniaxial stress [32, 34, 35, 84–86] or an in-plane magnetic field [87, 88] while cooling through the structural transition temperature T_s.

2.1.4 Phase diagram

The generic phase diagram of the 122 family of FeSCs is depicted in Fig. 2.6. As in the cuprates, there is a region of magnetic ordering near zero doping, and superconductivity emerges on charge doping with either holes or electrons, while at the same time the magnetism is suppressed. Doping, in this respect, is achieved via the replacement of, for instance, Ba by K in $BaFe_2As_2$. The neutral Ba atom has the electronic configuration $[Xe]6s^2$ while the neutral K atom has $[Ar]4s^1$ configuration. Hence, one hole is added to the unit cell by replacing Ba with K. Replacing

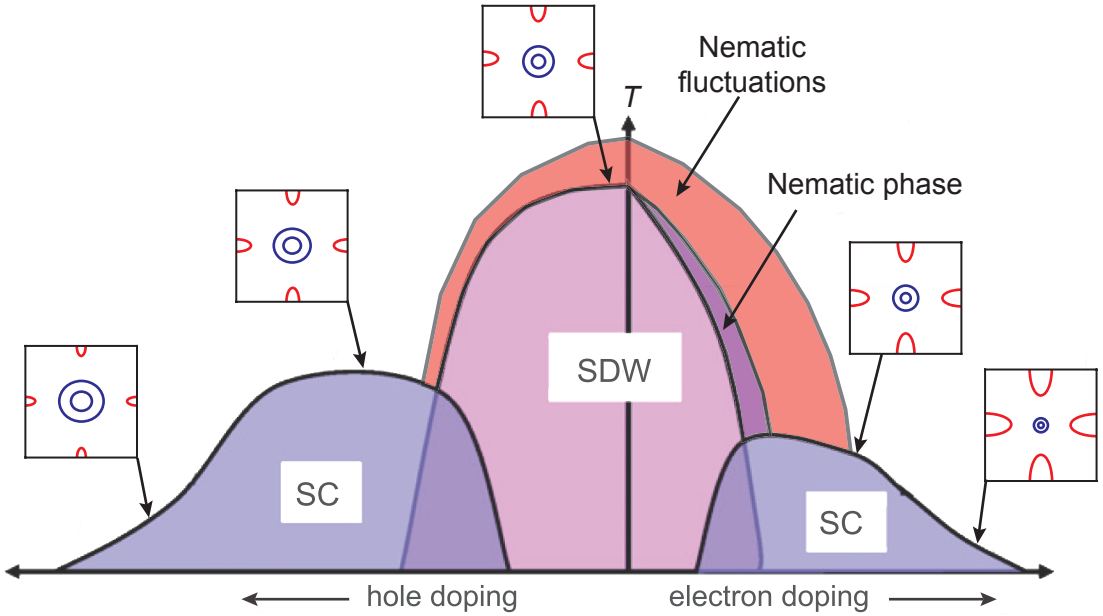

Figure 2.6: Schematic phase diagram of FeSCs, along with the doping induced change of the FS. Shown is also the nematic phase (indicated with dark-purple color), a regime with broken fourfold rotational symmetry but preserved translational and time-reversal symmetry, and the region showing strong (fourfold symmetric) nematic fluctuations. Adapted from [12] and [30].

Fe ($[Ar]3d^64s^2$) by Co ($[Ar]3d^74s^2$), on the other hand, nominally adds one electron per unit cell (see, however, [70]). The maximal critical temperatures T_c up to which superconductivity occurs were found to be 39 K upon hole-doping and 26 K via electron-doping.

The doping-induced change of the FS, namely the shrinking of hole- and growing of electron-pockets upon electron doping (and vice versa) is indicated in the Fig. 2.6[2]. It is evident that doping also alters the nesting conditions between hole- and electron-like sheets. While these conditions are optimal at zero doping, nesting worsens when going away from this composition. Consequently, the SDW order is destabilized. This happens simultaneously with the emergence of the superconducting phase, suggesting an intimate relation between superconductivity and magnetism. Therefore, the pairing via the exchange of spin-fluctuations was anticipated early on after the discovery of this material class [15].

A more careful examination of the phase diagram reveals that there is another non-superconducting ordered state besides magnetism. At a certain temperature

[2]The circular hole and elliptical electron FSs are an abstraction. Hopping of electrons between Fe via the As atoms leads to the hybridization of the electron pockets. While some groups find the effect to be weak [89, 90], others observe considerable reconstruction resulting in "propeller-like" FSs [91].

$T_{\mathrm{nem}} = T_{\mathrm{s}}$, the system spontaneously breaks the symmetry between x and y directions in the Fe-plane, reducing the rotational point group symmetry of the lattice from tetragonal to orthorhombic, while time reversal symmetry is preserved. Only upon further cooling time-reversal symmetry is finally broken when entering the magnetically ordered state. This phase, located between the structural and magnetic transition, is referred to as the nematic phase. In some materials, such as hole-doped $Ba_{1-x}K_xFe_2As_2$, the tetragonal-to-orthorhombic and magnetic transitions are simultaneous and first order ($T_{\mathrm{s}} = T_{\mathrm{m}}$), whereas in electron-doped $Ba(Fe_{1-x}Co_x)_2As_2$ they are split ($T_{\mathrm{s}} > T_{\mathrm{m}}$) and, with the exception of very small Co concentration, second order [30]. As doping increases, the T_{s} line tracks the T_{m} line across the phase diagram, approaching the superconducting dome. The nematic phase has received a lot of attention from the theoretical, as well as the experimental side, as it is not clear whether this order supports or counteracts superconductivity [30]. As it also plays the key role in Ch. 6, the nematic phase is discussed in more detail in Sec. 2.3.

2.2 Pairing symmetry

In Ch. 5, sharp modes in the B_{1g} spectrum of superconducting $Ba_{0.6}K_{0.4}Fe_2As_2$ are interpreted as the signature of bound pairs which are formed by anisotropies of the BCS interaction potential $V(\mathbf{k}, \mathbf{k}')$. It is the purpose of this section to give an overview of the theoretical concepts which are needed to understand the formation of bound pairs in the excitation spectrum of superconductors. For a start the BCS interaction potential $V(\mathbf{k}, \mathbf{k}')$ is introduced and the term "residual interactions" is explained. For a classification of the symmetry properties $V(\mathbf{k}, \mathbf{k}')$ is expanded into the set of crystal harmonics of the D_{4h} point group (Sec. 2.2.1). In Sec. 2.2.2 a summary of the currently available experimental results on possible gap symmetries of the FeSCs is given, followed by a discussion about which coefficients in the crystal harmonics expansion must be eliminated in order to avoid inconsistencies with the experimental findings. The remaining orthogonal pairing-channels are in agreement with either a conventional pairing mechanism, a pairing mechanism based on orbital fluctuations or with a mechanism that requires a sign change of the order parameter between the FS sheets of the paired electrons. The latter requirement is compatible with pairing via magnetic interactions, which is briefly addressed in Sec. 2.2.3. Finally, in Sec. 2.2.4, the formation of bound pairs of quasiparticles as a consequence of residual interactions in $V(\mathbf{k}, \mathbf{k}')$ is discussed.

2.2.1 The BCS interaction potential

In 1956 Bardeen, Cooper and Schrieffer (BCS) showed that as a consequence of an attractive interaction the Fermi gas of conduction electrons shows an instability towards the condensation of paired electrons (Cooper-pairs) into a coherent boson-like ground state [2,3], giving a microscopic explanation for superconductivity. The attractive interaction between two electrons which is necessary to form the Cooper-pair can be described by virtual exchange-bosons with momentum $\mathbf{q}$ being emitted by one electron and reabsorbed by an other one within the time-uncertainty $\Delta t = 1/\omega_q$. Due to momentum conservation and the fact that the exchange bosons have relatively small energy compared to the Fermi energy, the phase space for such scattering processes diminishes rapidly for electron-pairs other than those having wave vectors $-\mathbf{k}$ and $\mathbf{k}$. This leads to the correlation of electrons at ($\mathbf{k}$,$-\mathbf{k}$) as for them the attractive interaction becomes optimal [see Fig. 2.7 (a)]. In the new ground state, quasiparticles at $\mathbf{k}$ reduce their energy by the value $\Delta_{\mathbf{k}}(T)$ with respect to the Fermi level. $\Delta_{\mathbf{k}}(T)$ is given by the BCS gap equation [92]

$$\Delta_{\mathbf{k}}(T) = -\sum_{\mathbf{k}'} V_{\mathbf{k},\mathbf{k}'} \Delta_{\mathbf{k}'} \frac{\tanh(E_{\mathbf{k}'}/k_B T)}{2E_{\mathbf{k}'}} \tag{2.1}$$

where $2\Delta_{\mathbf{k}}(T)$ is the minimal energy that must be invested for quasiparticles to be excited from ground state. $V_{\mathbf{k},\mathbf{k}'} = V(\mathbf{k},\mathbf{k}')$ denotes the BCS interaction potential which describes the interaction between two electrons at ($\mathbf{k}$,$-\mathbf{k}$) that is effective over the whole FS. Bardeen, Cooper and Schrieffer considered quantized lattice vibrations (phonons) as mediators of the attractive interaction but in principle other bosonic particles like polarons, plasmons or magnetic excitations are also candidates in the framework of the BCS theory.

The macroscopic coherent wave function which describes the pair-condensate has the same symmetry as the gap and can be identified with the Ginzburg-Landau order parameter of the superconductor. It is a two-fermion wave function and thus must obey fermion anticommutation relations. As a consequence, for singlet pairing ($S=0$, antisymmetric spin component), the spatial part of the wave function must be symmetric ($L=0,2,\ldots$). For triplet pairing ($S=1$, symmetric spin component) the spatial part must be antisymmetric ($L=1,3,\ldots$). The related pairing state is then called an $s-, d-, g-, \ldots$ and $p-, f-, h-, \ldots$ wave state, respectively. In order to solve the BCS gap equation Bardeen, Cooper and Schrieffer made the approximation of an isotropic interaction potential $V(\mathbf{k},\mathbf{k}')=-V_0$ ($V_0>0$) for quasiparticle

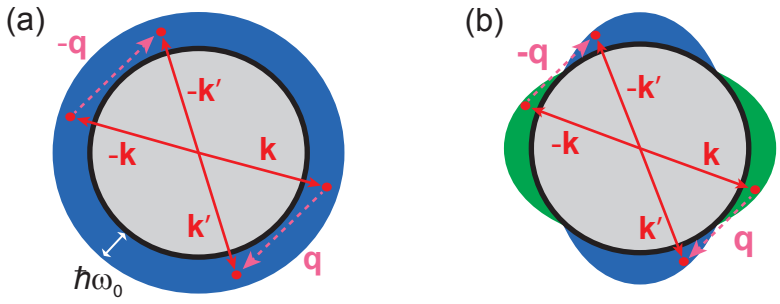

Figure 2.7: The pair-scattering process. (a) Conventional scattering process that leads to Cooper-pair formation of electrons with momenta $-\mathbf{k}$ and $\mathbf{k}$. (b) Scattering process from an interaction which requires a sign change of the order parameter. This process is orthogonal to the process in (a).

energies $\xi_{\mathbf{k}} \leq \omega_0$ and 0 otherwise[3] [3]. Therefore, the order parameter of this "conventional" mechanism is a singlet s-wave. However, in principle, $V(\mathbf{k}, \mathbf{k}')$ depends on momentum, hence can be anisotropic and may even be positive (repulsive[4]) for all or some wave vectors $\mathbf{k}$.

Superconductivity can be characterized as "unconventional" if the superconducting ground state has a symmetry different from the usual BCS ground state [93]. Since superconductivity is an instability of the "Fermi sea", the symmetry of the FS is considered as a reference. In a crystal, the FS will be unchanged under all of the point group symmetry operations of the crystal, hence one can define superconductivity as conventional if $\Delta_{\hat{R}\mathbf{k}} = \Delta_{\mathbf{k}}$, where $\hat{R}$ is any symmetry operation in the point group. In contrast superconductivity will be defined to be unconventional if $\Delta_{\hat{R}\mathbf{k}} \neq \Delta_{\mathbf{k}}$ for at least one symmetry operation $\hat{R}$. Thus, for a given crystal structure, the irreducible representations classify the distinct possible pairing states. For this purpose, it is convenient to expand the interaction potential $V(\mathbf{k}, \mathbf{k}')$ into a complete set of orthonormal functions, for instance crystal harmonics $\Phi_n^\mu(\mathbf{k})$ [19, 94]:

$$V_{\mathbf{k},\mathbf{k}'} = \sum_{n=0}^{\infty} \sum_{\mu=1}^{M} \Phi_n^\mu(\mathbf{k}') V_n^\mu \Phi_n^\mu(\mathbf{k})^*. \tag{2.2}$$

The outer sum runs over n counting higher order terms, the inner sum is over the irreducible representations of the given crystal symmetry. In Eq. (2.2) the interaction is assumed to be diagonal. V_n^μ is the (constant) potential in a given channel which is proportional to the BCS-type coupling constant via $\lambda_n^\mu = N_F V_n^\mu$ with N_F the density of states. Within the expansion, the leading term reflects the ground state

[3] For electron-phonon coupling ω_0 is approximately the Debye frequency.

[4] Repulsive interactions originate from the bare Coulomb repulsion between two electrons or from magnetic interactions (see Sec. 2.2.3).

of the system since, at zero temperature, all Cooper-pairs will condense in this pairing-channel as this yields the highest energy reduction. The other terms reflect subdominant components of the interaction potential which do not contribute to Cooper-pair formation.

If we consider a system of conduction electrons having a nearly spherical FS, it is convenient to use spherical harmonics for the expansion in Eq. (2.2). Let the system be close to a magnetic instability, then magnetic fluctuations may play the role of exchange bosons that mediate the pairing. However, we will see in Sec. 2.2.3 that this interaction is repulsive and therefore requires a sign change of the order parameter between the paired electrons. If the pairing mediated by magnetic fluctuations yields overall less condensation energy than the conventional mechanism (phonons), the result is that the superconducting ground state of the system has s-wave symmetry [Fig. 2.7 (a)]. Nevertheless, there is a subdominant (residual) pairing channel due to magnetic interactions which is, because of the required sign-change of the order parameter [Fig. 2.7 (b)], orthogonal to the dominant pairing channel (it has d-wave symmetry). The superconductivity is conventional, because the ground state has s-wave symmetry, which stays unchanged under all symmetry operations $\hat{R}$ of the point group of the spherical FS. This is not the case for the d-wave state (it has, for instance, only 2-fold rotational symmetry). Thus a d-wave ground state would be an unconventional superconducting state according to the definition introduced above.

2.2.2 Gap structure in the FeSCs

After the introduction of some general concepts of the interaction potential it is appropriate to discuss the specific case of FeSCs. For these materials a number of coefficients in the expansion (2.2) can be eliminated using information provided by experiments. We start with an experiment which can differentiate between spin-singlet and triplet pairing. A triplet Cooper-pair with $S_z = \pm 1$ can screen an external magnetic field. The spin-orbit interaction can prevent this for some directions, but not for others. A way to probe the latter is via the Knight shift measurement which has been performed on several FeSCs [25, 95–101] and it was found that the Knight shift decreases in all crystallographic directions, practically excluding triplet symmetries [12]. Regarding the symmetry of the spatial part of the wave function, this leaves only the even irreducible representations of the D_{4h} point group. The lowest order approximations are (cf. [102]): A_{1g} [1], A_{2g} [$xy(x^2-y^2)$], B_{1g} [x^2-y^2], B_{2g} [xy], and E_g [xz,yz] [103]. The even representations of the D_{4h} point group are

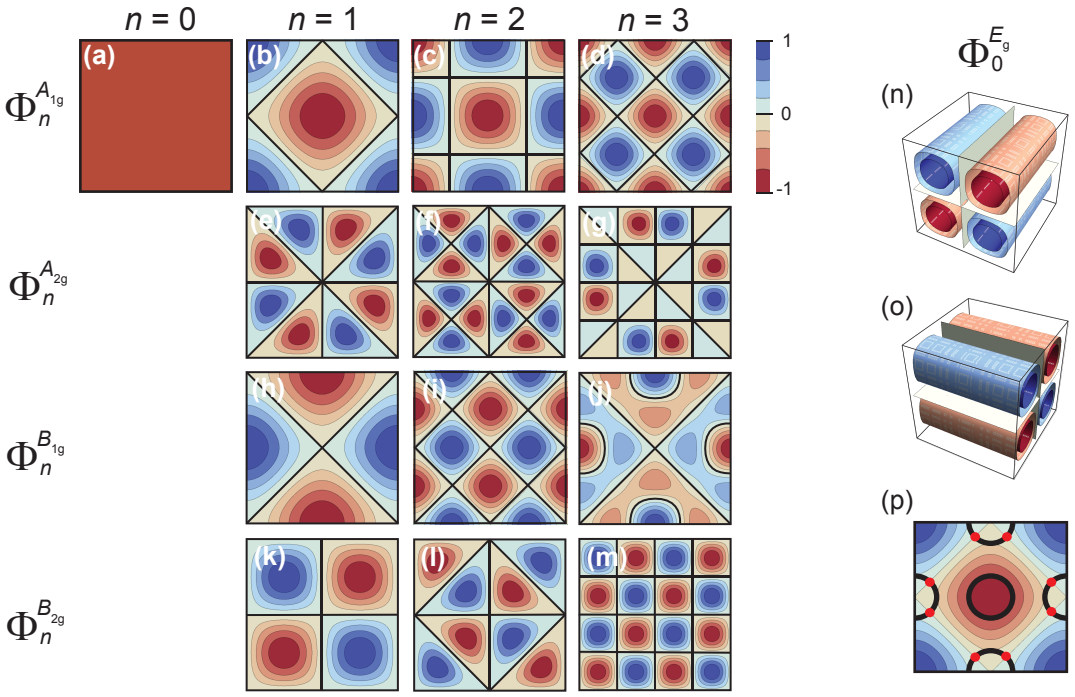

Figure 2.8: (D_{4h}) crystal harmonics. Displayed are the even irreducible representations of the (D_{4h}) point group: (a)-(m) A_{1g}, A_{2g}, B_{1g}, B_{2g} (up to the 3rd order); (n)-(o) only the 1st order of the 2D-basis of the E_g representation is shown. (p) To determine which basis function requires nodes of the order parameter on the FS one overlaps it with the 2D FS of FeSCs. This is done here for the 1st order A_{1g} basis function. The positions of nodes are marked with red dots.

displayed in Fig. 2.8 (a)-(o), up to third order.

Deriving a consistent picture of the gap symmetry in the FeSCs constitutes a challenge, in particular when all families of iron-pnictides and -chalcogenides are included. This is due to the wide diversity of experimental results for the gap structure, which vary between isotropic to very anisotropic or even nodal gaps for the different compounds, see Appendix 8.A. However, it is convenient to start with optimally doped $Ba_{1-x}K_xFe_2As_2$. Slightly anisotropic but clean gaps have been reported for this composition by bulk-sensitive experiments [25–28]. This is compatible with a conventional s-wave order parameter [Fig. 2.8 (a)] or with a so-called extended s-wave order-parameter, which is equivalent to the 2nd order A_{1g} basis function, displayed in Fig. 2.8 (c). As will be pointed out in the next section such an order parameter is in agreement with pairing via magnetic interactions. All other symmetries give rise to nodal gaps, which have not been observed at optimal hole-doping and can therefore be excluded.

This shall be discussed in detail using Fig. 2.8. To determine which order pa-

rameter symmetry requires nodes on the FS the related basis function is overlapped with the FS of FeSCs. An example is given in Fig. 2.8 (p). B_{2g} symmetry of the gap would imply gap nodes on the electron- and hole-pockets at the principle axes of the 1 Fe BZ. Even more nodes occur if higher order terms of the B_{2g} symmetry are considered. The same argument holds for the case of the A_{2g} symmetry. Already the lowest order implies nodes on the principal axes of the 1 Fe BZ on all pockets and four additional nodes at the 1 Fe BZ diagonals on the hole pocket. Higher A_{2g} orders imply even larger numbers of nodes. The E_g symmetry can also be excluded since for the quasi-2D FS centered around the ΓZ-line of the three dimensional 1 Fe BZ, nodes would appear on all FSs in the z-direction at the $(k_x, k_y, k_z = 0)$ plane. The 1st order of the A_{1g} symmetry implies gap nodes on the electron sheets as indicated in panel Fig. 2.8 (p). The 3rd order implies gap nodes on all pockets, if the pockets are big enough, or is equivalent to the case of the conventional s-wave gap for sufficiently small FSs[5]. Finally, the B_{1g} symmetry implies nodes on the hole-pocket at the 1 Fe BZ diagonals and can therefore also be excluded. This leaves the possibilities of a conventional s-wave or an extended s-wave order parameter for optimally doped $Ba_{1-x}K_xFe_2As_2$.

An alternative explanation of the superconducting pairing mechanism is in agreement with the conventional s-wave (in the context of FeSCs also often referred to as s_{++}). It is based on orbital fluctuations, that is, for instance, the fluctuating unequal occupation of the iron d_{xz} and d_{yz} orbitals, playing the role of the virtual exchange particles [16, 104, 105] (see Sec. 2.3.3). On the other hand, the extended s-wave order parameter (in the context of FeSCs also often referred to as $s_{\pm}$) is in agreement with a scenario relying on magnetic interactions. A model in which antiferromagnetic spin-fluctuations mediate the attractive interaction between electrons is also in agreement with the majority of (bulk-) experiments [12]. Therefore, a few remarks on spin-fluctuation mediated pairing follow in the next section.

2.2.3 Pairing via magnetic interactions

The electron-phonon mechanism is not strong enough to explain the observed critical temperatures in FeSCs [107]. Therefore, electronic pairing mechanisms were discussed to be responsible for the attractive interaction between the electrons in these materials. While there are many candidates for electronic pairing, magnetic in-

[5] Some authors predicted the appearance of a small hole-like γ-pocket located at (π, π) for hole doping [12]. If this pocket is involved in Cooper-pair formation, the 3rd order of the A_{1g} symmetry is not equivalent to the conventional s-wave case and may not be neglected.

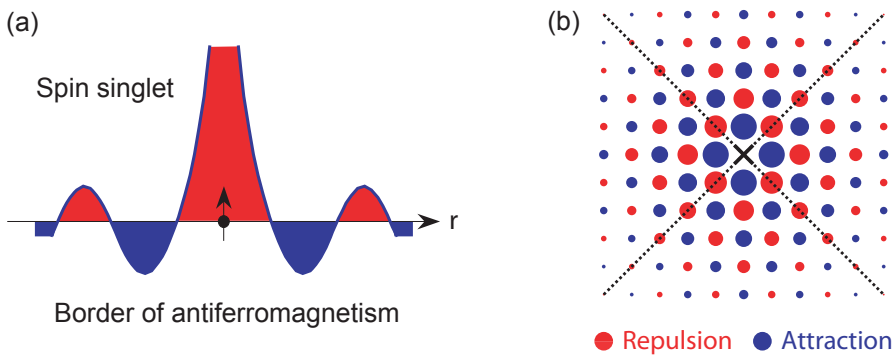

Figure 2.9: Illustration of the spin-spin QP interaction in a metal. Panel (a) depicts the spin-spin interaction potential versus distance r produced by a test spin at rest in a material on the border of long-range antiferromagnetic order. The interaction potential shown oscillates between attractive and repulsive regions in space (spin-singlet state). Panel (b) shows a graphical representation of the static magnetic interaction potential in real space of a system on the border of antiferromagnetism as seen by a QP moving on a square crystal lattice. The other QP is at the origin (denoted by a cross). The dashed lines show the regions where the d-wave Cooper-pair state has vanishing amplitude. This is the state that best matches the oscillations of the potential, in that a QP has minimal probability of being on lattice sites when the potential induced by the QP at the origin is repulsive. The size of the circle on each lattice site is a representation of the absolute magnitude of the potential. Adapted from [106].

teractions were proposed early on [15], because, like in the cuprates or heavy-fermion systems, the superconducting phase is found in close proximity to a magnetically ordered phase. Magnetic interactions are operative in the superfluid phases of ^{3}He that has been identified to form a neutral spin-triplet p-wave condensate [108] and they are discussed to be relevant for some heavy-fermion compounds [109] and the cuprates [110].

The spin-spin quasiparticle interaction potential of a system close to an antiferromagnetic instability is illustrated in Fig. 2.9 (a). It has both attractive as well as repulsive regions in space, but is, integrated over r, repulsive. The issue is whether a Cooper-pair wavefunction can be constructed that has a large amplitude in the regions where the interaction is attractive and a small amplitude elsewhere. The spin-spin interaction potential oscillates between attractive and repulsive regions with a period comparable to the lattice spacing, see Fig. 2.9 (b). The dashed lines in Fig. 2.9 (b) show the regions where the d-wave Cooper-pair state has vanishing amplitude. This state matches the oscillations of the potential, in that a QP has smaller probability of being on lattice sites where the potential is repulsive. However, since available states for pairing are restricted to close proximity of the FS, the pair-wave function must oscillate in space with the wavevector that connects the

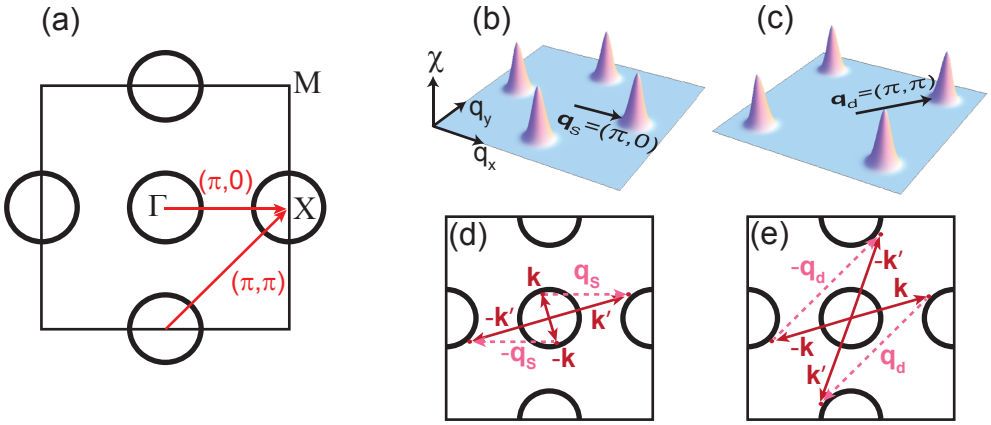

Figure 2.10: Pairing channels in FeSCs. (a) FS topology of the FeSCs with nesting vectors. In this multiband superconductor one has to distinguish between intraband and interband scattering processes. Of the latter, two scattering processes are special, because their scattering vectors connect nested FSs. The nesting leads to a peaked spin susceptibility [as indicated in the panels (b) and (c)], and thus to a pairing potential which is peaked at the same positions. Therefore, the scattering processes with $\mathbf{q}_s$ and $\mathbf{q}_d$ are more effective than the other ones and the system develops an order parameter which enables either the interaction (d) [$s_\pm$] or (e) [$d_{x^2-y^2}$] to be attractive.

FSs associated with the paired QP [106].

The fact that, in the singlet channel[6], spin fluctuation exchange can realize only superconducting states having a sign-changing order parameter can also be understood by looking at the form of the singlet interaction for AFM spin fluctuations [12, 110]:

$$V(\mathbf{k},\mathbf{k}') = \frac{3}{2}\bar{U}^2\chi(\mathbf{q}) \overset{\text{RPA}}{=} \frac{3}{2}\bar{U}^2\frac{\chi_0(\mathbf{q})}{1-\bar{U}\chi_0(\mathbf{q})} \tag{2.3}$$

where $\bar{U}$ is the screened Hubbard repulsion ($\bar{U} > 0$), χ the spin susceptibility and $\chi_0(\mathbf{q})$ is the noninteracting susceptibility of the (continuum) Fermi gas, i.e. the Lindhard function. Suppose that the susceptibility is strongly peaked near some wave vector $\mathbf{Q}$ (for instance due to FS-nesting). This implies that $V(\mathbf{Q})$ is also peaked at this wave vector, but is always positive (repulsive). However, examination of the BCS gap equation (2.1) shows that for this interaction an isotropic gap cannot be a solution, but if the state changes sign,

$$\Delta_{\mathbf{k}} = -\Delta_{\mathbf{k}+\mathbf{Q}} \tag{2.4}$$

a solution will be allowed [12].

[6]Like the FeSCs, cuprates and heavy-fermion compounds are spin-singlet superconductors [12].

In the case of a single FS, superconductivity driven by spin-fluctuations will necessarily be nodal. This situation is probably realized in the cuprates, and possibly in hole-overdoped KFe_2As_2. However, the majority of FeSCs are multiband systems and a nodeless though sign-changing gap structure may be realized. As pointed out in Sec. 2.1.2, the FS of the FeSCs is characterized by small concentric hole pockets around the Γ point and slightly elliptical electron pockets around the M points. Modeling these pockets in the simplest possible way, allowing for one hole and one electron pocket, leads to a very simple generalization of the "standard" argument for d-wave pairing in the cuprates [12, 15].

In a weak-coupling picture, the nearly nested electron and hole pockets lead to a spin susceptibility peaked strongly near $\mathbf{q}_s = (\pi, 0)$ in the 1 Fe zone [Fig. 2.10 (b) and (d)]. The gap equation (2.1) then admits a solution with the property (2.4) if there is a sign change of $\Delta_{\mathbf{k}}$ between electron and hole pockets. However, there is also a competing pairing channel because of the nesting vector $\mathbf{q}_d = (\pi, \pi)$ between the electron-pockets [Fig. 2.10 (c) and (e)]. In this case, the sign change of $\Delta_{\mathbf{k}}$ occurs between the electron pockets. The lowest order symmetry associated with the nesting vector $\mathbf{q}_s = (\pi, 0)$, is the so-called $s_\pm$ symmetry, the lowest order symmetry associated with the nesting vector $\mathbf{q}_d = (\pi, \pi)$, is the $d_{x^2-y^2}$ symmetry [cf. Fig. 2.8 (c) and (h)]. It apparently depends on the nesting conditions, and thus on details of the FS, which of the two pairing states can provide more condensation energy and consequently is the ground state of the system. Theoretical studies [59, 111, 112] find that $s_\pm$-wave (A_{1g}) and $d_{x^2-y^2}$-wave (B_{1g}) superconductivity both can occur in multiband models of the pnictides, with the pairing strength or T_c of the $s_\pm$-wave state typically being larger.

2.2.4 Residual interactions and collective modes

The most rigorous description of collective excitations of the pair-condensate was given by Bardasis and Schrieffer [20], using the RPA arguments of Anderson [113–115]. Two types of collective excitations are involved in the theory: a bound pair of QPs whose center-of-mass $[(\mathbf{r}_1 + \mathbf{r}_2)/2]$ propagates with momentum $\hbar\mathbf{q}$ deriving from interactions between particles in states $-\mathbf{k}$ and $\mathbf{k}' \neq \mathbf{k}$, and bound-pairs of QPs which are formed by orthogonal components of the interaction potential $V(\mathbf{k}, \mathbf{k}')$. The former excitation has a symmetry such that it couples to the long range Coulomb forces which shift its energy to the plasma frequency. Rickayzen [116] showed that this collective excitation plays a crucial role for the gauge-invariance of the Meissner ef-

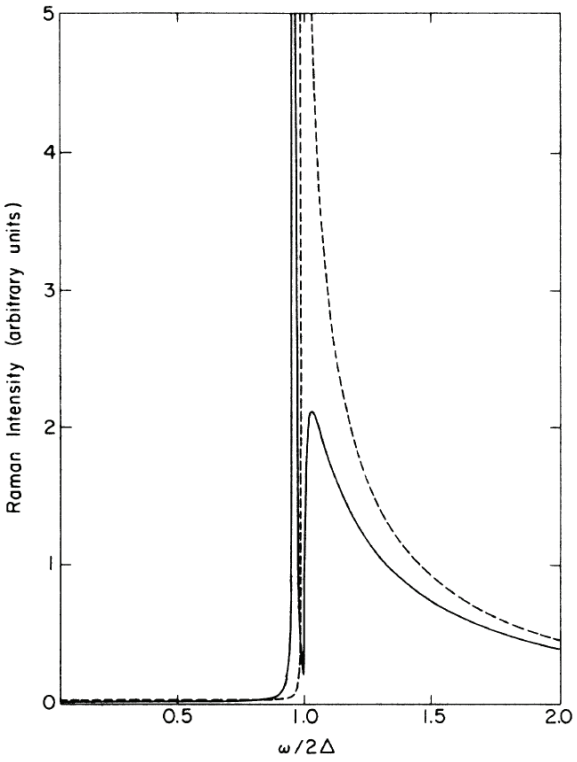

Figure 2.11: Typical spectrum of Raman scattering in a BCS superconductor with (solid line) and without (dashed line) final-state interaction. The square-root singularity is removed by the attractive interaction between the two excited single QPs and the spectral weight is transferred into the δ-like peak that signals the formation of an $L \neq 0$ pair (from [22]).

fect[7]. The second type of collective excitation is interpreted as an exciton-like bound pair of QPs, which has a symmetry orthogonal to the symmetry of the Cooper-pairs of the ground state and an energy which lies inside of the superconducting gap. When a Cooper-pair is broken, this gives rise to two QPs which are excited from the (initial) pair state to above the gap edge (final state) and are affected by those parts of the interaction which are orthogonal to the ground state. Hence the residual interaction is also referred to as final-state interaction (FSI). Bardasis and Schrieffer expanded the interaction potential $V(\mathbf{k}, \mathbf{k}')$ into spherical harmonics and characterized the bound pairs in terms of the quantum numbers L and M involved in the potential expansion. They showed that for a bound L-state (corresponding to the $p, d, f, \ldots$ excitons) to exist, the L-wave part of the interaction potential $V(\mathbf{k}, \mathbf{k}')$ must be non-zero on the FS. If the L-wave potential is repulsive, particle-hole pairs are formed, as opposed to particle-particle pairs in case of an attractive L-wave potential [20].

A detailed study of how the FSI modifies the Raman response of isotropic superconductors was presented by Monien and Zawadovski [22]. Without the FSI, the Raman spectrum exhibits a square-root singularity at $\omega = 2\Delta$, due to pair-breaking. This square-root singularity is removed by FSI, and spectral weight is transferred

[7] This excitation is known as Anderson-Bogoliubov sound mode.

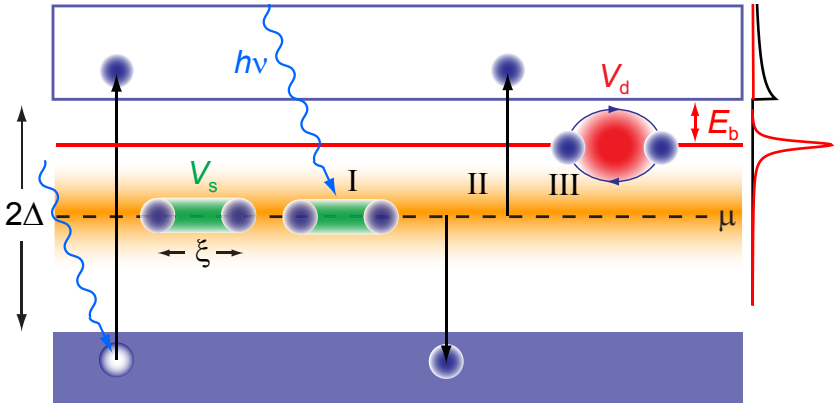

Figure 2.12: Mechanism for Bardasis-Schrieffer excitonic modes. For details and description see text.

into the δ-like peak that signals the breaking of an $L=0$ Cooper-pair and its recombination in an $L\neq 0$ exciton (Fig. 2.11). The energy difference between the δ-like peak and the gap edge reflects the relative strength of the residual interaction with respect to the binding energy of the ground state. Moreover, it was shown that the relative weights of the various $L\neq 0$ channels in the Raman spectra are determined by the polarization dependent selection rules. The effect of impurity scattering on the excitons has been studied [117–120], and it has been shown that the presence of impurities decreases the energy of the bound states causing them to move closer to the gap edge. Additionally it was shown that the strength of the $L\neq 0$ excitons diminishes rapidly with disorder [120].

The light scattering mechanism is shown schematically for an isotropic gap in Fig. 2.12. Photons ($h\nu$) scatter from both unpaired electrons in the Bogoliubov QP bands (left) and Cooper-pairs at the chemical potential μ (right) [121]. In either case an energy of at least 2Δ must be invested, and an electron-hole pair and two unpaired electrons are created, respectively. The two electrons, separated by 2Δ, which remain within a volume characterized by the coherence length ξ_0 are affected by the components of the interaction potential $V(\mathbf{k},\mathbf{k}')$ which are orthogonal to the pairing channel and form a bound state of energy E_b inside the gap. The δ-like modes appear at $\Omega_b = 2\Delta - E_b$ below the gap edge with E_b being the binding energy of the BS exciton [21,22]. E_b is related to the coupling strength in the subdominant channel via $E_b/2\Delta \approx (V_d/V_s)^2$.

Since theories that rely on spin-fluctuation pairing find that s-wave and d-wave superconductivity are two competing instabilities in multiband models of the iron-pnictides, with the s-wave instability winning the competition for the majority of parameter sets, this raises the possibility that there could be an excitonic collective mode formed by the subdominant d-wave pairing channel. It was pointed out that such a mode with angular momentum $L=2$ could be excited from an s-wave su-

perconducting state by Raman scattering [13] and that the observation of the mode would provide evidence that there is a pairing interaction in both the A_{1g} and B_{1g} pairing channels, with the A_{1g} interaction being stronger. This issue was addressed theoretically by Scalapino *et al.*, who calculated the Raman spectrum of a two-band model of iron-based superconductors, considering the residual B_{1g} pairing channel and found a collective d-wave exciton mode that appears in B_{1g} symmetry [17].

2.3 Nematic phase

FeSCs are investigated not only because of superconductivity but also for their peculiar normal-state properties. Of particular interest is the so-called nematic phase, a region of the phase diagram where the C_4 symmetry is broken but the $O(3)$ spin-rotational symmetry is preserved. The interest in the nematic phase derives from the assumption that the microscopic mechanisms behind nematicity and pairing in FeSCs are intimately connected [30, 122]. In Ch. 6, inelastic light scattering results on fluctuations of the nematic order in $Ba(Fe_{1-x}Co_x)_2As_2$ will be presented which allow for the determination of the microscopic origin of the nematic phase in this compound. Therefore, this section contains a discussion of the nematic state in FeSCs. After a brief introduction of the basic concept (Sec. 2.3.1), two microscopic models for the origin of nematicity will be introduced in Secs. 2.3.2 and 2.3.3.

2.3.1 Nematicity and its relation to the pairing mechanism

The origin of the behavior of classical complex fluids lies in the microscopic structure of the molecules, i.e. their anisotropic shapes and interactions. Upon cooling such a classical liquid, it may enter a so-called nematic phase, a state of matter in which the rotational invariance of the system gets broken spontaneously and the fluid exhibits orientational order, without showing any long-range translational order (see Fig. 2.13). In contrast, quantum versions of liquid crystal phases typically arise in strongly correlated systems whose constituents are electrons and hence are point particles. Thus the physical origin of quantum liquid crystal phases is very different from that of classical ones. Nonetheless, one uses the term electronic nematic to denote an electron fluid that spontaneously breaks a symmetry of the underlying Hamiltonian which contains the symmetry of interchanging two axes of the system. If the electrons exist in a solid, it is thus the point group symmetry of the host crystal

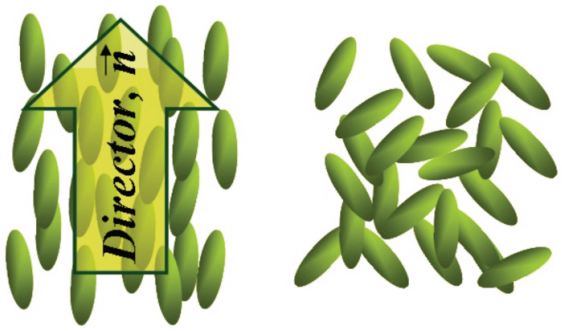

Figure 2.13: Schematic representation of a liquid crystal in the nematic phase (left) and in the isotropic phase (right). The average orientation is represented by the nematic order parameter (director) **n**. Taken from [124].

that is spontaneously broken. But still, as a characteristic feature of a nematic phase, inversion, time-reversal and translational symmetries are conserved [123].

A realization of such a phase can be found in the phase diagram of FeSCs (the dark purple shaded region in Fig. 2.6). The stripe spin-density wave order at $T<T_{\mathrm{m}}$ with ordering vectors $(0,\pi)$ or $(\pi,0)$ is often preceded by a phase with broken C_4 tetragonal symmetry, signaled by a structural distortion and the development of large anisotropies in several quantities such as dc resistivity [34,35], optical conductivity [85,125,126], local density of states [33] or orbital occupancy [32]. At the same time, long-range magnetic order is still absent, and thus the $O(3)$ spin-rotational (and time-reversal) symmetry remains unbroken. This is by definition a nematic phase. The phase transition lines T_{s} and T_{m}, which border the nematic phase, track each other across all the phase diagrams of 1111 and 122 materials [48], even inside the superconducting dome [127].

Early theoretical proposals suggested that the tetragonal-to-orthorhombic transition may be driven by electronic rather than structural degrees of freedom, since the observed electron anisotropies turned out to be much larger than explainable by a small structural distortion [30]. Two alternative scenarios for the nematic order have been proposed. One is based on orbital ordering: it induces the structural transition and triggers the magnetic transition at a lower temperature by renormalizing the exchange constants [128–138]. An alternative, magnetic scenario, relies on anisotropic spin-fluctuations which break the rotational symmetry of the lattice and, only upon further cooling down, the spin-rotational symmetry [30, 48]. This leads to an intermediate phase with a broken tetragonal symmetry but no long-range magnetic order. Orbital order is induced by the anisotropic magnetic fluctuations, since Fermi pockets at $(0,\pi)$ and $(\pi,0)$ are constituted by different orbitals.

The primary challenge is to distinguish which of the two order parameters that become both non-zero simultaneously at the structural transition, is the primary order parameter, that is, its fluctuations drive the nematic instability. The spin-

nematic order parameter is defined by a static spin susceptibility which is different along the $\mathbf{q}_x$ and $\mathbf{q}_y$ directions. In contrast, the orbital order parameter is defined, for instance, by the unequal occupation of the d_{xz} and d_{yz} orbitals.

Answering this question might turn out crucial for the understanding of superconductivity in FeSCs. If the transition at T_s is of electronic origin, then it is probably driven by the same fluctuations that give rise to superconductivity and magnetic order. The microscopic reasoning for either spin- or orbital fluctuation mediated pairing as well as magnetic or orbital scenarios for electronic nematicity follows from two different assumptions about the sign of the effective inter-pocket interaction V_{inter} [30]. Repulsive inter pocket interaction, $V_{\text{inter}} > 0$, enhances spin fluctuations and gives rise to both magnetism and nematicity. At the same time spin fluctuations peaked at $\mathbf{q}_x$ and $\mathbf{q}_y$ support either unconventional $s_\pm$ superconductivity, in which the gap has a different sign on the hole and on the electron pocket, or $d_{x^2-y^2}$ superconductivity, where the gaps on inequivalent electron pockets have opposite sign [12,30,139]. On the other hand, an attractive inter-pocket interaction, $V_{\text{inter}} < 0$, enhances orbital fluctuations peaked at $\mathbf{q}_x$ and $\mathbf{q}_y$. This supports a superconducting instability towards an s_{++} state, a conventional pairing state where the gap function has the same sign on all pockets [30, 139]. Therefore, identifying the driving force behind nematicity in FeSCs may also pin down the mechanism of superconducting pairing in these materials, as each scenario for electronic nematicity entails a particular superconducting pairing state [30, 140].

2.3.2 Spin-driven electronic nematicity

The content of this subsection largely follows the argumentation of two references by Fernandes *et al.* [30, 48]. Thereby an itinerant model is adopted in which the nature of the so-called Ising-nematic phase has a clear interpretation in terms of magnetic fluctuations. This interpretation is motivated by the observation that most Fe-based superconductors exhibit stripe type magnetic order with ordering vectors $\mathbf{q}_x = (\pi, 0)$ or $\mathbf{q}_y = (0, \pi)$, that is spins are parallel to each other along one direction and antiparallel along the other [141]. This order breaks not only the $O(3)$ spin-rotational symmetry, but it also breaks the 90° lattice rotational (C_4) symmetry to 180° (C_2) by selecting the ordering vector to be either $\mathbf{q}_x$ or $\mathbf{q}_y$ [30]. The two degenerate magnetic ground states[8] $|\psi_X\rangle$ [Fig. 2.14 (a)] and $|\psi_Y\rangle$ [Fig. 2.14 (b)] associated with $\mathbf{q}_x$ and $\mathbf{q}_y$ are described by the magnetic order parameters $\mathbf{M}_X$ and $\mathbf{M}_Y$. In terms of these order

[8] Like in an Ising AFM where spins can point either up or down, hence the name "Ising-nematic"

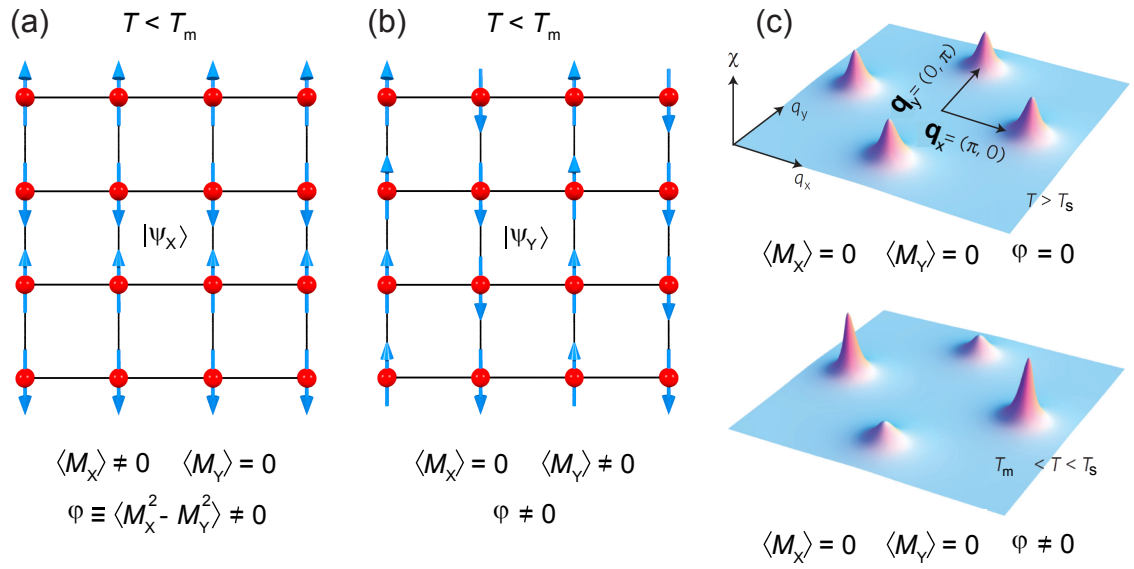

Figure 2.14: Spin nematic order in both real and momentum space. The system has two degenerate stripe magnetic ground states (a) $|\psi_{\mathrm{X}}\rangle$ and (b) $|\psi_{\mathrm{Y}}\rangle$ with ordering vectors $\mathbf{q}_{\mathrm{x}} = (\pi, 0)$ and $\mathbf{q}_{\mathrm{y}} = (0, \pi)$. (c) Onset of nematic order in the paramagnetic phase in terms of the magnetic susceptibility $\chi(\mathbf{q})$ across the first BZ. At high temperatures $T \gg T_{\mathrm{s}}$, fluctuations near the two stripe magnetic ordering vectors are equally strong, $\langle M_{\mathrm{X}}^2 \rangle = \langle M_{\mathrm{Y}}^2 \rangle$. On lowering the temperature, at T_{s} fluctuations associated with one of the stripe states become stronger (in the figure $\langle M_{\mathrm{X}}^2 \rangle > \langle M_{\mathrm{Y}}^2 \rangle$, stronger fluctuations around one ordering vector yield stronger intensity and narrower peaks [48]) and the tetragonal symmetry is broken inside the unit cell while at the same time spin rotational $O(3)$ symmetry is *not* broken since this phase transition occurs already above the magnetic ordering temperature T_{m}. Adapted from [30].

parameters, the breaking of the $O(3)$ symmetry implies $\langle M_i \rangle \neq 0$, while breaking of the tetragonal symmetry implies $\langle M_{\mathrm{X}}^2 \rangle \neq \langle M_{\mathrm{Y}}^2 \rangle$ and thus $\varphi = \langle M_{\mathrm{X}}^2 - M_{\mathrm{Y}}^2 \rangle \neq 0$ [30].

In a mean-field approach both $O(3)$ and C_4 symmetries are broken simultaneously at T_{m}. The instability towards stripe magnetic order is associated with the divergence of the static spin susceptibility $\chi_{\mathrm{mag}}(\mathbf{q})$. When the effective inter-pocket interaction V_{inter} is positive (repulsive), the spin-susceptibility gets enhanced as $\chi_{\mathrm{mag}}(\mathbf{q}) = \chi_0(\mathbf{q})/[1 - V_{\mathrm{inter}}\chi_0(\mathbf{q})]$, and at some $T = T_{\mathrm{m}}$, χ_{mag} diverges. However, including fluctuations of the nematic order parameter φ, yields [30]

$$\chi_{\mathrm{nem}} = \frac{T \sum\limits_q \chi_{\mathrm{mag}}^2(\mathbf{q})}{1 - gT \sum\limits_q \chi_{\mathrm{mag}}^2(\mathbf{q})} \tag{2.5}$$

where T is the temperature, g the nematic coupling constant and χ_{mag} is the magnetic susceptibility. $\sum_q \chi_{\mathrm{mag}}^2(\mathbf{q})$ diverges at T_{m}. Eq. (2.5) then shows that the nematic susceptibility diverges at higher temperature $T_{\mathrm{s}} > T_{\mathrm{m}}$, namely when

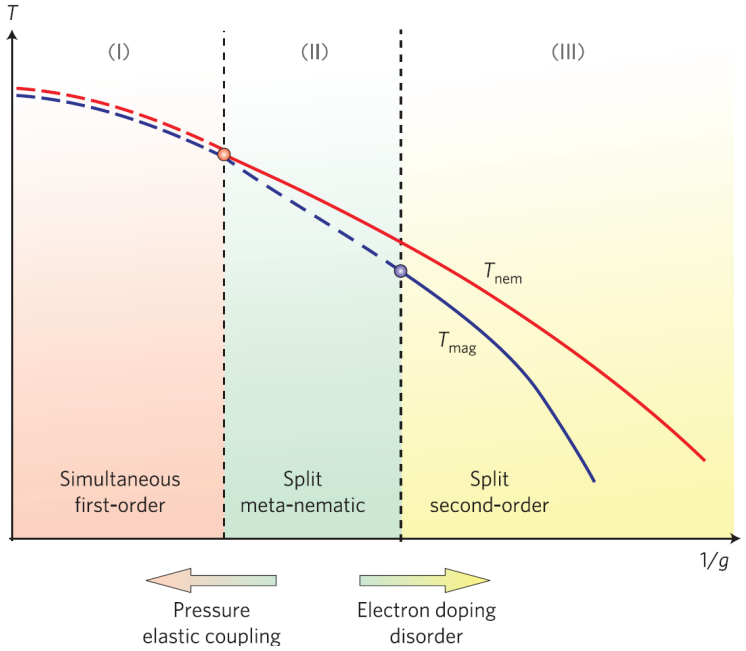

Figure 2.15: Evolution of the character of the magnetic and nematic transitions in the spin-driven nematic theory. The inverse nematic coupling g acts as control parameter, which changes as a function of doping, disorder, pressure and elastic coupling. Adopted from reference [30].

$gT\sum_q \chi^2_{\mathrm{mag}}(\mathbf{q}) = 1$, that is at sufficiently large but still finite magnetic correlation length. Thus, fluctuations split the two transitions giving rise to an intermediate phase at $T_{\mathrm{m}} < T < T_{\mathrm{s}}$, where the tetragonal symmetry is broken ($\varphi \neq 0$) but the spin-rotational symmetry is not ($\langle M_i \rangle = 0$) [48]. This is by definition a nematic order which is driven by spin fluctuations of unequal strength in the $\mathbf{q}_{\mathrm{x}}$ and $\mathbf{q}_{\mathrm{y}}$ directions.

The nematic coupling strength g sets, if positive, the magnetic ground state of the system to be of the stripe type. It is linked to the inter pocket interaction ($g \propto V^2_{\mathrm{inter}}$) and its strength determines the character of the magnetic and nematic transitions in the spin-driven nematic theory. The inverse nematic coupling g, which changes as a function of various control parameters like pressure or doping, determines if the phase transitions are first or second order (see Fig. 2.15). Eq. (2.5) is not limited to the itinerant approach employed in [30] and [48] but emerges in a similar fashion from any model of stripe magnetism, the only difference being the microscopic expression for the nematic coupling g [30]. Moreover, Eq. (2.5) naturally ties the nematic and magnetic transition temperatures over the entire phase diagram without fine-tuning of parameters which provides a strong argument in favor of spin-driven nematicity.

In the Ising-nematic model the tetragonal to orthorhombic structural transition is triggered by anisotropic spin fluctuations which also impose orbital order, because

the Fermi pockets centered at $(\pi, 0)$ and $(0, \pi)$ have different orbital character. In this scenario the orbital and Ising-nematic order parameters are linearly coupled via $\langle \Delta_{\mathrm{Orb}} \rangle = \omega/a \langle M_{\mathrm{X}}^2 - M_{\mathrm{Y}}^2 \rangle$, with a the tetragonal lattice constant and ω describing the coupling strength [48], i.e., the development of one order triggers the development of the other. The same reasoning also applies to the interplay between the Ising-nematic and orthorhombic orders. Their order parameters are also linearly linked via $\langle \varepsilon_{\mathrm{s}} \rangle = \lambda_{\mathrm{sl}}/c_0^{\mathrm{s}} \langle M_{\mathrm{X}}^2 - M_{\mathrm{Y}}^2 \rangle$, with λ_{sl} being the magneto-elastic coupling constant and c_0^{s} the shear modulus. Note that the coupling to structural degrees of freedom also renormalizes the nematic coupling constant as [48]

$$\tilde{g} = g + \frac{\lambda_{\mathrm{sl}}^2}{c_0^{\mathrm{s}}}. \tag{2.6}$$

Finally, the anisotropy in the spectrum of magnetic fluctuations leads to anisotropic scattering of electrons, resulting in different in-plane resistivities along x and y directions [142].

It is currently under debate whether the Ising-nematic and the structural transition occur at the same temperature or if the nematic order sets in at much higher temperatures than T_{s}. Transport studies on *detwinned* crystals found a strong resistivity anisotropy that emerges below the structural transition temperature T_{s} [34] (which is also the temperature at which the orbital order arises). On the other hand, recent magnetic torque [46], scanning tunneling spectroscopy [45] and inelastic neutron scattering [143] experiments, also with *detwinned* crystals, suggest that the nematic order sets in at higher T. This is as well possible within the Ising-nematic model as the proportionally coefficient ω scales with the chemical potential μ (and thus with doping) and is, generally, small. As a result, if the orthorhombic order is induced by Ising-nematic order at $T = T_{\mathrm{s}}$, the orthorhombic order parameter is initially small and may become visible only at some distance below the Ising-nematic transition [48].

2.3.3 Orbital-driven electronic nematicity

The simplest model for orbital driven nematicity is very similar to the one introduced above. The main difference is the sign of the interaction V_{inter} between electron and hole pockets. If it is negative, the orbital susceptibility is enhanced rather than the the spin susceptibility as $\chi_{\mathrm{orb}}(\mathbf{q}) = \chi_0(\mathbf{q})/[1 + V_{\mathrm{inter}}\chi_0(\mathbf{q})]$ diverges at $\mathbf{q}_{\mathrm{x}}$ or $\mathbf{q}_{\mathrm{y}}$ at a certain T_{orb}. This divergence would signal the onset of an orbitally ordered state with ordering vectors $\mathbf{q}_{\mathrm{x}}$ or $\mathbf{q}_{\mathrm{y}}$ corresponding to the order parameters W_{X} and W_{Y}. Such

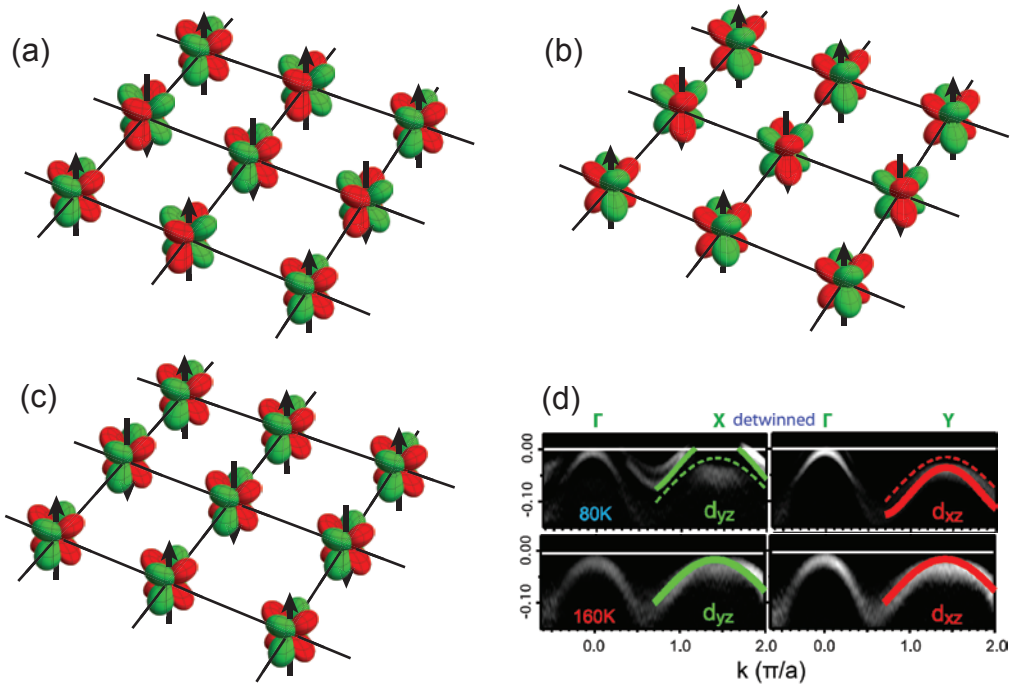

Figure 2.16: (a) Antiferro-, (b) stripe- and (c) ferro-orbital ordered states possibly stable together with a spin-stripe state in FeSCs [128]. (d) Only ferro-OO has been observed experimentally within ARPES experiments [32].

an order breaks the translational symmetry and, like in the magnetic scenario, breaks also an additional C_4 symmetry if only one order parameter becomes non-zero. Fluctuations could then as well split the temperatures at which the translational and the C_4 symmetries are broken, in a similar manner to Eq. (2.5). Then, in the intermediate temperature range $T_{\mathrm{orb}} < T < T_{\mathrm{nem}}$, the system spontaneously develops an orbital order in which $\langle W_{\mathrm{X}}^2 \rangle \neq \langle W_{\mathrm{Y}}^2 \rangle$ while $\langle W_{\mathrm{X}} \rangle = \langle W_{\mathrm{Y}} \rangle = 0$. A structural distortion and the difference between $\langle M_X^2 \rangle$ and $\langle M_Y^2 \rangle$ appear instantly once orbital order sets in. However, in such a scenario magnetic order is not naturally linked to nematicity [30, 48].

It has been shown, starting from a strong-coupling viewpoint, that three different types of orbital order (OO) could be realized accompanying the stable experimentally observed spin-stripe state in FeSCs [128]. Those are the so-called antiferro-, stripe- and ferro-orbital ordered states, depicted in Fig. 2.16 (a), (b) and (c), respectively. Of these, only the latter two break the in-plane rotational symmetry, possibly giving rise to nematicity.

Ferro-OO is the unequal occupation of the bands deriving from d_{xz} and d_{yz} orbitals. An examination of Fig. 2.16 (c) reveals that there is no finite ordering vector associated with ferro-OO, or in other words, its ordering vector is $\mathbf{q}_{\mathrm{c}}^{\mathrm{ferro}} = (0, 0)$.

Ferro-OO has been experimentally detected within ARPES (Fig. 2.16 (d), [32]) and X-ray linear dichroism (XLD) [144] experiments on detwinned $Ba(Fe_{1-x}Co_x)_2As_2$ samples. The ARPES experiment finds a splitting of the originally degenerate d_{xz} and d_{yz} bands occurring at the structural transition and having a magnitude of approximately 60 meV. In addition, the electronic anisotropy seen in the orbital degree of freedom is observed at temperatures well above the structural transition in *detwinned* crystals, while orbital order is absent above T_s in samples where no detwinning stress is applied. The XLD experiment confirms both, the existence of ferro-OO below T_s and the OO-signal well above the structural and magnetic transition temperatures in detwinned samples. Moreover, the presence of ferro-OO can also explain the experimentally observed in-plane resistivity anisotropy [137].

Stripe-OO corresponds to the formation of zigzag chains of d_{xz} and d_{yz} orbitals along the antiferromagnetically coupled spin-direction [Fig. 2.16 (d)]. Interestingly, the stripes in the magnetic and orbital sectors have the same orientations and thus exhibit an ordering vector $\mathbf{q}_c^{\text{stripe}} = (0, \pi)$ equivalent with the SDW vector. Stripe-OO is also the only one which would fit to the simple orbital driven nematic scenario outlined above. However, stripe-OO is expected to lead to a displacement pattern of the As ions, which can in principle be observed in X-ray diffraction experiments and might even be directly visible within resonant X-ray diffraction at the iron K-edge [128]. However, this has not been observed experimentally suggesting that from the three possible orbitally ordered states shown in Fig. 2.16 (a)-(c), ferro-OO is the one which is realized, at least in $Ba(Fe_{1-x}Co_x)_2As_2$.

Chapter 3

Theory of electronic Raman scattering

It is the purpose of this chapter to give a brief summary of the theoretical concepts which are essential for the understanding of the experimental results and their implications presented in this thesis. It is, however, not intended to give a pedagogical introduction into Raman scattering. The reader who prefers a more detailed introduction to the subject is referred to the review article by Devereaux and Hackl [19] and references therein.

3.1 The Raman effect

Raman scattering is the inelastic scattering of (visible) light, in which an incident photon characterized by $(\mathbf{k}_i, \omega_i, \mathbf{e}_i)$ is scattered into another state $(\mathbf{k}_s, \omega_s, \mathbf{e}_s)$, thereby transferring energy and momentum to a target material. During this instantaneous process, which takes place within the time interval Δt, the material makes a transition from an initial $|I\rangle$ to a final state $|F\rangle$ via a (virtual) intermediate level $|\nu\rangle$. If $|F\rangle$ is lower (higher) in energy than $|I\rangle$, the process is called an Anti-Stokes (Stokes) process. Both cases are illustrated in Fig. 3.1 (a) and (b). Since the process must satisfy energy and momentum conservation

$$\hbar\Omega = \hbar\omega_i - \hbar\omega_s \tag{3.1}$$

$$\hbar\mathbf{q} = \hbar\mathbf{k}_i - \hbar\mathbf{k}_s, \tag{3.2}$$

scattered photons exhibit a blue shift $-\hbar\Omega$ (red shift $\hbar\Omega$) with respect to the incident

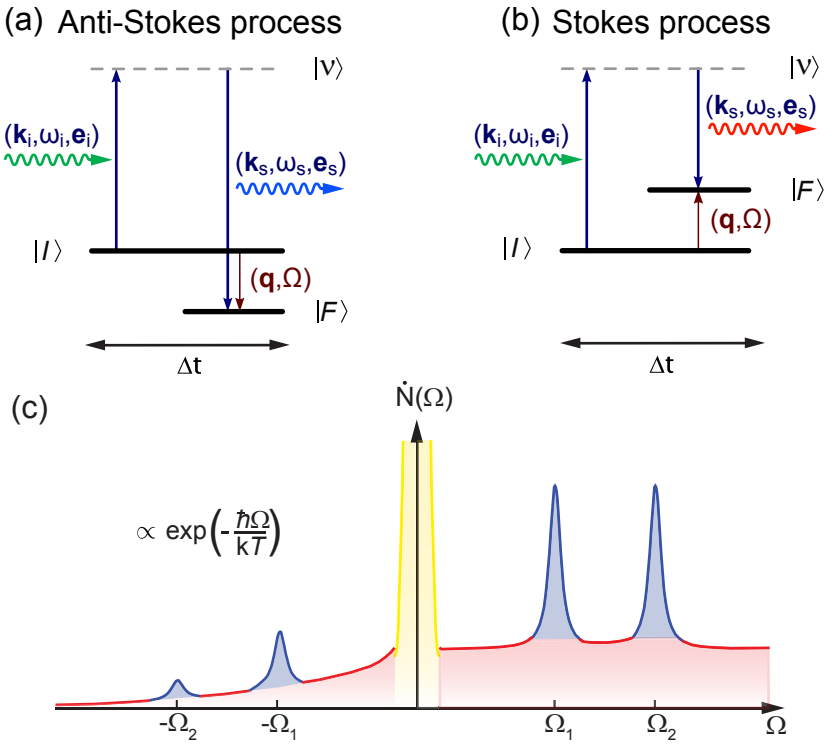

Figure 3.1: Anti-Stokes (a) and Stokes (b) process. In the former case, an excitation is annihilated in the sample while in the latter case an excitation is created. The scattered photon thus is blue- (red-) shifted with respect to the incident photon. $\hbar\mathbf{k}_i$ ($\hbar\mathbf{k}_s$) is the momentum, $\hbar\omega_i$ ($\hbar\omega_i$) the energy and $\mathbf{e}_i$ ($\mathbf{e}_s$) the complex polarization vector of the incident (scattered) photon. (c) Schematic Raman spectrum with contributions from phonons (blue) and electrons (red) in the Anti-Stokes and Stokes channel. The intensity of excitations in the Anti-Stokes channel is weaker by a factor of $\exp(-\hbar\Omega/\mathrm{k}T)$, see Sec. 3.3. The peak at $\Omega = 0$ (yellow) corresponds to elastic scattering of photons.

photons in an Anti-Stokes (Stokes) process. The low temperature Raman studies presented in Chs. 5 and 6 show Stokes spectra, as on this side the intensity does not decay exponentially with decreasing temperature.

3.2 Coupling to light via electrons

In a solid, inelastic scattering of light induces variations of the electronic charge density in the illuminated region of a sample which may lead to the creation of many types of excitations. When high energy electron-hole pairs excited by the photons couple to the conduction electrons of a metal the process is referred to as electronic Raman scattering (ERS). The fraction of inelastically scattered light contains information about the excitations, manifested in characteristic signatures in the Raman spectrum. Such a spectrum is illustrated schematically in Fig. 3.1 (c). The sharp

peaks (blue) correspond to optical phonons which sit on top of a continuum of particle-hole excitations (red). Experimentally, Raman spectroscopy measures the rate of photons with frequency ω_i that are scattered into a solid angle interval between Ω and $d\Omega$ and a frequency window between ω_s and $d\omega_s$ per second. This rate is proportional to the differential light scattering cross section

$$\dot{N}(\omega, T) \propto \frac{\partial^2 \sigma}{\partial \Omega \, \partial \omega_s} = \hbar r_0^2 \, \frac{\omega_s}{\omega_i} \, \mathcal{R}, \tag{3.3}$$

where $r_0 = e^2/4\pi\varepsilon_0 mc^2$ is the Thomson radius of an electron, and $\mathcal{R}$ the transition rate determined via Fermi's golden rule,

$$\mathcal{R} = \frac{1}{\mathcal{Z}} \sum_{I,F} \exp^{-\beta E_I} \, |M_{F,I}|^2 \, \delta(E_F - E_I - \hbar\Omega), \tag{3.4}$$

with $\mathcal{Z}$ the partition function, $\beta = 1/k_\mathrm{B}T$ and $M_{F,I} = \langle F| \, M \, |I\rangle$ the transition matrix element with the effective light scattering operator M which describes the interaction between light and sample. The sum represents a thermodynamic average over possible initial and final states with $\mathbf{k}$ vectors in the solid angle element $d\Omega$ of the many-electron system having energies E_I, E_F, respectively.

A general expression for the matrix element $M_{F,I}$ for Raman scattering is found considering a Hamiltonian for N electrons coupled to an electromagnetic field [145, 146]:

$$H = \sum_i^N \frac{[\hat{\mathbf{p}}_i + (e/c)\hat{\mathbf{A}}(\mathbf{r}_i)]^2}{2m} + H_\mathrm{Coulomb} + H_\mathrm{fields}, \tag{3.5}$$

where $\hat{\mathbf{p}} = -i\hbar\nabla$ is the momentum operator, e is the magnitude of the elementary charge, and c is the speed of light. $\hat{\mathbf{A}}(\mathbf{r}_i)$ is the vector potential of the field at $\mathbf{r}_i$ and m is the electron mass. H_Coulomb represents the Coulomb interaction and H_fields is the free electromagnetic part. Expanding the kinetic energy yields

$$\begin{aligned} H = H_0 + H_\mathrm{fields} \quad &+ \underbrace{\frac{e}{2mc} \sum_i [\hat{\mathbf{p}}_i \cdot \hat{\mathbf{A}}(\mathbf{r}_i) + \hat{\mathbf{A}}(\mathbf{r}_i) \cdot \hat{\mathbf{p}}_i]}_{H_\mathrm{I}} \\ &+ \underbrace{\frac{e^2}{2mc^2} \sum_i \hat{\mathbf{A}}(\mathbf{r}_i) \cdot \hat{\mathbf{A}}(\mathbf{r}_i)}_{H_\mathrm{II}}, \end{aligned} \tag{3.6}$$

with $H_0 = (1/2m) \sum_i \hat{\mathbf{p}}_i^2 + H_\mathrm{Coulomb}$ the unperturbed Hamiltonian of the electron

system. $M_{F,I}$ has contributions from either of the last three terms in Eq. (3.6). H_{I} couples the electron's current to a single photon and H_{II} couples the electron's charge to two photons. Let $|\alpha\rangle$ denote eigenstates of H_0 with eigenvalues E_α: $H_0 |\alpha\rangle = E_\alpha |\alpha\rangle$. Then, the general expression for the matrix elements of $M = H_{\mathrm{I}} + H_{\mathrm{II}}$ in second quantized notation[1] reads [19]

$$\begin{aligned} M_{F,I} &= \mathbf{e}_i \cdot \mathbf{e}_s \sum_{\alpha,\beta} \rho_{\alpha,\beta}(\mathbf{q}) \langle F| c_\alpha^\dagger c_\beta |I\rangle \\ &\quad + \frac{1}{m} \sum_{\nu} \sum_{\alpha,\alpha',\beta,\beta'} p_{\alpha,\alpha'}(\mathbf{q}_s)\, p_{\beta,\beta'}(\mathbf{q}_i) \\ &\quad \times \left(\frac{\langle F| c_\alpha^\dagger c_{\alpha'} |\nu\rangle \langle \nu| c_\beta^\dagger c_{\beta'} |I\rangle}{E_I - E_\nu + \hbar\omega_i} \right. \\ &\quad \left. + \frac{\langle F| c_\beta^\dagger c_{\beta'} |\nu\rangle \langle \nu| c_\alpha^\dagger c_{\alpha'} |I\rangle}{E_I - E_\nu - \hbar\omega_s} \right). \end{aligned} \tag{3.7}$$

Here $|I\rangle$, $|F\rangle$, $|\nu\rangle$ represent the initial, final and intermediate many-electron states having energies $E_{I,F,\nu}$, respectively. $\rho_{\alpha,\beta}(\mathbf{q}) = \int d^3r \varphi_\alpha^*(\mathbf{r}) e^{i\mathbf{q}\cdot\mathbf{r}} \varphi_\beta(\mathbf{r}) = \langle \alpha| e^{i\mathbf{q}\cdot\mathbf{r}} |\beta\rangle$ is the matrix element for single-particle density fluctuations involving states α, β and the momentum density matrix element is given by $p_{\alpha,\beta}(\mathbf{q}_{i,s}) = \langle \alpha| \mathbf{p} \cdot \mathbf{e}_{i,s} e^{\pm i\mathbf{q}_{i,s}\cdot\mathbf{r}} |\beta\rangle$. The first term in the expression arises from the two-photon scattering term H_{II} in Eq. (3.6) in *first*-order perturbation theory. The remaining terms arise from the single-photon scattering term H_{I} in Eq. (3.6) in *second*-order perturbation theory via intermediate states ν and involve different time-orderings of photon absorption and emission. The $\mathbf{p}\cdot\mathbf{A}$ coupling does not enter $M_{F,I}$ in *first*-order since the average of the momentum operator is zero.

At this point, simplifying assumptions have to be made in order to evaluate the matrix elements for Raman scattering in Eq. (3.7). In the following, the limit of noninteracting electrons is discussed.

[1] The single-particle wave function and its conjugate are given by $\psi(\mathbf{r}) = \sum_\alpha c_\alpha \varphi_\alpha(\mathbf{r})$ and $\psi^\dagger(\mathbf{r}) = \sum_\alpha c_\alpha^\dagger \varphi_\alpha^*(\mathbf{r})$ with φ, φ^* the eigenstates of the Hamiltonian H_0. Electron states α, β are created or annihilated by $c_\alpha^\dagger$, c_β, respectively, and the indices refer to the quantum numbers associated with the state.

3.3 Single-particle excitations and weak correlations

Assuming that the intermediate many-particle states only differ from the initial and final states by single-electron excitations, Eq. (3.7) can be simplified by replacing E_ν in the denominators by $E_I - E_{\beta'} + E_\beta$ and $E_I - E_{\alpha'} + E_\alpha$ in the first and second terms, respectively, and using the closure relation $\sum_\nu |\nu\rangle \langle\nu| = 1$. Commutator algebra eliminates the four-fermion matrix element and

$$M_{F,I} = \sum_{\alpha,\beta} \gamma_{\alpha,\beta} \, \langle F| \, c_\alpha^\dagger c_\beta \, |I\rangle \,, \tag{3.8}$$

where

$$\gamma_{\alpha,\beta} = \rho_{\alpha,\beta}(\mathbf{q}) \, \mathbf{e}_i \cdot \mathbf{e}_s + \frac{1}{m} \sum_{\beta'} \left(\frac{p^s_{\alpha,\beta'} p^i_{\beta',\beta}}{E_\beta - E_{\beta'} + \hbar\omega_i} + \frac{p^i_{\alpha,\beta'} p^s_{\beta',\beta}}{E_\beta - E_{\beta'} - \hbar\omega_s} \right). \tag{3.9}$$

Now the Raman response [Eq. (3.3)] simplifies to a correlation function $\tilde{S}$ of an effective charge density $\tilde{\rho}$,

$$\frac{\partial^2\sigma}{\partial\Omega \, \partial\omega_s} = \hbar r_0^2 \, \frac{\omega_s}{\omega_i} \, \tilde{S}(\mathbf{q}, i\Omega \to \Omega + i0). \tag{3.10}$$

Here the Raman effective density-density correlation function is

$$\tilde{S}(\mathbf{q}, i\Omega) = \sum_I \frac{e^{-\beta E_I}}{\mathcal{Z}} \int d\tau \, e^{i\Omega\tau} \, \langle I| \, T_\tau \, \tilde{\rho}(\mathbf{q}, \tau) \tilde{\rho}(-\mathbf{q}, 0) \, |I\rangle \,, \tag{3.11}$$

T_τ is the complex time τ ordering operator, and

$$\tilde{\rho}(\mathbf{q}) = \sum_{\mathbf{k},\sigma} \gamma(\mathbf{k}, \mathbf{q}) \, c^\dagger_{\mathbf{k}+\mathbf{q},\sigma} c_{\mathbf{k},\sigma}. \tag{3.12}$$

the effective charge density operator representing a weighed momentum average of the charge density. Here $c^\dagger_{\mathbf{k}+\mathbf{q},\sigma}$ and $c_{\mathbf{k},\sigma}$ are the creation and annihilation operators of the electrons with spin σ and momentum $\mathbf{k}+\mathbf{q}$ and $\mathbf{k}$, respectively. The scattering amplitude (or Raman vertex) $\gamma(\mathbf{k}, \mathbf{q})$ is determined from the Raman matrix elements and polarization vectors of incident and scattered photons as

$$\gamma(\mathbf{k}, \mathbf{q}) = \sum_{\alpha,\beta} e_i^\alpha \gamma_{\alpha,\beta}(\mathbf{k}, \mathbf{q}) e_s^\beta. \tag{3.13}$$

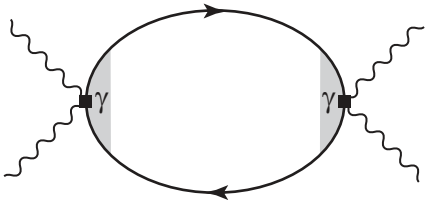

Figure 3.2: Feynman diagram of the polarization bubble. Wavy and solid lines represent photonic and fermionic propagators, respectively. γ denotes the k-dependent Raman vertex.

The Raman vertex is a 3×3 tensor from which elements are projected out according to Eq. (3.13). The single tensor components read

$$\gamma_{\alpha,\beta}(\mathbf{k},\mathbf{q}) = \delta_{\alpha,\beta} + \frac{1}{m}\sum_{\mathbf{k}_\nu}\left(\frac{\langle\mathbf{k}+\mathbf{q}|\, p_s^\beta\, |\mathbf{k}_\nu\rangle\, \langle\mathbf{k}_\nu|\, p_i^\alpha\, |\mathbf{k}\rangle}{E_\mathbf{k} - E_{\mathbf{k}_\nu} + \hbar\omega_i} + \frac{\langle\mathbf{k}+\mathbf{q}|\, p_i^\alpha\, |\mathbf{k}_\nu\rangle\, \langle\mathbf{k}_\nu|\, p_s^\beta\, |\mathbf{k}\rangle}{E_{\mathbf{k}+\mathbf{q}} - E_{\mathbf{k}_\nu} - \hbar\omega_s}\right) \tag{3.14}$$

with $p_{i,s}^\alpha = p^\alpha e^{\pm i\mathbf{q}_{i,s}\cdot\mathbf{r}}$ the projected momentum operators.

Returning to Eq. (3.11) and noting that, in general, a correlation function $\tilde{S}_{AB}(\mathbf{r},t) := \langle\hat{A}(\mathbf{r},t)\hat{B}(0,0)\rangle$ of two observables $\hat{A}(\mathbf{r},t)$ and $\hat{B}(\mathbf{r},t)$ is given in terms of a susceptibility via the fluctuation-dissipation theorem $\chi''_{AB}(\Omega) = (2\hbar)^{-1}(1 - e^{-\hbar\Omega/\mathrm{k}T})\tilde{S}_{AB}(\Omega)$ [147, 148], $\tilde{S}$ can be written as

$$\tilde{S}(\mathbf{q},\Omega) = -\frac{1}{\pi}\{1+n(\Omega,T)\}\,\tilde{\chi}''_{\gamma\gamma}(\mathbf{q},\Omega), \tag{3.15}$$

with $n(\Omega,T)$ the Bose-Einstein distribution and

$$\tilde{\chi}_{\gamma\gamma}(\mathbf{q},\Omega) = \int_0^{1/T} d\tau e^{-i\Omega\tau}\,\langle T_\tau[\tilde{\rho}_\mathbf{q}(\tau)\tilde{\rho}_{-\mathbf{q}}(0)]\rangle. \tag{3.16}$$

Thus for noninteracting electrons the Raman response is given as a two-particle effective density correlation function and can be calculated using, e.g., diagrammatic techniques. The Feynman diagram which has to be evaluated in this case is shown in Fig. 3.2. It describes the creation of electron-hole pairs within a single band. The wavy and solid lines represent photonic and fermionic propagators (Green's functions) and the black squares correspond to the vertices γ depending upon the incident and scattered photon frequencies.

Using the principle of detailed balance, $S_{BA}(-\Omega) = e^{-\hbar\Omega/\mathrm{k}T}S_{AB}(\Omega)$, another useful expression can be obtained: With Eqs. (3.3) and (3.11), in the important case of small frequency shifts $\Omega \ll \omega_i$, the intensities of scattered photons from a Stokes and anti-Stokes process are connected as

$$\frac{\dot{N}_{AS}}{\dot{N}_{ST}} = \exp\left(-\frac{\hbar\Omega}{\mathrm{k}T}\right). \tag{3.17}$$

Eq. (3.17) can be used to determine the temperature of the laser spot. The exponential decay of the scattering intensity on the AS side was already shown in Fig. 3.1 (c).

The charge fluctuations inside the unit cell created by light scattering are coupled via the long range Coulomb interaction to charge fluctuations in other cells. Therefore, screening effects have to be considered which reduce the scattering cross section at small q. The general expression for the screened Raman response function $\chi^{sc}_{\gamma,\gamma}$ can be written as [22, 24]

$$\chi^{sc}_{\gamma,\gamma} = \chi_{\gamma,\gamma} + \frac{\chi_{\gamma,1}\chi_{1,\gamma}}{\chi_{1,1}} + \frac{\chi_{\gamma,1}\chi_{1,\gamma}}{\chi^2_{1,1}}\chi_{sc} \tag{3.18}$$

where $\chi_{sc} = \chi_{1,1}(1-\nu_q\chi_{1,1})^{-1}$. In the expression, the subscript γ denotes the effective Raman density and 1 denotes the pure charge density, obtained when the momentum-dependent vertex γ is replaced by a constant. The first term is the bare response for a neutral system and the other terms represent the backflow needed to enforce particle number conservation and gauge invariance. These terms are important for light scattering configurations which transform according to the symmetry of the lattice, such as A_{1g} in D_{4h} crystals. For crossed light polarizations projecting out representations of lower symmetry than that of the lattice (for instance B_{1g} and B_{2g} in a D_{4h} crystal) backflow terms make no corrections to the Raman scattering cross section [19].

3.4 Selection rules

The sum over the intermediate states $\mathbf{k}_\nu$ in Eq. (3.14) includes states of the conduction band as well as states separated from the conduction band. Now the fact can be used that the vertex $\gamma_{\alpha,\beta}(\mathbf{k},\mathbf{q})$ depends on polarization, but does not depend sensitively on $\mathbf{q}$ for $q \ll k_F$. In this case, matrix elements for transitions into the conduction band are smaller by a factor of (ν_F/c^2) than the other terms and can be neglected [145]. In addition, if one excludes resonant scattering by assuming that $\hbar\omega_{i,s} \ll |\varepsilon_{\mathbf{k}_\nu} - \varepsilon_{\mathbf{k}}|$, the widely used effective-mass approximation

$$\gamma_{\alpha,\beta}(\mathbf{k}, q\to 0) \propto \frac{1}{\hbar^2}\frac{\partial^2\varepsilon_{\mathbf{k}}}{\partial k_\alpha \partial k_\beta} \tag{3.19}$$

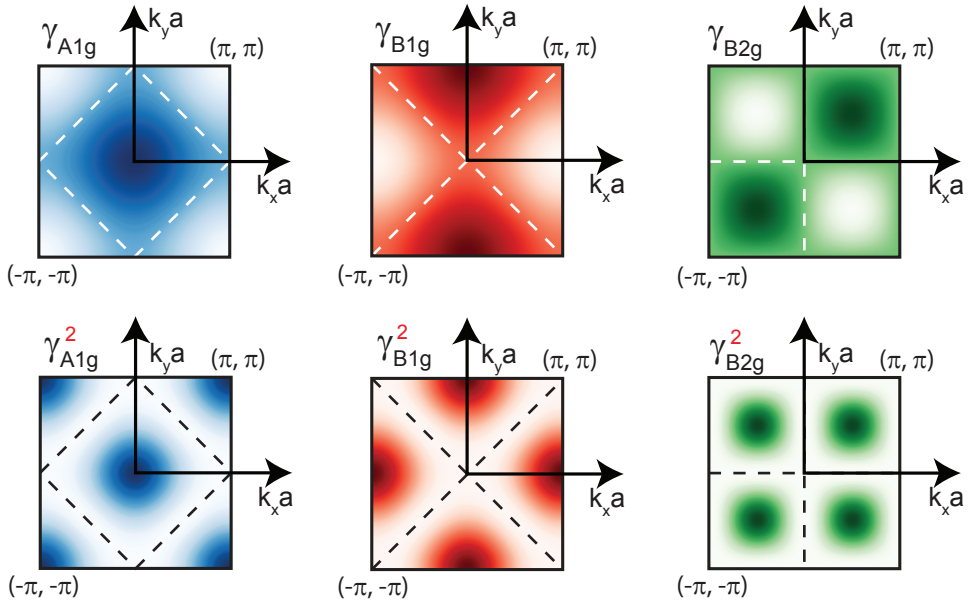

Figure 3.3: Top: Schematic illustration of first order Raman vertices γ_μ for polarization orientations transforming as $\mu = A_{1g}$, B_{1g} and B_{2g} for a D_{4h} crystal. Bottom: γ_μ^2 gives the weighing of the light-scattering transition. Taken from [150].

is recovered (see Appendix E in [149]). The Raman vertex is thus proportional to the second derivatives of the conduction band $\varepsilon_{\mathbf{k}}$ projected by the polarization vectors of incident and scattered photons[2]. Thus the curvature of the bands and the orientations of the light polarizations determine which carriers close to the FS are involved in the light scattering process in different regions of the Brillouin zone. If a model band structure is available, which can be obtained, for instance, by a tight-binding fit to a DFT band structure, details in the Raman response can be traced back to specific portions of the FS.

However, even without detailed knowledge of the band structure, symmetry arguments can be applied to gain insight into the types of excitations created by incident photons. The polarization dependence of Raman scattering can be generally classified using arguments of group theory. The charge-density fluctuations brought about by light scattering are modulated in directions determined by the polarizations of the incident and scattered photons. Therefore, these density fluctuations have a symmetry determined by the way in which the light is oriented. As a result, the charge-density fluctuations obey the symmetry rules associated with

[2]In the experiment, e_i^α and e_s^β are usually chosen to point along the crystal axes of the system under investigation. In cuprates or in iron-based systems, both having tetragonal crystal-structure and a FS topology with quasi-2D character, one is often interested in the carrier dynamics in the ab plane and $k_{\alpha,\beta}$ are momenta pointing along the a or b axis of the crystal.

the scattering geometry. The Raman matrix elements $M_{F,I}$ can be decomposed into basis functions Φ_μ of the irreducible point group of the crystal [21, 22, 151–153]

$$M_{F,I}(\mathbf{q} \to 0) = \sum_\mu M_\mu \Phi_\mu, \tag{3.20}$$

with μ representing an irreducible representation of the point group. Which set of μ contributes to the sum is determined by the orientation of incident and scattered polarization directions. For the D_{4h} group of the tetragonal lattice, relevant for cuprates and iron-based systems, the decomposition reads [19]

$$\begin{aligned} M_{F,I} \;=\; & \frac{1}{2}\mathcal{O}_{A_{1g}^{(1)}}(e_i^x e_s^x + e_i^y e_s^y) + \frac{1}{2}\mathcal{O}_{A_{1g}^{(2)}}(e_i^z e_s^z) \\ & + \frac{1}{2}\mathcal{O}_{B_{1g}}(e_i^x e_s^x - e_i^y e_s^y) \;+\; \frac{1}{2}\mathcal{O}_{B_{2g}}(e_i^x e_s^y - e_i^y e_s^x) \\ & + \frac{1}{2}\mathcal{O}_{A_{2g}}(e_i^x e_s^y - e_i^y e_s^x) \;+\; \frac{1}{2}\mathcal{O}_{E_g^{(1)}}(e_i^x e_s^z + e_i^z e_s^x) \\ & + \frac{1}{2}\mathcal{O}_{E_g^{(2)}}(e_i^y e_s^z + e_i^z e_s^y) \end{aligned} \tag{3.21}$$

with the projected operators $\mathcal{O}_\mu$ describing the light-matter interaction. Eq. (3.21) connects the light polarizations $e_{i,s}^{x,y,z}$ with the symmetry contributions to the matrix element. The basis functions (e.g. crystal harmonics) of the D_{4h} point group have already been introduced in Sec. 2.2.1 (see Fig. 2.8). Since the Raman vertex $\gamma(\mathbf{k}, q \to 0)$ has the same symmetry as the matrix elements [19] it can be expanded into the same set of basis functions $\Phi_\mu(\mathbf{k})$. A subset of D_{4h} vertex components (A_{1g}, B_{1g} and B_{2g}) is shown in Fig. 3.3.

The scattering intensity is proportional to $|M_{FI}|^2$ and therefore the Raman response is proportional to $\gamma^2(\mathbf{k}, q \to 0)$, displayed in Fig. 3.3. Considering the generic FS of FeSCs (Fig. 2.2), it is evident that polarizations projecting out the A_{1g} symmetry highlight the Raman response of excitations on the hole bands. The Raman response of excitations on the electron pockets is obtained choosing polarizations projecting out the B_{1g} symmetry. On the other hand, since in the case of FeSCs the B_{2g} vertex component is sensitive in regions of the BZ where no bands cross the Fermi-level, the Raman response in this channel is expected to be small.

From Eq. (3.21), one observes that in most cases the pure symmetries cannot be accessed individually by a single set of polarizations, but that a linear combination of two symmetries is obtained from most combinations of light scattering polarizations. Fig. 3.4 summarizes all in-plane polarization combinations and the related obtained

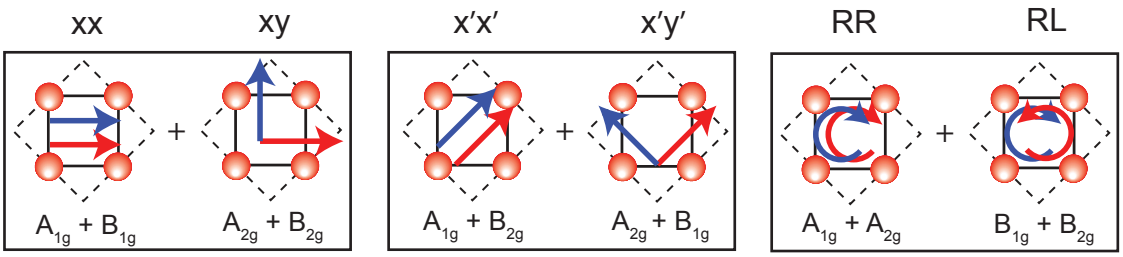

Figure 3.4: Scattering geometry of incoming (blue arrow) and scattered photons (red arrow) and projected symmetries for the *ab* plane of an FeSCs. The red spheres mark the position of the Fe atoms and the solid and dashed lines are the 1 Fe and 2 Fe unit cell (as adopted from [150]).

symmetries. Using the linear combinations

$$\begin{aligned} I_{\mathrm{A1g}} &= (1/3)[(xx + x'x' + RR) - (1/2)\,(xy + x'y' + RL)], \\ I_{\mathrm{A2g}} &= (1/3)[(xy + x'y' + RR) - (1/2)\,(xx + x'x' + RL)], \\ I_{\mathrm{B1g}} &= (1/3)[(xy + x'x' + RL) - (1/2)\,(xx + x'y' + RR)], \\ I_{\mathrm{B2g}} &= (1/3)[(xx + x'y' + RL) - (1/2)\,(xy + x'x' + RR)], \end{aligned} \tag{3.22}$$

the individual symmetry contributions are accessed. Thus, due to the dependence of the light scattering rate on $\mathbf{k}$, Raman scattering is one of the few spectroscopic probes able to examine charge excitations in different regions of the Brillouin zone.

3.5 Finite correlations

In the following, inelastic light scattering in systems with electronic correlations is shortly addressed. Interactions between electrons or electrons and lattice are essential for the formation of the superconducting state and lead to a variety of excitations in a solid which can be probed by electronic Raman scattering.

3.5.1 Normal state: particle-hole excitations

It was shown in Sec. 3.3 for weak correlations that to obtain the Raman response function $\chi''_{\gamma\gamma}$ for the creation of particle-hole excitations, one has to evaluate the bubble-diagram depicted in Fig. 3.2. The electrons are, in this limit, described by the so-called bare propagator, or Green's function $G^0(\mathbf{k}, z) = (z - \xi_{\mathbf{k}})^{-1}$ with $\xi_{\mathbf{k}} = \varepsilon_{\mathbf{k}} - \mu$ denoting the bare electronic band dispersion $\varepsilon_{\mathbf{k}}$ minus the chemical

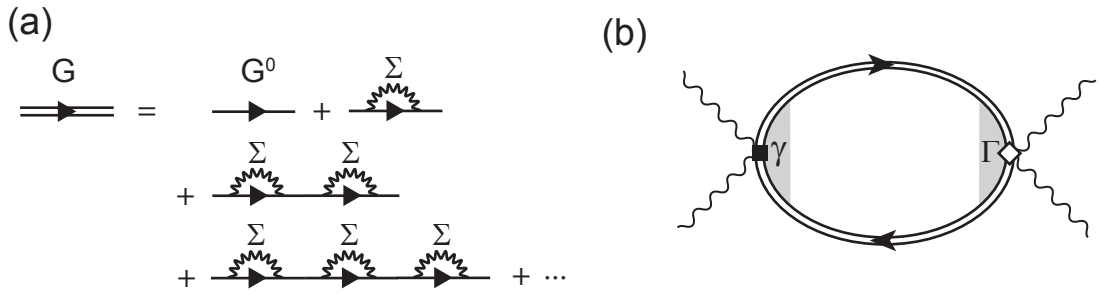

Figure 3.5: (a) Diagrammatic representation of the Dyson equation. (b) Diagrammatic representation of the Raman response function for the creation of particle-hole pairs, involving interactions.

potential μ.

Correlations can be introduced perturbatively. The bare propagator is then replaced by the renormalized propagator via the Dyson equation [154] $G^{-1}(\mathbf{k}, z) = G^0(\mathbf{k}, z)^{-1} - \Sigma(\mathbf{k}, z) = z - \xi_{\mathbf{k}} - \Sigma(\mathbf{k}, z)$, which is illustrated in Fig. 3.5 (a). $\Sigma = \Sigma' + i\Sigma''$ denotes the electronic self-energy, its real and imaginary parts describing the renormalization of the particle energy and the damping of the particle motion due to interactions, respectively [154]. Moreover, vertex-corrections have to be introduced. The general expression for the two-particle correlation function describing the non-resonant Raman response reads [19]

$$\chi_{\gamma,\Gamma}(\mathbf{q} = 0, i\Omega) = -\frac{2}{V\beta} \sum_{i\omega} \sum_{\mathbf{k}} \gamma(\mathbf{k})\, G(\mathbf{k}, i\omega)\, G(\mathbf{k}, i\omega + i\Omega)\, \Gamma(\mathbf{k}, i\omega, i\Omega). \tag{3.23}$$

Similar expressions are obtained for $\chi_{\gamma,1}$ and $\chi_{1,1}$ where the vertices γ and Γ are successively replaced by 1 to be inserted into Eq. (3.18). The renormalized vertex is given by a Bethe-Salpeter Equation:

$$\begin{aligned} \Gamma(\mathbf{k}, i\omega, i\Omega) = \gamma(\mathbf{k}) + \frac{1}{V\beta} \sum_{i\omega'} \sum_{\mathbf{k}'} V(\mathbf{k} - \mathbf{k}', i\omega - i\omega') \\ \times\ G(\mathbf{k}', i\omega')\, G(\mathbf{k}', i\omega' + i\Omega) \\ \times\ \Gamma(\mathbf{k}', i\omega', i\Omega). \end{aligned} \tag{3.24}$$

Here $V(\mathbf{k}, \omega)$ is the generalized electron-electron interaction. The Feynman-diagram which includes vertex- as well as the self-energy corrections to the Green's functions is shown in Fig. 3.5 (b). In the limit of weakly interacting electrons ($V(\mathbf{k}, \omega) \to 0$,

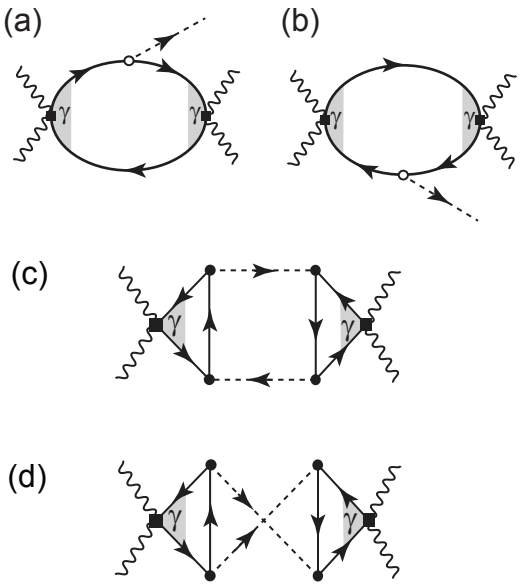

Figure 3.6: Top: Feynman diagrams which describe the 3rd order perturbation calculation of first-order Raman scattering by lattice vibrations involving intermediate electron-hole pair states. The Raman vertices are indicated by black squares, the electron-lattice vertex is represented by an empty circle and the dotted line represents the phonon. (a) shows the electron contribution and (b) the hole contribution. Adapted from [156]. Bottom: Direct (c) and crossed (d) diagrams for the fluctuation contribution to the Raman response. Black squares indicate Raman vertices while the electron-fluctuation vertices are represented by full circles. Here the dashed lines correspond to fluctuation-propagators. Adapted from [157].

$\Sigma \to 0$) one obtains

$$\chi''_{\gamma,\gamma}(\Omega) = \frac{2}{V}\sum_{\mathbf{k}} \gamma^2(\mathbf{k}) \int_{-\infty}^{\infty} \frac{d\omega}{\pi}\, G''(\mathbf{k},\omega)\, G''(\mathbf{k},\omega+\Omega) \times [f(\omega) - f(\omega+\Omega)]. \tag{3.25}$$

which corresponds to the bare bubble diagram (Fig. 3.2). In a multiband system, contributions of individual bands must be added up. The effect of the long range Coulomb interaction is treated formally in the same way as in Eq. (3.18). However, Coulomb-coupling between the bands introduces mixing terms in channels that have the full lattice symmetry [155].

3.5.2 Normal state: higher order diagrams

There are also contributions to the inelastic light-scattering cross-section, that derive from higher order processes than self-energy corrections to the fermionic propagators and vertex renormalizations. Prominent examples are light-scattering from optical phonons or two-magnon scattering which always happens via the intermediate creation of particle-hole pairs through the Raman vertex. The former scattering process is shown in Fig. 3.6 (a) and (b).

A process which is of particular interest for this thesis is the inelastic light-scattering from charge- and/or spin-fluctuations, represented by the direct (c) and

crossed (d) Aslamazov-Larkin (AL) diagrams in the lower part of Fig. 3.6. Particle-hole pairs scatter via the exchange of two fluctuations with opposite momenta $\mathbf{q}$ and $-\mathbf{q}$, hence preserving $\mathbf{q}_{\text{tot}} = 0$, and thus opening up an additional channel for the Raman response. The three fermion matrix elements (solid triangles in the diagrams) introduce new selection rules which can be used to identify the wave-vector of the order associated with the fluctuations. This matter is further discussed in chapter 6.

3.5.3 Superconducting state

In the superconducting state the Raman response is given by generalizing Eqs. (3.23) and (3.24) in particle-hole space using the Pauli matrices and Nambu notation [158]

$$\chi_{\gamma,\gamma}(\mathbf{q}=0,i\Omega) = -\frac{2}{V\beta}\sum_{i\omega}\sum_{\mathbf{k}} \mathrm{Tr}\big[\hat{\gamma}(\mathbf{k})\,\hat{G}(\mathbf{k},i\omega)\,\hat{\Gamma}(\mathbf{k},i\omega,i\Omega)\,\hat{G}(\mathbf{k},i\omega+i\Omega)\big] \quad (3.26)$$

where Tr denotes the trace, and

$$\begin{aligned}\hat{\Gamma}(\mathbf{k},i\omega,i\Omega) = \hat{\gamma}(\mathbf{k}) + \frac{1}{V\beta}\sum_{i\omega'}\sum_{\mathbf{k}'} V_i(\mathbf{k}-\mathbf{k}',i\omega-i\omega') \\ \times\ \hat{\tau}_i\,\hat{G}(\mathbf{k}',i\omega')\,\hat{\Gamma}(\mathbf{k}',i\omega',i\Omega) \\ \times\ \hat{G}(\mathbf{k}',i\omega'+i\Omega)\,\hat{\tau}_i.\end{aligned} \quad (3.27)$$

Here the bare Raman vertex of coupling to charge is $\hat{\gamma} = \hat{\tau}_3\gamma$ and the interaction V_i determines the channel of the vertex corrections. For example, $V_{i=3}$ corresponds to interactions coupling to electronic charge, while $V_{i=0}$ corresponds to spin interactions [19]. In the BCS approximation and for singlet pairing, the matrix Green's functions appearing in Eqs. (3.26) is given by

$$\hat{G}(\mathbf{k},i\omega) = \frac{i\omega\hat{\tau}_0 + \varepsilon(\mathbf{k})\hat{\tau}_3 + \Delta(\mathbf{k})\hat{\tau}_1}{(i\omega)^2 + E^2(\mathbf{k})} \quad (3.28)$$

with $E^2(\mathbf{k}) = \xi^2(\mathbf{k}) + \Delta^2(\mathbf{k})$ the QP energies, $\xi(\mathbf{k})$ the band dispersion and $\Delta(\mathbf{k})$ the energy gap. In addition, in the weak-coupling limit $V_{i=3} = -V$ applies for phonon mediated pairing.

Neglecting vertex corrections and taking the limit $\mathbf{q} \to 0$, the Raman response in a superconductor with n bands crossing the Fermi level is obtained by evaluating the Matsubara frequency sum in Eq. (3.26) yielding

$$\chi_{\gamma\gamma}(\Omega) = \sum_{n} \sum_{\mathbf{k}} \gamma_n^2(\mathbf{k}) \lambda_n(\mathbf{k}, \Omega) \tag{3.29}$$

where

$$\lambda_n(\mathbf{k}, \Omega) = \tanh\left(\frac{E_n(\mathbf{k})}{2k_B T}\right) \frac{4|\Delta_n(\mathbf{k})|^2 / E_n(\mathbf{k})}{4E_n(\mathbf{k}) - (\hbar\Omega + i\delta)^2} \tag{3.30}$$

is the Tsuneto-Maki function for the n^{th} band. Neglecting band-structure effects and assuming circular FSs, the imaginary part of the expression for the response at $T = 0$ can be transformed into [159]

$$\chi''_{\gamma\gamma}(\Omega) = 4\pi \sum_{n} \left\langle \frac{\gamma_n^2(\mathbf{k}) |2\Delta_n(\mathbf{k})|^2}{\Omega \sqrt{\Omega^2 - |2\Delta_n(\mathbf{k})|^2}} \right\rangle, \tag{3.31}$$

where $\Omega > |2\Delta_n(\mathbf{k})|$ and $\langle ... \rangle$ denotes an average over the FS sheet n. Eq. (3.31) can be used to fit the experimentally obtained spectra of a multiband system. Using Raman vertices either obtained due to an effective-mass approximation [Eq. (3.19)] or an expansion in BZ harmonics, the only relevant physical parameters that are varied to achieve the best agreement with the data are $\mathbf{k}$-dependent gaps $\Delta_n(\mathbf{k})$ for each FS. However, including backflow is not straight forward for a multiband system. In case of a single band the full response is once again given by inserting Eq. (3.31) into Eq. (3.18). In multiband systems where the bands are coupled by the long-range Coulomb interaction, mixing terms appear in channels which have the full lattice symmetry (like the A_{1g} channel in D_{4h} crystals) and have therefore to be taken into account [155].

Chapter 4

Experiment

In electronic Raman scattering experiments, approximately one out of 10^{13} incoming photons is scattered inelastically per second, meV bandwidth and steradian [19]. The already low scattering cross section is reduced further in metals or superconductors due to the small light-matter interaction volume (penetration depth). Photons which have lost energy by breaking Cooper-pairs in iron-based materials, for instance, are as rarely detected as one every few seconds. Here, the Raman setup allowing for the detection of inelastically scattered photons with extremely low scattering rates is briefly described.

4.1 Incident light path

Fig. 4.1 shows a schematic drawing of the experimental setup. As light source either a continuous wave Ar^+ laser (Coherent Innova 304C, 6 discrete wavelengths between 457.9 nm and 514.6 nm are available) or a Nd-YAG diode-pumped solid state laser (Klastech Scherzo, $\lambda = 532\,\mathrm{nm}$) can be selected via a removable mirror (M1). The beam emitted by the solid state laser has a smaller beam diameter ($\varnothing = 800\,\mu\mathrm{m}$) than that of the Ar^+ laser ($\varnothing = 1600\,\mu\mathrm{m}$). This mismatch must be corrected by a two-achromat system [L1, $f_1 = 30\,\mathrm{mm}$ and L2, $f_2 = 60\,\mathrm{mm}$] sharing a common focal point. The correction is necessary due to the light-path being adjusted to the diameter of the Ar^+ laser beam.

A pinhole system (PH1), consisting of two achromats and a circular aperture ($\varnothing = 30\,\mu\mathrm{m}$) serves as spatial filter, removing divergent components of the laser beam. Moreover, large portions of light originating from the other allowed transitions in the plasma are suppressed. The remaining plasma line intensity is blocked by a prism monochromator (PMC), which disperses the laser light, projecting it onto

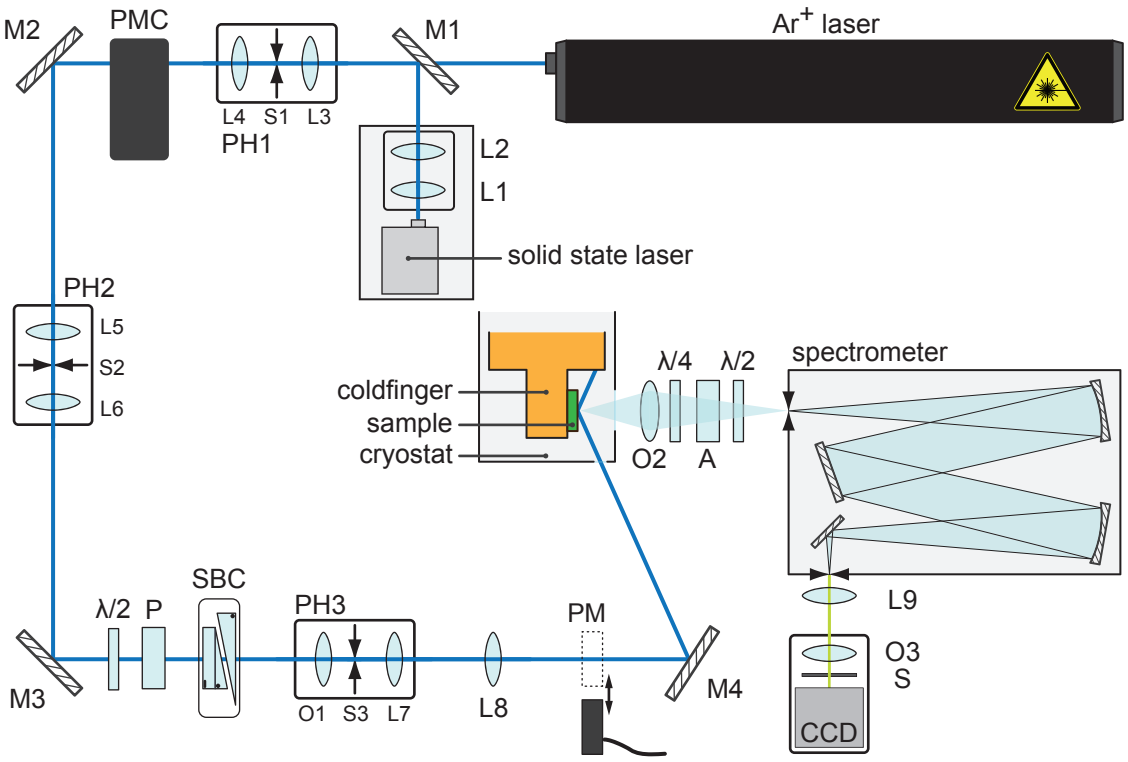

Figure 4.1: Schematic drawing of the Raman experiment. For details and description see text. Adapted from [160].

a slit where only monochromatic light of a selected wavelength can pass, thus suppressing plasma lines which differ by more than $30\,\mathrm{cm}^{-1}$ from the laser line. Plasma lines which can not be blocked by the PMC are blocked by a second spatial filter (PH2) which consists of two achromats and a slit (S2) which is adjustable perpendicular to the dispersion direction of the PMC. The intensity of the pre-polarized laser beam is controlled by rotating its polarization with a $\lambda/2$-plate with respect to the desired polarization chosen with a Glan-Thompson polarizer (P). The resulting laser power is quantified via a digital laser power meter (PM).

The polarization of incoming photons is prepared via the combination of the Glan-Thompson polarizer and a Soleil-Babinet compensator (SBC) which facilitates independent control over polarization and phase of the light, thus allowing the preparation of any desired polarization state. The capability of doing so is of vital importance as in a Raman experiment it is crucial to control the polarization state of the incident light after transmission into the sample. Since the polarization inside the sample matters, the change of the polarization upon entering the metallic

samples must be anticipated[1].

The spatial filter PH3 with a small circular aperture ($\varnothing = 10\,\mu m$) removes self-interference effects introduced by the polarizer and/or compensator and provides a Gaussian beam profile[2]. Finally, the beam is focused on the sample surface with the achromatic lens L8 after transmitting through the optical window of the cryostat.

4.2 Cryogenic environment

The sample is mounted on the cold finger of a cryogenically pumped ^{4}He flow cryostat providing a vacuum of better than 10^{-6} mbar and an accessible temperature range of $1.8\,K \leq T \leq 340\,K$. The temperature of the sample-holder is measured via a Si-diode. Incident and scattered photons enter and leave the cryogenic environment via two optical windows. A detailed description of the cryostat can be found in Ref. [161].

Before the sample is mounted, the orientation of the crystal-axes must be determined via a Laue experiment. If one is interested in the carrier dynamics regarding certain directions in a material, the crystal axes must be adjusted properly with respect to the scattering geometry and the light polarizations. For instance, in cuprates and FeSCs which have quasi 2-dimensional FSs one is interested in the carrier dynamics within the CuO_2 and (1Fe-) FeAs planes. Raman scattering provides this kind of information via the selection rules. However, the polarizations of incident and scattered photons have to exhibit certain geometries with respect to the ab plane of the D_{4h} crystal. Controlling the polarizations is thus simplified by mounting the sample in a way that the crystal a and b axes match the x and y directions of the laboratory system.

The scattering geometry is shown schematically in Fig. 4.2. Panel (a) shows an example in which the incident photons exhibit a polarization pointing along the x-axis of the laboratory system, while from the inelastically scattered light only photons exhibiting a polarization pointing along the y-axis of the laboratory system are chosen by the analyzer. According to panel (b), which displays a properly adjusted sample with the orientation of a generic FeAs plane matching the xy plane of the laboratory system, this scattering geometry will project out the A_{2g} and B_{2g} symmetry components of the Raman response function as discussed in Sec. 3.4.

In the experiment the incident beam encloses an angle of 66° with respect to the

[1] A thorough introduction into the preparation of the polarization state with the above mentioned optical components can be found in [160].

[2] PH4 uses a microscope objective lens (O1) instead of an achromat, as this provides a diffraction-limited focal point.

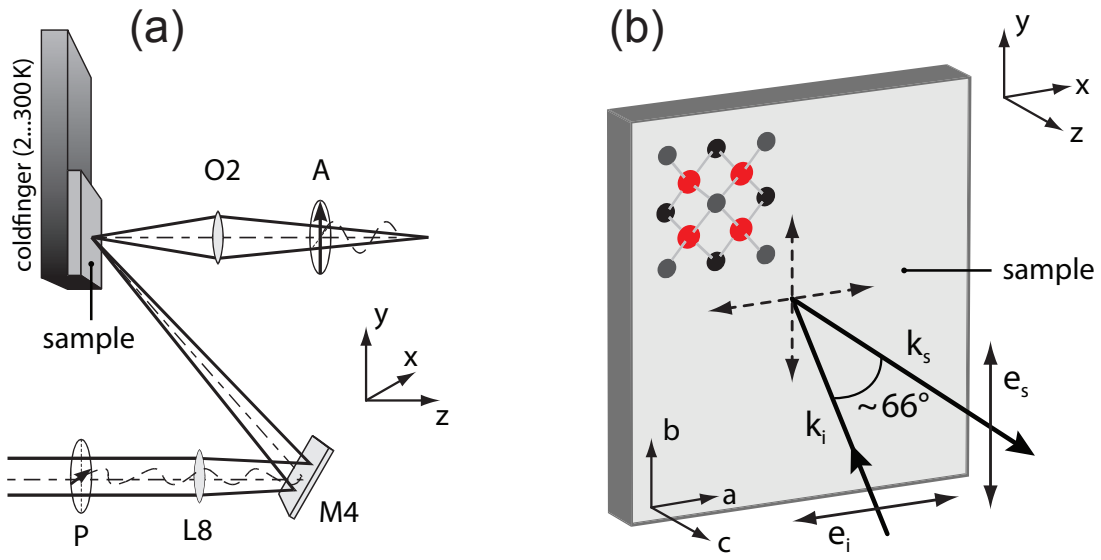

Figure 4.2: (a) Sketch of the scattering geometry, involving a set of polarization orientations of incident and scattered photons. (b) Orientation of the crystal axes of the sample with respect to the scattering geometry. Adapted from [160].

surface normal of the sample, which is close to the pseudo-Brewster angle and thus minimizes the intensity of specularly reflected light polarized parallel to the plane of incidence. The remaining part of this light does not enter the objective lens (O2) and is absorbed by a beam stopper. The portion of the light which was scattered inelastically is collected by the objective lens (O2) and focused on the entrance slit of the spectrometer. This geometry guarantees a minimum of elastically scattered light entering the spectrometer. However, it can cause contributions of symmetries which are projected out by polarization combinations where the incident beam is polarized parallel to the crystallographic c-axis. In a D_{4h} crystal, this leads to contributions of phonons with E_g symmetry in x′y′, yy, yx, RR and RL scattering geometries. However, the contributions to the electronic continuum are expected to be small in materials with quasi 2-dimensional FS topology.

4.3 Detection of scattered photons

Before the Raman light enters the spectrometer, the polarization of scattered photons is selected by the combination of a $\lambda/4$ retardation plate and an analyzer (A). For linear polarizations of scattered photons one does not need the retardation plate and simply adjusts its fast or slow axis parallel to the transmission axis of the analyzer. Circular polarizations can be selected only with the fast or slow axis of the

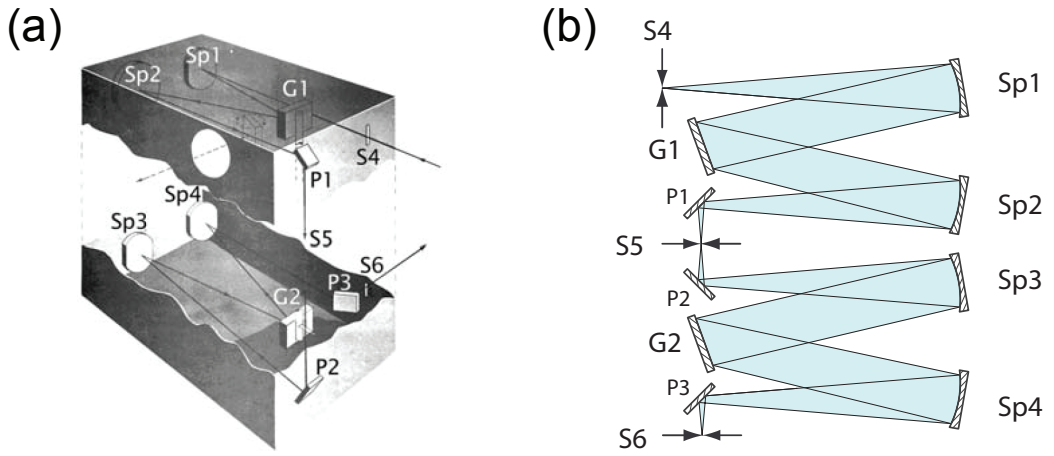

Figure 4.3: (a) 3D and (b) 2D illustration of the double monochromator used for the Raman measurements.

$\lambda/4$-plate being rotated by 45° with respect to the direction selected by the analyzer. The $\lambda/2$-plate positioned after the analyzer facilitates the rotation of the selected linear polarization to the x-axis of the laboratory system, which is the direction of maximal transmission of the spectrometer.

The spectrometer is a Jarrell-Ash 25-100 double monochromator with the gratings mounted in Czerny-Turner configuration as illustrated in Fig. 4.3. The two monochromator stages are symmetrically coupled and each have a focal length of 1 m. Light entering the first stage of the spectrometer through the entrance slit (S4) is collimated by the first spherical mirror (Sp1) and reflected as a parallel beam on the grating G1. The dispersed light is then collected by a second spherical mirror (Sp2) which projects the dispersed beam on the intermediate slit (S5) selecting a small frequency band for the transmission into the second stage of the spectrometer. The second stage reverses the dispersion of the frequency band which was introduced in the first stage and produces a real image of the intensity distribution of light at S4 on the exit slit of the spectrometer (S6). However, the image is created exclusively by photons within the energy interval chosen by the position and width of the intermediate slit S5. Thereby, the spectrometer acts as an effective band pass filter.

The fraction of inelastically scattered light which passes the double monochromator is subsequently focused by an achromatic lens (L9) and a camera objective (O3) on a cryogenically cooled CCD detector (Princeton Instruments, PyLoN:100BR_exCelon). The spectra are acquired point by point with the CCD chip acting as a single channel detector. The measured quantity is the scattering rate $\dot{N}$

integrated within the dwell time as a function of energy ω_s of the scattered photons. The intensity is then plotted versus the transmitted energy $\Omega = \omega_i - \omega_s$, usually given in wavenumbers (cm^{-1}). This energy unit is related to the more common unit eV via

$$\tilde{\nu} = \frac{1}{\lambda} = \frac{E}{h \cdot c} = 8065.54\,\mathrm{cm}^{-1}\mathrm{eV}^{-1} \cdot E. \tag{4.1}$$

The measured spectra need to be corrected for the sensitivity of the experimental setup and the selected width of the entrance slit of the spectrometer (S4). Crucial parts like the gratings or the CCD sensor have characteristic efficiencies which vary over a wide frequency range. A calibration yields the transmission coefficient $T(\omega_s)$ of the entire setup, which can be found in Ref. [150].

All spectra shown in this thesis are presented in units of counts per second and Milliwatt ($\mathrm{counts\,s}^{-1}\,\mathrm{mW}^{-1}$) if not indicated otherwise. They are corrected for the response of the instrument and divided by the Bose-Einstein thermal factor $\{1+n(\Omega,T)\}$ yielding the Raman response function $R\chi''_{\gamma\gamma}(\Omega,T)$ (see Sec. 3.3). Here, R is a constant absorbing effects of experimental details such as sample surface quality, scattering geometry, et cetera.

4.4 Samples

The optimally doped $Ba_{0.6}K_{0.4}Fe_2As_2$ single crystals used in the experiment were grown with the self-flux method. The X-ray diffraction patterns taken on these samples show only [00l] peaks which is a sign for very good crystallinity. Specific heat measurements reveal a residual coefficient γ_0 of about $1\,\mathrm{mJ/mol\,K}^2$, indicating very clean samples. The resistivity curve shows a very sharp transition to the superconducting state, starting at about 39.0 K, and ending at about 38.5 K, sug-

	T_c	ΔT_c	T_s	T_m	reference	sample ID
$Ba_{0.6}K_{0.4}Fe_2As_2$	39 K	0.25 K	-	-	[162]	#100805a1
$Ba_{0.6}K_{0.4}Fe_2As_2$	39 K	0.25 K	-	-	[162]	#100909a1
$Rb_{0.8}Fe_{1.6}Se_2$	32 K	1.50 K	-	-	[163]	#111029
$BaFe_2As_2$	-	-	134 K	134 K	[29]	#100310a1
$Ba(Fe_{0.975}Co_{0.025})_2As_2$	-	-	102.8 K	98 K	[29]	#131028a1
$Ba(Fe_{0.949}Co_{0.051})_2As_2$	18 K	1.00 K	52 K	37 K	[29]	#100121a1

Table 4.1: Table of the studied samples, with the corresponding superconducting transition temperatures T_c and widths ΔT_c, structural and magnetic transition temperatures T_s and T_m, respectively, reference and sample ID.

gesting very homogeneous doping. Further details about the preparation and the characterization can be found in Ref. [162].

$Rb_{0.8}Fe_{1.6}Se_2$ single crystals were prepared by the Bridgman method. The preparation and characterization details of the samples investigated here are given in Ref. [163]. Polycrystalline FeSe synthesized from high-purity elements (99.98 % Fe and 99.999 % Se and 99.75 % Rb) were used as starting materials. Handling of the reaction mixtures was done in an argon box with residual oxygen and water content of less than 1 ppm. The composition of the grown samples was determined by wavelength dispersive spectroscopy (WDS) using the electron probe micro-analyzer (EPMA) Cameca SX50 with an accuracy of 0.5 % for Fe and 1 % for Se. The sharp superconducting transition with an onset temperature of 32.4 K was demonstrated by susceptibility and specific heat measurements. Recently, evidence was reported that $Rb_{0.8}Fe_{1.6}Se_2$ is a system with macroscopically phase-separated antiferromagnetic insulating and metallic (superconducting) layers [164–166]. However, both the well defined $\mathbf{Q}$ vectors of the spin resonance in neutron scattering [167] and the selection rules in our light scattering experiments show that the different layers have equivalent crystallographic orientations.

The single crystals of undoped and electron-doped $Ba(Fe_{1-x}Co_x)_2As_2$ were grown using a self-flux technique and have been characterized by Chu *et al.* [29]. The cobalt concentration was determined by microprobe analysis. As shown in the phase diagram (Fig. 2.6), the material exhibits a structural and a magnetic phase-transition. The corresponding critical temperatures, T_s and T_m, are close to 134 K in the undoped case and cannot be distinguished. Co-doping increases the temperature-gap ΔT between the two transitions, which at nominally $x = 0.025$ doping has already a magnitude of approximately $\Delta T = 5$ K, becoming as large as $\Delta T = 15$ K for $x = 0.051$ Co-doping. Transition temperatures, references and sample IDs of all studied samples are summarized in table 4.1.

Chapter 5

Evidence of near-degenerate pairing channels in FeSCs

The following chapter summarizes inelastic light-scattering results which provide insight into the interaction potential $V(\mathbf{k}, \mathbf{k}')$ of FeSCs. Sharp modes in the Raman response of optimally doped $Ba_{1-x}K_xFe_2As_2$ are interpreted as spectroscopic fingerprints of Bardasis-Schrieffer excitons. Their observation allows the identification of a strong subdominant component of the interaction potential. The chapter also contains a proposal on how the dominant and subdominant components of $V(\mathbf{k}, \mathbf{k}')$ may evolve across the generic phase diagram of FeSCs. The proposed scenario is then tested against earlier results. Parts of this chapter have been published in Ref. [168].

5.1 Experimental results

This section contains inelastic light scattering results on the superconducting states of the hole-doped iron-pnictide $BaFe_2As_2$ and the iron chalcogenide $Rb_{0.8}Fe_{1.6}Se_2$. Across the hole-doped side of the generic phase diagram (see Fig. 2.6), only the optimally doped $Ba_{0.6}K_{0.4}Fe_2As_2$ was available for experiments.

5.1.1 Experimental results: $Ba_{0.6}K_{0.4}Fe_2As_2$

Fig. 5.1 shows Raman spectra measured in the normal and superconducting states of $Ba_{0.6}K_{0.4}Fe_2As_2$. Normal state spectra (light blue), were taken at 45 K, well above the superconducting transition temperature T_c. Spectra taken in the superconducting state (dark blue) were obtained at 8 K. Spectra plotted with full lines in panels

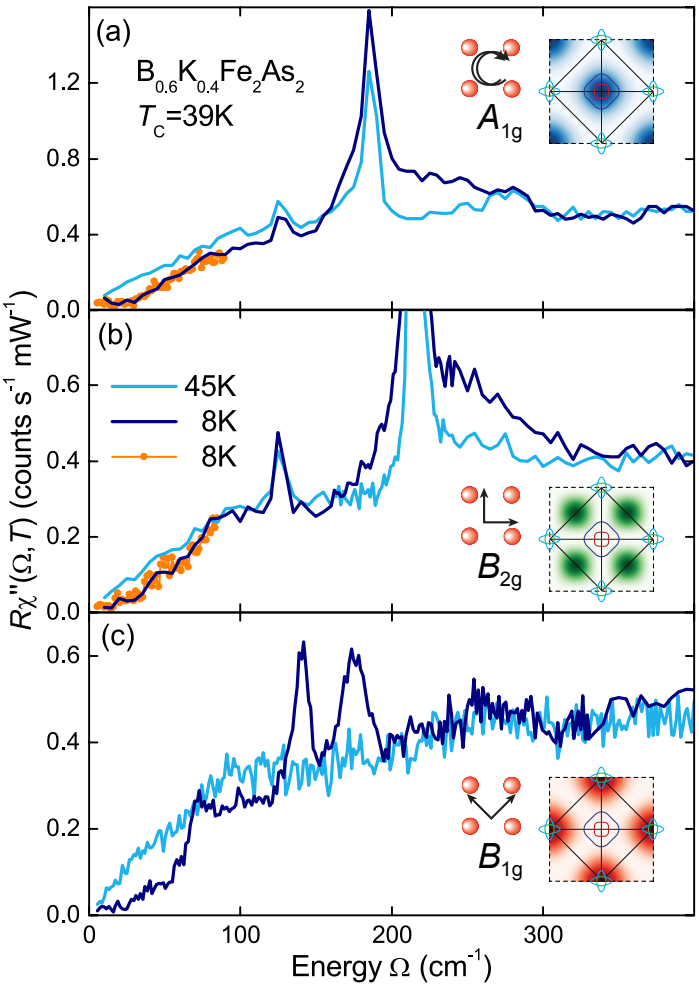

Figure 5.1: Normal and superconducting Raman spectra of $Ba_{0.6}K_{0.4}Fe_2As_2$ at temperatures as indicated. The spectra plotted with full lines in panel (a) and (b) are measured with a resolution of $6.5\,\mathrm{cm}^{-1}$ whereas the spectra in panel (c) and the spectra displayed with orange points are measured with a resolution of $4.7\,\mathrm{cm}^{-1}$. The insets show the correspondence between light polarizations and sensitivities in momentum space for the 1 Fe unit cell.

(a) and (b) are measured with a resolution of $6.5\,\mathrm{cm}^{-1}$ whereas the spectra in panel (c) and the spectra displayed with orange points are measured with a resolution of $4.7\,\mathrm{cm}^{-1}$. As indicated in the insets of the figure which depict the Raman vertex, panels (a), (b) and (c) show the A_{1g}, B_{2g} and B_{1g} Raman response, respectively. As discussed in Sec. 3.4, the different symmetries project out different high-symmetry domains of the 1 Fe BZ (cf. Sec 3.4).

The sharp structures at $185\,\mathrm{cm}^{-1}$ and $215\,\mathrm{cm}^{-1}$ in A_{1g} and B_{2g} symmetry, which broaden below T_c, correspond to the A_{1g}(As) and the B_{1g} [2 Fe cell notation] (Fe) lattice-vibrations, respectively. Due to a finite projection of the polarization vectors of the incident laser-light on the crystallographic c-axis (see Sec. 4.2), the E_g (Fe,As) phonon is visible at $125\,\mathrm{cm}^{-1}$ in both the A_{1g} and B_{2g} spectra [169]. The strength of electron-phonon coupling in FeSCs has been addressed by several authors [170–173] and is generally found to be too weak to account for the high transition temperatures of these materials [107].

Figure 5.2 displays the B_{1g} (Fe) phonon at $215\,\mathrm{cm}^{-1}$ in the normal (light blue)

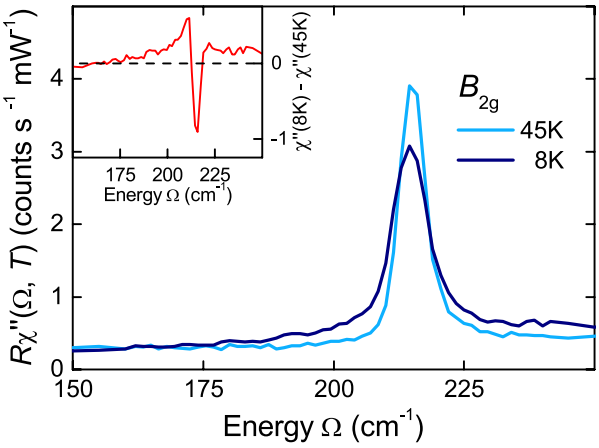

Figure 5.2: B_{2g} phonon softening. The phonon has an almost Lorentzian shape and its linewidth broadens by approximately 2.5 cm^{-1} upon cooling from the normal (light blue) to the superconducting state (dark blue). The phonon softening is less than 2 cm^{-1}. These findings are compatible with weak electron-phonon coupling.

and the superconducting state (dark blue). For a phonon near the pair-breaking threshold 2Δ, the linewidth is predicted to grow due to the enhancement of the density of states at the gap edge, and there can be either pronounced softening or hardening depending on which side of the threshold the phonon is located [174]. In the present case the linewidth-broadening upon cooling to the superconducting state is clearly visible, but does not exceed 2.5 cm^{-1} (FWHM). No substantial shift or change of symmetry is observed. A close look reveals that the phonon softens slightly by less than 2 cm^{-1} and the phonon line shape remains almost a Lorentzian, compatible with weak electron-phonon coupling.

We now focus on the spectroscopic imprints of superconductivity on the electronic continua. These imprints are observed, against expectation, in all symmetries. Below a symmetry independent threshold of approximately 25 cm^{-1} the response in the superconducting state is very small and nearly energy independent. Although the intensity is not exactly zero it is safe to conclude that there is a full gap on all bands having a magnitude of at least $0.9\,k_B T_c$. The spectral weight which is removed by the opening of the superconducting gap is shifted to the higher energy part of the spectra. Excess intensity can be found between 160 cm^{-1} and 265 cm^{-1} in A_{1g} , between 170 cm^{-1} and 340 cm^{-1} in B_{2g} and between 130 cm^{-1} and 195 cm^{-1} in B_{1g} symmetry. The important secondary structures of the spectra between the minimal and the maximal gaps are better resolved in the difference spectra $\Delta R\chi'' = R\chi''(\Omega, 8K) - R\chi''(\Omega, 45K)$ plotted in Fig. 5.3. In this way, the redistribution of spectral weight as a consequence of the superconducting transition is highlighted and the contributions from phonons are by and large subtracted out. Only the Fe vibration at 215 cm^{-1} in the B_{2g} spectrum (B_{1g} phonon in the crystallographic cell) has an anomalous intensity for its proximity to the gap edge. The anomalous phonon contribution to the spectrum is truncated in Fig. 5.3. Both

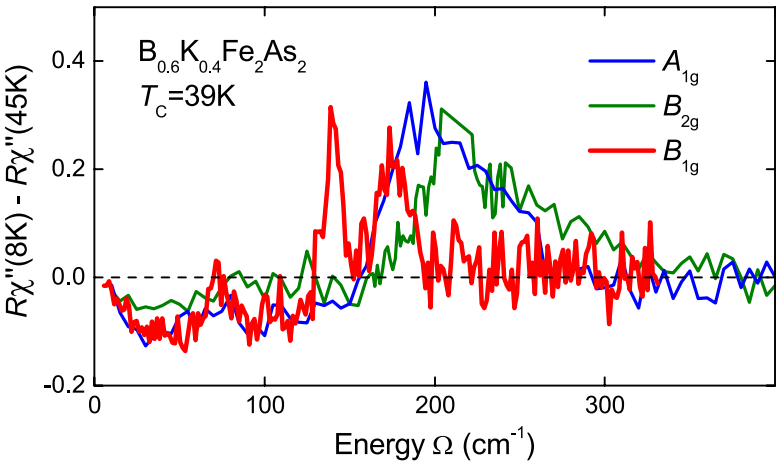

Figure 5.3: Difference between superconducting and normal-state spectra. In B_{2g} symmetry (green), the phonon at 215 cm^{-1} is truncated for having a higher intensity below T_c.

the A_{1g} and B_{2g} spectra have edge-like onsets above approximately 150 cm^{-1} before reaching distinct maxima at 190 and 210 cm^{-1}, respectively, and decaying slowly towards higher energies. The shapes of these features are characteristic for fairly isotropic superconducting gaps [19]. The observation of such a pair-breaking peak in the A_{1g} channel suggests that a gap opens up on one of the central hole pockets. This is in agreement with ARPES results, which find a large gap on the inner hole pocket.

In B_{2g} symmetry, the observation of a pair-breaking feature is unexpected. The absence of Fermi sheets in the regions which are marked in green color in the insets of Fig. 5.1, implies that a gap feature in this symmetry is at odds with the selection rules. Since the feature is strong, it is difficult to justify this observation by the fact that the outer hole (β) band has a large Fermi momentum $k_F(\beta)$ at which the B_{2g} vertex reaches already 20% of its maximum. This applies in particular considering that ARPES finds the gap on this outer hole-pocket to be much smaller. It is, however, possible to explain the observed feature when the backfolding of the 1 Fe cell band structure in the crystallographic 2 Fe cell is considered, see Sec. 5.2.

A look to the lower energy part of the spectra reveals a shoulder at approximately 80 cm^{-1} in all symmetries. Since the outer hole-pocket is located in a region of the BZ where all vertices have finite values, the shoulder could be due to a small gap on this FS which is in line with the results of ARPES experiments [64, 89, 175].

The B_{1g} Raman response (red curve in Fig. 5.3) exhibits three narrow features at 72 cm^{-1}, 140 cm^{-1} and 175 cm^{-1}, the narrowest being the one at 140 cm^{-1}. While the signatures in A_{1g} and B_{2g} symmetry are broad and asymmetric, as expected for a coherence peak [19,22], the features in B_{1g} symmetry are too sharp (even though not resolution limited) and symmetric, to account for ordinary pair-breaking. Phonon

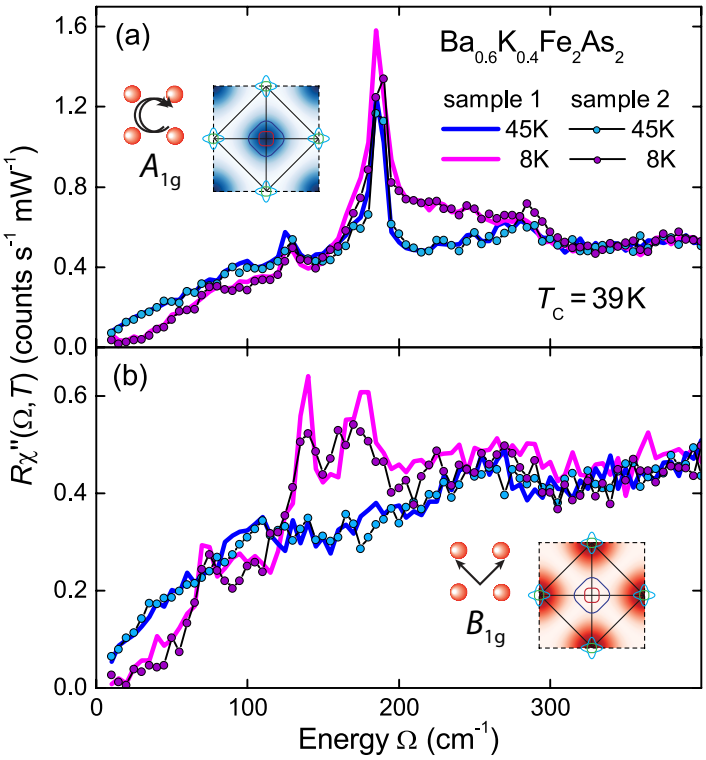

Figure 5.4: Comparison of the spectra of two different single crystals of $Ba_{0.6}K_{0.4}Fe_2As_2$ (raw data). Without adjustment all intensities coincide, except for the two prominent modes in B_{1g} diminishing considerably.

enhancement or enhancement of defect induced vibrational modes due to a coupling to the redistribution of QP excitations below T_c are not likely to be responsible for the observed peaks.

A phonon-enhancement, as observed in multilayer Hg-based cuprates [176], is attributed to self-energy effects. However, in the cuprates the enhanced phonons are already visible above T_c and, in some cases, show a strong asymmetry due to the Fano effect. There are no lines above T_c in the B_{1g} response of $Ba_{0.6}K_{0.4}Fe_2As_2$ and the new modes are symmetric.

After excluding phonons it is sensible to interpret the sharp structures in the (1 Fe) B_{1g} Raman response in terms of signatures of the superconducting state. The observation of sharp and symmetric modes is compatible with scattering from exciton-like pairs of QPs bound by residual interactions in the pairing potential, which have been introduced in Sec. 2.2.4. The appearance of such excitations depends intimately on the polarization geometries of incident and scattered photons and on the given FS topology, just as it is the case for the pair-breaking signatures of ordinary Cooper-pairs. A detailed discussion of this matter can be found in Sec. 5.2.

It depends crucially on the quality of the used single-crystals, if the observation of the excitonic modes is possible or not since the modes get considerably damped by impurity scattering [120]. A comparison between spectra of two single crystals from

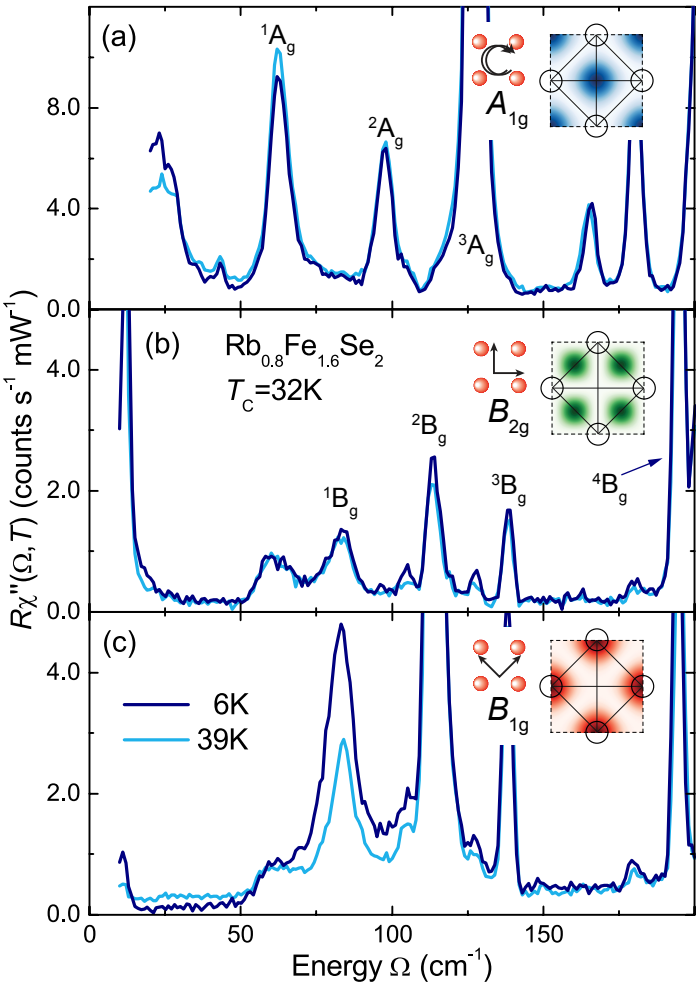

Figure 5.5: Normal and superconducting Raman spectra of $Rb_{0.8}Fe_{1.6}Se_2$ at temperatures as indicated. The insets show the correspondence between light polarizations and sensitivities in momentum space for the 1 Fe unit cell.

the same batch is shown in Fig. 5.4. The spectra are well reproducible concerning the overall intensity and the major part of the spectral shape. A closer look reveals small differences. The phonon line at 180 cm^{-1} [Fig. 5.4 (a)] and the superconductivity-induced structures at 140 and 170 cm^{-1} [Fig. 5.4 (b)] are a little more pronounced in sample 1 than in sample 2 indicating a slightly smaller impurity concentration in sample 1. This shows that very small changes in the impurity concentration are probably enough to suppress the collective modes. The Figs. 5.1 and 5.3 show the results from sample 1.

5.1.2 Experimental results: $Rb_{0.8}Fe_{1.6}Se_2$

It was pointed out in section 2.1.1 that $Rb_{0.8}Fe_{1.6}Se_2$ crystals belong to a different space group than the 122-family of pnictides. While the latter have D_{4h} symmetry, the selenide compounds exhibit the lower C_{4h} symmetry, which is important for the symmetry assignment of phonons. Since the investigation focuses on the

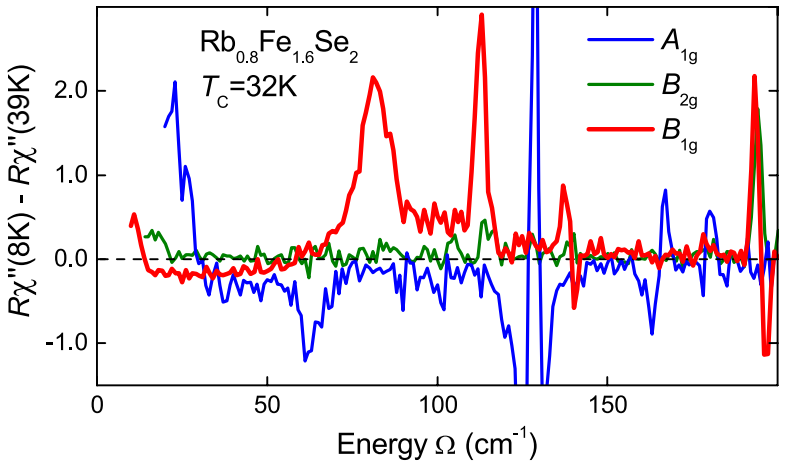

Figure 5.6: The difference spectra highlight the absence of pair-breaking in B_{2g} and most likely also in A_{1g} symmetry. Only the B_{1g} spectra show the features typical for a superconductor.

electronic properties (in particular the superconducting energy gap) of the sample, the polarizations of the incident and scattered light in the experiment were chosen according to the 1 Fe unit cell, just as in $Ba_{0.6}K_{0.4}Fe_2As_2$ and $Ba(Fe_{1-x}Co_x)_2As_2$. This choice also provides better comparability with the results in the aforementioned compounds. Therefore, in the following the spectra will be labeled according to the D_{4h} point group symmetries A_{1g}, B_{1g} and B_{2g}. However, phonons are labeled according to the C_{4h} point group symmetries A_g and B_g.

The symmetry-dependent Raman response of $Rb_{0.8}Fe_{1.6}Se_2$ is shown in Fig. 5.5. Due to diffuse scattering from sample surface irregularities there is a relatively strong increase towards the laser line. All spectra have in common that the phononic contribution is much stronger than the electronic continuum and in the case of the 122-pnictides. This might be caused by the electronic properties of the insulating layers in the material since there is no contribution from electronic Raman scattering. The energy gap between the occupied and empty states of the insulating layers is much larger than $300\,\mathrm{cm}^{-1}$. Some phonon modes can be identified by comparing the spectra to the ones given in [177]. Typically, phonons which have B_g symmetry show up in both the B_{1g} and B_{2g} spectra, whereas the A_g phonons are present only in the A_{1g} spectrum.

The difference between the normal (light blue) and the superconducting state spectra (dark blue), is less pronounced than in $Ba_{0.6}K_{0.4}Fe_2As_2$ or $Ba(Fe_{1-x}Co_x)_2As_2$. In the A_{1g} and B_{2g} spectra, the relative difference between the normal and the superconducting state is weak and absent, respectively. This is attributed to the fact that the band structure of $Rb_{0.8}Fe_{1.6}Se_2$ [178, 179] does not have FS crossings close to the sensitivity maxima of the related form factors shown in the insets of Fig. 5.5. An appreciable difference between superconducting and normal state spec-

tra is present only in B_{1g} symmetry [Fig. 5.5 (c)] where the response from the large electron pockets is projected out. The suppression of the low-temperature spectra due to the gap and the excess intensity at and above 2Δ can be considered typical features of a superconductor [19]. The relative changes of below and above a threshold at approximately $60\,\mathrm{cm}^{-1}$ reach 80% and 30%, respectively. Below $60\,\mathrm{cm}^{-1}$, the intensity is only weakly energy dependent, indicating a clean isotropic gap. The phonons at $80\,\mathrm{cm}^{-1}$ and $115\,\mathrm{cm}^{-1}$, close to the gap edge, gain intensity below T_c as expected for weak electron-phonon coupling. The effects of superconductivity on the Raman response are highlighted in Fig. 5.6 where the difference spectra $\Delta R\chi''(\Omega, \Delta T) = R\chi''(\Omega, 8\,\mathrm{K}) - R\chi''(\Omega, 39\,\mathrm{K})$ are shown.

5.2 Discussion

We start with a discussion of the sharp, symmetric structures that emerge in the Raman spectra of $Ba_{0.6}K_{0.4}Fe_2As_2$ upon cooling to the superconducting state. The section proceeds with a proposal for the gap distribution on the multiple FSs of $Ba_{0.6}K_{0.4}Fe_2As_2$. Finally, the section concludes with a discussion of the idea of competing superconducting ground states in the family of 122 pnictides. It is argued that this physical picture may help interpreting earlier results on $Ba(Fe_{1-x}Co_x)_2As_2$ [150].

5.2.1 Bardasis-Schrieffer modes in $Ba_{0.6}K_{0.4}Fe_2As_2$

Theoretical studies of spin fluctuations using either random-phase approximation (RPA) [59, 111] or numerical functional renormalization-group (RG) calculations [112] show consistently that $s_\pm$- (A_{1g}) and d-wave (B_{1g}) instabilities can occur in multiband models of iron-pnictides. As a consequence, an excitonic collective mode formed by the subdominant interaction is expected to exist in the excitation spectrum of these materials. The case of an $s_\pm$-wave ground state with a subdominant d-wave pairing channel has been discussed by Scalapino *et al.* [17]. They point out that a collective mode originating in a bound state with angular momentum $L = 2$ could be excited from an s-wave superconducting state and calculated the Raman response using a three-band model. In this model the FS consists of one hole band encircling Γ and two electron bands around X and Y. The s-wave part V_s (A_{1g}) of the pairing interaction connects the hole and electron pockets while the d-wave part V_d (B_{1g}) of the pairing interaction connects the two electron pockets [see Fig. 5.7 (a)]. Effects of intraband pairing are neglected.

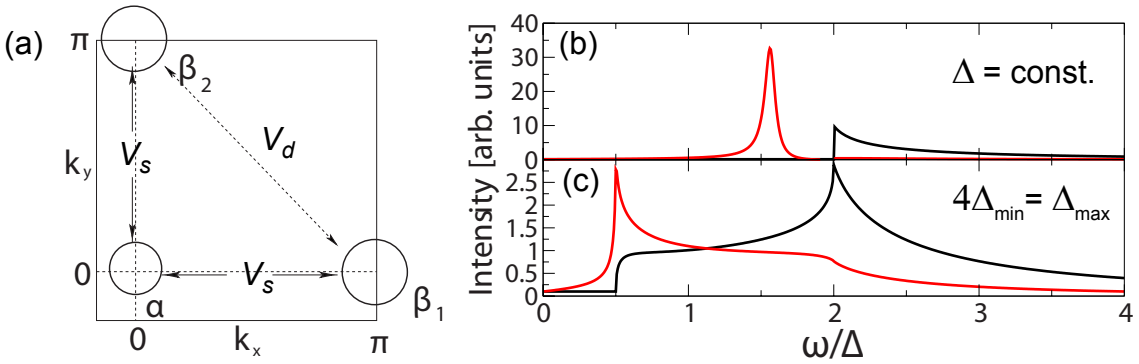

Figure 5.7: Raman response of FeSCs with competing pairing channels. (a) Model FS of FeSCs used in [17]. The FS consists of only one hole pocket (α) encircling the Γ-point of the 1 Fe/cell Brillouin zone and two electron pockets (β_1 and β_2) at $(0,\pi)$ and $(\pi,0)$, respectively. The s-wave part (A_{1g}) of the pairing interaction connecting the α and β Fermi sheets is denoted by V_s. The d-wave part (B_{1g}) of the pairing interaction connecting the β_1 and β_2 Fermi sheets is denoted by V_d. (b),(c) Calculated B_{1g} Raman response for an isotropic gap and a strongly anisotropic ($4\Delta_{\rm min} = \Delta_{\rm max}$) gap. If the subdominant contribution to the pairing potential is negligible ($V_d = 0$), the Raman spectra have the typical shape (black curves). Collective modes emerge and draw spectral weight from the higher energy portion of the response, when the subdominant contribution becomes considerable. The red curves display the case for $V_s = 1$ and $V_d = 0.5$. Adopted from [17].

Panels (b) and (c) of Fig. 5.7 show the calculated B_{1g} Raman response for an isotropic and a strongly anisotropic ($4\Delta_{\rm min} = \Delta_{\rm max}$) gap, respectively. If the subdominant contribution to the pairing potential is negligible ($V_d = 0$), the Raman spectra exhibit the typical pair-breaking features (black curves). Collective modes emerge and drain spectral weight from higher energies, when the subdominant contribution increases (red curves). Fig. 5.7 shows the case for $V_s = 1$ and $V_d = 0.5$. The frequency and damping of the collective mode depend on the difference of coupling strengths in the s- and d-wave pairing channels and on the anisotropy of the s-wave gap on the β FSs, respectively. In the case of an isotropic gap, an essentially undamped mode appears below 2Δ, capturing most of the spectral weight from the pair-breaking peak. For an anisotropic gap without nodes, a well defined collective-mode appears at frequencies slightly below $2\Delta_{\rm min}$, removing the singularity of the bare response at $2\Delta_{\rm max}$ and transferring spectral weight to lower energies. In general, an isotropic gap will lead to a sharp mode, while an anisotropic gap leads to a broader resonance.

Symmetry considerations can be used to determine the collective mode contributions from the interplay of dominant and subdominant pair interactions and polarization geometries. The d-wave interaction contribution to the Raman response is proportional to [17]

$$\chi''_{\mathrm{CM}}(\omega) \propto \mathrm{Im} \int_0^{2\pi} g^d_\beta(\theta)\gamma_\beta(\theta)\Delta_\beta(\theta)\bar{P}(\omega,\theta)d\theta \tag{5.1}$$

where $g^d_\beta(\theta)$ is a symmetry form factor which parameterizes the d-wave part of the interaction potential and depends upon the angle of $\mathbf{k}$ on the β-FS measured from the k_x axis. $\gamma_\beta(\theta)$ is the Raman vertex, $\Delta_\beta(\theta)$ is the $s_\pm$ gap function on the β-band and $\bar{P}(\omega,\theta)$ is the response kernel determining the shape and position of the mode, see Eq. (12) in Ref. [17]. The integral represents an angular average and thus the collective mode contribution to the Raman response will vanish unless the product $g^d_\beta(\theta)\gamma_\beta(\theta)\Delta_\beta(\theta)\bar{P}(\omega,\theta)$ transforms as A_{1g}. Since $\Delta_\beta(\theta)$ and $\bar{P}(\omega,\theta)$ both have A_{1g} symmetry[1], the product $g^d_\beta(\theta)\gamma_\beta(\theta)$ also needs to transform as A_{1g}. Thus, since $g^d_\beta(\theta)$ has B_{1g} symmetry, a collective mode will appear only for a B_{1g} Raman vertex. This is fortunate, because in this way the mode will not be coupled to long range Coulomb forces, which nominally push A_{1g} collective mode contributions up to the plasma frequency [17] thus inhibiting its experimental detection. Note that the Raman vertex in Eq. (5.1) enters the response function in a linear fashion as opposed to regular pair-breaking, where it enters quadratically. Therefore, the observation of the mode in the Raman response directly reflects the $d_{x^2-y^2}$ symmetry of the pair-wave function of the observed exciton-like modes.

In the experiment (Fig. 5.3) the B_{1g} response exhibits not one but three narrow structures at $72\,\mathrm{cm}^{-1}$, $140\,\mathrm{cm}^{-1}$ and $175\,\mathrm{cm}^{-1}$. At least the feature at $140\,\mathrm{cm}^{-1}$ is too sharp and symmetric to originate from ordinary pair-breaking. However, all three features occur only when the sample enters the superconducting state (see Sec. 5.1.1). At the same time, broad and symmetric gap structures at 190 and $210\,\mathrm{cm}^{-1}$ in the A_{1g} and B_{2g} response (Fig. 5.3) indicate the presence of gaps with gap-maxima well above the energies of the sharp B_{1g} features. Moreover, the signature of a smaller gap can be found at $80\,\mathrm{cm}^{-1}$ in both A_{1g} and B_{2g} symmetry. From the synopsis of the theoretical results comprised above and the experimental findings, it is sensible to interpret at least the sharp peak at $140\,\mathrm{cm}^{-1}$ in the B_{1g} response as spectroscopic signature of a Bardasis-Schrieffer (BS) exciton which is excited out of an $s_\pm$ ground state. Motivated by the observation of in total three gaps in the other symmetries also the peaks at $72\,\mathrm{cm}^{-1}$ and $175\,\mathrm{cm}^{-1}$ will be interpreted as excitons in the following, since then each exciton can be assigned to a particular gap and it is possible to derive a gap distribution from the Raman spectra which is compatible with what has been reported from other experiments.

[1] Note that the case of a dominant $s_\pm$-wave interaction is discussed.

The modes at 140 cm^{-1} and 175 cm^{-1} correspond to the A_{1g} and B_{2g} gap structures at 190 cm^{-1} and 210 cm^{-1} implying binding energies E_b of 50 cm^{-1}, and 35 cm^{-1}, respectively, and indicate that V_d is smaller but of the same order of magnitude as V_s [22]. The bound state at 73 cm^{-1} corresponds to the minimum at 80 cm^{-1} of the strongly momentum dependent gap on the δ band as predicted by Scalapino and Devereaux [17], implying a binding energy E_b of 7 cm^{-1}. This scenario in a natural way explains all three symmetric peaks which appear in (the proper) B_{1g} symmetry and provides direct evidence of a strongly anisotropic pairing potential resulting from a superposition of V_s and V_d. Since the collective modes drain intensity from the gap features [17, 22] direct pair-breaking peaks cannot be resolved in B_{1g} symmetry. This effect provides the most compelling evidence for the proper interpretation of the in-gap modes.

5.2.2 Gap distribution in $Ba_{0.6}K_{0.4}Fe_2As_2$

The recombination of electrons of a broken Cooper-pair into Bardasis-Schrieffer excitons explains the sharp and symmetric peaks in the B_{1g} spectra shown in Fig. 5.3. However, the analysis is incomplete without interpreting the origin of the pair-breaking feature observed in B_{2g} symmetry. It turns out that this issue can be resolved by considering the influence of the As atoms on the band structure.

The electronic and crystallographic unit cells have been introduced already in Sec. 2.1.2. The 1 Fe unit cell is an abstraction which is useful for the analysis of the electronic properties in a similar fashion as the CuO_2 planes in the cuprates [19]. For the presence of the As layers the crystallographic unit cell is larger by a factor of two and rotated by 45° as indicated in Fig. 2.2. It is important to note that, while the roles of the B_{1g} and B_{2g} symmetries are interchanged upon going from the 1 Fe to the 2 Fe cell, the independent projections of the electron and hole bands are maintained. In particular, the A_{1g} spectra project the hole bands while the electron bands are projected in B_{2g} symmetry if the 2 Fe cell is used as in Ref. [180]. While the crystallographic cell is the only possible choice for the general symmetry assignment of phonons [169], it is less useful for the interpretation of the electronic excitations in the Raman spectra. For the latter purpose, the 1 Fe cell is better suited since all bands reasonably close to the Fermi level derive from Fe 3d-orbitals (see Sec. 2.1.2).

The 2 Fe cell can then be treated as a weak superstructure which causes a backfolding of the electron pocket at $(0, \pi)$ on top of the electron pocket at $(\pi, 0)$. This situation is illustrated in Fig. 5.8 (a) and (b). The backfolding leads to a hybridiza-

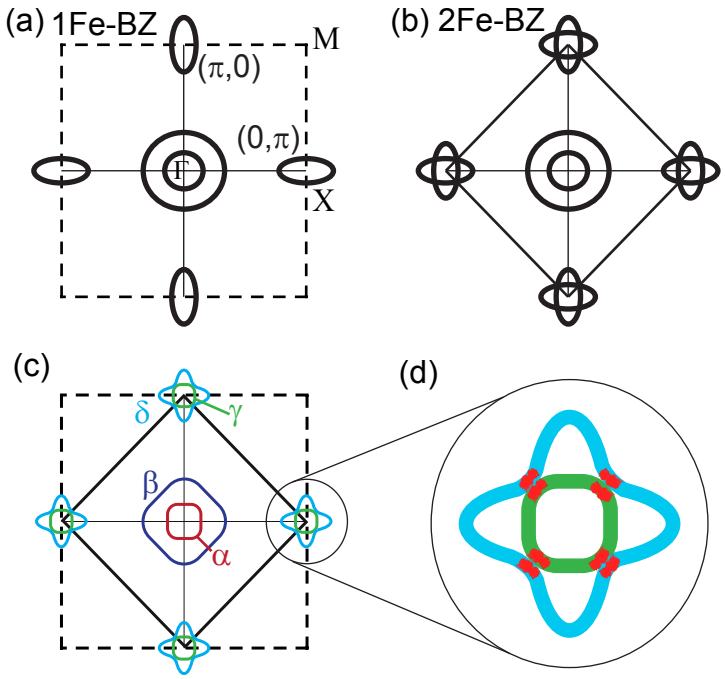

Figure 5.8: The 1 Fe BZ, displayed in panel (a), is more suitable for the interpretation of the Raman data. However, the 2 Fe cell can be treated as a weak superstructure which causes a backfolding of the electron pocket at $(0, \pi)$ on top of the electron pocket at $(\pi, 0)$ [panel (b)]. The consequence is a hybridization of the electron pockets and resulting hot spots on the electron-bands where the Raman response is greatly enhanced [panels (c) and (d)].

tion of the electron bands, producing a strong curvature of the resulting electron pockets labeled γ and δ in Fig. 5.8 (c). As a reference, the band structure based on the ARPES data is shown [89]. Strong curvature results in hot spots for the Raman response which is proportional to the inverse effective mass of the charge carriers, see Fig. 5.8 (d). Calculations based on a realistic band structure show that the B_{2g} vertex is enhanced by a factor of approximately 2-5 in the hybridized regions of the electron-like FSs [181].

Major parts of the gap-distribution on the various bands have been assigned already in section 5.1.1, but some open questions remained. When the hot spots of the Raman vertex and the existence of in-gap modes are considered, it is possible to consistently pin down the gap anisotropy on the various bands. The following analysis rests on four assumptions:

1. The electronic bands are comparable to the findings from band structure calculations and ARPES, see Fig. 5.8 (c).

2. The symmetry dependence is given by the lowest order Brillouin zone (BZ) harmonics. Here, the 1 Fe unit cell is most appropriate. Then, for each projected symmetry, the sensitivity varies as a squared trigonometric function as indicated in the insets of Figs. 5.1 and 5.5.

3. The sensitivity may be enhanced substantially around lifted band degeneracy points as indicated in Fig. 5.8 (d) [61, 181].

4. In $Ba_{0.6}K_{0.4}Fe_2As_2$, Bardasis Schrieffer (BS) modes exist on the electron bands and are qualitatively described by the model calculations of Scalapino and Devereaux [17]. Beyond the model we assume that the d-wave interaction can also lead to a collective mode on the hole bands.

As a consequence of assumptions (1) and (2) the dominant contribution to the A_{1g} spectrum results from a large gap on at least one of the hole bands. Since the spectrum has a relatively sharp edge below approximately $190\,\mathrm{cm}^{-1}$ [see Figs. 5.1 (a) and 5.3] the large gap is nearly isotropic. The existence of a BS mode at $140\,\mathrm{cm}^{-1}$ in B_{1g} symmetry below this edge and its small width, indicating a long lifetime [Figs. 5.1 (c) and 5.3], argues the same way [assumption (4)]. Although the edge is pronounced, the intensity does not vanish below the threshold. Rather there is a secondary feature at approximately $80\,\mathrm{cm}^{-1}$ below which the intensity decays continuously down to approximately $25\,\mathrm{cm}^{-1}$ where it finally vanishes. This implies that the gap on one of the hole bands must be as small as $25\,\mathrm{cm}^{-1}$.

For pinpointing the small and the large gap and the anisotropy, information from the B_{2g} spectrum is necessary. Here features are observed at low and high energies in similar but not identical spectral positions as in A_{1g} symmetry. The peak at $210\,\mathrm{cm}^{-1}$ is at higher energy than that in A_{1g} symmetry and, therefore, does not contain contributions from a gap on the hole bands. The feature at $80\,\mathrm{cm}^{-1}$ indicates that the smaller anisotropic gap opens up on the β band since the B_{2g} vertex is negligible on the α band. For symmetry reasons the B_{2g} vertex is also small on the electron bands but is enhanced along the line $(\pi, 0)$–$(0, \pi)$ due to the focusing effect [assumption (3)]. Therefore, the gap must be slightly larger at the band degeneracy point of the electron bands (see Fig. 5.8) than on the α band. Since the B_{2g} spectrum has only one well-defined threshold, the gaps on the γ and on the δ bands are similar at the degeneracy points. For the existence of another BS mode at $175\,\mathrm{cm}^{-1}$ in the B_{1g} spectrum at least one of the gaps is essentially isotropic.

More details for the electron bands can be derived from the B_{1g} spectrum. Along with the strong BS modes at 140 and $175\,\mathrm{cm}^{-1}$ a well defined but weak peak is observed at $73\,\mathrm{cm}^{-1}$ slightly below the shoulder at $80\,\mathrm{cm}^{-1}$ in A_{1g} and B_{2g} symmetry. Such a structure appears typically below the minimal gap of a broad distribution [17]. Therefore, one of the gaps on the electron bands is expected to vary between a maximum at $2\Delta_0 \approx 210\,\mathrm{cm}^{-1}$ and a minimum at $80\,\mathrm{cm}^{-1}$. Since the maxima are pinned by the degeneracy points, the minima are expected on the principle axes and the BZ edges, assuming the lowest order momentum dependence of the gap. From that we conclude that the γ surface hosts the isotropic gap. Otherwise, the slightly

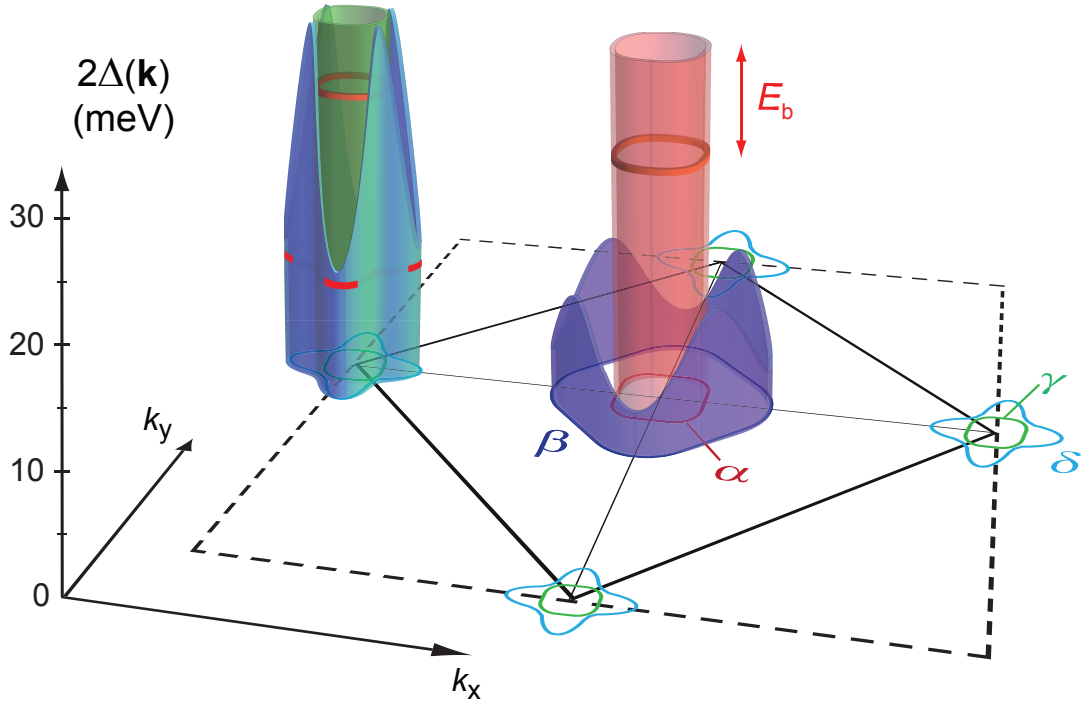

Figure 5.9: Most probable anisotropy of the energy gap in $Ba_{0.6}K_{0.4}Fe_2As_2$. In the text, arguments are provided how the gap distribution shown here is derived from Fig. 5.1. The energy of the bound state E_b (red line) is largest on the α band.

different gaps on the central hole and the outer electron band would be projected out by the A_{1g} vertex, which is as large as 20% at the crossing points of the δ band with the principle axes and the BZ edges, and smear out the threshold there.

It is important to note that pair-breaking peaks at the expected energy of approximately $210\,\mathrm{cm}^{-1}$ are not observed in the B_{1g} spectrum where the strongest contribution from the gaps on the γ and the δ bands are expected. The reason for the absence of pair-breaking features is the existence of BS modes which in any of the scenarios studied so far drain intensity from the coherence peaks at the gap edge [17, 21, 22]. Consequently, the missing intensity in the range of the gap on the γ and the δ bands is direct evidence for the interpretation of the narrow B_{1g} modes in terms of excitons.

In summary, the well-defined distinct edges in A_{1g} and B_{2g} symmetry indicate that large but slightly different isotropic gaps open up on the inner hole (α) and electron (γ) bands. Anisotropic gaps reside on the respective outer bands, β and δ, ranging from 25 to $80\,\mathrm{cm}^{-1}$ and from 80 to $210\,\mathrm{cm}^{-1}$. The gap on the β band is responsible for the low energy threshold at $25\,\mathrm{cm}^{-1}$ which is seen consistently in all symmetry projections. The largest gap exists on the γ band where the s

and the d interaction cooperate. The orientation of the anisotropic gaps cannot be pinned down with ultimate certainty but any choice other than indicated in Fig. 2.12 would entail inconsistencies. By and large the results are consistent with those from ARPES [64, 89, 175] except for the strong anisotropies on the β and δ bands. However, for unclear reasons ARPES is notoriously insensitive to gap anisotropies in the Fe-based superconductors although small or vanishing gaps have been observed by various techniques (see Sec. 2.2.2). A detailed comparison of the the gap-magnitudes found by other methods and by Raman scattering can be found in Appendix 8.A of this thesis.

Finally, a 2D FS approximation was used for the argumentation. Whether or not the anisotropy is in the (k_x, k_y)-plane or entangled with the k_z dispersion was not a subject of the discussion and is beyond the scope of the present qualitative analysis. A quantitative study of the Bardasis-Schrieffer excitons using numerical methods is necessary to confirm the outlined explanation. Such an analysis of the Raman spectra presented in Fig. 5.3, based on LDA band structure calculations and the subsequent estimation of effective Raman vertices was recently performed by Böhm *et al.* [159]. The numerical results are in general agreement with the above interpretation. The Raman spectra could be reproduced quantitatively with estimates for the magnitude and momentum space structure of the $s_\pm$ pairing gap on different FS sheets. The main difference to the proposal given in the two previous sections is the identification of only one collective mode, namely the one located at $140\,\mathrm{cm}^{-1}$ in the B_{1g} spectrum. The feature at $175\,\mathrm{cm}^{-1}$ derives from pair-breaking of Cooper-pairs formed by the dominant $s_\pm$ pairing interaction. Its untypical symmetric shape can be explained by noticing that the spectral weight which is transferred into the collective mode, stems predominantly from the high energy tail of the coherence peak. The subdominant $d_{x^2-y^2}$ pairing channel is shown to be as strong as 60% of that in the dominant $s_\pm$ channel.

5.2.3 Doping dependent gap symmetry in $\mathbf{Ba(Fe_{1-x}Co_x)_2As_2}$

The presence of the BS mode in the Raman spectrum of optimally hole-doped Ba-K-122 implies a strong but subdominant $d_{x^2-y^2}$ pairing channel and naturally leads to the question if a competition of pairing channels might explain the large diversity of gap structures reported for FeSCs [12]. A scenario for $Ba(Fe_{1-x}Co_x)_2As_2$, which is based on such a competition of near-degenerate $s_\pm$ and $d_{x^2-y^2}$ components of the interaction potential $V(\mathbf{k}, \mathbf{k}')$ is outlined in the following.

The interpretation relies on the concept of pairing via magnetic interactions. The

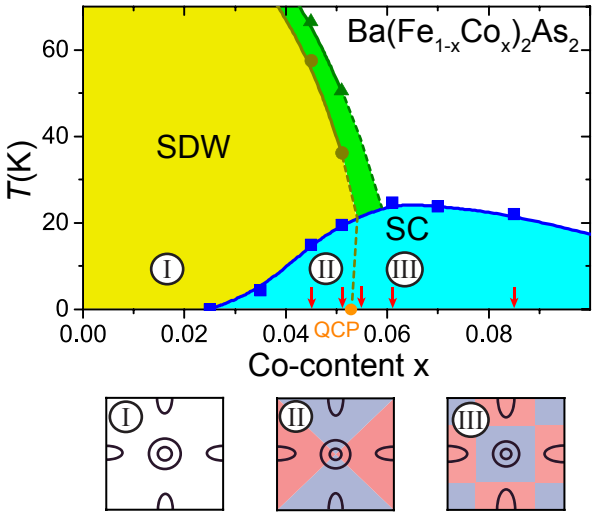

Figure 5.10: Proposal for the gap evolution in $Ba(Fe_{1-x}Co_x)_2As_2$ with doping, relying on the concept of pairing via magnetic interactions and almost degenerate $s_\pm$ and $d_{x^2-y^2}$ pairing channels. Shown is a segmentation of the phase diagram into four regions of which some are dominated by the $s_\pm$ and others by the $d_{x^2-y^2}$ component of $V(\mathbf{k}, \mathbf{k}')$.

discussion will focus on how the gap evolves with doping, ranging from the undoped compound to the electron-overdoped regime. The phase diagram (Fig. 5.10) is segmented into four regions, where some are dominated by the $s_\pm$ and others by the $d_{x^2-y^2}$ component of $V(\mathbf{k}, \mathbf{k}')$. Note, that the proposal given in the following ignores certain aspects which are known to be relevant for the physics of Fe-based superconductors. For instance, it is known that the orbital character of the band structure plays a crucial role in the formation of the SDW, as well as for pairing. However, this aspect will not be discussed. Similarly, it has been conjectured that FeSCs may be in an intermediate regime between itinerant and localized magnetism [141, 182], where here only the itinerant aspect is addressed.

At first we will revisit some earlier results obtained by Muschler [150] [see Fig. 5.11]. The data are presented here in the same fashion as in Sec. 5.1. Difference spectra are shown in Fig. 5.11 which highlight the spectroscopic imprints of the superconducting gap. The left column (A_{1g}) shows the response from the hole-like FSs while the middle column displays the response which is expected to originate from the electron pockets. The B_{2g} response is not shown here since for all doping levels no difference appears between spectra obtained in the normal and in the superconducting state[2].

Fig. 5.11 (a)-(d) show the results for two underdoped compounds. At 4.5% Co doping ($T_c = 14\,\mathrm{K}$), the response from the hole bands (A_{1g}) is exactly zero. The increase below $15\,\mathrm{cm}^{-1}$ is attributed to an elastic contribution from the laserline. In the B_{1g} spectrum there is a weak signature signalling the opening of a small gap on the electron pockets with a maximum of approximately $25\,\mathrm{cm}^{-1}$, as indicated by a

[2]The B_{2g} spectra can be found in [150]

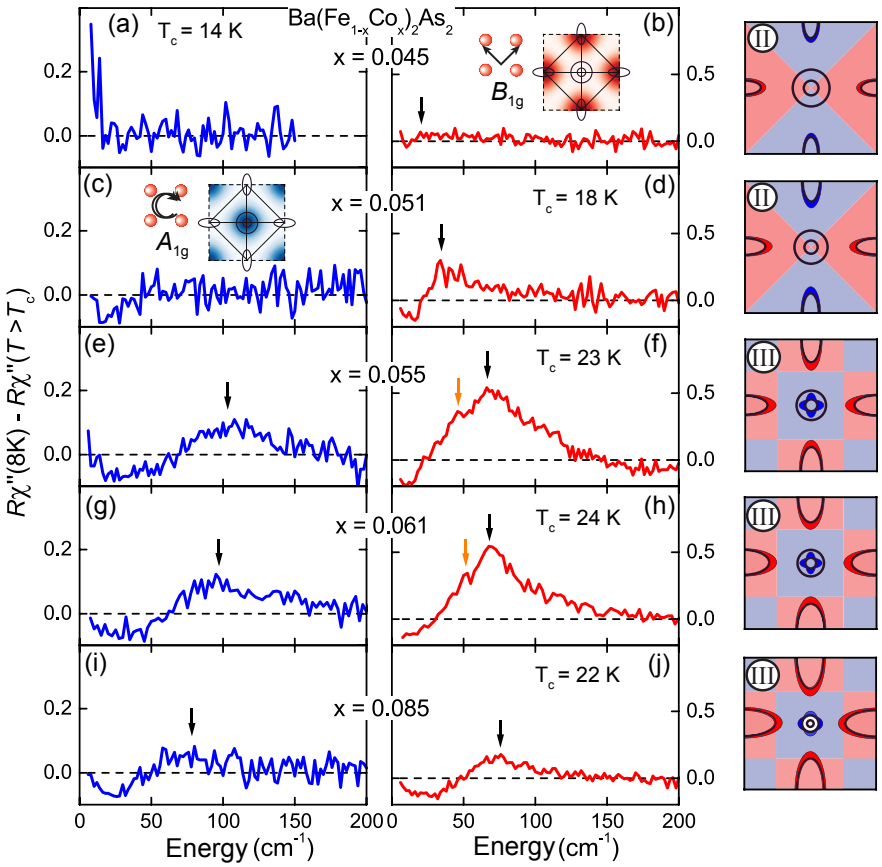

Figure 5.11: Doping dependence of the gap in $Ba(Fe_{1-x}Co_x)_2As_2$. A_{1g} (blue) and B_{1g} (red) difference spectra are shown for five doping concentrations (a)-(e). On the right hand side, the order parameters which correspond to the regions II and III in the PD (Fig. 5.10) are illustrated. They are overlapped with generic FSs which evolve with electron-doping. The gaps on the FS sheets are indicated with red and blue color. For details and description see text. Adapted from [150].

black arrow. This signature becomes more pronounced in the compound with 5.1% Co doping ($T_c = 18$ K). An anisotropic gap opens up on the electron bands having a maximum of approximately 35 cm^{-1}. An examination of the raw data [Fig. 5.12 (d)] reveals that the gap may have a minimum threshold of approximately 8 cm^{-1}. The response coming from the hole-pockets is still zero, indicating a vanishingly small or absent gap. The observation of anisotropic gaps in underdoped $Ba(Fe_{1-x}Co_x)_2As_2$ was also reported from heat transport [183, 184] and penetration depth measurements [185]. However, the absence of a gap on the hole pockets as seen in our Raman experiment suggests that superconductivity originates from pairing of electrons from the electron FSs, implying a nodeles $d_{x^2-y^2}$ order parameter, as indicated on the right hand side of Fig. 5.11.

At optimal doping [5.11 (e)-(h)] the spectra exhibit two major differences to

the spectra of the underdoped compounds: First, besides the large gap on the electron FS sheets, a large gap on the hole-pockets appears. Both gaps have the same order of magnitude. Second, there is a huge change in the intensity of both A_{1g} and B_{1g} spectra. Both changes occur within only 0.4 % electron doping, at a composition which is close to the AFM quantum critical point [cf. Fig. 5.10] [90]. The observed gaps are highly anisotropic, but nodeless, as can be seen from the raw data [5.12 (e)-(h)]. The B_{1g} low-energy Raman susceptibility is proportional to $\sim\sqrt{\Omega}$, suggesting that the gap on the electron FS is nodeless but has a minimum close to zero energy [180]. The A_{1g} intensity varies faster than linear following $\Omega^{1.5}$. If there is a threshold, it must be smaller than $30\,\mathrm{cm}^{-1}$. This would translate into a minimal gap $\Delta_{\mathrm{min}} \leq 2\,\mathrm{meV}$ somewhere on the hole pockets. The observation of anisotropic but nodeless gaps in optimally doped samples via Raman scattering [180, 186] is in agreement with results from heat transport [184] and penetration depth [185] measurements. Even more importantly, the Raman experiments show that the gaps reside on the electron as well as the hole FSs, which implies an $s_{\pm}$ order parameter.

Fig. 5.11 (i) and (j) comprise the results on an overdoped compound. Anisotropic gaps reside on the hole and electron pockets with maxima of approximately $75\,\mathrm{cm}^{-1}$, respectively. The raw data reveal a minimal gap of $\Delta_{\mathrm{min}} \leq 25\,\mathrm{cm}^{-1}$ on the hole- and an even smaller minimal gap on the electron FSs [180], in agreement with the highly anisotropic gaps observed in heat transport [183, 184] and penetration depth [185] experiments. The finite gaps on all bands suggest an $s_{\pm}$ order parameter at this composition. Summarizing, the Raman data suggest that the order parameter switches from $d_{x^2-y^2}$ to $s_{\pm}$ symmetry upon doping somewhere near the magnetic quantum critical point.

The emergence of superconductivity in underdoped compositions coincides with marked changes in the FS topology, at a so-called Lifshitz transition [90, 187]. The presence of AFM order leads to a reconstruction of the electronic structure via the folding of the central hole pocket on top of the elliptical electron pocket at the X-point. This leads to the appearance of petal-like hole pockets at the X-point, see Fig. 5.13 (c). The electron- and hole-bands hybridize and an anisotropic SDW gap opens at the Fermi level. At low doping [Fig. 5.13 (b1)], portions of the lower hole band are above the Fermi level, giving rise to the petal-like hole pockets shown in Fig. 5.13 (c). Electron doping leads to the disappearance of these pockets [Fig. 5.13 (b2)], marking a radical change of the FS topology. ARPES measurements [90] at 13 K show that the transition occurs between 3.4 % and 4.7 % doping,

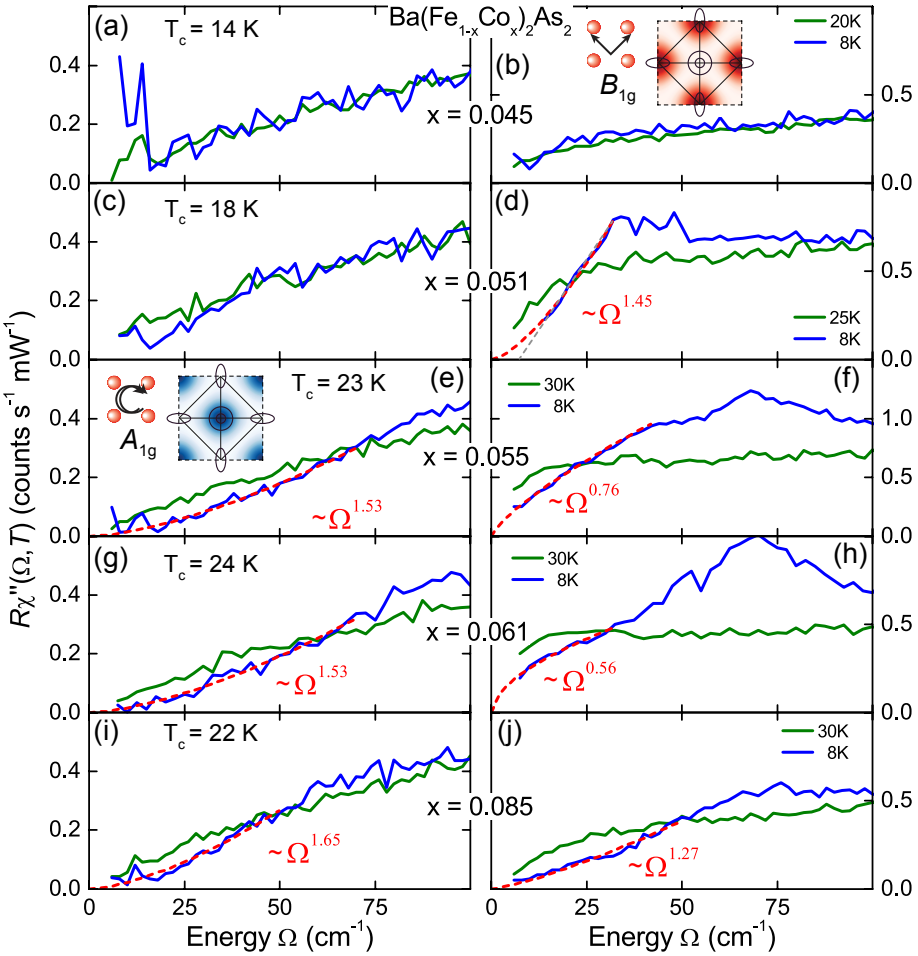

Figure 5.12: Doping dependent Raman spectra of $Ba(Fe_{1-x}Co_x)_2As_2$ above (green) and below (blue) T_c in A_{1g} and B_{1g} symmetry. The B_{1g} are published in [150]. For details and description see text. Adapted from [150].

simultaneously with the onset of superconductivity [Fig. 5.13 (a)]. The ARPES measurements also suggest that the transition does not occur via an intermediate state, with completely gapped Fermi pockets at the X-point [Fig. 5.13 (b2)]. Instead, the transition to the state shown in Fig. 5.13 (b3) and (d) occurs without the absence of Fermi sheets at the X-point at any measured doping level, and the elliptical electron pockets appear immediately after the petals are gone [90].

In a scenario of competing pairing channels, the Lifshitz transition marks the opening of the d-wave pairing channel as the phase space for scattering between the electron pockets becomes huge. If a combination of d-wave pairing and $(\pi, 0)$ SDW order leads to a higher energy reduction than $s_{\pm}$-wave pairing alone, both instability coexist in region (II) of the phase-diagram. Upon further doping with electrons this coexistence persists, until magnetism disappears completely at the magnetic QCP

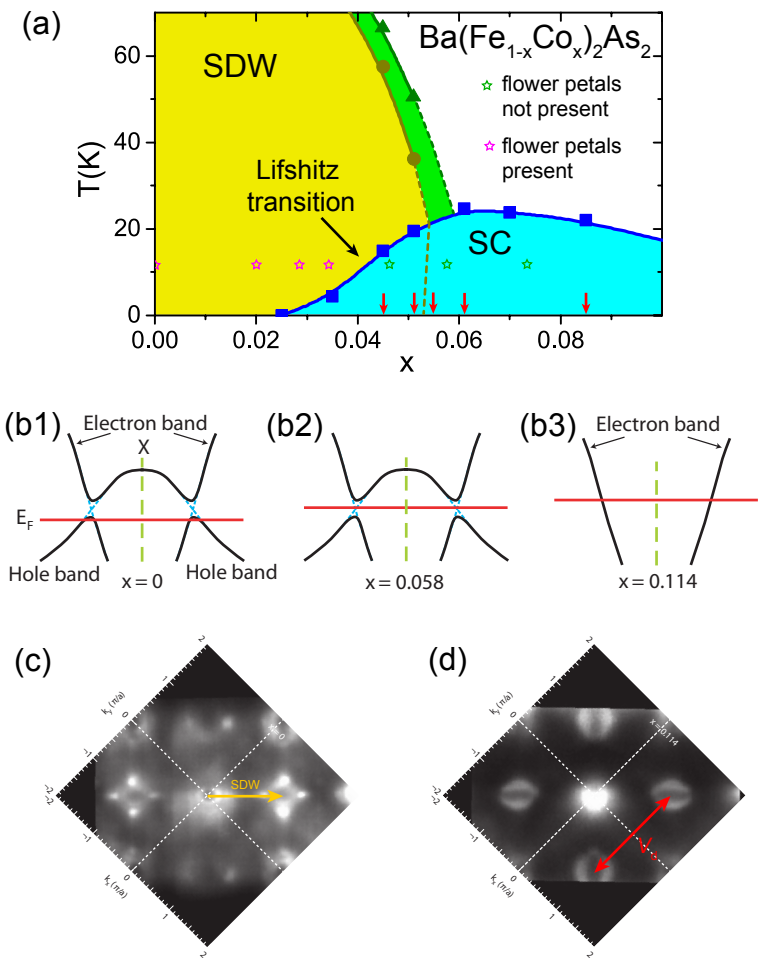

Figure 5.13: Lifshitz transition in $Ba(Fe_{1-x}Co_x)_2As_2$. (a) Phase diagram based on transport measurements as adopted from [29], with ARPES data (from Ref. [90]) on the presence of small hole-like pockets (flower-petals), that appear in the SDW phase. The pockets disappear at the Lifshitz transition. The red arrows indicate the sample compositions which belong to the data presented in Fig. 5.11. (b) Schematic representation of the Lifshitz transition (from Ref. [90]). (c) Low T ARPES spectra (from Ref. [90]) of undoped $x=0$ and overdoped $x = 0.114$ $Ba(Fe_{1-x}Co_x)_2As_2$.

at $x \approx 5.2$ [90] in favor of the $s_{\pm}$ channel.

Finally, an examination of the B_{1g} spectra of the near-optimal and optimally doped compounds [Fig. 5.11 (f) and (h)] reveals weak sub-gap features, indicated with orange arrows, which may be the heavily damped[3] spectroscopic remnants of BS excitons, formed by the d-wave part of $V(\mathbf{k}, \mathbf{k}')$. However, this last point needs further investigation. If the features could be identified as BS excitons, their doping dependent position with respect to the gap-edge might shed light on the interplay between the two pairing channels. Recently, high-quality crystals with hole-underdoped and overdoped compositions have become available for experiment. Since damping of the modes does not seem to play an important role in the hole-doped crystals, an experimental investigation appears to be more promising on this side of the phase diagram.

[3]The damping is expected to occur in systems with low-lying quasi-particles.

Chapter 6

Spin-driven nematic order in $Ba(Fe_{1-x}Co_x)_2As_2$

This chapter summarizes inelastic light-scattering results on the nematic phase in $Ba(Fe_{1-x}Co_x)_2As_2$. A broad peak which emerges in B_{1g} symmetry upon cooling the samples to the SDW ordering temperature T_m is interpreted as the signature of nematic fluctuations. The symmetry and temperature dependence of the peak suggests a magnetic origin of nematicity in this compound.

6.1 Experimental results

Inelastic light scattering results acquired in the normal state of underdoped samples are presented. The undoped compound, as well as samples with 2.5 % and 5.1 % doping concentration have been investigated. The results are shown in the following sections 6.1.1, 6.1.2 and 6.1.3, respectively.

6.1.1 Experimental results: $BaFe_2As_2$

Figure 6.1 shows the temperature evolution of the A_{1g} and B_{1g} Raman susceptibilities of undoped $BaFe_2As_2$. The spectra were taken at constant temperatures ranging from 300 K to 8 K.

The A_{1g} response [Fig. 6.1 (a)] exhibits the expected As-lattice vibration at 185 cm^{-1}. The broader feature at 265 cm^{-1} is the E_g Fe-As phonon, which shows up in the A_{1g} spectra due to the finite overlap of the light polarizations with the crystallographic c-axis in the experiment, cf. Sec. 4.2. Both features sit on top of a particle-hole continuum, which shows only a weak temperature dependence as one

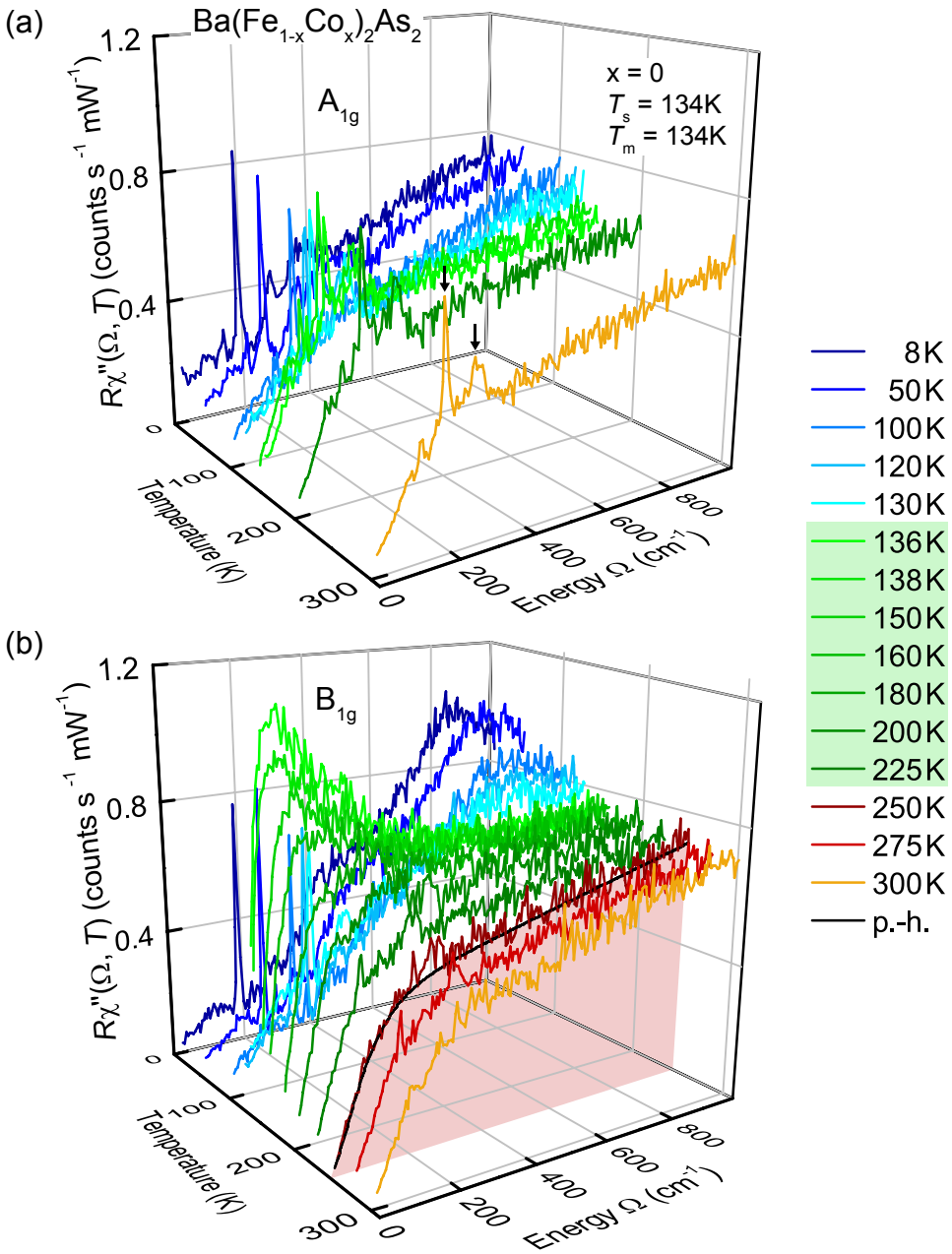

Figure 6.1: (a) A_{1g} and (b) B_{1g} Raman susceptibilities of undoped $BaFe_2As_2$. The spectra are taken at temperatures ranging from 300 K to 8 K. The temperature range in which fluctuations are observed is shaded green. The black line in panel (b) is a fit to the 250 K particle-hole continuum [Eq. (6.6)], which is subtracted from the spectra in order to obtain the fluctuation contribution to the Raman susceptibility, see Sec. 6.2.2. Parts of the spectra were obtained in collaboration with Bernhard Muschler and are published in [150].

approaches the magneto-structural phase transition at 134 K. Below the transition temperature, there is a decrease of spectral weight below 400 cm^{-1} which becomes more pronounced with decreasing temperature. This behavior can be assigned to the opening of the anisotropic SDW gap [150, 173]. At the same time an increase of spectral weight in the high energy part of the spectra is observed which leads to a broad hump with a maximum at about 800 cm^{-1} in the 8 K spectrum. It was argued that this feature is due to interband scattering, the final state of the process being located in a "shadow" band which emerges as a result of backfolding due to the SDW superstructure [173].

The temperature dependence of the B_{1g} spectra [Fig. 6.1 (b)] is substantially different. The temperature range between 300 K and 250 K is also dominated by the weakly temperature dependent particle-hole contribution. However, with decreasing temperature the initial slope of the spectra starts to increase rapidly, and a broad peak emerges which sharpens, while its maximum shifts to lower energies as the temperature is reduced further. The integrated intensity of the spectra has a pronounced maximum just above the magneto-structural transition temperature $T_{\mathrm{s/m}} = 134\,\mathrm{K}$. Upon further reducing the temperature, the peak disappears at the phase transition. Note that the rate of change in which the peak gains integrated intensity drastically increases as one approaches $T_{\mathrm{s/m}}$, reminiscent of a divergent behavior. As in the A_{1g} channel, the imprints of the SDW gap and the opening of the interband scattering channel dominate the low-temperature B_{1g} response. Simultaneously, the symmetry-forbidden A_{1g} phonon appears at 185 cm^{-1} as soon as the magneto-structural transition occurs. Although puzzling at first glance, the presence of the A_{1g} phonon in the B_{1g} susceptibility is not quite surprising. The B_{1g} response is sensitive to an inequivalence of the a and b directions, which is introduced by the spin-density-wave and/or the structural distortion. As a consequence there is leakage of the A_{1g} response into the B_{1g} channel.

The broad peak visible in the B_{1g} Raman response is assigned to fluctuations of some type of nematic order which disappear at the magneto-structural phase transition. Currently, the nature of these fluctuations is a matter of extensive debate. Since at the magneto-structural transition, magnetic ordering (in form of a spin-density-wave) and charge ordering (in form of orbital ordering) set in simultaneously, the question arises whether the fluctuations observed in the Raman response are associated with the magnetic or the charge order. To that end, we investigate underdoped $\mathrm{Ba(Fe_{1-x}Co_x)_2As_2}$, as this provides the possibility to explore the regime between the magnetic and structural transition, e.g. the nematic phase.

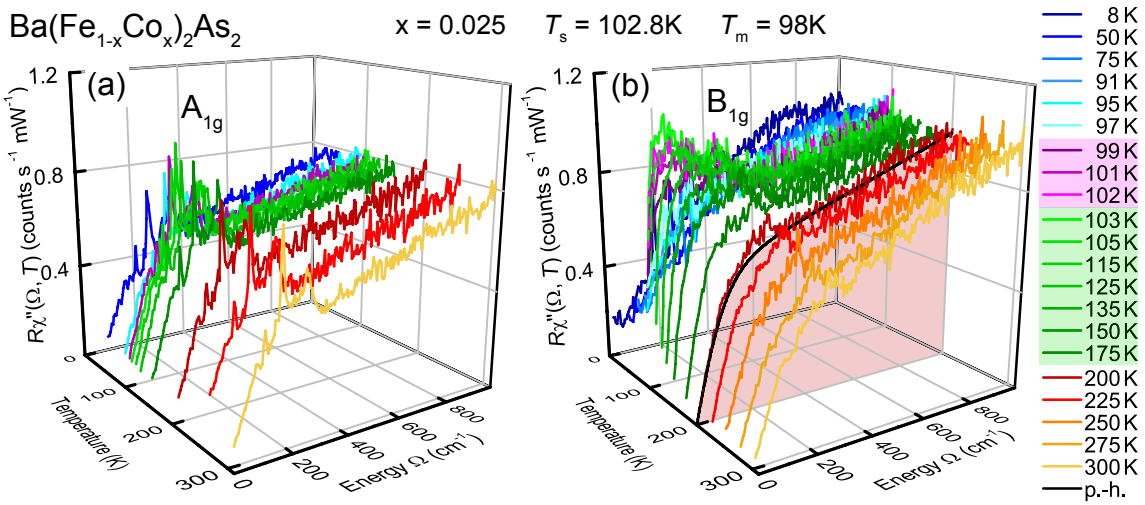

Figure 6.2: (a) A_{1g} and (b) B_{1g} Raman spectra of underdoped $Ba(Fe_{1-x}Co_x)_2As_2$. The temperature regimes in which fluctuations are observed are shaded green ($T > T_s$) and purple ($T_m < T < T_s$).

6.1.2 Experimental results: $Ba(Fe_{0.975}Co_{0.025})_2As_2$

Fig. 6.2 illustrates the A_{1g} (a) and B_{1g} (b) Raman susceptibilities of underdoped $Ba(Fe_{0.975}Co_{0.025})_2As_2$, plotted in the same manner as for the undoped compound. As in Fig. 6.1, the A_{1g} response shows little temperature dependence despite the SDW signature (the loss of spectral weight at low energies for spectra taken at $T < T_m \approx 98\,\mathrm{K}$). The high-temperature B_{1g} response shows a weakly temperature-dependent particle-hole continuum, the initial slopes of the spectra increase slightly as the temperature is reduced. At $T < 200\,\mathrm{K}$, a stronger increase in the initial slopes of the spectra indicates a finite contribution from fluctuations that grows with decreasing temperature until a maximum of the integrated intensity is reached for the 102.8 K spectrum. Again, an increase in the rate of change for the integrated intensity is visible as the temperature approaches $T_s = 102.8\,\mathrm{K}$, where the intensity reaches a maximum. Interestingly, upon lowering the temperature below T_s, but staying well above T_m, the fluctuation peak does not disappear, but just loses intensity, and finally disappears at the magnetic phase transition at $T_m \approx 98\,\mathrm{K}$ (see also Fig. 6.3).

The low-temperature B_{1g} response ($T < T_m$) exhibits the expected reduction of spectral weight at energies $\Omega < 300\,\mathrm{cm}^{-1}$, indicating the opening of the SDW gap that is somewhat smaller in comparison to the undoped compound. The excess intensity at higher energies ($\Omega > 600\,\mathrm{cm}^{-1}$) signals the opening of the interband scattering channel although this feature is less pronounced than in the undoped

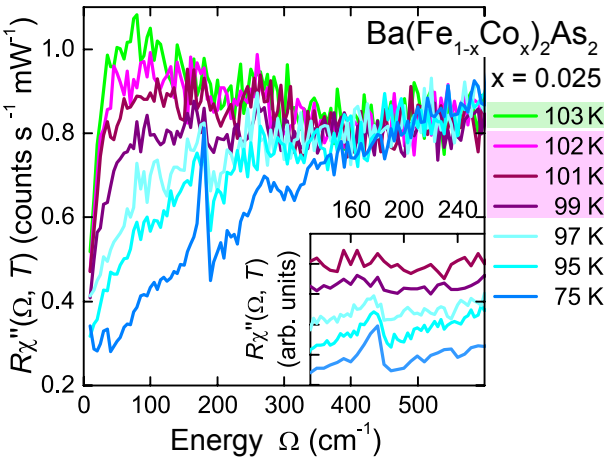

Figure 6.3: B_{1g} Raman susceptibility of $Ba(Fe_{0.975}Co_{0.025})_2As_2$ for temperatures in close to T_m. The fluctuation peak does not disappear abruptly at T_s, but slowly decreases as the temperature approaches T_m. In the orthorhombic/paramagnetic phase, there is no sign of a phonon. Below T_m, a Fano-shaped phonon appears at 180 cm^{-1}.

compound. Note that the symmetry-forbidden A_{1g} phonon is present, as in the undoped compound, but shows up only below the magnetic transition temperature T_m in the doped sample. This is highlighted in Fig. 6.3, which shows the B_{1g} susceptibility of $Ba(Fe_{0.975}Co_{0.025})_2As_2$ for temperatures close to the magnetic ordering temperature T_m. In the orthorhombic/paramagnetic phase, there is no indication of a phonon. As the temperature drops below T_m, a Fano-shaped phonon line appears at approximately 180 cm^{-1} and gains intensity when the temperature is reduced further. Whatever is responsible for the presence of the symmetry-forbidden phonon, the temperature dependence of the feature argues that it is the magnetic phase transition rather than the structural one that triggers it's appearance.

6.1.3 Experimental results: $Ba(Fe_{0.949}Co_{0.051})_2As_2$

Finally, underdoped $Ba(Fe_{0.949}Co_{0.051})_2As_2$, which in addition to the nematic and magnetic phase also exhibits superconductivity, has been investigated. The temperature dependent Raman susceptibilities are shown in Fig. 6.4 (a) (A_{1g}) and (b) (B_{1g}). The A_{1g} response in the tetragonal state ($T_s = 53$ K) shows weak temperature dependence without any sign of a fluctuation contribution. In contrast to the lower doped compounds, the opening of the SDW gap is not visible in the A_{1g} response. A considerable fluctuation contribution can be found in the B_{1g} symmetry for temperatures below 200 K where an increase of the initial slope of the spectra is observed. This contribution grows with decreasing temperature and is largest for the 70 K spectrum.

The structural and magnetic phase transitions in this sample take place at $T_s =$ 53 K and $T_m = 37$ K, respectively. The only spectrum taken at an intermediate temperature, the 50 K spectrum, does not decrease substantially in comparison to

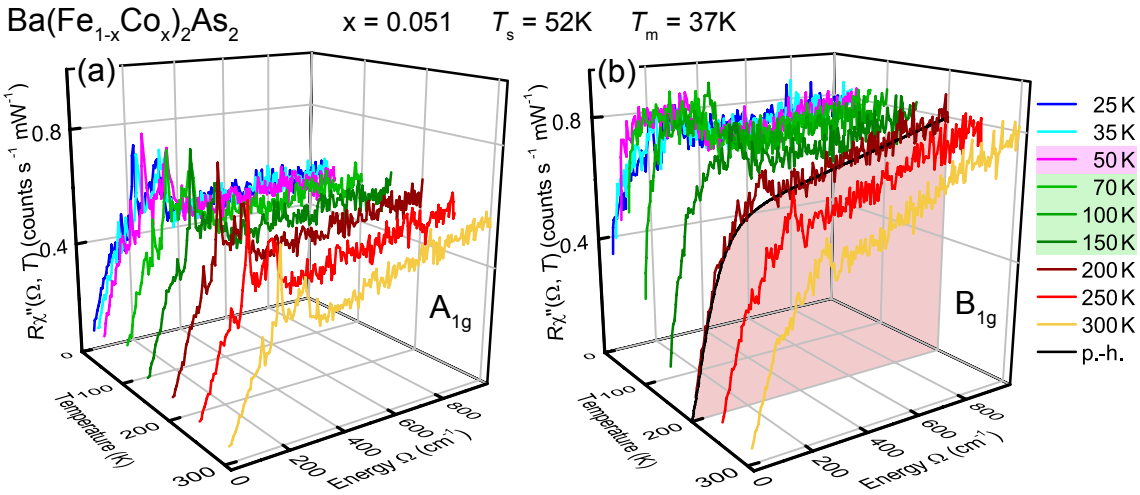

Figure 6.4: (a) A_{1g} and (b) B_{1g} Raman spectra of slightly underdoped $Ba(Fe_{0.949}Co_{0.051})_2As_2$, which, in addition to the nematic ($T_s = 53\,K$) and magnetic ($T_m = 37\,K$) phases also becomes superconducting at temperatures below 19.5 K. A fluctuation signal can be found in the B_{1g} symmetry for temperatures below 200 K. The spectra are taken from [150] and have been replotted here in the same fashion as for the $x = 0$ and $x = 0.025$ samples.

the 70 K spectrum. However, since spectra at temperatures just slightly above T_s are missing, and only one spectrum in the nematic regime is available, a statement on the temperature dependence of the fluctuations for $T_m < T < T_s$ is not possible and the qualitative discussion in the next section is restricted to the fluctuation regime in the tetragonal phase.

The Raman spectra allow some general statements on the temperature- and doping-dependence of the fluctuations. With increasing doping, the temperature at which the fluctuations set in drops from approximately 250 K in the undoped sample to somewhat below 200 K in the sample with 5.1 % Co content. Another clearly visible trend is that the maximum of the fluctuation peak shifts to lower energy with increasing doping. Unfortunately, it is not trivial to determine the exact temperature at which fluctuations emerge since the fluctuation contibution is small just below the onset-temperature and sits on top of a weakly temperature-dependent particle-hole background. Disentangling the fluctuation and particle-hole contribution in the Raman response is therefore a prerequisite for a quantitative analysis of the fluctuations. Such an analysis is given in section 6.2.

6.2 Discussion

We wish to identify the origin of the fluctuation signal observed in the B_{1g} Raman response. To this end, the onset temperatures $T_{\mathrm{f}}(x)$, the spectral shape, the selection rules and the detailed temperature dependence close to the magneto-structural transitions will be scrutinized.

6.2.1 Relaxation rate analysis

It is necessary to isolate the fluctuation contribution to the Raman response from the particle-hole continuum. If we assume that the latter is only weakly temperature-dependent, it is enough to pin down the temperature T_{f} at which fluctuations start to emerge, and subtract a spectrum taken at a temperature slightly higher than T_{f} from the Raman spectra obtained at temperatures $T_{\mathrm{m}} < T < T_{\mathrm{f}}$. If the assumption of a constant particle-hole continuum is relaxed, one has to model the continuum by fitting spectra that do not have contributions from fluctuations, and extrapolate the fits to temperatures where fluctuations are present.

In the following, we extract carrier lifetimes $\tau_{\gamma\gamma}(\Omega, T)$ or scattering rates $\Gamma_{\gamma\gamma} = 1/\tau_{\gamma\gamma}$ along with mass enhancement factors $1+\lambda_{\gamma\gamma}(\Omega, T)$ from the bare particle-hole Raman susceptibility, which then can be compared with the findings of transport measurements. For the analysis it is assumed that as soon as these quantities are no longer in accordance with the transport results, the Raman response no longer originates from particle-hole excitations alone. Given the excellent agreement of Raman and transport relaxation rates at high temperatures this is a safe assumption.

The extraction of relaxation rates and mass enhancement factors works via the relaxation or memory function approach proposed by Götze and Wölfle [188], which is a standard procedure in infrared (IR) or optical spectroscopy to derive the complex conductivity from the reflectivity [189]. Opel *et al.* [190] adopted this method for the Raman susceptibility and showed in particular that absolute numbers for all quantities can be obtained [150, 160, 190, 191]. A few remarks on the quantities that can be derived from the spectra will be given in the following.

The imaginary part of the Raman spectral function $\chi''_{\gamma\gamma}(\Omega, T)$, which is obtained from the experiment is connected with the dynamic (Raman) relaxation rate $\Gamma_{\gamma\gamma}(\Omega, T)$ and the mass enhancement factor $1 + \lambda_{\gamma\gamma}(\Omega, T)$ via

$$\chi''_{\gamma\gamma}(\Omega, T) = \frac{\Omega\Gamma_{\gamma\gamma}(\Omega, T)}{\Omega^2[1 + \lambda_{\gamma\gamma}(\Omega, T)]^2 + \Gamma^2_{\gamma\gamma}(\Omega, T)}. \tag{6.1}$$

The equation can serve as a starting point to extract $\Gamma_{\gamma\gamma}(\Omega, T)$ and $1 + \lambda_{\gamma\gamma}(\Omega, T)$ numerically from the Raman data. The index γ is short hand for $\gamma(\mathbf{k})$ and represents the Raman vertex which projects out symmetry dependent parts of the Brillouin zone and thus $\Gamma_{\gamma\gamma}$ and $\lambda_{\gamma\gamma}$ reflect $\mathbf{k}$-dependent properties. Consequently, given the specific FS topology of $Ba(Fe_{1-x}Co_x)_2As_2$, the scattering rates which are extracted from the A_{1g} and B_{1g} Raman susceptibilities presented in Sec. 6.1, measure the effective scattering rates of QPs from the hole-bands and electron-bands of the particular material. In this context $\Gamma_{\gamma\gamma}(\Omega, T)$ can be best thought of as a $\mathbf{k}$-resolved Raman resistivity. In the same manner $1 + \lambda_{\gamma\gamma}(\Omega, T) = m^*/m_b$ with m_b the band mass, describes a frequency- and band-dependent mass enhancement that measures the strength of interactions of the QPs either among each other or with other excitations such as phonons. Since we seek to compare the Raman results with resistivity measurements, we can use the fact that in the static limit, the scattering rate $\Gamma_{\gamma\gamma}(\Omega \to 0, T) \equiv \Gamma_0(T) = 1/\tau_0(T)$ is equivalent with the inverse of the static two particle lifetime. In the Drude model the latter is related to the dc-resistivity of a metal [190]

$$\Gamma_0(T) = \frac{1}{\tau(T)} = 1.08 \cdot \rho(T) \cdot \omega_{\mathrm{pl}}^2 \tag{6.2}$$

with $\Gamma_0(T)$ given in cm^{-1}, $\rho(T)$ being the resistivity [$\mu\Omega$cm] and ω_{pl} the plasma frequency [eV].

Fig. 6.5 shows the dynamic relaxation rates $\Gamma_{\gamma\gamma}(\Omega, T)$ of $Ba(Fe_{0.975}Co_{0.025})_2As_2$ derived from the energy dependent response $R\chi''_{\gamma\gamma}(\Omega, T)$ displayed in Fig. 6.2 for temperatures $T < T_{\mathrm{s}}$, (a) and (b), and $T > T_{\mathrm{s}}$, (c) and (d). Above T_{s}, the scattering rates have little structure and a similar spectral shape at intermediate and high energies, where all curves exhibit a similar finite slope and have a tendency to become flat. At low energies, $\Gamma_{\gamma\gamma}(\Omega, T)$ starts with zero slope for all $T > T_{\mathrm{s}}$ in the A_{1g} symmetry [panel (c)] and for temperatures $T > 150\,\mathrm{K}$ in the B_{1g} symmetry [panel (d)]. In the range $T_{\mathrm{s}} > T > 150\,\mathrm{K}$, all B_{1g} scattering rates start with a finite slope close to zero energy. This slope tends to become larger as one approaches the structural phase transition temperature T_{s}. The $T > T_{\mathrm{s}}$ A_{1g} scattering rates differ only by a small constant offset which is approximately proportional to temperature. They clearly exhibit an overall weaker temperature dependence than the B_{1g} scattering rates above T_{s} where the offset is larger and not proportional to temperature. Below T_{s}, also the A_{1g} scattering rates exhibit a small initial slope and a general trend towards an increasing initial slope is observed at low T, cf. Fig. 6.5 (a). This trend is even stronger pronounced in the B_{1g} symmetry, cf. Fig. 6.5 (b). Below T_{m},

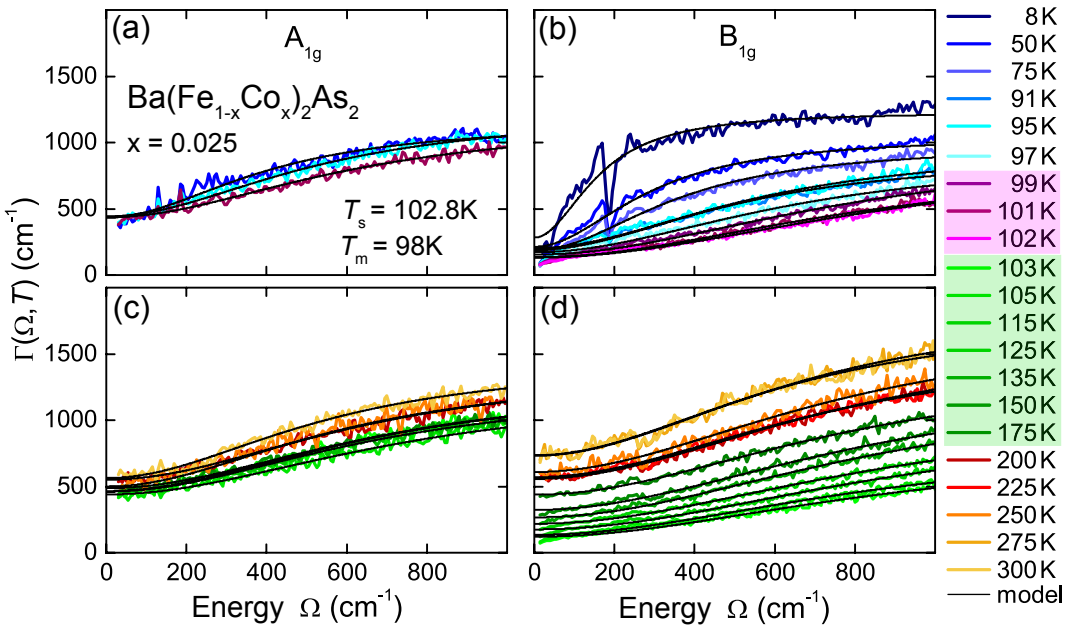

Figure 6.5: Temperature and symmetry dependence of the $Ba(Fe_{0.975}Co_{0.025})_2As_2$ relaxation rates $\Gamma_{\gamma\gamma}(\Omega,T)$ for temperatures $T<T_s$ [panels (a) and (b)] and $T>T_s$ [panels (c) and (d)]. The rates were obtained, using the procedure described by Opel *et al.* [190], from the energy dependent response $R\chi''_{\gamma\gamma}(\Omega,T)$ displayed in Fig. 6.2. The smooth black lines correspond to a fit with the parallel resistor model of Hussey *et al.* [192].

an additional feature in the B_{1g} scattering rate appears at $180\,\mathrm{cm}^{-1}$, which is an artifact originating from the symmetry-forbidden A_{1g} phonon-mode which sits on top of the B_{1g} particle-hole continuum.

In summary, the rates reflect the variation of the raw data (Fig. 6.2) but, due to the extraction procedure [190], show some features in a more pronounced fashion such as the low-energy variation with temperature. Note however, that the memory function approach for the extraction of scattering rates is valid, strictly speaking, only for particle-hole excitations. Due to the presence of SDW correlations, the physical meaning of scattering rates $\Gamma_{\gamma\gamma}(\Omega, T<T_m)$ is therefore questionable. Hence scattering rates obtained at $T<T_m$ will not be considered for further discussions.

In order to reliably extract the zero-energy extrapolation values of $\Gamma_{\gamma\gamma}(\Omega\to 0,T)$ from the dynamic scattering rates (Fig. 6.5) we use the phenomenological parallel resistor model with a quadratic energy dependence at $\Omega\to 0$ [192–195]

$$\frac{1}{\Gamma_{\gamma\gamma}(\Omega,T)} = \frac{1}{\Gamma^{*}_{\gamma\gamma}(\Omega,T)} + \frac{1}{\Gamma^{\max}_{\gamma\gamma}(T)}. \tag{6.3}$$

where $\Gamma^{*}_{\gamma\gamma}(\Omega,T) = c(T) + a(T)\Omega^2$ dominates at low frequencies while $\Gamma^{\max}_{\gamma\gamma}(T)$ describes the high energy part. Eq. (6.3) yields functions having the correct ana-

lytical behavior in the limits $\Omega \to 0$ and $\Omega \to \infty$: (i) $\Gamma_{\gamma\gamma}(\Omega, T)$ (as opposed to the imaginary part of the single particle self energy Σ'') is a symmetric function, $\Gamma_{\gamma\gamma}(-\Omega, T) = \Gamma_{\gamma\gamma}(\Omega, T)$, (ii) $\lambda_{\gamma\gamma}(\Omega \to 0, T > 0)$ is finite and symmetric, and (iii) $\Gamma_{\gamma\gamma}(\Omega, T)$ saturates at high energy. The latter condition is a restriction in the spirit of the Mott-Joffe-Regel limit [196, 197] that applies when the quasi-particle mean free path at high temperature becomes progressively shorter and finally comparable to the lattice constant. As phonons dominate the scattering in metals at high temperatures, the mean free path cannot decrease below the lattice constant and the resistivity saturates. In the case of two-particle response functions there are contributions to the carrier response beyond the mean free path, and general statements as to the high-energy behavior become impossible [198]. Inversion of Eq. (6.3) yields

$$\Gamma_{\gamma\gamma}(\Omega, T) = \frac{[c(T) + a(T)\Omega^2] \cdot \Gamma_{\gamma\gamma}^{\max}(T)}{c(T) + a(T)\Omega^2 + \Gamma_{\gamma\gamma}^{\max}(T)}, \tag{6.4}$$

with the zero frequency limit $\Gamma_{\gamma\gamma}(0, T)$ given by

$$\Gamma_{\gamma\gamma}(0, T) = \frac{c(T)\Gamma_{\gamma\gamma}^{\max}(T)}{c(T) + \Gamma_{\gamma\gamma}^{\max}(T)}. \tag{6.5}$$

The fits to the relaxation rates $\Gamma_{\gamma\gamma}(\Omega, T)$ according to Eq. (6.4) correspond to the black lines in Fig. 6.5. As expected, the $\Omega \to 0$ extrapolation depends on both the high frequency limit $\Gamma_{\gamma\gamma}^{\max}(T)$ and the offset $c(T)$.

Fig. 6.6 shows the symmetry dependent static Raman relaxation rates $\Gamma_0(T)$ of $Ba(Fe_{1-x}Co_x)_2As_2$ for the three doping levels (a) $x = 0$, (b) $x = 0.025$ and (c) $x = 0.051$. Each point in Fig. 6.6 is obtained from Eq. (6.5)[1]. For comparison, all panels show the in-plane (dc) resistivities ρ_{ab} (black line, right axis) of samples from the same batch [29], which are converted into relaxation rates $\Gamma_\rho(T)$ using Eq. (6.2). The plasma frequencies which are used for the conversion (cf. Fig. 6.6) are in good agreement with optical spectroscopy data [199–203]. From the dynamic relaxation rates of the $x = 0.025$ sample (Fig. 6.5), it was already evident that the $T > T_s$ B_{1g} scattering rates exhibit a stronger temperature dependence than those of the A_{1g} channel. This behavior is reproduced in the static limit, displayed in Fig. 6.6 (b). Starting at 300 K, the average of $\Gamma_{A1g}(0, T)$ and $\Gamma_{B1g}(0, T)$ tracks $\Gamma_\rho(T)$ until the temperature reaches approximately 200 K. This behavior is to be expected if the Raman relaxation rates express **k**-resolved transport properties. At lower temperatures, $\Gamma_{A1g}(0, T)$ continues to follow $\Gamma_\rho(T)$, but $\Gamma_{B1g}(0, T)$ begins to deviate,

[1] The $x = 0$ and $x = 0.051$ relaxation rates and fits can be found in Appendix 8.C.

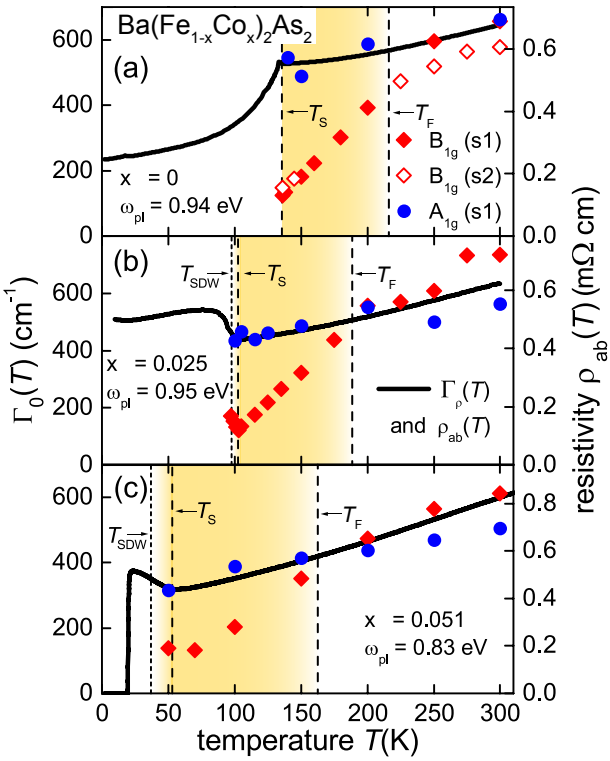

Figure 6.6: Static relaxation rates and transport data. Panels (a)-(c) show the doping dependent Raman relaxation rates $\Gamma_{\gamma\gamma}(\Omega=0,T)$ for A_{1g} (blue symbols) and B_{1g} (red symbols) symmetries as derived from $\Gamma_{\gamma\gamma}(\Omega,T)$ (see text). The in-plane (dc) resistivity ρ_{ab} (black line, right axis) [29] is converted into a relaxation rate $\Gamma_\rho(T)$ using a Drude model [Eq. (6.2)]. The plasma frequencies used for the conversion are indicated in each panel. Note that in (a) results of two samples are summarized.

the difference becoming more pronounced as the temperature approaches T_s.

It is inadequate to interpret this behavior in terms of an increasing lifetime $\tau=1/\Gamma$ of particle-hole excitations in the B_{1g} channel, since this would still require the condition $[\Gamma_{A1g}(0,T)+\Gamma_{B1g}(0,T)]/2 \approx \Gamma_\rho(T)$ to be fulfilled. In contrast, it is more sensible to argue that the premise of $R\chi''_{\gamma\gamma}(\Omega,T)$ being dominated by particle-hole excitations is not correct as soon as the Raman relaxation rates, on average, do no longer coincide with the rates derived from the transport measurements. Consequently, the deviation of the B_{1g} scattering rate results from an additional contribution to the Raman response, which grows upon approaching the nematic transition. In the following, we will presume that the drop in the B_{1g} relaxation rates derives from fluctuations and assign the onset of fluctuations to the temperature T_f, where the B_{1g} scattering rates begin to deviate from the transport data. Finally, it is worth noting that the B_{1g} scattering rate once more proceeds parallel to $\Gamma_\rho(T)$ in the narrow temperature interval between the magnetic and nematic transition, signaling a weakening influence of fluctuations.

The temperature interval in which fluctuations contribute to the Raman response is colored yellow in Fig. 6.6. The $BaFe_2As_2$ scattering rate shows a similar temperature dependence as the one of the $x = 0.025$ sample. While the A_{1g} scattering rate tracks $\Gamma_\rho(T)$ from room temperature down to T_m, the B_{1g} rate does so only

down to the temperature $T_f = (215 \pm 10)$ K, below which it decreases stronger than $\Gamma_\rho(T)$. Note that the empty B_{1g} data points correspond to a measurement of a second sample which, at high temperatures, exhibits a somewhat lower scattering rate than sample 1. A comparable behavior is found for the scattering rates of the $x = 0.051$ sample, even if the deviations of the B_{1g} scattering rates from the transport data are less pronounced than at lower doping concentrations, see Fig. 6.6 (c). Replacing 2.5 % [5.1 %] of iron by cobalt leads to a decrease of T_f to (190 ± 10) K [(160 ± 10) K], see Fig. 6.6 (b) and (c), respectively. Simultaneously, the temperature range in which fluctuations contribute to the Raman response becomes broader with doping.

It should be noted that ARPES measurements on $Ba(Fe_{1-x}Co_x)_2As_2$ reveal an anisotropic energy splitting of the d_{xz} and d_{yz} bands in *stressed* crystals [32], that persists up to a temperature which approximately coincides with T_f. Moreover, the temperature window in which the splitting is observed appears to be larger closer to the superconducting dome, a trend also seen in transport measurements [47]. These observations are in line with the existence of a regime exhibiting a large nematic susceptibility which is responsible for the deformation of the electronic ground state in response to a symmetry breaking perturbation. It stands to reason that the observed fluctuation contribution to the B_{1g} Raman response derives from nematic fluctuations.

6.2.2 Aslamazov-Larkin fluctuations

Having identified the onset temperatures T_f, we can go on and isolate the fluctuation contributions from the spectra $R\chi''_{\gamma\gamma}(\Omega, T)$ shown in Sec. 6.1. This will be done in the following exemplary for the sample with 2.5 % Co doping. At this composition there is a sufficiently large temperature gap of approximately 5 K between the structural and magnetic phase transitions. This is of importance as it will prove crucial for the later analysis to determine the behavior of the fluctuations between the two transitions.

Above $T_f(2.5\%) \approx 190$ K, $R\chi''_{\gamma\gamma}(\Omega, T)$ reflects the bare particle-hole contribution to the Raman response. Fluctuations set in below this temperature and persist down to $T_m(2.5\%) = 98$ K, as is evident from the Raman susceptibility (see Fig. 6.3). In order to approximate the temperature dependent particle-hole continuum between these two temperatures, we fit the 300 K and 97 K spectra by

$$\chi''_{\mathrm{cont}}(\Omega, T) = a(T) \cdot \tanh\left(\frac{\Omega}{c}\right) + b(T) \cdot \left(\frac{\Omega}{c}\right) \tag{6.6}$$

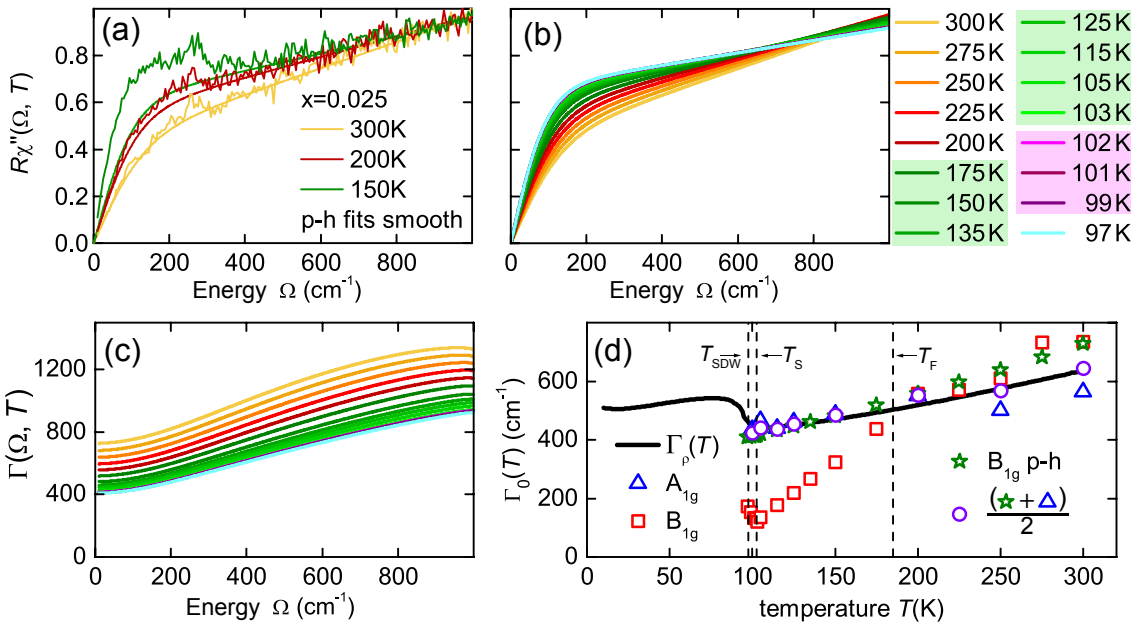

Figure 6.7: Approximation of the p-h continuum for $Ba(Fe_{0.975}Co_{0.025})_2As_2$. (a) Fits to the electronic continuum according to Eq. (6.6), shown explicitly along with three spectra. (b) Continuum approximation and (c) the resulting dynamic relaxation rates for all temperatures $T > T_m$. (d) Static relaxation rate of the continuum approximation, along with the A_{1g} and B_{1g} relaxation rates derived from experiment. The average of the experimental A_{1g} and the B_{1g} continuum approximation relaxation rate (violet circles) by and large reflects the experimental resistivity data.

with $a(T) = a_1 - a_2 \cdot T$, $b(T) = b_1 + b_2 \cdot T$. a and b depend linearly on temperature with the coefficients $a_1 = 0.82379$, $a_2 = 0.00138$, $b_1 = -0.00923$ and $b_2 = 0.00028$ fixed for doping $x = 0.025$. c corresponds to the relaxation rate Γ and is adjusted to reproduce the data above T_f and the resistivity. Eq. (6.6) exhibits the correct analytical behavior at $\Omega \to 0$, and provides an excellent fit to the continuum. Fits to the continuum are shown explicitly along with three spectra in Fig. 6.7 (a). The deviations from the fits to the 150 K and 200 K spectra derive from fluctuations.

The approximation to the p-h continuum and the resulting dynamic relaxation rates for all temperatures $97\,K \leq T \leq 300\,K$ are shown in Fig. 6.7 (b) and (c), respectively. The static relaxation rates of the approximation, derived from the dynamic ones as described in the last section, are plotted as green stars in Fig. 6.7 (d), along with the A_{1g} and B_{1g} relaxation rates derived from experiment. As expected, the average of the experimental A_{1g} and the B_{1g} relaxation rates of the approximated continuum by and large reflect the experimental resistivity data, confirming that the temperature dependent continuum displayed in Fig. 6.7 (b) is indeed appropriate.

The subtraction of the continuum from the spectra yields the bare fluctuation

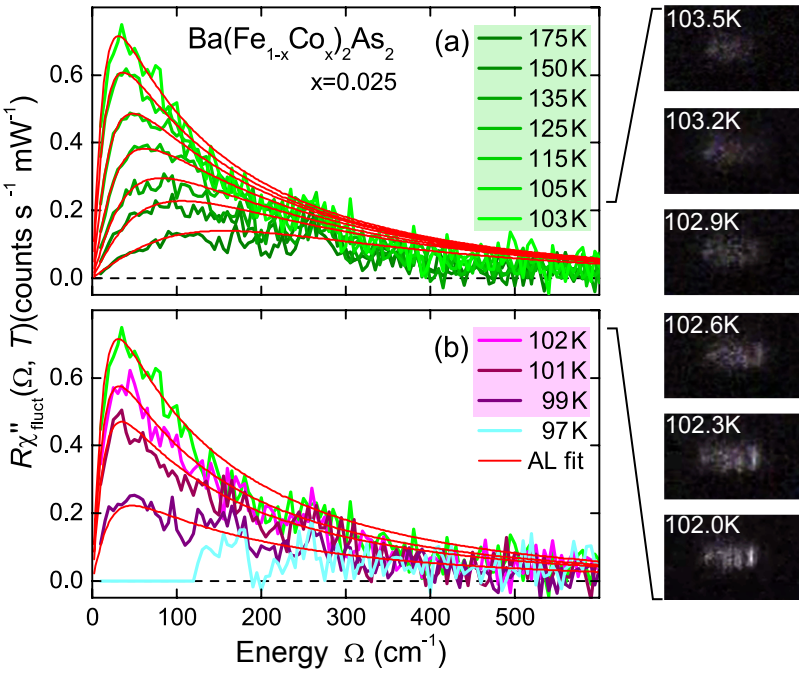

Figure 6.8: Bare fluctuation contribution to the Raman susceptibility in the tetragonal (a) and the nematic phase (b). The red curves correspond to the theoretical Raman response contribution of 2D nearly critical spin and/or charge fluctuations [Eq. (6.8)]. The right hand side of the figure shows the appearance of stripes in the laser focus, signaling the tetragonal to orthorhombic phase transition at T_s (see text).

contribution that is shown in Fig. 6.8 (a) and (b) for the tetragonal and the nematic phase, respectively. The 175 K spectrum exhibits a broad maximum at 150 cm^{-1}. On lowering the temperature, the integrated intensity increases rapidly, the maximum becomes more distinct and shifts to lower energies while approaching T_s.

This trend has been observed earlier [204], where it was interpreted as a fingerprint of an incipient charge-nematic order that fully develops at T_s. The authors argue that, owing to the nature of the Raman experiment in which the light couples to the charge of the electron rather than to the spin degree of freedom, the nematic susceptibility measurable in the Raman experiment originates from anisotropic charge fluctuations. However, the charge nematic transition temperature extracted in Ref. [204] is off by at least 50 K over the whole doping range. Moreover, a comparison of the Raman data to measurements of the orthorhombic lattice stiffness [51, 52] implies that charge nematicity is coupled too weakly to the lattice to drive the structural transition. Thus, Gallais *et al.* [204] conclude that charge nematicity is not the only nematic degree of freedom in $Ba(Fe_{1-x}Co_x)_2As_2$, but that the precise nature of this additional contribution cannot be identified in the Raman experiment.

Recently, two theories have been put forward suggesting that either the magnetic moments of the iron atoms (ordering below T_m) or the iron d-orbital degrees of freedom (assumed to order below T_s) provide the driving mechanism for nematicity (see Sec. 2.3). Therefore, we performed inelastic light scattering experiments also in the small temperature window of the nematic phase between $T_m \approx (98 \pm 0.5)\,\mathrm{K} < T < T_s \approx (102.8 \pm 0.1)\,\mathrm{K}$. We were able to determine T_s precisely by the appearance of twin boundaries at T_s. The image of the focus is shown as a function of temperature on the right hand side of Fig. 6.8. The direct reflex of the elastically scattered laser light does not enter the observation optics (see Sec. 4.1). As a consequence, the laser focus is hardly visible on a very smooth sample surface. This is the case above 102.9 K, where no additional structures are visible in the spot. Upon cooling down to 102.0 K, vertical stripes appear in the focal spot. They are faint already at 102.6 K and finally become clearly visible at 102.3 K. The vertical stripes derive from stray light of the laser from particles adsorbed at the polar twin-boundaries. Note, that for $T_s \approx 102.8\,\mathrm{K}$ the doping is slightly below the nominal value according to the phase diagram of Chu *et al.* [29]. The magnetic transition at T_m is expected to occur at approximately 5 K below T_s. Indeed, a signature of this transition can be identified in the B_{1g} Raman response, where the symmetry-forbidden A_{1g} phonon at $180\,\mathrm{cm}^{-1}$ evolves between 99 K and 97 K (see Sec. 6.1.2).

Three spectra obtained in the nematic phase are plotted with a violet color scheme Fig. 6.8 (b). Surprisingly, the fluctuations do not disappear directly below T_s. Instead, the intensity decreases continuously and the maximum stays pinned at the same energy. These observations cast doubt on an interpretation of the observed peak in terms of orbital fluctuations, as orbital order is established at T_s [32], while the observed fluctuations persist down to T_m. However, while a close relation to magnetism is evident, the peak does not reflect the temperature dependence of the magnetic susceptibility either, as it does clearly not diverge at the magnetic phase transition, but rather shows a cusp at the structural transition.

In the following, we present an explanation in terms of a spin-nematic fluctuation scenario alternative to the one given in Ref. [204]. For a quantitative analysis we apply the functions derived by Caprara *et al.* [157], which have already been used for the cuprates [205] and tritellurides [61], describing the symmetry-dependent Raman response contribution of 2D nearly critical spin and/or charge fluctuations. The theory describes the Raman response contribution deriving from the exchange of two fluctuations with opposite momenta $\mathbf{q}$ and $-\mathbf{q}$, hence preserving the $\mathbf{q}_{\mathrm{total}} = 0$ selection rule. Thus, the scattering from these soft collective modes (CMs) provides

an additional scattering channel besides the bare particle-hole bubble presented in Sec. 3.3. The theory is based on the work of Aslamazov and Larkin on fluctuations in the conductivity of superconductors [206], hence the soft CMs are also referred to as Aslamazov-Larkin (AL) fluctuations. Caprara *et al.* show that the role of charge- and spin-fluctuations and their particular contributions to the Raman response can be disentangled, given that both kinds of modes are peaked at distinct characteristic wave vectors $\mathbf{q}_\lambda$, the index $\lambda = c, s$ referring to the charge- or spin-character of the CMs [207]. The leading order AL diagrams which, in good approximation, describe the fluctuation contribution to the Raman response are shown in Figs. 6.9 (a) and (b). Each dashed line represents a bosonic CM propagator depending on the Matsubara frequencies ω_m on the imaginary time axis

$$D(\mathbf{q}, \omega_m) = \frac{1}{|\omega_m| + \nu|\mathbf{q} - \mathbf{q}_\lambda| + m(T)} \tag{6.7}$$

with ν a constant electronic energy scale and $m(T) \propto \xi^{-2}$ the mass of the CM which encodes the proximity of the electron system to long-range charge- and/or spin-order. This propagator is largest at zero frequency and $\mathbf{q} = \mathbf{q}_\lambda$, the wave vector setting the modulation of the most singular fluctuations.

Evaluating the diagrams in Fig. 6.9 yields the symmetry-dependent Raman response contribution from fluctuations [157]

$$\Delta\chi''_{\gamma\gamma} = \Lambda^2_{\gamma\gamma} \int_0^\infty dz \, [b(z - \Omega/2) - b(z + \Omega/2)] \, \frac{z_+ z_-}{z_+^2 - z_-^2} \, [F(z_-) - F(z_+)] \, . \tag{6.8}$$

where $b(z)$ is the Bose distribution function,

$$F(z) \equiv \frac{1}{z} \left[\arctan\left(\frac{\Omega_0}{z}\right) - \arctan\left(\frac{m}{z}\right) \right], \tag{6.9}$$

$z_\pm \equiv [z \pm \Omega/2][1 + (z \pm \Omega/2)^2/\Omega_0^2]$, and $\Omega_0 \sim (100{-}500)\,\mathrm{cm}^{-1}$ is an ultraviolet cutoff.

The AL fits to $R\chi''_{\mathrm{fluct}}(\Omega, T)$ are displayed in Fig. 6.8 as red curves. All fits were obtained by varying the only adjustable parameter $m(T)$. By determining the overall intensity at 103 K, the spectra at all other temperatures can be reproduced satisfactorily with this single parameter as visualized in Fig. 6.8. The overall good agreement between theory and experiment suggests that the functions by Caprara *et al.* capture the essential physics of the observed fluctuations.

The approach does not naturally explain why the fluctuations, after showing a distinct spectral-weight maximum at 103 K (just slightly above T_s), survive in

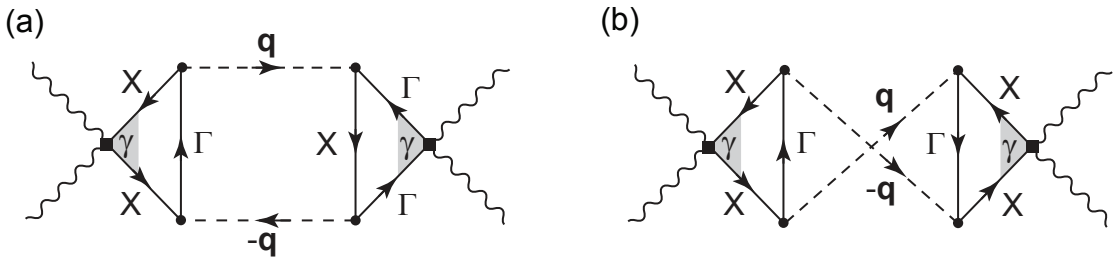

Figure 6.9: Direct (a) and crossed (b) diagrams for the fluctuation contributions to Raman spectra. The squares denote Raman vertices which carry the $\gamma(\mathbf{k})$ factor, while the circles represent spin-fermion vertices which carry the Pauli matrix. Solid lines represent fermionic QP propagators and dashed lines represent CM propagators.

the nematic phase and only disappear below T_{m}. Furthermore, since the fits can be applied on charge/orbital- as well as spin-fluctuations, the question about the nature of the fluctuations is still not answered. However, one can take advantage of related selection rules to single out fluctuations associated with certain critical wave vectors.

6.2.3 Aslamazov-Larkin selection rules

Similar to the case of creation of particle-hole pairs, inelastic light scattering from fluctuations obeys selection rules that will be used to explain why the fluctuations appear only in B_{1g} symmetry. Those are carried by an expression given by the fermionic loop (that is the solid-line triangle, representing three fermion propagators) in Figs. 6.9 (a) and (b), having the form [157]

$$\Lambda_{\gamma\gamma}(\Omega_l, \mathbf{q}, \omega_m) = CT \sum_n \sum_{\mathbf{k}} \gamma(\mathbf{k}) G(\mathbf{k}, \epsilon_n + \Omega_l) G(\mathbf{k} - \mathbf{q}, \epsilon_n - \omega_m) G(\mathbf{k}, \epsilon_n) \quad (6.10)$$

which enters Eq. (6.8) quadratically. The dominant contributions of the diagrams in Figs. 6.9 (a) and (b) occur if $\mathbf{q} = \mathbf{q}_\lambda$, see Eq. (6.7), thus it is convenient to set $\mathbf{q} = \mathbf{q}_\lambda$ in Eq. (6.10). Since the loop contains the symmetry factor $\gamma(\mathbf{k})$ linearly inside the momentum integral the sign of $\gamma(\mathbf{k})$ is crucial. For each given $\mathbf{q}_\lambda$, to avoid cancellations in Eq. (6.10), the sum over $\mathbf{k}$ must encounter FS points connected by $\mathbf{q}_\lambda$ without the vertex $\gamma(\mathbf{k})$ between $\mathbf{k}$ and $\mathbf{k} + \mathbf{q}_\lambda$ changing sign.

To further illustrate the Aslamazov-Larkin selection rules, we quickly review the case of $La_{2-x}Sr_xCuO_4$ (LSCO) discussed in Ref. [207]. In the so-called pseudo gap region, there is a wealth of experimental evidence for short-range charge- and/or

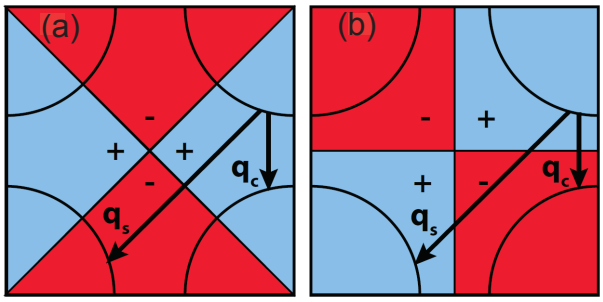

Figure 6.10: LSCO FS with hot spots, connected by the characteristic wave vectors of charge- ($\mathbf{q}_c$) and spin-scattering ($\mathbf{q}_s$), as adopted from Ref. [207]. In panels (a) and (b) the sign structures of the form factors for the B_{1g} and B_{2g} channels are plotted, respectively.

spin-ordered states [208–213]. The near-critical fluctuations associated with these instabilities are strongly peaked around $\mathbf{q}_c = 2\pi(\pm 0.2, 0)$ and $\mathbf{q}_s = (\pi, \pi)$ [207] and connect hot spots near $(\pm\pi, 0)$ and $(0, \pm\pi)$ [214]. For the Raman experiment, this has the consequence that fluctuations of the charge order are visible only in the B_{1g} symmetry while those of the spin-order only appear in the B_{2g} symmetry. This is illustrated schematically in Fig. 6.10 (a) and (b) for the B_{1g} and B_{2g} Raman vertex, respectively. In the B_{1g} symmetry, $\mathbf{q}_c$ connects hot spots where the vertex does not change sign and cancellations in Eq. (6.10) can be avoided. At the same time, $\mathbf{q}_s$ connects hot spots where the vertex *does* change sign, thus canceling out any signal of spin-fluctuations in the B_{1g} channel. The inverse situation is realized for the B_{2g} Raman vertex.

In iron-based materials, either spin fluctuations or fluctuations of various types of orbital order are expected to play the key-role in the formation of the nematic phase, and possibly also of the superconducting state [30]. The spin fluctuations are associated with the nesting vector $\mathbf{q}_s = (\pm\pi, 0), (0, \pm\pi)$, while for the case of orbital fluctuations, different critical vectors are possible, depending on which type of orbital order is finally realized below T_s (see Sec. 2.3.3). There are only two types of OO that break the C_4 rotational symmetry, and thus can possibly be responsible for the formation of the nematic phase in FeSCs. (i) Stripe-OO, corresponding to the formation of orbital zig-zag chains [Fig. 2.16 (d)], exhibits an ordering vector $\mathbf{q}_c^{\text{stripe}} = (\pm\pi, 0), (0, \pm\pi)$ equivalent with the SDW ordering vector. Therefore, it is not possible to distinguish stripe-orbital fluctuations from spin fluctuations, just by considering the AL selection rules in the FeSCs. However, stripe-OO, although potentially easily observable within X-ray diffraction experiments [128], has not yet been observed in FeSCs. As opposed to that, (ii) ferro-OO, that is the unequal occupation of iron d_{xz} and d_{yz} orbitals [Fig. 2.16 (e)], *has* been observed below T_s in $Ba(Fe_{1-x}Co_x)_2As_2$ by ARPES and XLD experiments [32, 144]. As there is no superstructure being introduced together with this ordering phenomenon the ordering vector is $\mathbf{q}_c^{\text{ferro}} = (0, 0)$. In this case, the AL selection rules allow for a

distinction between ferro-orbital and spin fluctuations in FeSCs.

If the ordering vector characterizing ferro-orbital fluctuations is used in Eq. (6.10), there are no cancellations in the **k**-summation, irrespective which symmetry is considered. In this case ferro-orbital fluctuations were visible in all symmetries (or in none, if orbital fluctuations couple weakly to the e-h pairs brought about by light scattering in general). Since we observe a fluctuation-contribution exclusively in the B_{1g} symmetry, the signal can not derive from ferro-orbital fluctuations.

The case of spin or stripe-orbital fluctuations is illustrated in Fig. 6.11. The panels (a), (b) and (c) show the A_{1g}, B_{1g} and B_{2g} Raman vertices projected on top of a generic FeSCs FS. Within the panels, the first and second order vertices (from Brillouin-zone harmonics) are shown, followed by the vertex derived from a realistic tight-binding band structure using the effective-mass approximation as adopted from [159]. $\mathbf{q}_s = (\pi, 0)$ $(= \mathbf{q}_c^{\text{stripe}})$ connects hot spots, which derive from improved nesting conditions between the circular hole- and slightly elliptic electron-pockets in these regions[2], see Fig. 6.12. Only for the 1st order A_{1g}, and the 1st and 2nd order B_{1g} vertices the sum over **k** encounters FS points connected by $\mathbf{q}_s$ without the vertex $\gamma(\mathbf{k})$ between **k** and $\mathbf{k}+\mathbf{q}_s$ changing sign. As opposed to that, $\gamma(\mathbf{k})$ *does* change sign in the B_{2g} and in the 2nd order A_{1g} symmetry, with the consequence that any fluctuation response gets canceled out in these symmetries.

In order to understand why there is no fluctuation signal observable in the A_{1g} channel, one has to compare the vertices approximated by the 1st and 2nd order BZ harmonics with the vertices derived from the effective mass approximation (see bottom of Fig. 6.11, [159]). The black frame represents the 1 Fe BZ ranging from $-\pi$ to π in each dimension k_x, k_y and k_z. There are three FSs in the center and two at each face (the outer ones are cut open to visualize the inner ones) showing the hole bands and electron bands, respectively. All three symmetries have a common color scale that shows the sign and intensity of the Raman vertex at the FS. For the A_{1g} symmetry, the effective mass approximation gives a positive value on all electron bands and a negative value on the central hole pockets. In particular, there are no sign changes of the vertex taking place anywhere at the FS, thus it is safe to say that the A_{1g} vertex, in terms of BZ harmonics, has 2nd order A_{1g} character. As a consequence, any signal deriving from fluctuations with $\mathbf{q}_s = (\pi, 0)$ cancels out in the A_{1g} channel.

Comparing the B_{1g} vertex to crystal harmonics leads to the conclusion that its

[2]Note that considering circular electron pockets (perfect nesting), one can make the same argument without the hot spots.

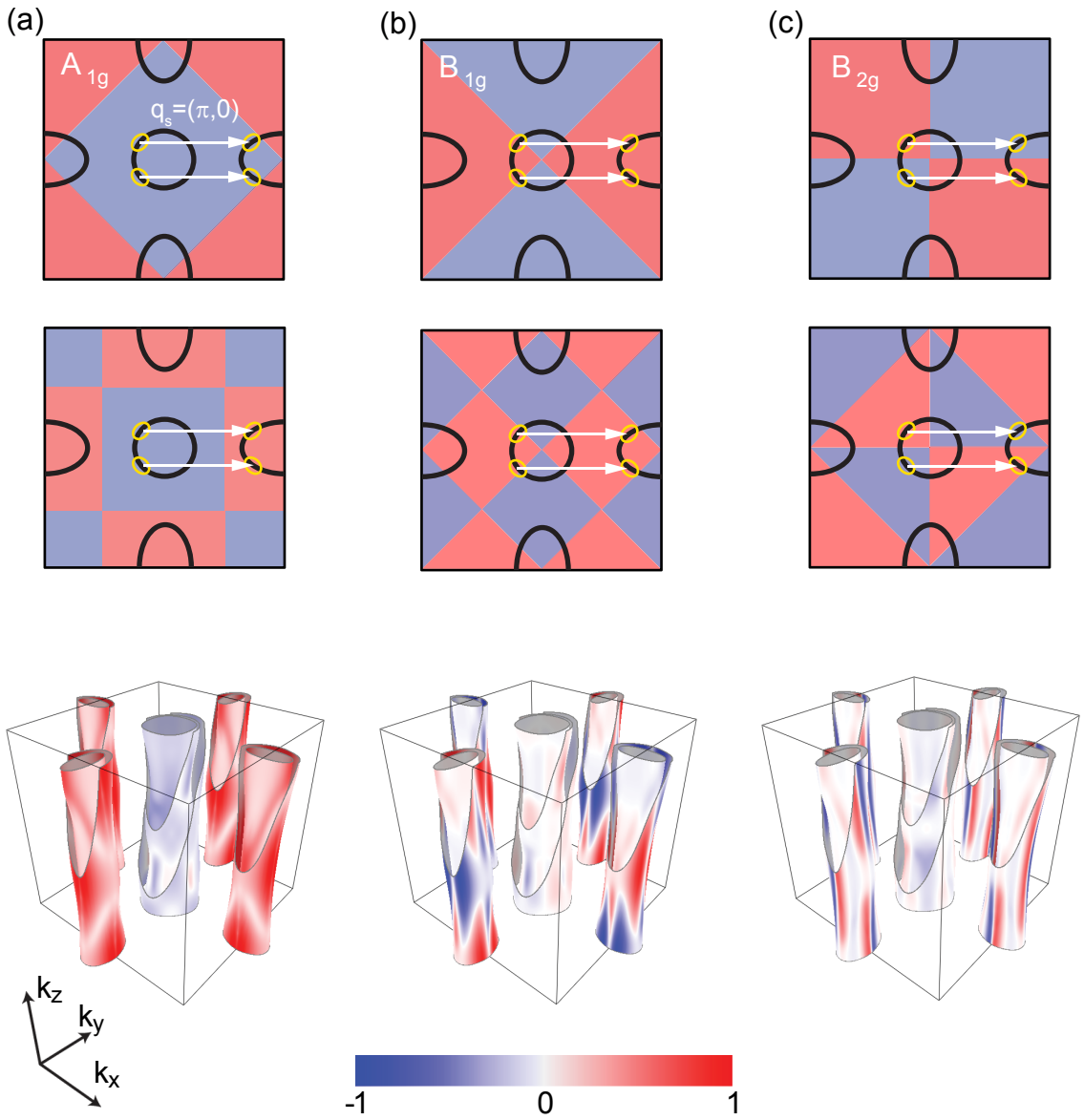

Figure 6.11: AL selection rules in FeSCs. Panels (a), (b) and (c) show the A_{1g}, B_{1g} and B_{2g} Raman vertices, respectively, shown along with a generic FeSCs FS. The two top rows depict the first two basis functions (crystal harmonics) of each symmetry. On the bottom, the vertex derived from a realistic tight-binding band structure with the effective-mass approximation is shown. Adapted from [159]. $\mathbf{q} = (\pi, 0)$ connects hot spots, which derive from nesting between the circular hole- and slightly elliptic electron-pockets. A finite fluctuation contribution to the Raman response is expected in symmetries where $\mathbf{q}$ connects FS portions having the same sign of the Raman vertex. In the present case, these are the 1st order A_{1g} and the 1st and 2nd order B_{1g} symmetries. A comparison with the vertex derived from the effective mass approximation explains the absence of a fluctuation signal in the A_{1g} channel (see text).

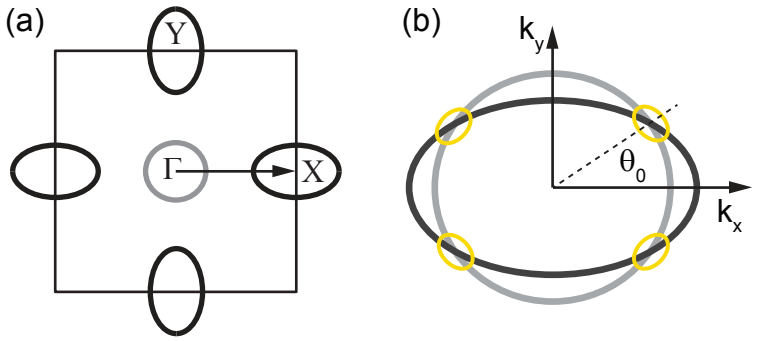

Figure 6.12: $\mathbf{q}$ connects hot spots (denoted by small yellow ellipses), which derive from locally improved nesting conditions between the round hole- and slightly elliptic electron-pockets.

character changes from 1st to 2nd and then back to 1st order, as one considers cuts with $k_z = \text{const.}$, going from $k_z = \pm\pi$ to $k_z = 0$. Therefore, since both a 1st and 2nd order character of the vertex does not lead to cancellations in Eq. (6.10), $\mathbf{q}_s = (\pi, 0)$ fluctuations are expected to emerge in the B_{1g} channel also from the more realistic effective mass approximation viewpoint. Finally, an examination of the B_{2g} vertex reveals that its character is mostly that of the 2nd order B_{2g} BZ harmonic. However, there are no harmonics in this channel in which $\mathbf{q}_s = (\pi, 0)$ fluctuations would not cancel out.

In summary, the AL selection rules clearly state that the observed fluctuation response which is present exclusively in the B_{1g} symmetry is compatible with $\mathbf{q} = (\pi, 0)$ critical fluctuations only. The signal therefore either derives from $\mathbf{q}_s = (\pi, 0)$ spin-fluctuations or, less likely, from $\mathbf{q}_c^{\text{stripe}} = (\pi, 0)$ stripe-orbital fluctuations. As opposed to that, $\mathbf{q}_c^{\text{ferro}} = (0, 0)$ ferro-orbital fluctuations can not be the origin of the fluctuation signal in the Raman response, since they would be visible in all symmetries.

6.2.4 Considering spin-fluctuations with finite interactions

After explaining the spectral shape and the selection rules we finally discuss the finite fluctuation intensity in the nematic phase along the lines of Karahasanović *et al.* [215]. To this end we now specialize to fluctuations of stripe-like magnetic order and assume interactions between the fluctuations. In addition the spin-nematic order is weakly coupled to the lattice.

In the presented model, spin fluctuations associated with the striped magnetic phase [ordering along $\mathbf{q}_x = (\pi, 0)$ or $\mathbf{q}_y = (0, \pi)$] stabilize the nematic phase [30] which pre-empts the magnetic phase. The nematic phase is then characterized by unequal strength of spin-fluctuations along the k_x and k_y directions in momentum space. Within the model, anisotropic spin-fluctuations are primarily responsible for the

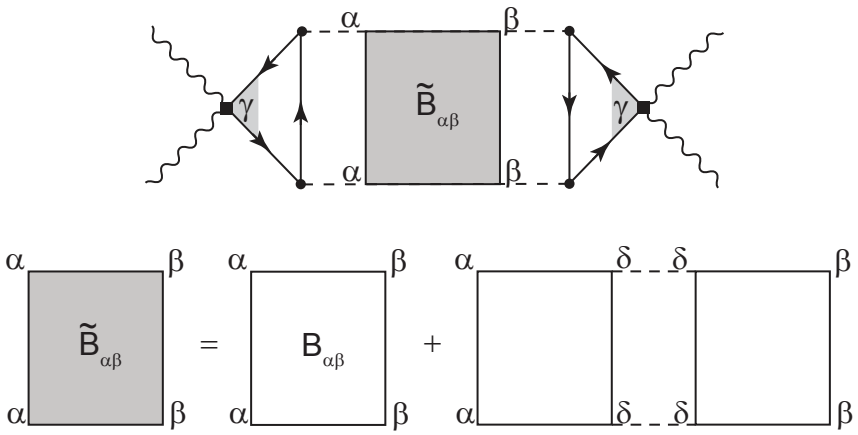

Figure 6.13: Higher order Aslamazov-Larkin diagrams for interacting fluctuations. The paramagnetic coupling between fluctuations mediated by fermions is obtained by inserting quaternions into the leading order Aslamazov-Larkin diagram. The re-summed box $\tilde{B}_{\alpha\beta}$ is shaded gray. The first index of the matrix B denotes the type $\alpha = X/Y$ of entering spin fluctuations, and the second index the type of exiting spin fluctuations.

anisotropies found in several spectroscopies [32,35,216], transport measurements [34, 47] and even cause the tetragonal to orthorhombic phase transition in the 122-family of iron pnictides. In this scenario, orbital-order and -fluctuations are only secondary effects which are caused by the anisotropic spin-fluctuations. The observation of orbital order and resistivity anisotropy at much higher temperatures [32, 144] is then just a consequence of the spin-nematic regime being extended, as the preferred orientation for the spin-fluctuations is chosen at much higher temperatures when an external (detwinning) stress is applied to the samples.

Karahasanović *et al.* analyze the fluctuation contribution to the Raman response function in the tetragonal phase, as the structural phase transition is approached. The leading order AL diagrams $R_0(\Omega)$ (Fig. 6.9) yield the noninteracting response and explain the selection rules (see Sec. 6.2.3). However, this diagram alone, which predicts the divergence of the response at the magnetic transition, cannot account for the rapid increase of the amplitude of the Raman response function as one approaches the *structural* transition, or the reduction of the signal inside the nematic phase $T_m < T < T_s$.

In order to describe this aspect, one has to account for the interactions between spin-fluctuations, which become crucial in the treatment of spin-driven nematicity, as has been shown in detail in Ref. [48]. The interactions between spin-fluctuations manifest themselves as a series of quaternion paramagnetic couplings mediated by fermions inserted into the leading order AL diagrams as shown in Fig. 6.13. The inserted fermionic boxes effectively resemble the nematic coupling constant g of the

theory (see Sec. 2.3.2). Karahasanović *et al.* show that for small frequencies Ω and in the large N-limit, after re-summing an infinite number of such boxed-like Aslamazov-Larkin diagrams one obtains the re-summed Raman response function $\tilde{R}(\Omega)$:

$$\tilde{R}(\Omega) \;=\; R_0(\Omega)\left[1+g\chi^{\rm el}_{\rm nem}(0)\right] \tag{6.11}$$

Eq. (6.11) states that the Raman response is proportional to the electronic contribution to the susceptibility of the nematic order parameter,

$$\chi^{\rm el}_{\rm nem}(0) \;=\; \frac{\int_{\mathbf{q}}\chi^2_{\rm mag}(\mathbf{q})}{1-g\int_{\mathbf{q}}\chi^2_{\rm mag}(\mathbf{q})}. \tag{6.12}$$

$\chi_{\rm mag}(\mathbf{q})$ represents the magnetic susceptibility that diverges at $T_{\rm m}$, and $\chi^{\rm el}_{\rm nem}(0)$ diverges at $T^*\geq T_{\rm m}$ as $|T-T^*|^{-1}$ in a mean-field scenario.

If the spins (or charges) couple to the lattice, the susceptibility of the nematic order parameter is given by [217]

$$\chi_{\rm nem}(0) \;=\; \frac{\int_{\mathbf{q}}\chi^2_{\rm mag}(\mathbf{q})}{1-[g+(\lambda^2_{\rm sl})/c^{\rm s}_0]\int_{\mathbf{q}}\chi^2_{\rm mag}(\mathbf{q})}. \tag{6.13}$$

where $\lambda_{\rm sl}$ denotes the magneto-elastic coupling, and $c^{\rm s}_0$ is the bare elastic constant. Obviously $\chi_{\rm nem}(0)$ diverges at higher temperature than $\chi^{\rm el}_{\rm nem}(0)$. Finally, $T_{\rm s}\geq T^*$ is identified with the structural phase transition.

T dependence of the nematic susceptibility ($T>T_{\rm s}$)

The nematic coupling constant has been evaluated as $g=\alpha/T^4$, where α is a factor that depends on the ellipticity of the electron pockets [48]. However, this has only a weak temperature dependence in the vicinity of the magnetic transition, and one might as well set $T=T_{\rm m}$, where $T_{\rm m}$ is the temperature at which magnetism sets in. The magnetic susceptibility in the classical regime is given by [218]

$$\chi_{\rm mag}(\mathbf{q}) = \frac{1}{r(T)+\mathbf{q}^2} \tag{6.14}$$

where $r(T) = T - T_m$ is the distance from the magnetic transition. One then finds that in $d = 2$ dimensions,

$$\int_{\mathbf{q}} \chi^2_{\rm mag}(\mathbf{q}) = \frac{1}{r(T)}. \tag{6.15}$$

Substituting the above, the nematic susceptibility is then

$$\begin{aligned} \chi_{\rm nem}(0) &= \frac{1}{r(T) - [g + \frac{\lambda^2_{sl}}{c^s_0}]} \\ &= \frac{1}{T - T_s} \end{aligned} \tag{6.16}$$

where $T_s = T_m + \frac{\alpha}{T^4_m} + \frac{\lambda^2_{sl}}{c^s_0}$, i.e. structural transition temperature is higher than the magnetic transition temperature [this can also be seen directly from Eq. (6.13)]. However, $\chi^{\rm el}_{\rm nem}$ and $\tilde{R}(\Omega)$ diverge at $T^* = T_m + \frac{\alpha}{T^4_m}$ [cf. (6.11) and (6.12)]. Since $T_s > T^*$ one concludes that the Raman response function develops only a maximum rather than a divergence at T_s. This is the central result of the analysis given in [215].

T dependence of the nematic susceptibility ($T_m > T > T_s$)

Using a simple argument, one can show that the nematic susceptibility inside the nematic (ordered) phase is smaller by a factor two than the susceptibility in the tetragonal (disordered) phase. The free energy as a function of the nematic order parameter ϕ is of the form [30, 218]

$$F(\phi) = \frac{a(T)}{2}\phi^2 + \frac{b}{4}\phi^4 - h\phi \tag{6.17}$$

where a field h conjugate to the nematic order parameter has been added and $a(T) = T - T_s$. After minimizing the free energy one obtains

$$a(T)\phi + b\phi^3 - h = 0 \tag{6.18}$$

Differentiating the equation above with respect to h, and by noting that $\frac{\partial\phi}{\partial h}|_{h=0} = \chi_{\rm nem}$, one obtains

$$\chi_{\rm nem} = \frac{1}{a(T) + 3b\phi^2} \tag{6.19}$$

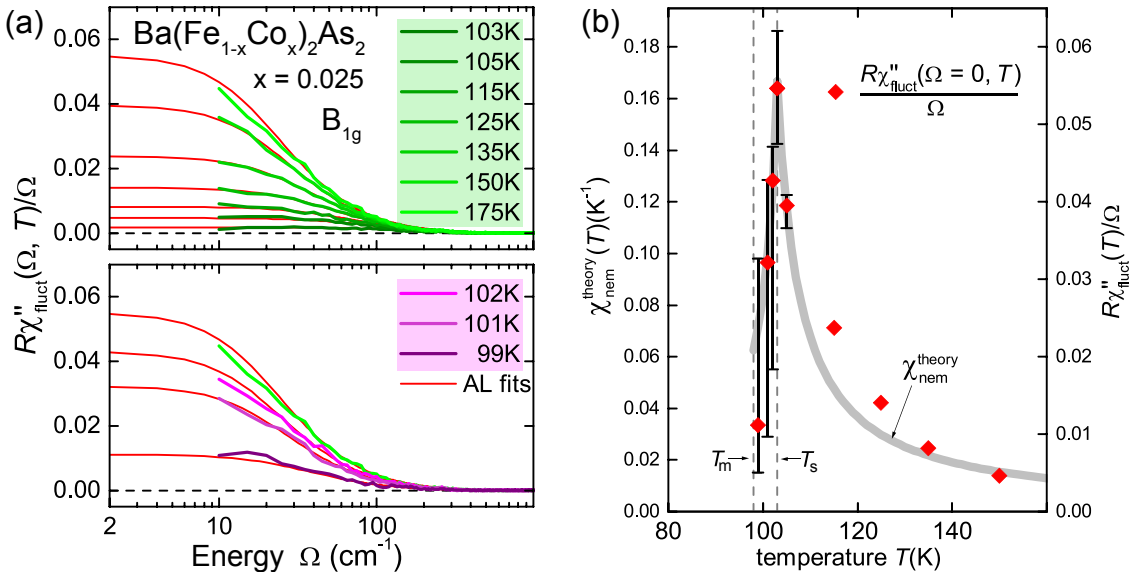

Figure 6.14: (a) T dependence of $R\chi''_{\rm fluct}/\Omega$. From $R\chi''_{\rm fluct}/\Omega$ the initial slope of $R\chi''_{\rm fluct}(\Omega,T)$ can be directly extracted as it is equal to the intersection of the curves with the ordinate, assuming a linear frequency dependence of $R\chi''_{\rm fluct}(\Omega,T)$ at small Ω. (b) Nematic susceptibility $\chi_{\rm nem}(0)$ as a function of temperature. The structural transition temperature is $T_{\rm s} > T_{\rm m}$, where $T_{\rm m}$ is the temperature at which magnetism sets in. The nematic susceptibility shows a pronounced maximum at the structural phase transition, and is smaller by a factor of two inside the nematic phase.

In the nematic phase $\phi^2 = -\frac{a(T)}{b}$ [which follows from Eq. (6.18)]. After substitution we conclude that inside the nematic phase the susceptibility is

$$\chi_{\rm nem}^{nem} = -\frac{1}{2a(T)}. \tag{6.20}$$

In the tetragonal phase $\phi = 0$ in Eq. (6.19) and $\chi_{\rm nem}^{\rm tet} = \frac{1}{a(T)}$. Therefore

$$\begin{aligned} \chi_{\rm nem}^{\rm nem} &= -\frac{1}{2(T-T_{\rm s})} \\ \chi_{\rm nem}^{\rm tet} &= \frac{1}{(T-T_{\rm s})}. \end{aligned} \tag{6.21}$$

Comparison of theory and experiment

The theoretical description presented above is valid only in the limit $\Omega \to 0$. The treatment of the interacting fluctuations at finite energies becomes very difficult [215]. However, the essential features of the phase transition follow already from the zero-energy approximation. The appropriate quantity for the analysis is the initial slope of the fluctuation spectra. Since, according to Eqs. (6.11)-(6.13), a divergence

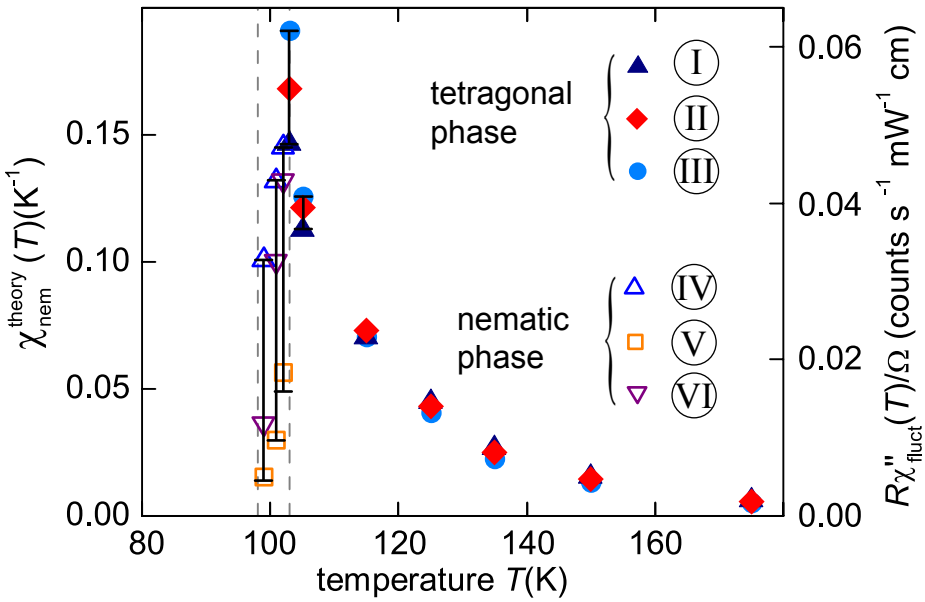

Figure 6.15: Initial slope of the Raman spectra of $Ba(Fe_{0.975}Co_{0.025})_2As_2$ after subtracting different particle-hole continua. In the tetragonal phase, the cases of a constant (solid blue triangles), a weakly temperature dependent (red diamonds) and strongly temperature dependent p-h continuum have been considered. In the nematic phase, the effect of adsorbates at the twin boundaries influencing the low-energy spectra outweighs the temperature dependence of the p-h continuum. Three cases, namely ignoring the effect (blue triangles), considering it to be fully present already directly below the structural phase transition (orange squares) and, representing the middle course, assuming the adsorbates to grow constantly between T_s and T_m (violet triangles), are shown. The complete analysis on the extraction of the initial slopes can be found in Appendix 8.B.

of the nematic susceptibility leads to a maximum of the Raman susceptibility, the initial slopes of $R\chi''_{\text{fluct}}(\Omega, T)$ are expected to reflect this maximum at T_s. In order to visualize the initial slopes of the experimental data and the according fits, we plot $R\chi''_{\text{fluct}}/\Omega$ [Fig. 6.14 (a)], from which the slope of $R\chi''_{\text{fluct}}(\Omega = 0, T)$ can be directly extracted as it is equal to the intersection of the curves with the ordinate, assuming a linear frequency dependence of $R\chi''_{\text{fluct}}(\Omega = 0, T)$ at small Ω. The slopes are extracted from AL fits of $R_0(\Omega)$ to the data rather than the data themselves because the data points close to zero energy depend critically on experimental details.

Fig. 6.14 (b) shows the temperature dependence of the theoretical nematic susceptibility in the tetragonal and the nematic phase (gray) along with the initial slopes of $R\chi''_{\text{fluct}}$ (red). We find qualitative agreement in the ranges $T_m < T < T_s$ and $T_s < T$.

To assign error bars to the data points presented in Fig. 6.14 it is necessary to investigate the dependence of the extracted initial slopes to the three major factors that influence the results of the above analysis. These are, in the tetragonal phase,

(i) the choice of the particle-hole background and (ii) the AL fit to the resulting fluctuation contribution to the experimentally obtained Raman response, which is basically done by hand. Thus, the above analysis was repeated assuming a p-h continuum that does not change with temperature and a p-h continuum that has a stronger temperature dependence than the one presented in Fig. 6.7. The detailed analysis can be found in Appendix 8.B. An important result of the analysis is that variations in the AL fit introduce only small deviations in the initial slopes. The change of the fluctuation response itself according to which respective p-h continuum is chosen outweighs possible inaccuracies of the fits.

Note that even for the chosen constant and strongly temperature dependent p-h continua, which represent the two extremes for the approximation of the continuum, our result is reproduced for both cases. The nematic susceptibilities which were extracted from spectra where a constant and strongly temperature dependent continuum was subtracted are shown as solid dark blue triangles and light blue circles in Fig. 6.15, respectively. The red diamonds represent the nematic susceptibility shown already in Fig. 6.14 (b). Above 110 K all three susceptibilities by and large coincide. Only below 110 K the susceptibilities from the constant and strong temperature-dependent continuum cases have a weaker and stronger divergent behavior, respectively. The susceptibility represented by the red diamonds is situated approximately in the middle between the extremal cases which we chose to define the upper and lower value of the error bars in Figs. 6.14(b) and 6.15.

In the nematic phase there is a third factor which has a strong influence on the analysis, that is (iii) the low energy spectra are superposed by elastic stray light being scattered into the spectrometer from adsorbates (in a high vacuum that means N_2 and H_2O), condensing at the twin-boundaries. Ignoring this effect, which is directly visible with our observation optics (see Fig. 6.8), leads to additional spurious intensity below T_m (see hatched area, left column in Fig. 8.3). Therefore we considered this effect and subtracted the low energy part of the original 97 K spectrum from the raw data obtained in the nematic phase. This was done in two different ways: In the first approach, the low energy part of the p-h continua for the temperatures 99 K, 101 K and 102 K were substituted up to 120 cm^{-1} with the low energy part of the original 97 K spectrum. The effect of the adsorbates are clearly visible in the low energy part of the 97 K spectrum as it is clearly not possible to extrapolate the low energy spectrum to zero. In a second approach it is assumed that the effect of elastically scattered photons influencing the low energy Raman signal of the nematic state spectra grows linearly with decreasing temperature. The obtained

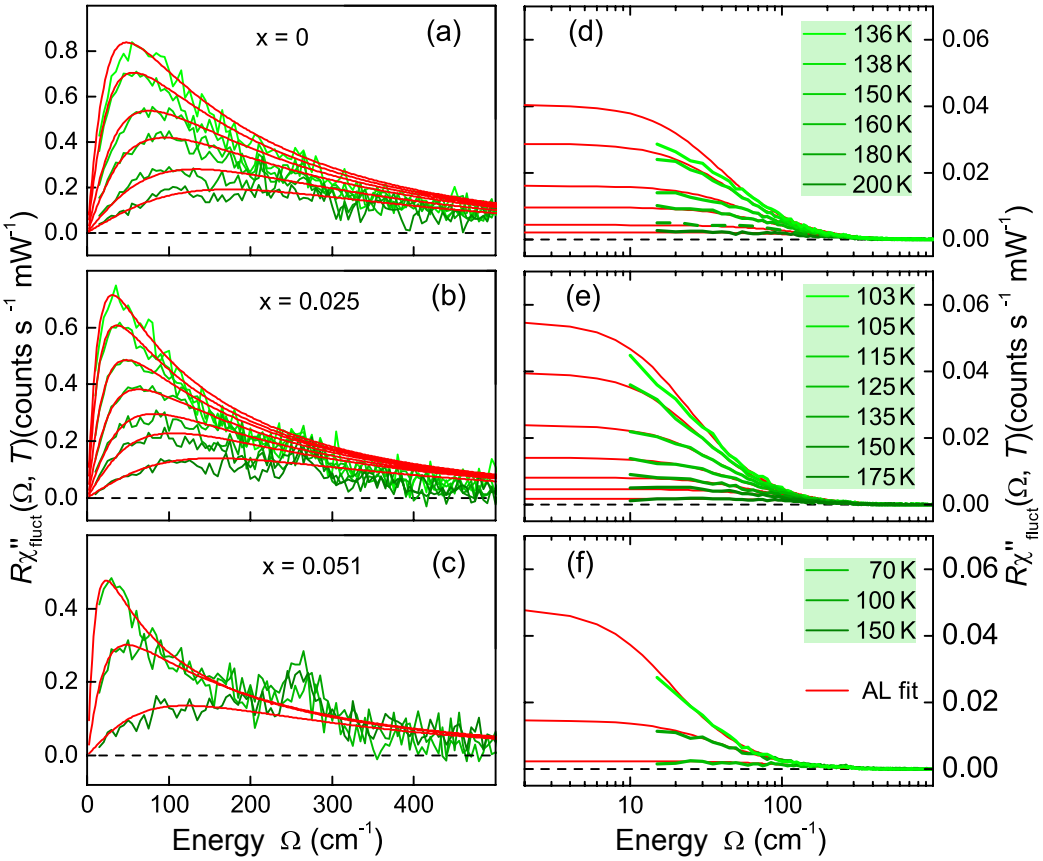

Figure 6.16: (a)-(c) Fluctuation contribution to the Raman response $R\chi''_{\text{fluct}}(\Omega, T)$ in $Ba(Fe_{1-x}Co_x)_2As_2$ along with AL fits as a function of doping. A higher Co-concentration leads to a stronger increase of the initial slopes when reducing the temperature towards the nematic transition. (d)-(e) $R\chi''_{\text{fluct}}(\Omega, T)/\Omega$ and AL fits on a logarithmic scale which highlights the low energy evolution of the spectra. The initial slopes (and thus the spin-nematic susceptibility) of $R\chi''_{\text{fluct}}(\Omega, T)$ can directly be extracted from the intersection of the AL fits with the ordinate. The trend of an increasing temperature window of critical fluctuations towards optimal Co-concentration is confirmed.

fluctuation spectra and according AL fits of both approaches are shown in Fig. 8.3. The resulting nematic susceptibilities are represented by orange squares and violet triangles in Fig. 6.15. Along with them, the case in which the adsorbates have not been taken into account is shown as blue triangles. However, the latter case gives unrealistic results due to the finite fluctuation response in the magnetically ordered phase. The error bars attached to the violet triangles are much larger than in the tetragonal phase, owing to the circumstance that we can only estimate the effect of the adsorbates. However, it is sensible to assume that the true susceptibility in the nematic phase can be found between the two extremal cases in which the adsorbates have not been taken into account and where they are assumed to be equal to that of the 97 K spectrum. We chose our error bars accordingly.

In summary, the Raman scattering results presented in this chapter support the spin-nematic model of Fernandes *et al.* [30,48]. First, the observed symmetry dependence of the fluctuations is in agreement with $\mathbf{q} = (\pi, 0)$ critical fluctuations only, which happens to be the SDW nesting vector. Second, the model by Fernandes *et al.* requires the nematic susceptibility to show a pronounced maximum at the structural phase transition, and not to be zero in the nematic phase.

On the other hand our results are at variance with the orbital-fluctuation model of Kontani *et al.* [50]. First, ferro-orbital fluctuations, the major contender in the orbital fluctuations model for nematicity and superconductivity in the FeSCs, would be observable in all symmetry channels whereas the experiment is compatible only with B_{1g} selection rules. Second, a finite fluctuation response in the nematic regime is at odds with the orbital fluctuations picture in general since orbital order is established at T_s, leaving no room for orbital fluctuations below that temperature.

6.2.5 Doping dependence

Having established that anisotropic spin-fluctuations are the driving force behind the nematic ordering in $Ba(Fe_{1-x}Co_x)_2As_2$, we move on and discuss their doping dependence in this last section. Fig. 6.16 shows the fluctuation contribution to the Raman response $R\chi''_{\text{fluct}}(\Omega, T)$ and the corresponding AL fits for (a) undoped $BaFe_2As_2$, (b) underdoped $Ba(Fe_{0.975}Co_{0.025})_2As_2$ and (c) underdoped $Ba(Fe_{0.949}Co_{0.051})_2As_2$. $R\chi''_{\text{fluct}}(\Omega, T)$ has been extracted from the Raman response (Figs. 6.1, 6.2 and 6.4) in the same way as discussed in the previous sections. The related relaxation rates, p-h continua and AL fit parameters are compiled in the Appendix.

Overall, the doping dependence shows that increasing the Co-concentration leads to a stronger increase of the initial slopes (which encode the electronic nematic susceptibility) when reducing the temperature towards the nematic transition. This is obvious regarding the evolution from an ensemble of relatively broad fluctuation peaks in the undoped compound to the ensemble of relatively narrow shapes of the fluctuation response in the $x = 0.051$ sample. The right hand side of Fig. 6.16 displays $R\chi''_{\text{fluct}}(\Omega, T)/\Omega$ from which the initial slopes of $R\chi''_{\text{fluct}}(\Omega, T)$ can be extracted directly.

Fig. 6.17 displays the magnitude of the spin-nematic susceptibility plotted as a color map in a doping-temperature phase diagram. Structural (nematic), magnetic and superconducting transition temperatures (T_s, T_m and T_c) are shown as green triangles, dark yellow dots and blue squares, respectively. The onset-temperatures of spin-fluctuations T_f are shown as black squares with error bars that derive from

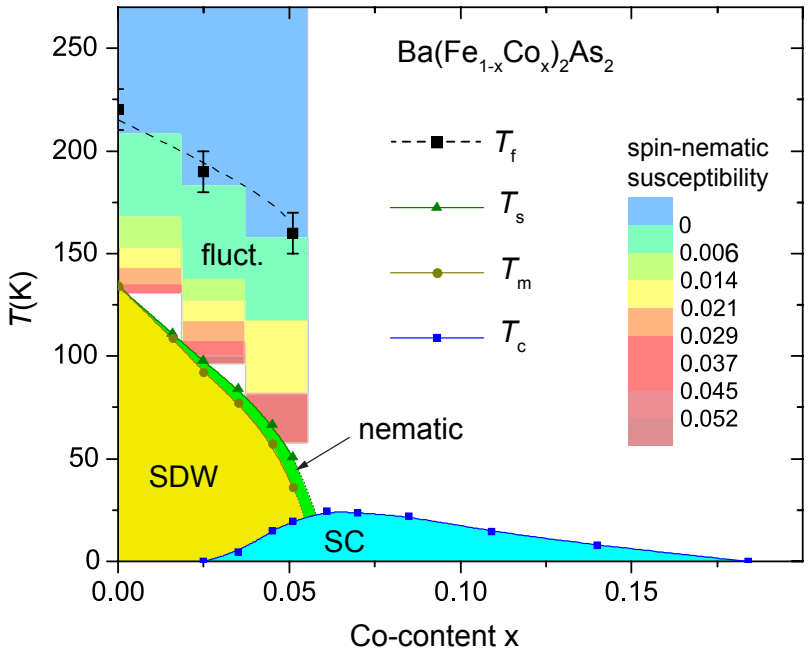

Figure 6.17: Phase diagram of $Ba(Fe_{1-x}Co_x)_2As_2$ as adapted from [29]. Structural (nematic), magnetic and superconducting transition temperatures (T_s, T_m and T_c) are shown as green triangles, dark yellow circles and blue squares, respectively. In addition, the evolution of the spin-nematic susceptibility versus doping and temperature is shown. The onset-temperatures of spin-fluctuations T_f are shown as black squares with error bars that derive from uncertainties in the static B_{1g} relaxation rates (see Fig. 6.6). The spin-nematic susceptibility is equivalent with the initial slopes of $R\chi''_{\mathrm{fluct}}(\Omega, T)$.

uncertainties in the static B_{1g} relaxation rates (see Fig. 6.6). The values of the spin-nematic susceptibility encoded in the color-map are equivalent to the initial slopes of $R\chi''_{\mathrm{fluct}}(\Omega, T)$.

The regime in which fluctuations are observed in our experiment is as broad as 100 K in the underdoped regime, becoming even broader when the composition approaches optimal doping. The wide temperature range suggests already that the signal derives from fluctuations of the primary order parameter, since fluctuations of the secondary order parameters appear only in the immediate vicinity of T_{nem} [30].

In the underdoped part of the phase diagram, the spin-nematic susceptibility increases rapidly in the vicinity of the structural phase boundary, by and large showing a Curie-Weiss-like temperature dependence as expected for a transition driven by thermal fluctuations. As the doping concentration increases, the intensity of fluctuations increases as well, in particular the critical regime of strong fluctuations (red color code) gets significantly broader towards optimal doping. This behavior does not reflect a simple Curie-Weiss law anymore, suggesting a growing importance of quantum fluctuations upon approaching optimal composition.

Chapter 7

Summary

This thesis reports a systematic study on the doping, temperature and momentum dependent electron dynamics in Fe-based superconductors using inelastic light scattering. The aim of this work was the investigation of the magnetic, nematic and superconducting instabilities, which are believed to be intertwined. The superconducting state was studied in $Ba_{0.6}K_{0.4}Fe_2As_2$. The investigation revealed the existence of bound states of electrons with non-zero angular momentum in the excitation spectrum. The energy, temperature and symmetry dependence of these so-called Bardasis-Schrieffer excitons was analyzed. In the normal state the focus was placed on the regime that is dominated by strong nematic fluctuations. The studies were performed in $Ba(Fe_{1-x}Co_x)_2As_2$ for the three compositions $x = 0$, $x = 0.025$ and $x = 0.051$. The variation with temperature of the fluctuation contribution to the Raman susceptibility was investigated in detail and analyzed theoretically. In addition, the critical wave vector of the fluctuations was identified to be $(\pi, 0)$ via the application of Aslamazov-Larkin selection rules. In combination with the temperature dependence, this allowed the identification of (i) the nature of the fluctuations and (ii) the origin of nematicity in $Ba(Fe_{1-x}Co_x)_2As_2$.

The study of hole-doped $Ba_{0.6}K_{0.4}Fe_2As_2$ revealed a combination of isotropic and anisotropic but finite superconducting gaps that are present on the different Fermi surface sheets. Large isotropic gaps with magnitudes of $190\,\mathrm{cm}^{-1}$ and $210\,\mathrm{cm}^{-1}$ reside on the central hole (α) and the inner electron (γ) bands, respectively. The outer hole (β) and electron (δ) bands host anisotropic gaps with gap minima as small as $25\,\mathrm{cm}^{-1}$ and $80\,\mathrm{cm}^{-1}$ [see Fig. 7.1 (a)]. An important result is the identification of Bardasis-Schrieffer modes in the B_{1g} spectrum of superconducting $Ba_{0.6}K_{0.4}Fe_2As_2$. This observation allowed the identification of a strong subdominant component in the BCS interaction potential $V(\mathbf{k}, \mathbf{k}')$. The energy distance of the mode with re-

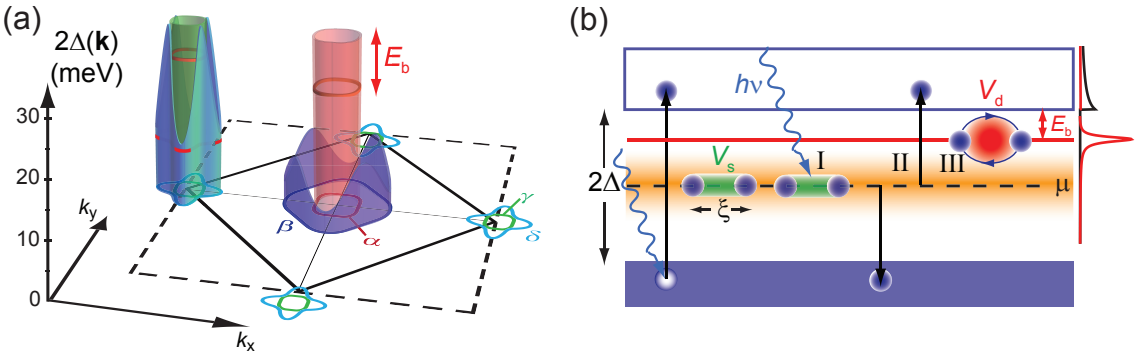

Figure 7.1: Central results of Ch. 5. (a) Superconducting gaps in $Ba_{0.6}K_{0.4}Fe_2As_2$ as seen via electronic Raman scattering. (b) Mechanism for Bardasis-Schrieffer excitonic modes.

spect to the gap edge [see Fig. 7.1 (b)] shows that this subdominant pairing channel is weaker, but of the same order of magnitude as the dominant channel. While the symmetry of the dominant channel could not be identified it was shown that the observation of the mode in the B_{1g} channel directly reflects the $d_{x^2-y^2}$ symmetry of the subdominant pairing channel. This is a strong piece of evidence that pairing in the subdominant channel is due to magnetic interactions. Finally, the idea of competing pairing channels was applied to interpret earlier results of Bernhard Muschler on electron-doped $Ba(Fe_{1-x}Co_x)_2As_2$ [150]. It was shown that the doping dependence of the superconducting state Raman spectra may be interpreted via a change of the pairing symmetry from $d_{x^2-y^2}$ to $s_\pm$ and back to $d_{x^2-y^2}$ as one proceeds from underdoped to overdoped compositions. However, this last point needs further investigation.

The isolation of the bare fluctuation contribution to the Raman susceptibility of $Ba(Fe_{1-x}Co_x)_2As_2$ was achieved via the identification of the onset temperatures of fluctuations T_f. The subsequent approximation of the particle-hole continuum by an analytic function enabled the extraction of the bare fluctuation signal which could be described in terms of Aslamasov-Larkin type of diagrams [cf. Fig. 7.2 (a)]. The theory imposes selection rules which require that the wave vector of the fluctuations connects FS sheets in regions of the BZ for which the Raman vertex $\gamma(\mathbf{k})$ does not change sign. Otherwise the fluctuation signal cancels out. It could be shown that the fluctuations observed in our experiments have a $(\pi, 0)$ wave vector, which happens to be the SDW vector. Another important result is the observation that the fluctuations persist in the nematic phase and only vanish below the magnetic ordering temperature T_m, providing strong evidence for a close relation with magnetism. In collaboration with Karahasanović *et al.* [215] it was shown, adopting the model of Fernandes *et al.* which is based on anisotropic spin-fluctuations [30, 48], that in the

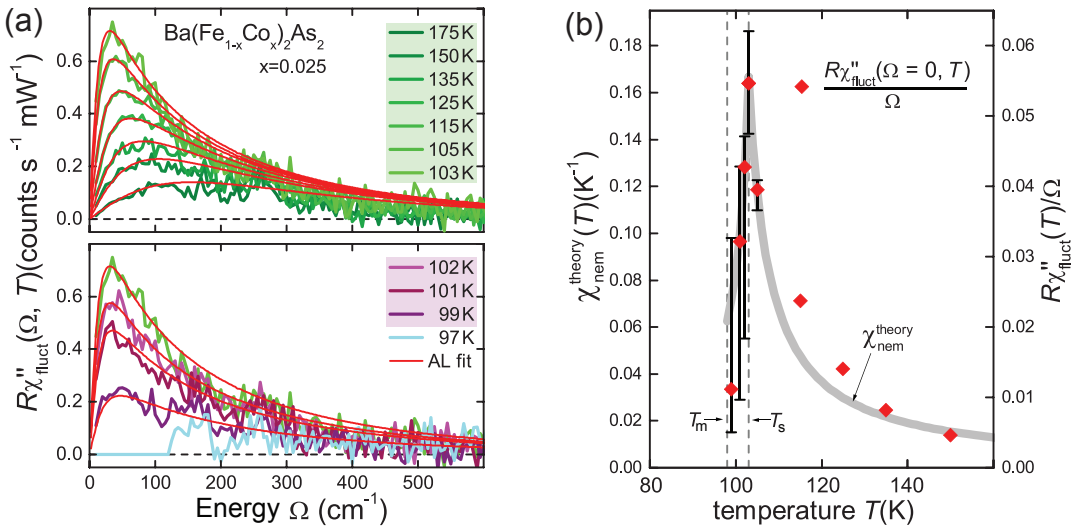

Figure 7.2: Central results of Ch. 6. (a) Fluctuation contribution to the Raman susceptibility in the tetragonal (top) and the nematic phase (bottom). The red curves correspond to the theoretical Raman response of nearly critical spin and/or charge fluctuations. (b) The Raman $\tilde{R}(\Omega)$ as well as the nematic susceptibility $\chi_{\mathrm{nem}}(0)$ as a function of temperature shows a pronounced maximum at the structural phase transition as expected within the spin-nematic scenario.

limit $\Omega \to 0$ the Raman susceptibility $\tilde{R}(\Omega)$ close to the nematic transition is proportional to the electronic contribution of the nematic susceptibility $\chi^{\mathrm{el}}_{\mathrm{nem}}(0)$. Taking coupling to the lattice into account, Curie-Weiss like behavior of $\tilde{R}(\Omega) \propto |T - T^*|^{-1}$ is expected. Since $T^* < T_{\mathrm{s}}$, the Raman response function develops only a maximum rather than a divergence at T_{s}. This is in exact agreement with our experiments [cf. Fig. 7.2 (b)]. Consequently spin-fluctuations of unequal strength in the $\mathbf{q}_{\mathrm{x}}$ and $\mathbf{q}_{\mathrm{y}}$ directions drive the series of phase transition at T_{s} and T_{m} and are responsible for the existence of the nematic phase in $\mathrm{Ba}(\mathrm{Fe}_{1-x}\mathrm{Co}_x)_2\mathrm{As}_2$.

Chapter 8

Appendices

8.A Gap structure and magnitude in FeSCs

Determining the possible pairing symmetries for FeSCs is challenging, because of the wide diversity of experimental results for the gap structure. While surface probes, such as ARPES [64, 89, 175, 219–223] show full gaps with no nodes, the situation is less clear for bulk probes. Magnetic penetration depth measurements give varying results ranging from a linear T-dependence of the low-T data in LaFePo [224, 225] and $BaFe_2As_{1-x}P_x$ [226], characteristic for the existence of line nodes, to an exponential T-dependence in $Ba_{1-x}K_xFe_2As_2$ [227] and LiFeAs [228], indicating fully gapped superconductivity. Other bulk probes like specific heat [229–236] and thermal conductivity [26, 183, 184, 237–240] measurements also draw a more diverse picture which points to a non-universal gap-structure. The results suggest that the gap changes from isotropic to a very anisotropic or even nodal structure as one examines different compounds of the FeSCs family or even different doping levels of the same compound. However, the vast majority of bulk probes gives consistent results comparing the same family members of the FeSCs and it was pointed out that one can explain the discrepancies between bulk and surface probes by mechanisms like surface electronic reconstruction or surface depairing [12]. In summary, experimental results suggest that the SC gap structure is sensitively related to details of the FS.

Two of the three compounds which have been investigated during this thesis belong to the 122-family of the iron-pnictides. $Ba(Fe_{1-x}Co_x)_2As_2$ and $Ba_{1-x}K_xFe_2As_2$ are considered to represent the electron-, respectively hole-doped side of the generic phase diagram shown in Fig. 2.6. For the gap anisotropy of these two compounds the available experimental data obtained by bulk-sensitive probes suggest that [12] in

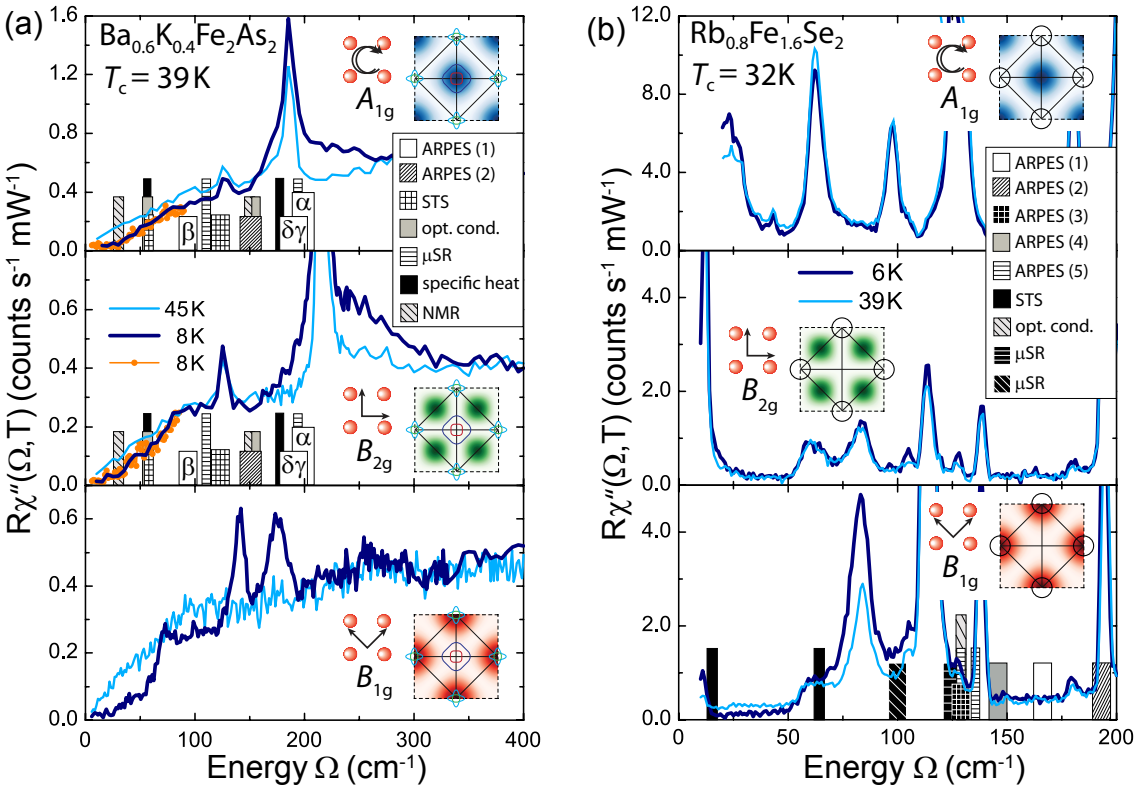

Figure 8.1: Raman spectra of $Ba_{0.6}K_{0.4}Fe_2As_2$ and $Rb_{0.8}Fe_{1.6}Se_2$ at temperatures as indicated along with the gaps 2Δ derived from other results (see also tables 8.1 and 8.2).

$Ba_{1-x}K_xFe_2As_2$ the gap changes its character from nodal to fully gapped and back to nodal as one goes from hole-overdoped KFe_2As_2 [241–243] to optimally doped $Ba_{0.6}K_{0.4}Fe_2As_2$ [25–28] and finally to the underdoped compounds [27].

Regarding the bulk-sensitive probes of the electron-doped side a somewhat different behavior can be identified. The gap seems to be much more anisotropic over the whole doping range with deep minima, or even weak (that means present only on small portions of the FS) nodes present in the under- and overdoped samples [183, 184]. At optimal doping ambiguous reports of either a still anisotropic but small gap [184–186] or QP excitations down to zero energy [180, 186] have been reported.

The third compound which was examined in this thesis, $Rb_{0.8}Fe_{1.6}Se_2$, belongs to the family of iron-chalcogenides with the generic chemical composition $A_xFe_{2-y}Se_2$. ARPES studies have revealed large electron- and in some cases the absence of hole-pockets at the Fermi level in these materials [178, 179], which is why this material class is often viewed as an electron-overdoped case in the family of FeSCs. In fact, there are multiple reports that these materials show mesoscopic phase separation with a phase exhibiting an insulating ground state with a $\sqrt{5}\times\sqrt{5}$ iron-vacancy pat-

tern and a phase that has a superconducting ground state which has the 122-crystal structure [57, 244–258], justifying that viewpoint (see also Sec. 2.1.1). Nevertheless, this is most likely an oversimplification, since the iron-chalcogenides seem to exhibit stronger correlations than the 122-pnictides. At particular compositions the low-temperature ground states are insulating and display antiferromagnetic order with large iron magnetic moment. This points to the relevance of Mott physics in these compounds [259–263].

The symmetry of the order parameter in the chalcogenides remains an open question. Via the study of low-temperature specific heat [264] and ARPES [178, 179] almost isotropic nodeless superconductivity was reported for $K_xFe_{2-y}Se_2$. This observation is compatible with an s- or a d-wave order parameter. However, several ARPES studies find a small electron pocket at the Γ-point in some of the iron-chalcogenides, exhibiting full gaps of roughly the same magnitude as on the BZ-boundary pockets [265–267], which would exclude the d wave nature of the gap. However, the same mechanisms that are responsible for purely isotropic gaps being observed by ARPES in the iron-pnictides could as well be at work in the iron-chalcogenides.

The gap magnitudes in $Ba_{0.6}K_{0.4}Fe_2As_2$ and $Rb_{0.8}Fe_{1.6}Se_2$ found by ARPES, STS, optical conductivity, μSR, specific heat and NMR experiments are summarized in Fig. 8.1 (a) and (b), respectively, along with the Raman results presented in this thesis. The results are obtained from scanning tunneling spectroscopy (STS), optical conductivity, nuclear magnetic resonance (NMR), angle resolved photoemission spectroscopy (ARPES) [64, 89, 175], specific heat (SH) [271], and muon spin rotation (μSR) [270] experiments. Not surprisingly, SH and μSR experiments report smaller values than ARPES measuring averages and truly momentum resolved quantities, respectively. The ARPES and Raman results agree qualitatively here. Rather surprisingly, the ARPES measurements indicate constant gaps in all compounds including $Ba(Fe_{0.939}Co_{0.061})_2As_2$ where the Raman scattering data are more consistent with a broad gap distribution [170, 180]. In $Ba(Fe_{0.939}Co_{0.061})_2As_2$, surface issues are unlikely to be sufficient an explanation. We rather believe that the band curvature varies substantially on the FS, and Raman scattering may project out other parts than ARPES.

In Tables 8.1 and 8.2 we compile the data on $Ba_{0.6}K_{0.4}Fe_2As_2$ and $Rb_{0.8}Fe_{1.6}Se_2$ in detail. The ARPES results in $Ba_{0.6}K_{0.4}Fe_2As_2$ (Table 8.1) reveal the biggest gaps on the inner central band (α) and on the electron bands (γ, δ) close to the degeneracy points (Fig. 5.8) while that on the β (in $Ba_{0.6}K_{0.4}Fe_2As_2$) band is smaller. All other

Table 8.1: Gap energies in $Ba_{0.6}K_{0.4}Fe_2As_2$ as derived from Raman scattering, ARPES, tunneling spectroscopy, optical conductivity, μSR, specific heat, and nuclear magnetic resonance.

method	Ref	2Δ [cm^{-1}]	2Δ [meV]	$2\Delta/k_BT_c$	comments
Raman	[168]	190	23.5	7.0	α-band
		25-80	3.1-9.9	0.9-3.0	β-band
		210	26.0	7.7	γ-band
		80-210	9.9-26.3	3.0-7.7	δ-band
ARPES (1)	[89], [64]	200	24.8	7.4	α-band
		95	11.8	3.5	β-band
		195	24.2	7.2	γ-band
		185	22.9	6.8	δ-band
ARPES (2)	[175]	150-160	18.6-19.8	5.5-5.9	α-band
		<65	<8.0	<2.4	β-band
		150	18.6	5.5	"x-pocket"
		145	18.0	5.3	"blades"
STS	[268]	58	7.2	2.2	small gap
		131	16.2	5.1	big gap
opt. cond.	[269]	60	7.4	2.2	small gap
		160	19.8	6.0	big gap
μSR	[270]	110	13.6	4.1	small gap
		194	24.1	7.2	big gap
specific heat	[271]	56	6.9	2.1	small gap
		177	21.9	6.5	big gap
NMR	[272]	30	3.7	1.11	small gap
		152	18.8	5.63	big gap

data except for Raman scattering are best described in terms of two essentially constant gaps in the range of $1-2$ and $4-7\,k_B T_c$. Although slightly smaller, the magnitudes are essentially in agreement with our own results.

However, we cannot derive with certainty how the gaps vary on the γ and δ band from our light scattering results in A_{1g} and B_{2g} symmetry. For further insight, we include the collective modes in our discussion. In the case of an anisotropic gap the bound state will appear close to gap minimum and become asymmetric [17]. Hence, the symmetric shapes of the B_{1g} modes at 140, and $175\,\mathrm{cm}^{-1}$ [Fig. 5.3] indicate that the related gaps from which the collective modes are pulled down are nearly isotropic and correspond to the superconductivity-induced A_{1g} and B_{2g} structures at 190 and $210\,\mathrm{cm}^{-1}$. The integrated intensities Z_d of the two high-energy modes are on the order of 10 and 30% of those of the pair-breaking features at 190 and $210\,\mathrm{cm}^{-1}$, respectively, as can be seen directly in Fig. 5.3. Recalling that $Z_d \propto E_b$ this is in qualitative agreement with the binding energies E_b. The shape of the weak mode at $73\,\mathrm{cm}^{-1}$ is not as well defined, and the mode can either couple to a nearly constant gap on the β band observed in A_{1g} and B_{2g} symmetry at $80\,\mathrm{cm}^{-1}$ or to the minimum of an anisotropic gap on the γ or δ band. The coupling to an isotropic β band leaves the intensity down to $25\,\mathrm{cm}^{-1}$ unexplained making the second possibility more likely and leaving room for an anisotropic β band.

Then, the β and the δ bands, in contrast to the α and γ bands, have relatively broad distributions of gaps ranging from 25 to $80\,\mathrm{cm}^{-1}$ and from 80 to $210\,\mathrm{cm}^{-1}$, respectively, with the minima at 25 and $80\,\mathrm{cm}^{-1}$ close to the principle axes and the BZ boundaries. This would explain the small but finite symmetry-independent intensity between 25 and $70\,\mathrm{cm}^{-1}$ without, however, resolving the conflict with the ARPES results. Although the conflict between ARPES and Raman scattering is more quantitative here than in $Ba(Fe_{0.939}Co_{0.061})_2As_2$ it remains to be explained. We therefore conclude that the analysis of the collective modes supports the gap distribution given in table 8.1 and in Fig. 5.9.

From these results, two messages can be derived: (i) The ground state in optimally doped $Ba_{1-x}K_xFe_2As_2$ is characterized by large nearly constant gaps with similar magnitude on the nearly perfectly nested inner hole and electron bands (α and γ) having the full symmetry of the lattice [15, 175]. (ii) The second strongest interaction channel has $d_{x^2-y^2}$ symmetry since all bound states appear in the B_{1g} spectra.

Yet, the Raman experiments cannot directly pin down the phase of the pairing state, and we are left with either a fully symmetric s_{++} state with the same phase

Table 8.2: Gap energies in $A_xFe_{2-y}Se_2$, $A = (K, Tl, Rb, Cs)$ as derived from Raman scattering, ARPES, scanning tunneling spectroscopy, optical conductivity, and μSR.

method/ compound	Ref.	2Δ [cm^{-1}]	2Δ [meV]	$2\Delta/k_BT_c$	comments
Raman $Rb_{0.8}Fe_{1.6}Se_2$, T_c=32K	[168]	80	9.9	3.6	M-point
ARPES (1) (K,Cs)Fe_2Se_2, T_c=30K	[178]	166	20.6	7.9	M-point
ARPES (2) $(Tl_{0.58}Rb_{0.42})Fe_{1.72}Se_2$, T_c=32K	[266]	193 242	23 30	9 11	M-point Γ-point
ARPES (3) $(Tl_{0.45}K_{0.34})Fe_{1.84}Se_2$, T_c=28K	[267]	129 –	16 –	6.6 –	M-point Γ-point
ARPES (4) $K_{0.68}Fe_{1.79}Se_2$, T_c=32K	[267]	145 –	18 –	6.5 –	M-point Γ-point
ARPES (5) (Tl,K)$Fe_{1.78}Se_2$, T_c=29K	[273]	137 129	17 16	6.8 6.4	M-point Γ-point
STS $K_xFe_{2-y}Se_2$, T_c=32K	[57]	16 64	2 8	0.7 2.9	small gap big gap
opt. cond. $Rb_xFe_{2-y}Se_2$, T_c=32K	[165]	<129	<16	<5.8	one gap model
μSR $Rb_xFe_{2-y}Se_2$, T_c=32.6K	[274]	124	15.4	5.5	one gap model
μSR $K_xFe_{2-y}Se_2$, T_c=31K	[274]	102	12.6	4.7	one gap model

on all FSs due to electron-phonon coupling or orbital fluctuations [16] or with the $s_{\pm}$ state due to spin fluctuations proposed first by Mazin and coworkers [15]. While electron-phonon interaction is considered too weak for transition temperatures well above 30 K [107, 171] coupling via orbital fluctuations cannot be excluded *a priori*. Even the resonance observed by neutron scattering experiments [275] is not ultimately conclusive and may also be explained by electron damping and correlation effects [104]. The experiments presented here tell us that the interaction potential in the subdominant channel favors a sign change between the electron pockets at $(\pm\pi, 0)$ and $(0, \pm\pi)$ and is therefore repulsive. Consequently, it stands to reason that the dominant channel has the same origin suggesting the $s_{\pm}$ gap to be more likely.

In $Rb_{0.8}Fe_{1.6}Se_2$ (Table 8.2) Raman scattering returns a gap slightly below $4\,k_BT_c$ while the magnitudes derived from ARPES are approximately twice as large. Optical conductivity and μSR are compatible with isotropic gaps having a slightly bigger magnitude than those derived from Raman scattering. Only scanning tunneling spectroscopy (STS) yields a substantial anisotropy and a small maximal gap below $3\,k_BT_c$. Given these discrepancies, a final conclusion as to the momentum dependence of the gap is probably premature. For a further analysis, the issues with the surface preparation and the layered structure of $Rb_{0.8}Fe_{1.6}Se_2$ need to be understood better. However, in comparison with $Ba_{0.6}K_{0.4}Fe_2As_2$ and $Ba(Fe_{0.939}Co_{0.061})_2As_2$ the modulation on the individual FSs seems to be the weakest one here. In addition, there is no indication of a gap in the A_{1g} and B_{2g} spectra. This is in agreement with the expectations if the central hole bands are absent and, respectively, the electron bands do not have a strong curvature induced by weak hybridization after downfolding the 1 Fe BZ as in $Ba_{0.6}K_{0.4}Fe_2As_2$ and $Ba(Fe_{0.939}Co_{0.061})_2As_2$ [181]. Given the weak electron-phonon coupling a pairing potential supporting a $d_{x^2-y^2}$ gap is indeed compatible with the data.

8.B Nematic suscebtibility: Errorbar determination

In this Appendix, the error bars which are given in Figs. 6.14 (b) and 6.15 are derived from assuming different extreme cases for the approximation of the p-h continuum. Overall, three major factors are considered which dominate the variation of results. These are, in the tetragonal phase, (i) the choice of the p-h background and (ii) the AL fit to the resulting fluctuation contribution to the experimentally obtained

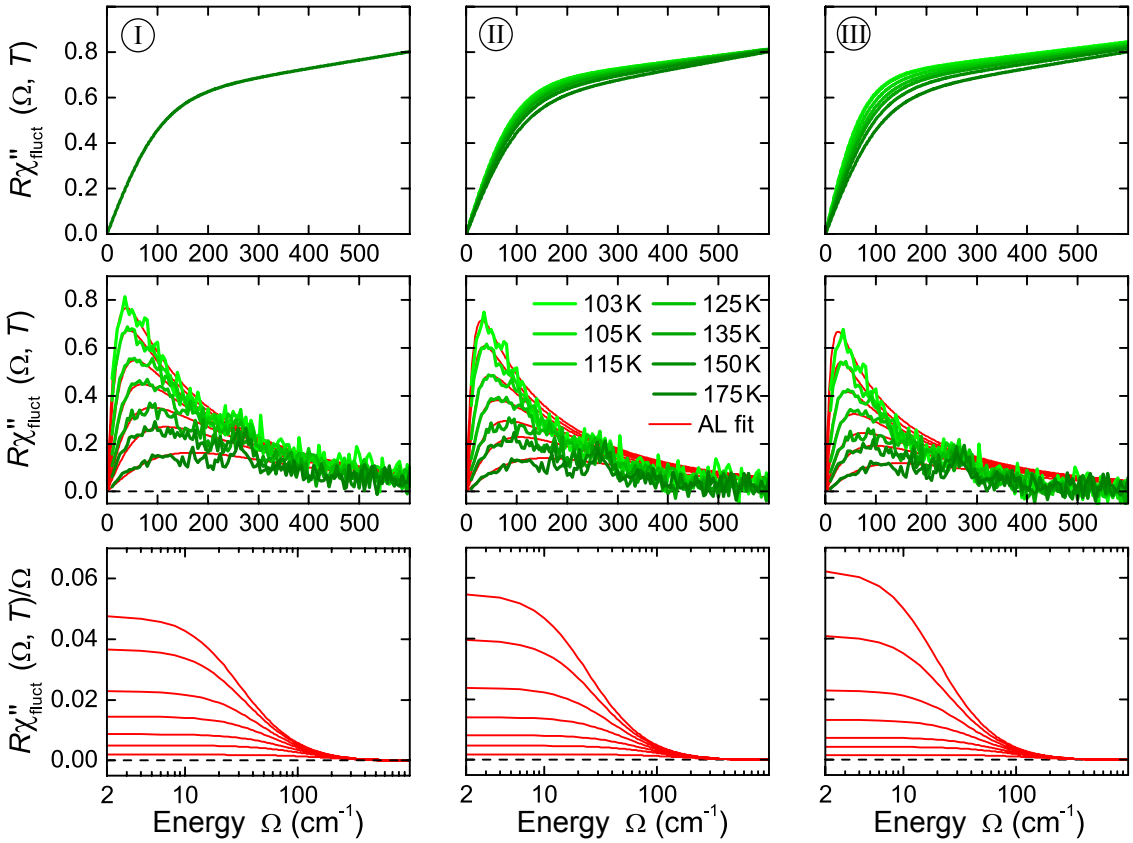

Figure 8.2: Error bar determination in the tetragonal phase. Three different cases for the approximation of the p-h continuum are considered: (I) a constant continuum, (II) a continuum varying in such way that the temperature dependence of the static B_{1g} relaxation rate reflects the resistivity data of the sample, (III) a continuum varying in such way that the temperature dependence of the static B_{1g} relaxation rate drops much stronger than would be justified by the resistivity.

Raman response, which is basically done by hand. In the nematic phase it is (iii) elastically scattered light which superimposes the low energy spectra which has the strongest influence on the analysis. The additional stray light derives from scattering from adsorbates condensing at the twin-boundaries of the now present twins.

Fig. 8.2 shows the analysis for the tetragonal phase. Additionally to the case presented in the main part of the thesis, where a p-h continuum was assumed which reflects the bulk resistivity of the sample (see Sec. 6.2.2, case II), we analyze two extreme cases: (I) the continuum having no temperature dependence at all and (III) the continuum varying in such way that the temperature dependence of the static B_{1g} relaxation rate drops much stronger than would be justified by the resistivity. The first row in Fig. 8.2 displays the p-h continua for the three cases, followed by the resulting fluctuation contributions to the Raman response together with the

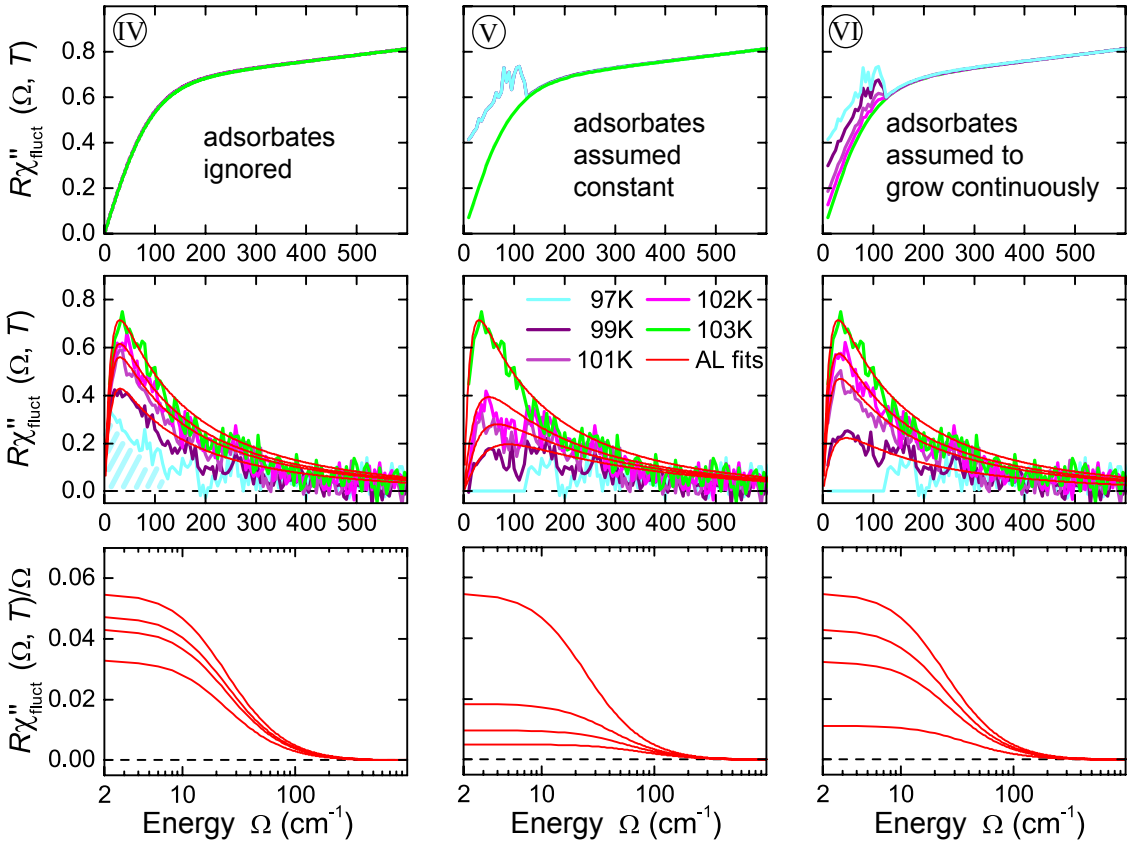

Figure 8.3: Error bar determination in the nematic phase. Three different cases for the approximation of the p-h continuum are considered: (IV) elastic scattering from adsorbates is ignored, (V) the influence of elastic scattering from adsorbates on the low energy spectra is assumed to grow in a linear fashion and (VI) adsorbates were assumed to have the maximal effect (which is showing the low energy behavior of the 97 K spectrum already at 102 K, just below the structural transition).

according AL fits in the second row of the figure. A general statement which can be made is that the inaccuracy of the AL fit is not the major error-source of the analysis. It is rather the change of the fluctuation response itself according to which respective p-h continuum is chosen which outweighs possible inaccuracies of the AL fits. The third row finally comprises the initial slopes for the three different cases (for clarity only the AL fits over omega are shown) which can be directly extracted from the intersection of the red curves with the ordinate. The temperature dependence of the these slopes are comprised in Fig. 6.15. We chose the extreme cases to define the upper and lower limit of the error bars given in the figure.

Fig. 8.3 shows the analysis for the nematic phase. Besides the case presented in the main part of the thesis, which assumes a constantly growing influence of elastic scattering from adsorbates [Fig. 8.3, case (V)], two more extreme cases are displayed

in the figure: (IV) elastic scattering from adsorbates is ignored in the analysis and (VI) the low energy part of the p-h continua for the temperatures 99 K, 101 K and 102 K were substituted up to 120 cm^{-1} with the low energy part of the original 97 K spectrum. As in Fig. 8.3, the first row displays the p-h continua for the three cases, followed by the resulting fluctuation contributions to the Raman response together with the according AL fits in the second row. It is evident from the fluctuation response that ignoring the effect of adsorbates [case (IV)] gives unphysical results, as the fluctuation contribution from the 97 K spectrum is nonzero at low energies (see hatched area in the left column of the figure), which finally results in much to high initial slopes of the spectra in the nematic phase. Thus we considered the effect of adsorbates and subtracted the low energy part of the original 97 K spectrum from the raw data obtained in the nematic phase. This was done in two different ways: In the first approach (case V), the low energy part of the p-h continua for the temperatures 99 K, 101 K and 102 K were substituted up to 120 cm^{-1} with the low energy part of the original 97 K spectrum. The effect of the adsorbates are clearly visible in the low energy part of the 97 K spectrum as it is clearly not possible to extrapolate the low energy spectrum to zero. In a second approach [case (VI)] it is assumed that the effect of elastically scattered photons influencing the low energy Raman signal of the nematic state spectra grows linearly with decreasing temperature. Again, the third row comprises the initial slopes for the three different cases (for clarity only the AL fits over omega are shown) which can be directly extracted from the intersection of the red curves with the ordinate. The temperature dependence of the slopes are as well comprised in Fig. 6.15. We chose the cases (IV) and (V) to define the upper and lower limit of the error bars.

8.C Dynamic relaxation rates of x = 0 and x = 0.051 samples

This Appendix contains the dynamic relaxation rates of $BaFe_2As_2$ for the compositions $x = 0$ and $x = 0.051$, from which the static relaxation rates shown in Fig. 6.6 (a) and (c) were extracted. The relaxation rates were obtained following the relaxation or memory function approach by Götze and Wölfle [188] in the same manner as described in Sec. 6.2.1. The zero energy extrapolation values were extracted from the dynamic scattering rates via a fit using the phenomenological parallel resistor model [Eq. (6.4)]. The fits are displayed with black lines in Figs. 8.4 and 8.5.

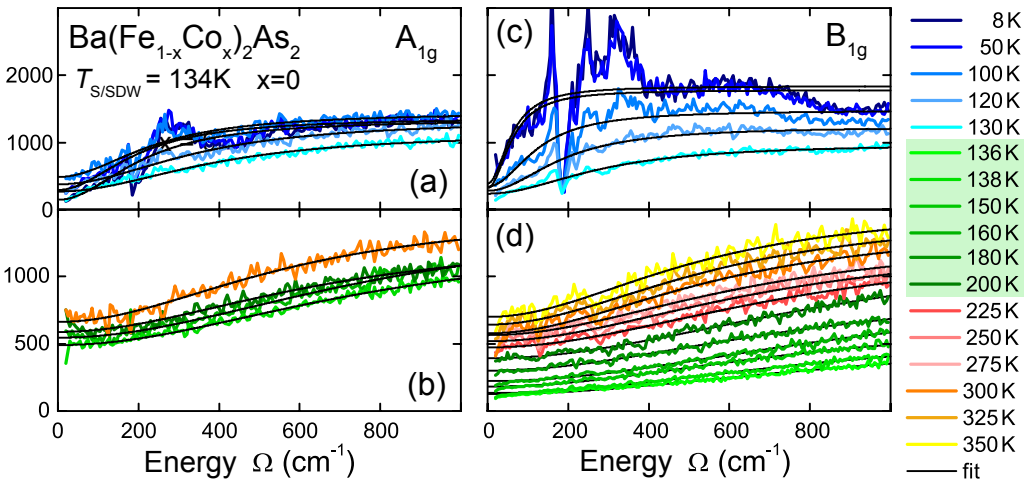

Figure 8.4: Temperature and symmetry dependence of the $BaFe_2As_2$ relaxation rates $\Gamma_{\gamma\gamma}(\Omega, T)$ for temperatures $T < T_{s/m}$ [panels (a) and (c)] and $T > T_{s/m}$ [panels (b) and (d)]. The rates were obtained, using the procedure described by Opel *et al.* [190], from the energy dependent response $R\chi''_{\gamma\gamma}(\Omega, T)$ displayed in Fig. 6.1. The smooth black lines correspond to a fit according to Eq. (6.4).

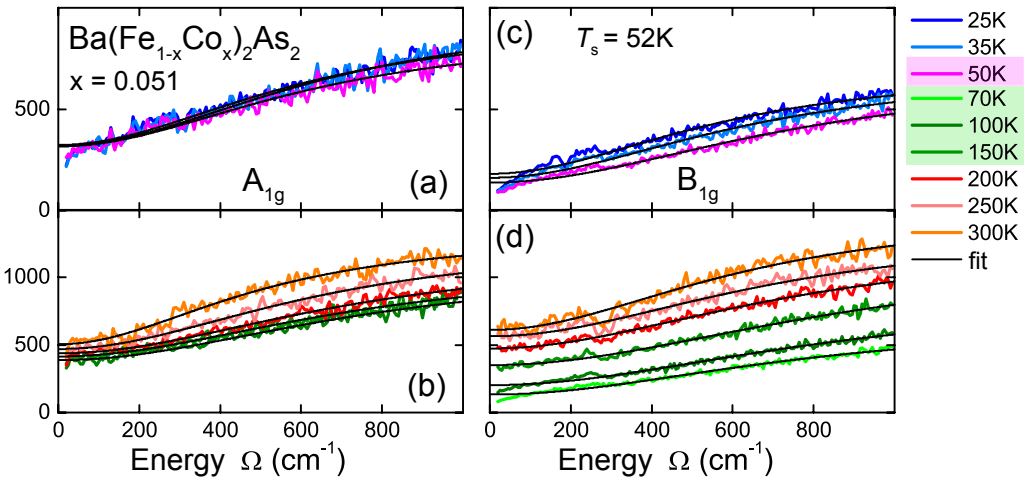

Figure 8.5: Temperature and symmetry dependence of the $Ba(Fe_{0.949}Co_{0.051})_2As_2$ relaxation rates $\Gamma_{\gamma\gamma}(\Omega, T)$ for temperatures $T < T_s$ [panels (a) and (c)] and $T > T_s$ [panels (b) and (d)].

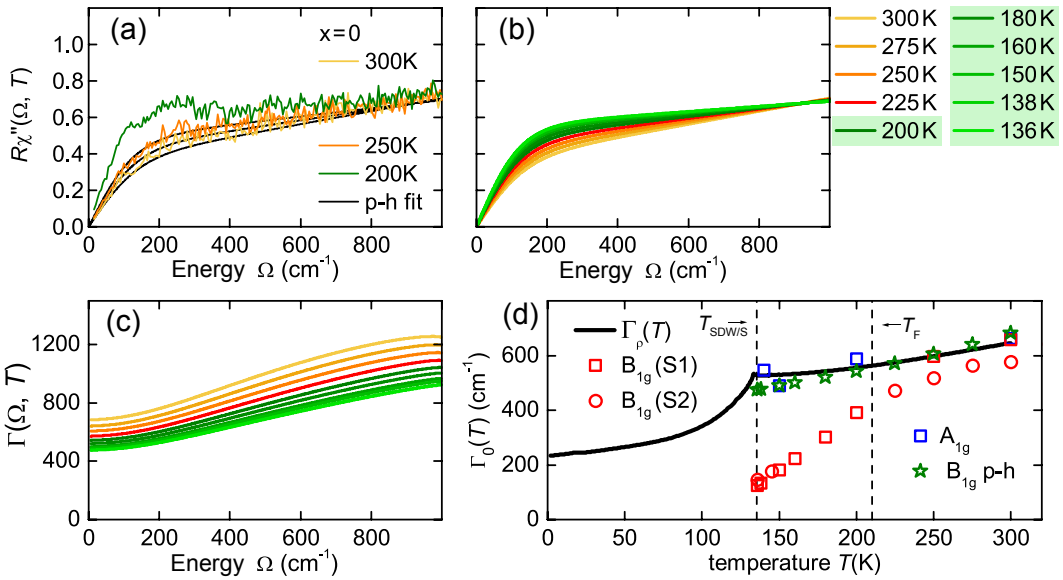

Figure 8.6: Approximation of the p-h continuum for $BaFe_2As_2$. (a) Fits to the experimental data according to Eq. (6.6), shown explicitly for three temperatures. (b) Continuum approximation and (c) the resulting dynamic relaxation rates for all temperatures $T > T_m$. (d) Static relaxation rate of the continuum approximation (green stars), along with the A_{1g} and B_{1g} relaxation rates derived from experiment. The B_{1g} continuum approximation relaxation rate by and large reflects the experimental resistivity data.

8.D Approximation of the p-h continua for x = 0 and x = 0.051 samples

This Appendix comprises the p-h continua of undoped ($x = 0$) and underdoped ($x = 0.051$) $Ba(Fe_{1-x}Co_x)_2As_2$, which have been used to extract the bare fluctuation response shown in Fig. 6.16 from the measured Raman susceptibility (Figs. 6.1 and 6.4). From the static relaxation rates (Fig. 6.6) the onset temperatures $T_f^{0\%} \approx 215\,\mathrm{K}$ and $T_f^{5.1\%} \approx 160\,\mathrm{K}$ can be identified. Above T_f, $R\chi''_{\gamma\gamma}(\Omega, T)$ reflects the bare particle-hole contribution to the Raman response. Fluctuations set in below T_f and do persist down to $T_{s/m}^{0\%} = 136\,\mathrm{K}$ and $T_m^{5.1\%} \approx 50\,\mathrm{K}$, respectively. The particle-hole continuum between T_f and T_m is approximated by a fit using Eq. (6.6), as described in Sec. 6.2.2. The according fitting parameters for the undoped sample are: $a_1 = 0.710$, $a_2 = -0.00120$, $b_1 = -0.0000350$ and $b_2 = 0.0000013$. The ones for the sample with 5.1% doping read: $a_1 = 0.715$, $a_2 = -0.00122$, $b_1 = -0.0000587$ and $b_2 = 0.0000013$. The $x = 0$ and $x = 0.051$ continua are shown in panel (b) of the Figs. 8.6 and 8.7, respectively.

The continua were chosen in a way such that the sum of the static A_{1g} and B_{1g} relaxation rates, obtained from a Kramers-Kronig analysis of the experimental

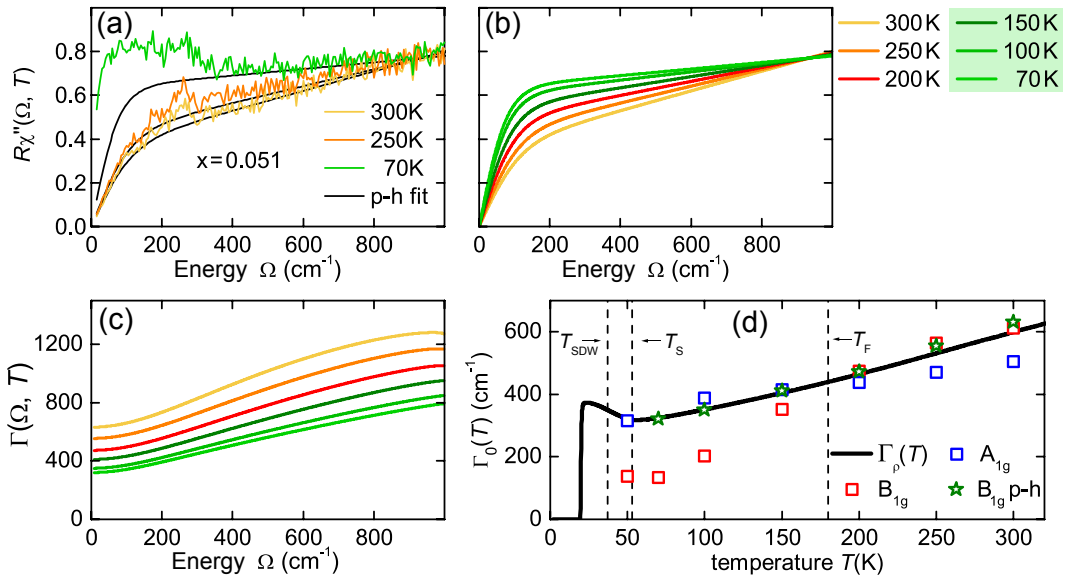

Figure 8.7: Approximation of the p-h continuum for $Ba(Fe_{0.949}Co_{0.051})_2As_2$. (a) Fits to the experimental data according to Eq. (6.6), shown explicitly for three temperatures. (b) Continuum approximation and (c) the resulting dynamic relaxation rates for all temperatures $T > T_m$. (d) Static relaxation rate of the continuum approximation (green stars), along with the A_{1g} and B_{1g} relaxation rates derived from experiment. The B_{1g} continuum approximation relaxation rate by and large reflects the experimental resistivity data.

A_{1g} Raman response and the B_{1g} p-h fit according to Eq. (6.6), respectively, reflect the experimentally obtained resistivity data of Chu *et al.* (Ref. [29]). The B_{1g} dynamic relaxation rates deriving from the fit are displayed in the panels (c), the static relaxation rates are plotted together with the resistivity data in the panels (d) of both figures.

8.E AL fit parameters

This Appendix chapter comprises the Aslamazov-Larkin fit parameters used in Eqs. (6.8) and (6.9) to fit the experimental data shown in Figs. 6.8 and 6.16. The fits are shown as smooth red curves in all figures. The aforementioned formulas read

$$\Delta\chi''_{\gamma\gamma} = \Lambda^2_{\gamma\gamma} \int_0^\infty dz \, [b(z-\Omega/2) - b(z+\Omega/2)] \, \frac{z_+ z_-}{z_+^2 - z_-^2} \, [F(z_-) - F(z_+)] \, . \tag{8.1}$$

with $b(z)$ the Bose distribution function,

$$F(z) \equiv \frac{1}{z} \left[\arctan\left(\frac{\Omega_0}{z}\right) - \arctan\left(\frac{m}{z}\right) \right] , \tag{8.2}$$

and $z_{\pm} \equiv (z \pm \Omega/2)(1 + (z \pm \Omega/2)^2 \Omega_0{}^2)$. The fit parameters are highlighted in red in the formulas for clarity.

Table 8.3: AL fit parameters for $Ba(Fe_{1-x}Co_x)_2As_2$, $x = 0$

T(K)	m(cm^{-1})	Ω_0(cm^{-1})	$\Lambda^2_{\gamma\gamma}$
136	13	350	0.21
138	16.5	350	0.21
150	21	350	0.21
160	28	350	0.21
180	44	350	0.21
200	65	350	0.21
225	120	350	0.21

Table 8.4: AL fit parameters for $Ba(Fe_{1-x}Co_x)_2As_2$, $x = 0.025$

T(K)	m(cm^{-1})	Ω_0(cm^{-1})	$\Lambda^2_{\gamma\gamma}$
99	12	350	0.065
101	8.5	350	0.095
102	7.75	350	0.105
103	7.5	350	0.125
105	9	350	0.125
115	12.3	350	0.125
125	16.8	350	0.125
135	23	350	0.125
150	32	350	0.125
175	55	350	0.125

Table 8.5: AL fit parameters for $Ba(Fe_{1-x}Co_x)_2As_2$, $x = 0.051$

T(K)	m(cm^{-1})	Ω_0(cm^{-1})	$\Lambda^2_{\gamma\gamma}$
70	5.5	350	0.091
100	12.5	350	0.091
150	38	350	0.091

Bibliography

[1] H. K. Onnes, *Further experiments with liquid helium D - On the change of the electrical resistance of pure metals at very low temperatures, etc V The disappearance of the resistance of mercury*, Proceedings of the Koninklijke Nederlandse Akademie van Wetenschappen **14**, 113 (1911).

[2] J. Bardeen, L. N. Cooper, and J. R. Schrieffer, *Microscopic Theory of Superconductivity*, Physical Review **106**, 162 (1957).

[3] J. Bardeen, L. N. Cooper, and J. R. Schrieffer, *Theory of Superconductivity*, Physical Review **108**, 1175 (1957).

[4] C. Varma, in *Superconductivity in d- and f-Band Metals*, edited by W. Buckel and W. Weber (Kernforschungszentrum Karlsruhe, 76131 Karlsruhe, 1982), p. 500.

[5] J. Bednorz and K. Müller, *Possible high-T_c superconductivity in the Ba-La-Cu-O system*, Zeitschrift für Physik B Condensed Matter **64**, 189 (1986).

[6] M. K. Wu, J. R. Ashburn, C. J. Torng, P. H. Hor, R. L. Meng, L. Gao, Z. J. Huang, Y. Q. Wang, and C. W. Chu, *Superconductivity at 93 K in a new mixed-phase Y-Ba-Cu-O compound system at ambient pressure*, Physical Review Letters **58**, 908 (1987).

[7] A. Schilling, M. Cantoni, J. D. Guo, and H. R. Ott, *Superconductivity above 130 K in the Hg-Ba-Ca-Cu-O system*, Nature **363**, 56 (1993).

[8] Y. Kamihara, T. Watanabe, M. Hirano, and H. Hosono, *Iron-Based Layered Superconductor $La[O_{1-x}F_x]FeAs$ ($x = 0.05 - 0.12$) with $T_c = 26K$*, Journal of the American Chemical Society **130**, 3296 (2008).

[9] C. Wang, L. Li, S. Chi, Z. Zhu, Z. Ren, Y. Li, Y. Wang, X. Lin, Y. Luo, S. Jiang, X. Xu, G. Cao, and Z. Xu, *Thorium-doping-induced superconductivity up to 56K in $Gd_{1-x}Th_xFeAsO$*, Europhysics Letters **83**, 67006 (2008).

[10] W. L. McMillan and J. M. Rowell, *Lead Phonon Spectrum Calculated from Superconducting Density of States*, Physical Review Letters **14**, 108 (1965).

[11] M. Rotter, M. Tegel, and D. Johrendt, *Superconductivity at* $38K$ *in the Iron Arsenide* $(Ba_{1-x}K_x)Fe_2As_2$, Physical Review Letters **101**, 107006 (2008).

[12] P. J. Hirschfeld, M. M. Korshunov, and I. I. Mazin, *Gap symmetry and structure of Fe-based superconductors*, Reports on Progress in Physics **74**, 124508 (2011).

[13] W.-C. Lee, S.-C. Zhang, and C. Wu, *Pairing State with a Time-Reversal Symmetry Breaking in FeAs-Based Superconductors*, Physical Review Letters **102**, 217002 (2009).

[14] R. Thomale, C. Platt, W. Hanke, and B. A. Bernevig, *Mechanism for Explaining Differences in the Order Parameters of FeAs-Based and FeP-Based Pnictide Superconductors*, Physical Review Letters **106**, 187003 (2011).

[15] I. I. Mazin, D. J. Singh, M. D. Johannes, and M. H. Du, *Unconventional Superconductivity with a Sign Reversal in the Order Parameter of* $LaFeAsO_{1-x}F_x$, Physical Review Letters **101**, 057003 (2008).

[16] H. Kontani and S. Onari, *Orbital-Fluctuation-Mediated Superconductivity in Iron Pnictides: Analysis of the Five-Orbital Hubbard-Holstein Model*, Physical Review Letters **104**, 157001 (2010).

[17] D. J. Scalapino and T. P. Devereaux, *Collective d-wave exciton modes in the calculated Raman spectrum of Fe-based superconductors*, Physical Review B **80**, 140512 (2009).

[18] T. P. Devereaux, D. Einzel, B. Stadlober, R. Hackl, D. H. Leach, and J. J. Neumeier, *Electronic Raman scattering in high-Tc superconductors: A probe of* $d_{x^2-y^2}$ *pairing*, Physical Review Letters **72**, 396 (1994).

[19] T. P. Devereaux and R. Hackl, *Inelastic light scattering from correlated electrons*, Reviews of Modern Physics **79**, 175 (2007).

[20] A. Bardasis and J. R. Schrieffer, *Excitons and Plasmons in Superconductors*, Physical Review **121**, 1050 (1961).

[21] M. V. Klein and S. B. Dierker, *Theory of Raman scattering in superconductors*, Physical Review B **29**, 4976 (1984).

[22] H. Monien and A. Zawadowski, *Theory of Raman scattering with final-state interaction in high-Tc BCS superconductors: Collective modes*, Physical Review B **41**, 8798 (1990).

[23] A. V. Chubukov, I. Eremin, and M. M. Korshunov, *Theory of Raman response of a superconductor with extended s-wave symmetry: Application to the iron pnictides*, Physical Review B **79**, 220501 (2009).

[24] T. P. Devereaux and D. Einzel, *Electronic Raman scattering in superconductors as a probe of anisotropic electron pairing*, Physical Review B **51**, 16336 (1995).

[25] M. Yashima, H. Nishimura, H. Mukuda, Y. Kitaoka, K. Miyazawa, P. M. Shirage, K. Kihou, H. Kito, H. Eisaki, and A. Iyo, *Strong-Coupling Spin-Singlet Superconductivity with Multiple Full Gaps in Hole-Doped $Ba_{0.6}K_{0.4}Fe_2As_2$ Probed by $^{5}7$Fe-NMR*, Journal of the Physical Society of Japan **78**, 103702 (2009).

[26] X. G. Luo, M. A. Tanatar, J.-P. Reid, H. Shakeripour, N. Doiron-Leyraud, N. Ni, S. L. Bud'ko, P. C. Canfield, H. Luo, Z. Wang, H.-H. Wen, R. Prozorov, and L. Taillefer, *Quasiparticle heat transport in single-crystalline $Ba_{1-x}K_xFe_2As_2$: Evidence for a k-dependent superconducting gap without nodes*, Physical Review B **80**, 140503 (2009).

[27] J.-P. Reid, M. A. Tanatar, X. G. Luo, H. Shakeripour, S. René de Cotret, N. Doiron-Leyraud, J. Chang, B. Shen, H.-H. Wen, H. Kim, R. Prozorov, and L. Taillefer, *Doping-induced vertical line nodes in the superconducting gap of the iron arsenide K-Ba122 from directional thermal conductivity*, ArXiv e-prints (2011).

[28] J. S. Bobowski, J. C. Baglo, J. Day, P. Dosanjh, R. Ofer, B. J. Ramshaw, R. Liang, D. A. Bonn, W. N. Hardy, H. Luo, Z.-S. Wang, L. Fang, and H.-H. Wen, *Precision microwave electrodynamic measurements of K- and Co-doped $BaFe_2As_2$*, Physical Review B **82**, 094520 (2010).

[29] J.-H. Chu, J. G. Analytis, C. Kucharczyk, and I. R. Fisher, *Determination of the phase diagram of the electron-doped superconductor $Ba(Fe_{1-x}Co_x)_2As_2$*, Physical Review B **79**, 014506 (2009).

[30] R. M. Fernandes, A. V. Chubukov, and J. Schmalian, *What drives nematic order in iron-based superconductors?*, Nature Physics **10**, 97 (2014).

[31] J. Zhao, D. T. Adroja, D.-X. Yao, R. Bewley, L. Shiliang, X. F. Wang, G. Wu, X. H. Chen, J. Hu, and P. Dai, *Spin waves and magnetic exchange interactions in $CaFe_2As_2$*, Nature Physics **5**, 555 (2009).

[32] M. Yi, D. Lu, J.-H. Chu, J. G. Analytis, A. P. Sorini, A. F. Kemper, B. Moritz, S.-K. Mo, R. G. Moore, M. Hashimoto, W.-S. Lee, Z. Hussain, T. P. Devereaux, I. R. Fisher, and Z.-X. Shen, *Symmetry-breaking orbital anisotropy observed for detwinned $Ba(Fe_{1-x}Co_x)_2As_2$ above the spin density wave transition*, Proceedings of the National Academy of Sciences **108**, 6878 (2011).

[33] T.-M. Chuang, M. P. Allan, J. Lee, Y. Xie, N. Ni, S. L. Bud'ko, G. S. Boebinger, P. C. Canfield, and J. C. Davis, *Nematic Electronic Structure in the 'Parent' State of the Iron-Based Superconductor $Ca(Fe_{1-x}Co_x)_2As_2$*, Science **327**, 181 (2010).

[34] J.-H. Chu, J. G. Analytis, K. De Greve, P. L. McMahon, Z. Islam, Y. Yamamoto, and I. R. Fisher, *In-Plane Resistivity Anisotropy in an Underdoped Iron Arsenide Superconductor*, Science **329**, 824 (2010).

[35] M. A. Tanatar, E. C. Blomberg, A. Kreyssig, M. G. Kim, N. Ni, A. Thaler, S. L. Bud'ko, P. C. Canfield, A. I. Goldman, I. I. Mazin, and R. Prozorov, *Uniaxial-strain mechanical detwinning of $CaFe_2As_2$ and $BaFe_2As_2$ crystals: Optical and transport study*, Physical Review B **81**, 184508 (2010).

[36] M. J. Lawler, K. Fujita, J. Lee, A. R. Schmidt, Y. Kohsaka, C. K. Kim, H. Eisaki, S. Uchida, J. C. Davis, J. P. Sethna, and E.-A. Kim, *Intra-unit-cell electronic nematicity of the high-T_c copper-oxide pseudogap states*, Nature **466**, 347 (2010).

[37] V. Hinkov, D. Haug, B. Fauqué, P. Bourges, Y. Sidis, A. Ivanov, C. Bernhard, C. T. Lin, and B. Keimer, *Electronic Liquid Crystal State in the High-Temperature Superconductor $YBa_2Cu_3O_{6.45}$*, Science **319**, 597 (2008).

[38] Y. Ando, K. Segawa, S. Komiya, and A. N. Lavrov, *Electrical Resistivity Anisotropy from Self-Organized One Dimensionality in High-Temperature Superconductors*, Physical Review Letters **88**, 137005 (2002).

[39] R. Daou, J. Chang, D. LeBoeuf, O. Cyr-Choiniere, F. Laliberte, N. Doiron-Leyraud, B. J. Ramshaw, R. Liang, D. A. Bonn, W. N. Hardy, and L. Taillefer, *Broken rotational symmetry in the pseudogap phase of a high-T_c superconductor*, Nature **463**, 519 (2010).

[40] W. Weber, *The phonons in high T_c A15 compounds*, Physica B **126**, 217 (1984).

[41] C. Fang, H. Yao, W.-F. Tsai, J. Hu, and S. A. Kivelson, *Theory of electron nematic order in LaFeAsO*, Physical Review B **77**, 224509 (2008).

[42] C. Xu, M. Müller, and S. Sachdev, *Ising and spin orders in the iron-based superconductors*, Physical Review B **78**, 020501 (2008).

[43] P. Chandra, P. Coleman, and A. I. Larkin, *Ising transition in frustrated Heisenberg models*, Physical Review Letters **64**, 88 (1990).

[44] S.-H. Baek, D. V. Efremov, J. M. Ok, J. S. Kim, J. van den Brink, and B. Büchner, *Orbital-driven nematicity in FeSe*, Nature Materials **14**, 210 (2015).

[45] E. P. Rosenthal, E. F. Andrade, C. J. Arguello, R. M. Fernandes, L. Y. Xing, X. C. Wang, C. Q. Jin, A. J. Millis, and A. N. Pasupathy, *Visualization of electron nematicity and unidirectional antiferroic fluctuations at high temperatures in NaFeAs*, Nature Physics **10**, 225 (2014).

[46] S. Kasahara, H. J. Shi, K. Hashimoto, S. Tonegawa, Y. Mizukami, T. Shibauchi, K. Sugimoto, T. Fukuda, T. Terashima, A. H. Nevidomskyy, and Y. Matsuda, *Electronic nematicity above the structural and superconducting transition in $BaFe_2(As_{1-x}P_x)_2$*, Nature **486**, 382 (2012).

[47] J.-H. Chu, H.-H. Kuo, J. G. Analytis, and I. R. Fisher, *Divergent Nematic Susceptibility in an Iron Arsenide Superconductor*, Science **337**, 710 (2012).

[48] R. M. Fernandes, A. V. Chubukov, J. Knolle, I. Eremin, and J. Schmalian, *Preemptive nematic order, pseudogap, and orbital order in the iron pnictides*, Physical Review B **85**, 024534 (2012).

[49] R. M. Fernandes and J. Schmalian, *Manifestations of nematic degrees of freedom in the magnetic, elastic, and superconducting properties of the iron pnictides*, Superconductor Science and Technology **25**, 084005 (2012).

[50] H. Kontani, T. Saito, and S. Onari, *Origin of orthorhombic transition, magnetic transition, and shear-modulus softening in iron pnictide superconductors: Analysis based on the orbital fluctuations theory*, Physical Review B **84**, 024528 (2011).

[51] R. M. Fernandes, L. H. VanBebber, S. Bhattacharya, P. Chandra, V. Keppens, D. Mandrus, M. A. McGuire, B. C. Sales, A. S. Sefat, and J. Schmalian, *Effects of Nematic Fluctuations on the Elastic Properties of Iron Arsenide Superconductors*, Physical Review Letters **105**, 157003 (2010).

[52] M. Yoshizawa, D. Kimura, T. Chiba, S. Simayi, Y. Nakanishi, K. Kihou, C.-H. Lee, A. Iyo, H. Eisaki, M. Nakajima, and S.-i. Uchida, *Structural Quantum Criticality and Superconductivity in Iron-Based Superconductor* $Ba(Fe_{1-x}Co_x)_2As_2$, Journal of the Physical Society of Japan **81**, 024604 (2012).

[53] J. Paglione and R. L. Greene, *High-temperature superconductivity in iron-based materials*, Nature Physics **6**, 645 (2010).

[54] T. Böhm, Master thesis, Technische Universität München, 2012.

[55] J. Guo, S. Jin, G. Wang, S. Wang, K. Zhu, T. Zhou, M. He, and X. Chen, *Superconductivity in the iron selenide* $K_xFe_2Se_2$ ($0 \leq x \leq 1.0$), Physical Review B **82**, 180520 (2010).

[56] E. Dagotto, *Colloquium: The unexpected properties of alkali metal iron selenide superconductors*, Reviews of Modern Physics **85**, 849 (2013).

[57] W. Li, H. Ding, P. Deng, K. Chang, C. Song, K. He, L. Wang, X. Ma, J.-P. Hu, X. Chen, and Q.-K. Xue, *Phase separation and magnetic order in K-doped iron selenide superconductor*, Nature Physics **8**, 126 (2012).

[58] M. Yi, D. H. Lu, J. G. Analytis, J.-H. Chu, S.-K. Mo, R.-H. He, M. Hashimoto, R. G. Moore, I. I. Mazin, D. J. Singh, Z. Hussain, I. R. Fisher, and Z.-X. Shen, *Unconventional electronic reconstruction in undoped* $(Ba, Sr)Fe_2As_2$ *across the spin density wave transition*, Physical Review B **80**, 174510 (2009).

[59] S. Graser, T. A. Maier, P. J. Hirschfeld, and D. J. Scalapino, *Near-degeneracy of several pairing channels in multiorbital models for the Fe pnictides*, New Journal of Physics **11**, 025016 (2009).

[60] D. J. Singh and M.-H. Du, *Density Functional Study of* $LaFeAsO_{1-x}F_x$*: A Low Carrier Density Superconductor Near Itinerant Magnetism*, Physical Review Letters **100**, 237003 (2008).

[61] H.-M. Eiter, M. Lavagnini, R. Hackl, E. A. Nowadnick, A. F. Kemper, T. P. Devereaux, J.-H. Chu, J. G. Analytis, I. R. Fisher, and L. Degiorgi, *Alternative route to charge density wave formation in multiband systems*, Proceedings of the National Academy of Sciences **110**, 64 (2013).

[62] D. J. Singh, *Electronic structure and doping in $BaFe_2As_2$ and LiFeAs: Density functional calculations*, Physical Review B **78**, 094511 (2008).

[63] I. Mazin and J. Schmalian, *Pairing symmetry and pairing state in ferropnictides: Theoretical overview*, Physica C: Superconductivity **469**, 614 (2009), superconductivity in Iron-Pnictides.

[64] H. Ding, P. Richard, K. Nakayama, K. Sugawara, T. Arakane, Y. Sekiba, A. Takayama, S. Souma, T. Sato, T. Takahashi, Z. Wang, X. Dai, Z. Fang, G. F. Chen, J. L. Luo, and N. L. Wang, *Observation of Fermi-surface dependent nodeless superconducting gaps in $Ba_{0.6}K_{0.4}Fe_2As_2$*, Europhysics Letters **83**, 47001 (2008).

[65] V. B. Zabolotnyy, D. S. Inosov, D. V. Evtushinsky, A. Koitzsch, A. A. Kordyuk, G. L. Sun, J. T. Park, D. Haug, V. Hinkov, A. V. Boris, C. T. Lin, M. Knupfer, A. N. Yaresko, B. Buchner, A. Varykhalov, R. Follath, and S. V. Borisenko, *(π,π) electronic order in iron arsenide superconductors*, Nature **457**, 569 (2009).

[66] K. Terashima, Y. Sekiba, J. H. Bowen, K. Nakayama, T. Kawahara, T. Sato, P. Richard, Y.-M. Xu, L. J. Li, G. H. Cao, Z.-A. Xu, H. Ding, and T. Takahashi, *Fermi surface nesting induced strong pairing in iron-based superconductors*, Proceedings of the National Academy of Sciences **106**, 7330 (2009).

[67] Y. Zhang, F. Chen, C. He, B. Zhou, B. P. Xie, C. Fang, W. F. Tsai, X. H. Chen, H. Hayashi, J. Jiang, H. Iwasawa, K. Shimada, H. Namatame, M. Taniguchi, J. P. Hu, and D. L. Feng, *Orbital characters of bands in the iron-based superconductor $BaFe_{1.85}Co_{0.15}As_2$*, Physical Review B **83**, 054510 (2011).

[68] T. Sudayama, Y. Wakisaka, K. Takubo, R. Morinaga, T. J. Sato, M. Arita, H. Namatame, M. Taniguchi, and T. Mizokawa, *Band Structure of the Heavily-Electron-Doped FeAs-Based* $Ba(Fe,Co)_2As_2$ *Superconductor Suppresses Antiferromagnetic Correlations*, Physical Review Letters **104**, 177002 (2010).

[69] Y. Sekiba, T. Sato, K. Nakayama, K. Terashima, P. Richard, J. H. Bowen, H. Ding, Y.-M. Xu, L. J. Li, G. H. Cao, Z.-A. Xu, and T. Takahashi, *Electronic structure of heavily electron-doped $BaFe_{1.7}Co_{0.3}As_2$ studied by angle-resolved photoemission*, New Journal of Physics **11**, 025020 (2009).

[70] H. Wadati, I. Elfimov, and G. A. Sawatzky, *Where Are the Extra d Electrons in Transition-Metal-Substituted Iron Pnictides?*, Physical Review Letters **105**, 157004 (2010).

[71] E. M. Bittar, C. Adriano, T. M. Garitezi, P. F. S. Rosa, L. Mendon ça Ferreira, F. Garcia, G. d. M. Azevedo, P. G. Pagliuso, and E. Granado, *Co-Substitution Effects on the Fe Valence in the* $BaFe_2As_2$ *Superconducting Compound: A Study of Hard X-Ray Absorption Spectroscopy*, Physical Review Letters **107**, 267402 (2011).

[72] C. Cao, P. J. Hirschfeld, and H.-P. Cheng, *Proximity of antiferromagnetism and superconductivity in $LaFeAsO_{1-x}F_x$: Effective Hamiltonian from ab initio studies*, Physical Review B **77**, 220506 (2008).

[73] A. F. Kemper, T. A. Maier, S. Graser, H.-P. Cheng, P. J. Hirschfeld, and D. J. Scalapino, *Sensitivity of the superconducting state and magnetic susceptibility to key aspects of electronic structure in ferropnictides*, New Journal of Physics **12**, 073030 (2010).

[74] J. W. Lynn and P. Dai, *Neutron studies of the iron-based family of high T_c magnetic superconductors*, Physica C: Superconductivity **469**, 469 (2009), superconductivity in Iron-Pnictides.

[75] M. D. Lumsden and A. D. Christianson, *Magnetism in Fe-based superconductors*, Journal of Physics: Condensed Matter **22**, 203203 (2010).

[76] D. Singh, *Electronic structure of Fe-based superconductors*, Physica C: Superconductivity **469**, 418 (2009), superconductivity in Iron-Pnictides.

[77] V. Brouet, M. Marsi, B. Mansart, A. Nicolaou, A. Taleb-Ibrahimi, P. Le Fèvre, F. Bertran, F. Rullier-Albenque, A. Forget, and D. Colson, *Nesting between hole and electron pockets in $Ba(Fe_{1-x}Co_x)_2As_2$ (x = 0–0.3) observed with angle-resolved photoemission*, Physical Review B **80**, 165115 (2009).

[78] C. Liu, G. D. Samolyuk, Y. Lee, N. Ni, T. Kondo, A. F. Santander-Syro, S. L. Bud'ko, J. L. McChesney, E. Rotenberg, T. Valla, A. V. Fedorov,

P. C. Canfield, B. N. Harmon, and A. Kaminski, *K-Doping Dependence of the Fermi Surface of the Iron-Arsenic* $Ba_{1-x}K_xFe_2As_2$ *Superconductor Using Angle-Resolved Photoemission Spectroscopy*, Physical Review Letters **101**, 177005 (2008).

[79] A. I. Coldea, J. D. Fletcher, A. Carrington, J. G. Analytis, A. F. Bangura, J.-H. Chu, A. S. Erickson, I. R. Fisher, N. E. Hussey, and R. D. McDonald, *Fermi Surface of Superconducting LaFePO Determined from Quantum Oscillations*, Physical Review Letters **101**, 216402 (2008).

[80] J. G. Analytis, J.-H. Chu, R. D. McDonald, S. C. Riggs, and I. R. Fisher, *Enhanced Fermi-Surface Nesting in Superconducting* $BaFe_2(As_{1-x}P_x)_2$ *Revealed by the de Haas van Alphen Effect*, Physical Review Letters **105**, 207004 (2010).

[81] Y. Qiu, W. Bao, Y. Zhao, C. Broholm, V. Stanev, Z. Tesanovic, Y. C. Gasparovic, S. Chang, J. Hu, B. Qian, M. Fang, and Z. Mao, *Spin Gap and Resonance at the Nesting Wave Vector in Superconducting* $FeSe_{0.4}Te_{0.6}$, Physical Review Letters **103**, 067008 (2009).

[82] M. A. Tanatar, A. Kreyssig, S. Nandi, N. Ni, S. L. Bud'ko, P. C. Canfield, A. I. Goldman, and R. Prozorov, *Direct imaging of the structural domains in the iron pnictides* AFe_2As_2 $(A = Ca, Sr, Ba)$, Physical Review B **79**, 180508 (2009).

[83] I. R. Fisher, L. Degiorgi, and Z. X. Shen, *In-plane electronic anisotropy of underdoped '122' Fe-arsenide superconductors revealed by measurements of detwinned single crystals*, Reports on Progress in Physics **74**, 124506 (2011).

[84] J. J. Ying, X. F. Wang, T. Wu, Z. J. Xiang, R. H. Liu, Y. J. Yan, A. F. Wang, M. Zhang, G. J. Ye, P. Cheng, J. P. Hu, and X. H. Chen, *Measurements of the Anisotropic In-Plane Resistivity of Underdoped FeAs-Based Pnictide Superconductors*, Physical Review Letters **107**, 067001 (2011).

[85] A. Dusza, A. Lucarelli, F. Pfuner, J.-H. Chu, I. R. Fisher, and L. Degiorgi, *Anisotropic charge dynamics in detwinned* $Ba(Fe_{1-x}Co_x)_2As_2$, Europhysics Letters **93**, 37002 (2011).

[86] Y. Kim, H. Oh, C. Kim, D. Song, W. Jung, B. Kim, H. J. Choi, C. Kim, B. Lee, S. Khim, H. Kim, K. Kim, J. Hong, and Y. Kwon, *Electronic structure of detwinned* $BaFe_2As_2$ *from photoemission and first principles*, Physical Review B **83**, 064509 (2011).

[87] J.-H. Chu, J. G. Analytis, D. Press, K. De Greve, T. D. Ladd, Y. Yamamoto, and I. R. Fisher, *In-plane electronic anisotropy in underdoped $Ba(Fe_{1-x}Co_x)_2As_2$ revealed by partial detwinning in a magnetic field*, Physical Review B **81**, 214502 (2010).

[88] Y. Xiao, Y. Su, W. Schmidt, K. Schmalzl, C. M. N. Kumar, S. Price, T. Chatterji, R. Mittal, L. J. Chang, S. Nandi, N. Kumar, S. K. Dhar, A. Thamizhavel, and T. Brueckel, *Field-induced spin reorientation and giant spin-lattice coupling in $EuFe_2As_2$*, Physical Review B **81**, 220406 (2010).

[89] K. Nakayama, T. Sato, P. Richard, Y.-M. Xu, Y. Sekiba, S. Souma, G. F. Chen, J. L. Luo, N. L. Wang, H. Ding, and T. Takahashi, *Superconducting gap symmetry of $Ba_{0.6}K_{0.4}Fe_2As_2$ studied by angle-resolved photoemission spectroscopy*, Europhysics Letters **85**, 67002 (2009).

[90] C. Liu, T. Kondo, R. M. Fernandes, A. D. Palczewski, E. D. Mun, N. Ni, A. N. Thaler, A. Bostwick, E. Rotenberg, J. Schmalian, S. L. Bud/'ko, P. C. Canfield, and A. Kaminski, *Evidence for a Lifshitz transition in electron-doped iron arsenic superconductors at the onset of superconductivity*, Nature Physics **6**, 419 (2010).

[91] A. Kordyuk, V. Zabolotnyy, D. Evtushinsky, A. Yaresko, B. Büchner, and S. Borisenko, *Electronic Band Structure of Ferro-Pnictide Superconductors from ARPES Experiment*, Journal of Superconductivity and Novel Magnetism **26**, 2837 (2013).

[92] R. Gross and A. Marx, *Festkörperphysik* (Oldenbourg Wissenschaftsverlag, Rosenheimer Straße 145, D-81671 München, 2012).

[93] J. Annett, *Superconductivity, Superfluids and Condensates*, *Oxford Master Series in Physics* (Oxford University Press, 198 Madison Avenue, New York, NY 10016, USA, 2004).

[94] P. B. Allen, *Fermi-surface harmonics: A general method for nonspherical problems. Application to Boltzmann and Eliashberg equations*, Physical Review B **13**, 1416 (1976).

[95] F. Ning, K. Ahilan, T. Imai, A. S. Sefat, R. Jin, M. A. McGuire, B. C. Sales, and D. Mandrus, *^{59}Co and ^{75}As NMR Investigation of Electron-Doped High T_c Superconductor $BaFe_{1.8}Co_{0.2}As_2$ ($T_c = 22\,\mathrm{K}$)*, Journal of the Physical Society of Japan **77**, 103705 (2008).

[96] H.-J. Grafe, D. Paar, G. Lang, N. J. Curro, G. Behr, J. Werner, J. Hamann-Borrero, C. Hess, N. Leps, R. Klingeler, and B. Büchner, ^{75}As *NMR Studies of Superconducting* $LaFeAsO_{0.9}F_{0.1}$, Physical Review Letters **101**, 047003 (2008).

[97] K. Matano, Z. A. Ren, X. L. Dong, L. L. Sun, Z. X. Zhao, and G. qing Zheng, *Spin-singlet superconductivity with multiple gaps in* $PrFeAsO_{0.89}F_{0.11}$, Europhysics Letters **83**, 57001 (2008).

[98] K. Matano, Z. Li, G. L. Sun, D. L. Sun, C. T. Lin, M. Ichioka, and G. qing Zheng, *Anisotropic spin fluctuations and multiple superconducting gaps in hole-doped* $Ba_{0.72}K_{0.28}Fe_2As_2$*: NMR in a single crystal*, Europhysics Letters **87**, 27012 (2009).

[99] P. Jeglič, A. Potočnik, M. Klanjšek, M. Bobnar, M. Jagodič, K. Koch, H. Rosner, S. Margadonna, B. Lv, A. M. Guloy, and D. Arčon, ^{75}*As nuclear magnetic resonance study of antiferromagnetic fluctuations in the normal state of LiFeAs*, Physical Review B **81**, 140511 (2010).

[100] Z. Li, Y. Ooe, X.-C. Wang, Q.-Q. Liu, C.-Q. Jin, M. Ichioka, and G.-q. Zheng, ^{75}*As NQR and NMR Studies of Superconductivity and Electron Correlations in Iron Arsenide LiFeAs*, Journal of the Physical Society of Japan **79**, 083702 (2010).

[101] Y. Nakai, T. Iye, S. Kitagawa, K. Ishida, S. Kasahara, T. Shibauchi, Y. Matsuda, and T. Terashima, ^{31}P *and* ^{75}As *NMR evidence for a residual density of states at zero energy in superconducting* $BaFe_2(As_{0.67}P_{0.33})_2$, Physical Review B **81**, 020503 (2010).

[102] J. Annett, N. Goldenfeld, and A. Leggett, *Constraints on the pairing state of the cuprate superconductors*, Journal of Low Temperature Physics **105**, 473 (1996).

[103] J. F. Annett, *Symmetry of the order parameter for high-temperature superconductivity*, Advances in Physics **39**, 83 (1990).

[104] S. Onari, H. Kontani, and M. Sato, *Structure of neutron-scattering peaks in both* s_{++}*-wave and* $s_{\pm}$*-wave states of an iron pnictide superconductor*, Physical Review B **81**, 060504 (2010).

[105] T. Saito, S. Onari, and H. Kontani, *Orbital fluctuation theory in iron pnictides: Effects of As-Fe-As bond angle, isotope substitution, and Z^2-orbital pocket on superconductivity*, Physical Review B **82**, 144510 (2010).

[106] P. Monthoux, D. Pines, and G. G. Lonzarich, *Superconductivity without phonons*, Nature **450**, 1177 (2007).

[107] L. Boeri, O. V. Dolgov, and A. A. Golubov, *Is $LaFeAsO_{1-x}F_x$ an Electron-Phonon Superconductor?*, Physical Review Letters **101**, 026403 (2008).

[108] A. J. Leggett, *A theoretical description of the new phases of liquid ^3He*, Reviews of Modern Physics **47**, 331 (1975).

[109] C. Pfleiderer and R. Hackl, *High-temperature superconductivity: Schizophrenic electrons*, Nature **450**, 492 (2007).

[110] D. Scalapino, *The case for $d_{x^2-y^2}$ pairing in the cuprate superconductors*, Physics Reports **250**, 329 (1995).

[111] K. Kuroki, S. Onari, R. Arita, H. Usui, Y. Tanaka, H. Kontani, and H. Aoki, *Unconventional Pairing Originating from the Disconnected Fermi Surfaces of Superconducting $LaFeAsO_{1-x}F_x$*, Physical Review Letters **101**, 087004 (2008).

[112] F. Wang, H. Zhai, and D.-H. Lee, *Antiferromagnetic correlation and the pairing mechanism of the cuprates and iron pnictides: A view from the functional renormalization group studies*, Europhysics Letters **85**, 37005 (2009).

[113] P. W. Anderson, *Coherent Excited States in the Theory of Superconductivity: Gauge Invariance and the Meissner Effect*, Physical Review **110**, 827 (1958).

[114] P. W. Anderson, *Random-Phase Approximation in the Theory of Superconductivity*, Physical Review **112**, 1900 (1958).

[115] N. N. Bogoljubov, V. V. Tolmachov, and D. V. Å irkov, *A New Method in the Theory of Superconductivity*, Fortschritte der Physik **6**, 605 (1958).

[116] G. Rickayzen, *Collective Excitations in the Theory of Superconductivity*, Physical Review **115**, 795 (1959).

[117] P. Fulde and S. Strassler, *Collective Excitations in Strong-Coupling Superconducting Alloys*, Physical Review **140**, A519 (1965).

[118] K. Maki and T. Tsuneto, *Effects of Impurity Scattering on Excitons in Superconductor*, Progress of Theoretical Physics **28**, 163 (1962).

[119] D. Belitz, S. De Souza-Machado, T. P. Devereaux, and D. W. Hoard, *Electromagnetic response of disordered superconductors*, Physical Review B **39**, 2072 (1989).

[120] T. P. Devereaux, *Theory for the effects of impurities on the Raman spectra of superconductors. II. Temperature dependence and influence of final-state interactions*, Physical Review B **47**, 5230 (1993).

[121] A. A. Abrikosov and L. A. Fal'kovskii, *Raman Scattering of Light in Superconductors*, Zh. Eksp. Teor. Fiz. **40**, 262 (1961), [Sov. Phys. JETP 13, 179 (1961)].

[122] S. Lederer, Y. Schattner, E. Berg, and S. A. Kivelson, *Enhancement of Superconductivity near a Nematic Quantum Critical Point*, Physical Review Letters **114**, 097001 (2015).

[123] E. Fradkin, S. A. Kivelson, M. J. Lawler, J. P. Eisenstein, and A. P. Mackenzie, *Nematic Fermi Fluids in Condensed Matter Physics*, Annual Review of Condensed Matter Physics **1**, 153 (2010).

[124] D. Koukou, *Advanced Elastomers - Technology, Properties and applications* (InTech, Janeza Trdine 9, 51000 Rijeka, Croatia, 2012).

[125] A. Dusza, A. Lucarelli, A. Sanna, S. Massidda, J.-H. Chu, I. R. Fisher, and L. Degiorgi, *Anisotropic in-plane optical conductivity in detwinned* $Ba(Fe_{1-x}Co_x)_2As_2$, New Journal of Physics **14**, 023020 (2012).

[126] M. Nakajima, T. Liang, S. Ishida, Y. Tomioka, K. Kihou, C. H. Lee, A. Iyo, H. Eisaki, T. Kakeshita, T. Ito, and S. Uchida, *Unprecedented anisotropic metallic state in undoped iron arsenide* $BaFe_2As_2$ *revealed by optical spectroscopy*, Proceedings of the National Academy of Sciences **108**, 12238 (2011).

[127] R. M. Fernandes, D. K. Pratt, W. Tian, J. Zarestky, A. Kreyssig, S. Nandi, M. G. Kim, A. Thaler, N. Ni, P. C. Canfield, R. J. McQueeney, J. Schmalian, and A. I. Goldman, *Unconventional pairing in the iron arsenide superconductors*, Physical Review B **81**, 140501 (2010).

[128] F. Krüger, S. Kumar, J. Zaanen, and J. van den Brink, *Spin-orbital frustrations and anomalous metallic state in iron-pnictide superconductors*, Physical Review B **79**, 054504 (2009).

[129] W. Lv, F. Krüger, and P. Phillips, *Orbital ordering and unfrustrated* $(\pi, 0)$ *magnetism from degenerate double exchange in the iron pnictides*, Physical Review B **82**, 045125 (2010).

[130] W. Lv and P. Phillips, *Orbitally and magnetically induced anisotropy in iron-based superconductors*, Physical Review B **84**, 174512 (2011).

[131] W.-G. Yin, C.-C. Lee, and W. Ku, *Unified Picture for Magnetic Correlations in Iron-Based Superconductors*, Physical Review Letters **105**, 107004 (2010).

[132] M. J. Calderón, B. Valenzuela, and E. Bascones, *Tight-binding model for iron pnictides*, Physical Review B **80**, 094531 (2009).

[133] E. Bascones, M. J. Calderón, and B. Valenzuela, *Low Magnetization and Anisotropy in the Antiferromagnetic State of Undoped Iron Pnictides*, Physical Review Letters **104**, 227201 (2010).

[134] M. J. Calderón, G. León, B. Valenzuela, and E. Bascones, *Magnetic interactions in iron superconductors studied with a five-orbital model within the Hartree-Fock and Heisenberg approximations*, Physical Review B **86**, 104514 (2012).

[135] P. M. R. Brydon, M. Daghofer, and C. Timm, *Magnetic order in orbital models of the iron pnictides*, Journal of Physics: Condensed Matter **23**, 246001 (2011).

[136] A. Nicholson, Q. Luo, W. Ge, J. Riera, M. Daghofer, G. B. Martins, A. Moreo, and E. Dagotto, *Role of degeneracy, hybridization, and nesting in the properties of multiorbital systems*, Physical Review B **84**, 094519 (2011).

[137] C.-C. Chen, J. Maciejko, A. P. Sorini, B. Moritz, R. R. P. Singh, and T. P. Devereaux, *Orbital order and spontaneous orthorhombicity in iron pnictides*, Physical Review B **82**, 100504 (2010).

[138] D.-Y. Liu, Y.-M. Quan, D.-M. Chen, L.-J. Zou, and H.-Q. Lin, *Ferro-orbital order induced by electron-lattice coupling in orthorhombic iron pnictides*, Physical Review B **84**, 064435 (2011).

[139] A. Chubukov, *Pairing Mechanism in Fe-Based Superconductors*, Annual Review of Condensed Matter Physics **3**, 57 (2012).

[140] R. M. Fernandes and A. J. Millis, *Nematicity as a Probe of Superconducting Pairing in Iron-Based Superconductors*, Physical Review Letters **111**, 127001 (2013).

[141] P. Dai, J. Hu, and E. Dagotto, *Magnetism and its microscopic origin in iron-based high-temperature superconductors*, Nature Physics **8**, 709 (2012).

[142] R. M. Fernandes, E. Abrahams, and J. Schmalian, *Anisotropic In-Plane Resistivity in the Nematic Phase of the Iron Pnictides*, Physical Review Letters **107**, 217002 (2011).

[143] X. Lu, J. T. Park, R. Zhang, H. Luo, A. H. Nevidomskyy, Q. Si, and P. Dai, *Nematic spin correlations in the tetragonal state of uniaxial-strained* $BaFe_{2-x}Ni_xAs_2$, Science **345**, 657 (2014).

[144] Y. K. Kim, W. S. Jung, G. R. Han, K.-Y. Choi, C.-C. Chen, T. P. Devereaux, A. Chainani, J. Miyawaki, Y. Takata, Y. Tanaka, M. Oura, S. Shin, A. P. Singh, H. G. Lee, J.-Y. Kim, and C. Kim, *Existence of Orbital Order and its Fluctuation in Superconducting* $Ba(Fe_{1-x}Co_x)_2As_2$ *Single Crystals Revealed by X-ray Absorption Spectroscopy*, Physical Review Letters **111**, 217001 (2013).

[145] D. Pines, P. Nozières, and P. Nozieres, *The Theory of Quantum Liquids* (WA Benjamin, New York, 1966).

[146] F. A. Blum, *Inelastic Light Scattering from Semiconductor Plasmas in a Magnetic Field*, Physical Review B **1**, 1125 (1970).

[147] H. Nyquist, *Thermal Agitation of Electric Charge in Conductors*, Physical Review **32**, 110 (1928).

[148] H. B. Callen and T. A. Welton, *Irreversibility and Generalized Noise*, Physical Review **83**, 34 (1951).

[149] N. Ashcroft and N. Mermin, *Solid state physics*, *Science: Physics* (Saunders College, Philadelphia, PA 19105, 1976).

[150] B. Muschler, Ph.d. thesis, Technische Universität München, 2012.

[151] B. S. Shastry and B. I. Shraiman, *Theory of Raman scattering in Mott-Hubbard systems*, Physical Review Letters **65**, 1068 (1990).

[152] T. P. Devereaux, *Theory for the effects of impurities on the Raman spectra of superconductors*, Physical Review B **45**, 12965 (1992).

[153] W. Hayes and R. Loudon, *Scattering of Light by Crystals*, *Dover Books on Physics* (Dover Publications, New York, 2012).

[154] G. Mahan, *Many-Particle Physics*, *Physics of Solids and Liquids* (Kluwer Academic, New York, 2000).

[155] T. P. Devereaux, A. Virosztek, and A. Zawadowski, *Multiband electronic Raman scattering in bilayer superconductors*, Physical Review B **54**, 12523 (1996).

[156] M. Cardona, A. Pinczuk, E. Burstein, R. Martin, M. Falicov, L. andKlein, M. Brodsky, A. Pine, and Y. Shen, *Light Scattering in Solids I*, *Topics in Applied Physics* (Springer-Verlag, Berlin, 1975).

[157] S. Caprara, C. Di Castro, M. Grilli, and D. Suppa, *Charge-Fluctuation Contribution to the Raman Response in Superconducting Cuprates*, Physical Review Letters **95**, 117004 (2005).

[158] Y. Nambu, *Quasi-Particles and Gauge Invariance in the Theory of Superconductivity*, Physical Review **117**, 648 (1960).

[159] T. Böhm, F. Kemper, A. B. Moritz, F. Kretzschmar, B. Muschler, H.-M. Eiter, R. Hackl, P. Devereaux, T. J. Scalapino, D. and H.-H. Wen, *Balancing Act: Evidence for a Strong Subdominant d-Wave Pairing Channel in* $Ba_{0.6}K_{0.4}Fe_2As_2$, Physical Review X **4**, 041046 (2014).

[160] W. Prestel, Ph.d. thesis, Technische Universität München, 2012.

[161] R. Hackl, Ph.d. thesis, Technische Universität München, 1987.

[162] B. Shen, H. Yang, Z.-S. Wang, F. Han, B. Zeng, L. Shan, C. Ren, and H.-H. Wen, *Transport properties and asymmetric scattering in* $Ba_{1-x}K_xFe_2As_2$ *single crystals*, Physical Review B **84**, 184512 (2011).

[163] V. Tsurkan, J. Deisenhofer, A. Günther, H.-A. Krug von Nidda, S. Widmann, and A. Loidl, *Anisotropic magnetism, superconductivity, and the phase diagram of* $Rb_{1-x}Fe_{2-y}Se_2$, Physical Review B **84**, 144520 (2011).

[164] V. Ksenofontov, G. Wortmann, S. A. Medvedev, V. Tsurkan, J. Deisenhofer, A. Loidl, and C. Felser, *Phase separation in superconducting and antiferromagnetic $Rb_{0.8}Fe_{1.6}Se_2$ probed by Mössbauer spectroscopy*, Physical Review B **84**, 180508 (2011).

[165] A. Charnukha, J. Deisenhofer, D. Pröpper, M. Schmidt, Z. Wang, Y. Goncharov, A. N. Yaresko, V. Tsurkan, B. Keimer, A. Loidl, and A. V. Boris, *Optical conductivity of superconducting $Rb_2Fe_4Se_5$ single crystals*, Physical Review B **85**, 100504 (2012).

[166] Y. Texier, J. Deisenhofer, V. Tsurkan, A. Loidl, D. S. Inosov, G. Friemel, and J. Bobroff, *NMR Study in the Iron-Selenide $Rb_{0.74}Fe_{1.6}Se_2$: Determination of the Superconducting Phase as Iron Vacancy-Free $Rb_{0.3}Fe_2Se_2$*, Physical Review Letters **108**, 237002 (2012).

[167] J. T. Park, G. Friemel, Y. Li, J.-H. Kim, V. Tsurkan, J. Deisenhofer, H.-A. Krug von Nidda, A. Loidl, A. Ivanov, B. Keimer, and D. S. Inosov, *Magnetic Resonant Mode in the Low-Energy Spin-Excitation Spectrum of Superconducting $Rb_2Fe_4Se_5$ Single Crystals*, Physical Review Letters **107**, 177005 (2011).

[168] F. Kretzschmar, B. Muschler, T. Böhm, A. Baum, R. Hackl, H.-H. Wen, V. Tsurkan, J. Deisenhofer, and A. Loidl, *Raman-Scattering Detection of Nearly Degenerate s-Wave and d-Wave Pairing Channels in Iron-Based $Ba_{0.6}K_{0.4}Fe_2As_2$ and $Rb_{0.8}Fe_{1.6}Se_2$ Superconductors*, Physical Review Letters **110**, 187002 (2013).

[169] A. P. Litvinchuk, V. G. Hadjiev, M. N. Iliev, B. Lv, A. M. Guloy, and C. W. Chu, *Raman-scattering study of $K_xSr_{1-x}Fe_2As_2$ ($x = 0.0, 0.4$)*, Physical Review B **78**, 060503 (2008).

[170] L. Chauvière, Y. Gallais, M. Cazayous, A. Sacuto, M. A. Méasson, D. Colson, and A. Forget, *Doping dependence of the lattice dynamics in $Ba(Fe_{1-x}Co_x)_2As_2$ studied by Raman spectroscopy*, Physical Review B **80**, 094504 (2009).

[171] M. Rahlenbeck, G. L. Sun, D. L. Sun, C. T. Lin, B. Keimer, and C. Ulrich, *Phonon anomalies in pure and underdoped $R_{1-x}K_xFe_2As_2$ ($R = Ba, Sr$) investigated by Raman light scattering*, Physical Review B **80**, 064509 (2009).

[172] K.-Y. Choi, P. Lemmens, I. Eremin, G. Zwicknagl, H. Berger, G. L. Sun, D. L. Sun, and C. T. Lin, *Self-energy effects and electron-phonon coupling in Fe-As superconductors*, Journal of Physics: Condensed Matter **22**, 115802 (2010).

[173] L. Chauvière, Y. Gallais, M. Cazayous, M. A. Méasson, A. Sacuto, D. Colson, and A. Forget, *Raman scattering study of spin-density-wave order and electron-phonon coupling in* $Ba(Fe_{1-x}Co_x)_2As_2$, Physical Review B **84**, 104508 (2011).

[174] T. P. Devereaux, *Symmetry dependence of phonon line shapes in superconductors with anisotropic gaps*, Physical Review B **50**, 10287 (1994).

[175] D. V. Evtushinsky, D. S. Inosov, V. B. Zabolotnyy, A. Koitzsch, M. Knupfer, B. Büchner, M. S. Viazovska, G. L. Sun, V. Hinkov, A. V. Boris, C. T. Lin, B. Keimer, A. Varykhalov, A. A. Kordyuk, and S. V. Borisenko, *Momentum dependence of the superconducting gap in* $Ba_{1-x}K_xFe_2As_2$, Physical Review B **79**, 054517 (2009).

[176] V. G. Hadjiev, X. Zhou, T. Strohm, M. Cardona, Q. M. Lin, and C. W. Chu, *Strong superconductivity-induced phonon self-energy effects in* $HgBa_2Ca_3Cu_4O_{10+\delta}$, Physical Review B **58**, 1043 (1998).

[177] A. M. Zhang, K. Liu, J. B. He, D. M. Wang, G. F. Chen, B. Normand, and Q. M. Zhang, *Effect of iron content and potassium substitution in* $A_{0.8}Fe_{1.6}Se_2$ *(A=K, Rb, Tl) superconductors: A Raman scattering investigation*, Physical Review B **86**, 134502 (2012).

[178] Y. Zhang, L. X. Yang, M. Xu, Z. R. Ye, F. Chen, C. He, H. C. Xu, J. Jiang, B. P. Xie, J. J. Ying, X. F. Wang, X. H. Chen, J. P. Hu, M. Matsunami, S. Kimura, and D. L. Feng, *Nodeless superconducting gap in* $A_xFe_2Se_2$ $(A = K, Cs)$ *revealed by angle-resolved photoemission spectroscopy*, Nature Materials **10**, 273 (2011).

[179] T. Qian, X.-P. Wang, W.-C. Jin, P. Zhang, P. Richard, G. Xu, X. Dai, Z. Fang, J.-G. Guo, X.-L. Chen, and H. Ding, *Absence of a Holelike Fermi Surface for the Iron-Based* $K_{0.8}Fe_{1.7}Se_2$ *Superconductor Revealed by Angle-Resolved Photoemission Spectroscopy*, Physical Review Letters **106**, 187001 (2011).

[180] B. Muschler, W. Prestel, R. Hackl, T. P. Devereaux, J. G. Analytis, J.-H. Chu, and I. R. Fisher, *Band- and momentum-dependent electron dynamics in*

superconducting $Ba(Fe_{1-x}Co_x)_2As_2$ as seen via electronic Raman scattering, Physical Review B **80**, 180510 (2009).

[181] I. I. Mazin, T. P. Devereaux, J. G. Analytis, J.-H. Chu, I. R. Fisher, B. Muschler, and R. Hackl, *Pinpointing gap minima in $Ba(Fe_{0.94}Co_{0.06})_2As_2$ via band-structure calculations and electronic Raman scattering*, Physical Review B **82**, 180502 (2010).

[182] M. D. Johannes and I. I. Mazin, *Microscopic origin of magnetism and magnetic interactions in ferropnictides*, Physical Review B **79**, 220510 (2009).

[183] J.-P. Reid, M. A. Tanatar, X. G. Luo, H. Shakeripour, N. Doiron-Leyraud, N. Ni, S. L. Bud'ko, P. C. Canfield, R. Prozorov, and L. Taillefer, *Nodes in the gap structure of the iron arsenide superconductor $Ba(Fe_{1-x}Co_x)_2As_2$ from c-axis heat transport measurements*, Physical Review B **82**, 064501 (2010).

[184] M. A. Tanatar, J.-P. Reid, H. Shakeripour, X. G. Luo, N. Doiron-Leyraud, N. Ni, S. L. Bud'ko, P. C. Canfield, R. Prozorov, and L. Taillefer, *Doping Dependence of Heat Transport in the Iron-Arsenide Superconductor $Ba(Fe_{1-x}Co_x)_2As_2$: From Isotropic to a Strongly k-Dependent Gap Structure*, Physical Review Letters **104**, 067002 (2010).

[185] L. Luan, T. M. Lippman, C. W. Hicks, J. A. Bert, O. M. Auslaender, J.-H. Chu, J. G. Analytis, I. R. Fisher, and K. A. Moler, *Local Measurement of the Superfluid Density in the Pnictide Superconductor $Ba(Fe_{1-x}Co_x)_2As_x$ across the Superconducting Dome*, Physical Review Letters **106**, 067001 (2011).

[186] L. Chauvière, Y. Gallais, M. Cazayous, M. A. Méasson, A. Sacuto, D. Colson, and A. Forget, *Impact of the spin-density-wave order on the superconducting gap of $Ba(Fe_{1-x}Co_x)_2As_2$*, Physical Review B **82**, 180521 (2010).

[187] E. D. Mun, S. L. Bud'ko, N. Ni, A. N. Thaler, and P. C. Canfield, *Thermoelectric power and Hall coefficient measurements on $Ba(Fe_{1-x}T_x)_2As_2$ (T = Co and Cu)*, Physical Review B **80**, 054517 (2009).

[188] W. Götze and P. Wölfle, *Homogeneous Dynamical Conductivity of Simple Metals*, Physical Review B **6**, 1226 (1972).

[189] J. W. Allen and J. C. Mikkelsen, *Optical properties of CrSb, MnSb, NiSb, and NiAs*, Physical Review B **15**, 2952 (1977).

[190] M. Opel, R. Nemetschek, C. Hoffmann, R. Philipp, P. F. Müller, R. Hackl, I. Tüttő, A. Erb, B. Revaz, E. Walker, H. Berger, and L. Forró, *Carrier relaxation, pseudogap, and superconducting gap in high-T_c cuprates: A Raman scattering study*, Physical Review B **61**, 9752 (2000).

[191] R. Nemetschek, Ph.d. thesis, Technische Universität München, 1998.

[192] N. E. Hussey, J. C. Alexander, and R. A. Cooper, *Optical response of high-T_c cuprates: Possible role of scattering rate saturation and in-plane anisotropy*, Physical Review B **74**, 214508 (2006).

[193] H. Wiesmann, M. Gurvitch, H. Lutz, A. Ghosh, B. Schwarz, M. Strongin, P. B. Allen, and J. W. Halley, *Simple Model for Characterizing the Electrical Resistivity in $A-15$ Superconductors*, Physical Review Letters **38**, 782 (1977).

[194] M. Gurvitch, *Ioffe-Regel criterion and resistivity of metals*, Physical Review B **24**, 7404 (1981).

[195] H.-M. Eiter, P. Jaschke, R. Hackl, A. Bauer, M. Gangl, and C. Pfleiderer, *Raman study of the temperature and magnetic-field dependence of the electronic and lattice properties of MnSi*, Physical Review B **90**, 024411 (2014).

[196] A. E. Ioffe and A. R. Regel, in *Progress in Semiconductors*, edited by A. F. Gibson (Heywood & Co. Ltd., London, 1960), Vol. 4, p. 237.

[197] N. F. Mott, *Conduction in non-crystalline systems IX. the minimum metallic conductivity*, Philosophical Magazine **26**, 1015 (1972).

[198] N. E. Hussey, K. Takenaka, and H. Takagi, *Universality of the Mott-Ioffe-Regel limit in metals*, Philosophical Magazine **84**, 2847 (2004).

[199] A. Lucarelli, A. Dusza, F. Pfuner, P. Lerch, J. G. Analytis, J.-H. Chu, I. R. Fisher, and L. Degiorgi, *Charge dynamics of Co-doped $BaFe_2As_2$*, New Journal of Physics **12**, 073036 (2010).

[200] J. J. Tu, J. Li, W. Liu, A. Punnoose, Y. Gong, Y. H. Ren, L. J. Li, G. H. Cao, Z. A. Xu, and C. C. Homes, *Optical properties of the iron arsenic superconductor $BaFe_{1.85}Co_{0.15}As_2$*, Physical Review B **82**, 174509 (2010).

[201] E. van Heumen, Y. Huang, S. de Jong, A. B. Kuzmenko, M. S. Golden, and D. van der Marel, *Optical properties of $BaFe_{2-x}Co_xAs_2$*, Europhysics Letters **90**, 37005 (2010).

[202] W. Z. Hu, J. Dong, G. Li, Z. Li, P. Zheng, G. F. Chen, J. L. Luo, and N. L. Wang, *Origin of the Spin Density Wave Instability in* $A\mathrm{Fe_2As_2}$ *(*$A = \mathrm{Ba, Sr}$*) as Revealed by Optical Spectroscopy*, Physical Review Letters **101**, 257005 (2008).

[203] A. Sanna, F. Bernardini, G. Profeta, S. Sharma, J. K. Dewhurst, A. Lucarelli, L. Degiorgi, E. K. U. Gross, and S. Massidda, *Theoretical investigation of optical conductivity in* $Ba(Fe_{1-x}Co_x)_2As_2$, Physical Review B **83**, 054502 (2011).

[204] Y. Gallais, R. M. Fernandes, I. Paul, L. Chauvière, Y.-X. Yang, M.-A. Méasson, M. Cazayous, A. Sacuto, D. Colson, and A. Forget, *Observation of Incipient Charge Nematicity in* $Ba(Fe_{1-x}Co_x)_2As_2$, Physical Review Letters **111**, 267001 (2013).

[205] L. Tassini, F. Venturini, Q.-M. Zhang, R. Hackl, N. Kikugawa, and T. Fujita, *Dynamical Properties of Charged Stripes in* $La_{2-x}Sr_xCuO_4$, Physical Review Letters **95**, 117002 (2005).

[206] L. Aslamasov and A. Larkin, *Effect of Fluctuations on the Properties of a Superconductor Above the Critical Temperature*, Soviet Physics Solid State **10**, 875 (1968).

[207] S. Caprara, C. Di Castro, B. Muschler, W. Prestel, R. Hackl, M. Lambacher, A. Erb, S. Komiya, Y. Ando, and M. Grilli, *Extracting the dynamical effective interaction and competing order from an analysis of Raman spectra of the high-temperature* $La_{2-x}Sr_xCuO_4$ *superconductor*, Physical Review B **84**, 054508 (2011).

[208] J. M. Tranquada, B. J. Sternlieb, J. D. Axe, Y. Nakamura, and S. Uchida, *Evidence for stripe correlations of spins and holes in copper oxide*, Nature **375**, 561 (1995).

[209] P. Abbamonte, A. Rusydi, S. Smadici, G. D. Gu, G. A. Sawatzky, and D. L. Feng, *Spatially modulated 'Mottness' in* $La_{2-x}Ba_xCuO_4$, Nature Physics **1**, 155 (2005).

[210] C. Howald, H. Eisaki, N. Kaneko, M. Greven, and A. Kapitulnik, *Periodic density-of-states modulations in superconducting* $Bi_2Sr_2CaCu_2O_{8+\delta}$, Physical Review B **67**, 014533 (2003).

[211] M. Vershinin, S. Misra, S. Ono, Y. Abe, Y. Ando, and A. Yazdani, *Local Ordering in the Pseudogap State of the High-Tc Superconductor $Bi_2Sr_2CaCu_2O_{8+\delta}$*, Science **303**, 1995 (2004).

[212] T. Hanaguri, C. Lupien, Y. Kohsaka, D.-H. Lee, M. Azuma, M. Takano, H. Takagi, and J. C. Davis, *A 'checkerboard' electronic crystal state in lightly hole-doped $Ca_{2-x}Na_xCuO_2C_{l2}$*, Nature **430**, 1001 (2004).

[213] K. Yamada, C. H. Lee, K. Kurahashi, J. Wada, S. Wakimoto, S. Ueki, H. Kimura, Y. Endoh, S. Hosoya, G. Shirane, R. J. Birgeneau, M. Greven, M. A. Kastner, and Y. J. Kim, *Doping dependence of the spatially modulated dynamical spin correlations and the superconducting-transition temperature in* $La_{2-x}Sr_xCuO_4$, Physical Review B **57**, 6165 (1998).

[214] A. Damascelli, Z. Hussain, and Z.-X. Shen, *Angle-resolved photoemission studies of the cuprate superconductors*, Reviews of Modern Physics **75**, 473 (2003).

[215] U. Karahasanovic, F. Kretzschmar, T. Boehm, R. Hackl, I. Paul, Y. Gallais, and J. Schmalian, *Manifestation of nematic degrees of freedom in the Raman response function of iron pnictides*, ArXiv e-prints (2015).

[216] G. Lang, H.-J. Grafe, D. Paar, F. Hammerath, K. Manthey, G. Behr, J. Werner, and B. Büchner, *Nanoscale Electronic Order in Iron Pnictides*, Physical Review Letters **104**, 097001 (2010).

[217] H. Kontani and Y. Yamakawa, *Linear Response Theory for Shear Modulus C_{66} and Raman Quadrupole Susceptibility: Evidence for Nematic Orbital Fluctuations in Fe-based Superconductors*, Physical Review Letters **113**, 047001 (2014).

[218] U. Karahasanovic, private communication, 2015.

[219] L. Zhao, H.-Y. Liu, W.-T. Zhang, J.-Q. Meng, X.-W. Jia, G.-D. Liu, X.-L. Dong, G.-F. Chen, J.-L. Luo, N.-L. Wang, W. Lu, G.-L. Wang, Y. Zhou, Y. Zhu, X.-Y. Wang, Z.-Y. Xu, C.-T. Chen, and X.-J. Zhou, *Multiple Nodeless Superconducting Gaps in $Ba_{0.6}K_0.4Fe_2As_2$ Superconductor from Angle-Resolved Photoemission Spectroscopy*, Chinese Physics Letters **25**, 4402 (2008).

[220] T. Kondo, A. F. Santander-Syro, O. Copie, C. Liu, M. E. Tillman, E. D. Mun, J. Schmalian, S. L. Bud'ko, M. A. Tanatar, P. C. Canfield, and A. Kaminski,

Momentum Dependence of the Superconducting Gap in $NdFeAsO_{0.9}F_{0.1}$ Single Crystals Measured by Angle Resolved Photoemission Spectroscopy, Physical Review Letters **101**, 147003 (2008).

[221] L. Wray, D. Qian, D. Hsieh, Y. Xia, L. Li, J. G. Checkelsky, A. Pasupathy, K. K. Gomes, C. V. Parker, A. V. Fedorov, G. F. Chen, J. L. Luo, A. Yazdani, N. P. Ong, N. L. Wang, and M. Z. Hasan, *Momentum dependence of superconducting gap, strong-coupling dispersion kink, and tightly bound Cooper pairs in the high-T_c $(SrBa)_{1-x}(K,Na)_xFe_2As_2$ superconductors*, Physical Review B **78**, 184508 (2008).

[222] S. V. Borisenko, V. B. Zabolotnyy, D. V. Evtushinsky, T. K. Kim, I. V. Morozov, A. N. Yaresko, A. A. Kordyuk, G. Behr, A. Vasiliev, R. Follath, and B. Büchner, *Superconductivity without Nesting in LiFeAs*, Physical Review Letters **105**, 067002 (2010).

[223] T. Shimojima, F. Sakaguchi, K. Ishizaka, Y. Ishida, T. Kiss, M. Okawa, T. Togashi, C.-T. Chen, S. Watanabe, M. Arita, K. Shimada, H. Namatame, M. Taniguchi, K. Ohgushi, S. Kasahara, T. Terashima, T. Shibauchi, Y. Matsuda, A. Chainani, and S. Shin, *Orbital-Independent Superconducting Gaps in Iron Pnictides*, Science **332**, 564 (2011).

[224] J. D. Fletcher, A. Serafin, L. Malone, J. G. Analytis, J.-H. Chu, A. S. Erickson, I. R. Fisher, and A. Carrington, *Evidence for a Nodal-Line Superconducting State in LaFePO*, Physical Review Letters **102**, 147001 (2009).

[225] C. W. Hicks, T. M. Lippman, M. E. Huber, J. G. Analytis, J.-H. Chu, A. S. Erickson, I. R. Fisher, and K. A. Moler, *Evidence for a Nodal Energy Gap in the Iron-Pnictide Superconductor LaFePO from Penetration Depth Measurements by Scanning SQUID Susceptometry*, Physical Review Letters **103**, 127003 (2009).

[226] K. Hashimoto, M. Yamashita, S. Kasahara, Y. Senshu, N. Nakata, S. Tonegawa, K. Ikada, A. Serafin, A. Carrington, T. Terashima, H. Ikeda, T. Shibauchi, and Y. Matsuda, *Line nodes in the energy gap of superconducting $BaFe_2(As_{1-x}P_x)_2$ single crystals as seen via penetration depth and thermal conductivity*, Physical Review B **81**, 220501 (2010).

[227] K. Hashimoto, T. Shibauchi, S. Kasahara, K. Ikada, S. Tonegawa, T. Kato, R. Okazaki, C. J. van der Beek, M. Konczykowski, H. Takeya, K. Hirata,

T. Terashima, and Y. Matsuda, *Microwave Surface-Impedance Measurements of the Magnetic Penetration Depth in Single Crystal $Ba_{1-x}K_xFe_2As_2$ Superconductors: Evidence for a Disorder-Dependent Superfluid Density*, Physical Review Letters **102**, 207001 (2009).

[228] H. Kim, M. A. Tanatar, Y. J. Song, Y. S. Kwon, and R. Prozorov, *Nodeless two-gap superconducting state in single crystals of the stoichiometric iron pnictide $LiFeAs$*, Physical Review B **83**, 100502 (2011).

[229] G. Mu, H. Luo, Z. Wang, L. Shan, C. Ren, and H.-H. Wen, *Low temperature specific heat of the hole-doped $Ba_{0.6}K_{0.4}Fe_2As_2$ single crystals*, Physical Review B **79**, 174501 (2009).

[230] G. Mu, X.-Y. Zhu, L. Fang, L. Shan, C. Ren, and H.-H. Wen, *Nodal Gap in Fe-Based Layered Superconductor $LaO_{0.9}F_{0.1-\delta}FeAs$ Probed by Specific Heat Measurements*, Chinese Physics Letters **25**, 2221 (2008).

[231] K. Gofryk, A. S. Sefat, E. D. Bauer, M. A. McGuire, B. C. Sales, D. Mandrus, J. D. Thompson, and F. Ronning, *Gap structure in the electron-doped iron-arsenide superconductor $Ba(Fe_{0.92}Co_0.08)_2As_2$: low-temperature specific heat study*, New Journal of Physics **12**, 023006 (2010).

[232] Y. Wang, J. S. Kim, G. R. Stewart, P. J. Hirschfeld, S. Graser, S. Kasahara, T. Terashima, Y. Matsuda, T. Shibauchi, and I. Vekhter, *Volovik effect in a highly anisotropic multiband superconductor: Experiment and theory*, Physical Review B **84**, 184524 (2011).

[233] S. Graser, G. R. Boyd, C. Cao, H.-P. Cheng, P. J. Hirschfeld, and D. J. Scalapino, *Determining gap nodal structures in Fe-based superconductors: Theory of the angle dependence of the low-temperature specific heat in an applied magnetic field*, Physical Review B **77**, 180514 (2008).

[234] B. Zeng, G. Mu, H. Luo, T. Xiang, I. Mazin, H. Yang, L. Shan, C. Ren, P. Dai, and H.-H. Wen, *Anisotropic structure of the order parameter in $FeSe_{0.45}Te_{0.55}$ revealed by angle-resolved specific heat*, Nature Communications **1**, 112 (2010).

[235] A. B. Vorontsov and I. Vekhter, *Nodes versus Minima in the Energy Gap of Iron Pnictide Superconductors from Field-Induced Anisotropy*, Physical Review Letters **105**, 187004 (2010).

[236] A. V. Chubukov and I. Eremin, *Angle-resolved specific heat in iron-based superconductors: The case for a nodeless extended s-wave gap*, Physical Review B **82**, 060504 (2010).

[237] L. Ding, J. K. Dong, S. Y. Zhou, T. Y. Guan, X. Qiu, C. Zhang, L. J. Li, X. Lin, G. H. Cao, Z. A. Xu, and S. Y. Li, *Nodeless superconducting gap in electron-doped $BaFe_{1.9}Ni_{0.1}As_2$ probed by quasiparticle heat transport*, New Journal of Physics **11**, 093018 (2009).

[238] V. Mishra, A. Vorontsov, P. J. Hirschfeld, and I. Vekhter, *Theory of thermal conductivity in extended-s state superconductors: Application to ferropnictides*, Physical Review B **80**, 224525 (2009).

[239] Y. Bang, *Volovik Effect in the $\pm s$-Wave State for the Iron-Based Superconductors*, Physical Review Letters **104**, 217001 (2010).

[240] V. Mishra, S. Graser, and P. J. Hirschfeld, *Transport properties of three-dimensional extended s-wave states in Fe-based superconductors*, Physical Review B **84**, 014524 (2011).

[241] C. Martin, R. T. Gordon, M. A. Tanatar, H. Kim, N. Ni, S. L. Bud'ko, P. C. Canfield, H. Luo, H. H. Wen, Z. Wang, A. B. Vorontsov, V. G. Kogan, and R. Prozorov, *Nonexponential London penetration depth of external magnetic fields in superconducting $Ba_{1-x}K_xFe_2As_2$ single crystals*, Physical Review B **80**, 020501 (2009).

[242] J. K. Dong, S. Y. Zhou, T. Y. Guan, H. Zhang, Y. F. Dai, X. Qiu, X. F. Wang, Y. He, X. H. Chen, and S. Y. Li, *Quantum Criticality and Nodal Superconductivity in the FeAs-Based Superconductor KFe_2As_2*, Physical Review Letters **104**, 087005 (2010).

[243] J.-P. Reid, M. A. Tanatar, A. Juneau-Fecteau, R. T. Gordon, S. R. de Cotret, N. Doiron-Leyraud, T. Saito, H. Fukazawa, Y. Kohori, K. Kihou, C. H. Lee, A. Iyo, H. Eisaki, R. Prozorov, and L. Taillefer, *Universal Heat Conduction in the Iron Arsenide Superconductor KFe_2As_2: Evidence of a d-Wave State*, Physical Review Letters **109**, 087001 (2012).

[244] J. Maletz, V. B. Zabolotnyy, D. V. Evtushinsky, A. N. Yaresko, A. A. Kordyuk, Z. Shermadini, H. Luetkens, K. Sedlak, R. Khasanov, A. Amato, A. Krzton-Maziopa, K. Conder, E. Pomjakushina, H.-H. Klauss, E. D. L. Rienks,

B. Büchner, and S. V. Borisenko, *Photoemission and muon spin relaxation spectroscopy of the iron-based $Rb_{0.77}Fe_{1.61}Se_2$ superconductor: Crucial role of the cigar-shaped Fermi surface*, Physical Review B **88**, 134501 (2013).

[245] A. M. Zhang, K. Liu, J. H. Xiao, J. B. He, D. M. Wang, G. F. Chen, B. Normand, and Q. M. Zhang, *Vacancy ordering and phonon spectrum of the iron-based superconductor $K_{0.8}Fe_{1.6}Se_2$*, Physical Review B **85**, 024518 (2012).

[246] A. M. Zhang, J. H. Xiao, Y. S. Li, J. B. He, D. M. Wang, G. F. Chen, B. Normand, Q. M. Zhang, and T. Xiang, *Two-magnon Raman scattering in $A_{0.8}Fe_{1.6}Se_2$ systems (A = K, Rb, Cs, and Tl): Competition between superconductivity and antiferromagnetic order*, Physical Review B **85**, 214508 (2012).

[247] Z. Wang, Y. J. Song, H. L. Shi, Z. W. Wang, Z. Chen, H. F. Tian, G. F. Chen, J. G. Guo, H. X. Yang, and J. Q. Li, *Microstructure and ordering of iron vacancies in the superconductor system $K_yFe_xSe_2$ as seen via transmission electron microscopy*, Physical Review B **83**, 140505 (2011).

[248] Z.-W. Wang, Z. Wang, Y.-J. Song, C. Ma, Y. Cai, Z. Chen, H.-F. Tian, H.-X. Yang, G.-F. Chen, and J.-Q. Li, *Structural Phase Separation in $K_{0.8}Fe_{1.6+x}Se_2$ Superconductors*, The Journal of Physical Chemistry C **116**, 17847 (2012).

[249] B. Shen, B. Zeng, G. F. Chen, J. B. He, D. M. Wang, H. Yang, and H. H. Wen, *Intrinsic percolative superconductivity in $K_xFe_{2-y}Se_2$ single crystals*, Europhysics Letters **96**, 37010 (2011).

[250] L. Simonelli, N. L. Saini, M. M. Sala, Y. Mizuguchi, Y. Takano, H. Takeya, T. Mizokawa, and G. Monaco, *Coexistence of different electronic phases in the $K_{0.8}Fe_{1.6}Se_2$ superconductor: A bulk-sensitive hard x-ray spectroscopy study*, Physical Review B **85**, 224510 (2012).

[251] A. Ricci, N. Poccia, G. Campi, B. Joseph, G. Arrighetti, L. Barba, M. Reynolds, M. Burghammer, H. Takeya, Y. Mizuguchi, Y. Takano, M. Colapietro, N. L. Saini, and A. Bianconi, *Nanoscale phase separation in the iron chalcogenide superconductor $K_{0.8}Fe_{1.6}Se_2$ as seen via scanning nanofocused x-ray diffraction*, Physical Review B **84**, 060511 (2011).

[252] A. Bosak, V. Svitlyk, A. Krzton-Maziopa, E. Pomjakushina, K. Conder, V. Pomjakushin, A. Popov, D. de Sanctis, and D. Chernyshov, *Phase coexistence*

in $Cs_{0.8}Fe_{1.6}Se_2$ as seen by x-ray mapping of reciprocal space, Physical Review B **86**, 174107 (2012).

[253] X. G. Luo, X. F. Wang, J. J. Ying, Y. J. Yan, Z. Y. Li, M. Zhang, A. F. Wang, P. Cheng, Z. J. Xiang, G. J. Ye, R. H. Liu, and X. H. Chen, *Crystal structure, physical properties and superconductivity in A $_xFe_2Se_2$ single crystals*, New Journal of Physics **13**, 053011 (2011).

[254] N. Lazarević, M. Abeykoon, P. W. Stephens, H. Lei, E. S. Bozin, C. Petrovic, and Z. V. Popović, *Vacancy-induced nanoscale phase separation in $K_xFe_{2-y}Se_2$ single crystals evidenced by Raman scattering and powder x-ray diffraction*, Physical Review B **86**, 054503 (2012).

[255] Y. Liu, Z. C. Li, W. P. Liu, G. Friemel, D. S. Inosov, R. E. Dinnebier, Z. J. Li, and C. T. Lin, *$K_xFe_{2-y}Se_2$ single crystals: floating-zone growth, transport and structural properties*, Superconductor Science and Technology **25**, 075001 (2012).

[256] V. Y. Pomjakushin, A. Krzton-Maziopa, E. V. Pomjakushina, K. Conder, D. Chernyshov, V. Svitlyk, and A. Bosak, *Intrinsic crystal phase separation in the antiferromagnetic superconductor $Rb_yFe_{2-x}Se_x$: a diffraction study*, Journal of Physics: Condensed Matter **24**, 435701 (2012).

[257] F. Chen, M. Xu, Q. Q. Ge, Y. Zhang, Z. R. Ye, L. X. Yang, J. Jiang, B. P. Xie, R. C. Che, M. Zhang, A. F. Wang, X. H. Chen, D. W. Shen, J. P. Hu, and D. L. Feng, *Electronic Identification of the Parental Phases and Mesoscopic Phase Separation of* $K_xFe_{2-y}Se_2$ *Superconductors*, Physical Review X **1**, 021020 (2011).

[258] W. Li, H. Ding, Z. Li, P. Deng, K. Chang, K. He, S. Ji, L. Wang, X. Ma, J.-P. Hu, X. Chen, and Q.-K. Xue, *KFe_2Se_2 is the Parent Compound of K-Doped Iron Selenide Superconductors*, Physical Review Letters **109**, 057003 (2012).

[259] C. Cao and J. Dai, *Electronic structure and Mott localization of iron-deficient $TlFe_{1.5}Se_2$ with superstructures*, Physical Review B **83**, 193104 (2011).

[260] Q. Luo, A. Nicholson, J. Riera, D.-X. Yao, A. Moreo, and E. Dagotto, *Magnetic state of $K_{0.8}Fe_{1.6}Se_2$ from a five-orbital Hubbard model in the Hartree-Fock approximation*, Physical Review B **84**, 140506 (2011).

[261] L. Craco, M. S. Laad, and S. Leoni, *Unconventional Mott transition in* $K_xFe_{2-y}Se_2$, Physical Review B **84**, 224520 (2011).

[262] Z. P. Yin, K. Haule, and G. Kotliar, *Kinetic frustration and the nature of the magnetic and paramagnetic states in iron pnictides and iron chalcogenides*, Nature Materials **10**, 932 (2011).

[263] P. Dai, J. Hu, and E. Dagotto, *Magnetism and its microscopic origin in iron-based high-temperature superconductors*, Nature Physics **8**, 709 (2012).

[264] B. Zeng, B. Shen, G. F. Chen, J. B. He, D. M. Wang, C. H. Li, and H. H. Wen, *Nodeless superconductivity of single-crystalline* $K_xFe_{2-y}Se_2$ *revealed by the low-temperature specific heat*, Physical Review B **83**, 144511 (2011).

[265] X.-P. Wang, P. Richard, X. Shi, A. Roekeghem, Y.-B. Huang, E. Razzoli, T. Qian, E. Rienks, S. Thirupathaiah, H.-D. Wang, C.-H. Dong, M.-H. Fang, M. Shi, and H. Ding, *Observation of an isotropic superconducting gap at the Brillouin zone centre of* $Tl_{0.63}K_{0.37}Fe_{1.78}Se_2$, Europhysics Letters **99**, 67001 (2012).

[266] D. Mou *et al.*, *Distinct Fermi Surface Topology and Nodeless Superconducting Gap in a* $(Tl_{0.58}Rb_{0.42})Fe_{1.72}Se_2$ *Superconductor*, Physical Review Letters **106**, 107001 (2011).

[267] L. Zhao *et al.*, *Common Fermi-surface topology and nodeless superconducting gap of* $K_{0.68}Fe_{1.79}Se_2$ *and* $(Tl_{0.45}K_{0.34})Fe_{1.84}Se_2$*superconductors revealed via angle-resolved photoemission*, Physical Review B **83**, 140508 (2011).

[268] L. Shan, Y.-L. Wang, B. Shen, B. Zeng, Y. Huang, A. Li, D. Wang, H. Yang, C. Ren, Q.-H. Wang, S. H. Pan, and H.-H. Wen, *Observation of ordered vortices with Andreev bound states in* $Ba_{0.6}K_{0.4}Fe_2As_2$, Nature Physics **7**, 325 (2011).

[269] A. Charnukha, O. V. Dolgov, A. A. Golubov, Y. Matiks, D. L. Sun, C. T. Lin, B. Keimer, and A. V. Boris, *Eliashberg approach to infrared anomalies induced by the superconducting state of* $Ba_{0.68}K_{0.32}Fe_2As_2$ *single crystals*, Physical Review B **84**, 174511 (2011).

[270] M. Hiraishi, R. Kadono, S. Takeshita, M. Miyazaki, A. Koda, H. Okabe, and J. Akimitsu, *Full Gap Superconductivity in* $Ba_{0.6}K_{0.4}Fe_2As_2$ *Probed by Muon Spin Rotation*, Journal of the Physical Society of Japan **78**, 023710 (2009).

[271] P. Popovich, A. V. Boris, O. V. Dolgov, A. A. Golubov, D. L. Sun, C. T. Lin, R. K. Kremer, and B. Keimer, *Specific Heat Measurements of $Ba_{0.68}K_{0.32}Fe_2As_2$ Single Crystals: Evidence for a Multiband Strong-Coupling Superconducting State*, Physical Review Letters **105**, 027003 (2010).

[272] Z. Li, D. L. Sun, C. T. Lin, Y. H. Su, J. P. Hu, and G.-q. Zheng, *Nodeless energy gaps of single-crystalline $Ba_{0.68}K_{0.32}Fe_2As_2$ as seen via ^{75}As NMR*, Physical Review B **83**, 140506 (2011).

[273] X.-P. Wang, T. Qian, P. Richard, P. Zhang, J. Dong, H.-D. Wang, C.-H. Dong, M.-H. Fang, and H. Ding, *Strong nodeless pairing on separate electron Fermi surface sheets in $(Tl, K)Fe_{1.78}Se_2$ probed by ARPES*, Europhysics Letters **93**, 57001 (2011).

[274] Z. Shermadini, H. Luetkens, R. Khasanov, A. Krzton-Maziopa, K. Conder, E. Pomjakushina, H.-H. Klauss, and A. Amato, *Superconducting properties of single-crystalline $A_xFe_{2-y}Se_2$ $A = Rb, K$) studied using muon spin spectroscopy*, Physical Review B **85**, 100501 (2012).

[275] A. D. Christianson, E. A. Goremychkin, R. Osborn, S. Rosenkranz, M. D. Lumsden, C. D. Malliakas, I. S. Todorov, H. Claus, D. Y. Chung, M. G. Kanatzidis, R. I. Bewley, and T. Guidi, *Unconventional superconductivity in $Ba_{0.6}K_{0.4}Fe_2As_2$ from inelastic neutron scattering*, Nature **456**, 930 (2008).

List of publications

1. **F. Kretzschmar**, B. Muschler, T. Böhm, A. Baum, R. Hackl, Hai-Hu Wen, V. Tsurkan, J. Deisenhofer & A. Loidl. Raman-Scattering Detection of Nearly Degenerate s-Wave and d-Wave Pairing Channels in Iron-Based $Ba_{0.6}K_{0.4}Fe_2As_2$ and $Rb_{0.8}Fe_{1.6}Se_2$ Superconductors. *Phys. Rev. Lett.* **110**, 187002 (2013).

2. T. Böhm, A. F. Kemper, B. Moritz, **F. Kretzschmar**, B. Muschler, H. M. Eiter, R. Hackl, D. J. Scalapino, T. P. Devereaux & Hai-Hu Wen. Balancing act: Evidence for a Strong Subdominant d-wave Pairing Channel in $Ba_{0.6}K_{0.4}Fe_2As_2$. *Phys. Rev. X.* **4**, 041046 (2014).

3. U. Karahasanović, **F. Kretzschmar**, T. Böhm, R. Hackl, I. Paul, Y. Gallais & J. Schmalian. Manifestation of nematic degrees of freedom in the Raman response function of iron pnictides. *arXiv* 1504.06841 (2015).

4. **F. Kretzschmar**, T. Böhm, U. Karahasanović, B. Muschler, A. Baum, D. Jost, J. Schmalian, M. Grilli, C. DiCastro, J. G. Analytis, J,-H. Chu, I. R. Fisher & R. Hackl. Nematic fluctuations and the magneto-structural phase transition in $Ba(Fe_{1-x}Co_x)_2As_2$. (unpublished).

Acknowledgment

Finally, I would like to thank numerous people for support and important contributions to this work:

- *Prof. Dr. Rudolf Gross* for giving me the opportunity to work on my PhD at the Walther-Meißner-Institut, his patience and support in the last years and helpful advice in every respect.

- *Dr. Rudi Hackl*, my academic advisor, for being a great mentor. Rudi, I want to thank you for your guidance and motivation during all stages of my scientific work. You create an atmosphere in which your students really feel part of the scientific community. I have enjoyed working in your group.

- *Prof. Dr. Ian Fisher, Dr. James Analytis, Dr. Jiun-Haw Chu, Prof. Dr. Hai-Hu Wen, Prof. Dr. Alois Loidl,* and *Dr. Vladimir Tsurkan* for providing and characterizing high quality $Ba(Fe_{1-x}Co_x)_2As_2$, $Ba_{0.6}K_{0.4}Fe_2As_2$ and $Rb_{0.8}Fe_{1.6}Se_2$ single crystals.

- *Prof. Dr. Tom Devereaux, Dr. Brian Moritz, Dr. Lex Kemper, Prof. Dr. Jörg Schmalian, and Dr. Una Karahasanivić, Prof. Dr. Carlo DiCastro, Dr. Sergio Caprara,* and *Dr. Marco Grilli* for theoretical support during the last years. I am particularly grateful to Tom, Brian and Lex for the hospitality and numerous social events during my stay at Stanford University which made my visit unforgettable. Who had thought that Karaoke actually is fun!

- *Prof. Dr. Dietrich Einzel* for the discussions on the theories of electronic Raman scattering and superconductivity and in particular his explanations of the complex collective excitations in superconductors, which play an important role in this dissertation.

- my fellow group members *Bernhard Muschler, Hans-Martin Eiter, Thomas Böhm, Andreas Baum, Nitin Chelwani,* and *Bea Botka* for the pleasant atmosphere in the Raman group and for many fruitful discussions.

- *David Hoch, Roland Richter, Daniel Jost, Michael Rehm,* and *Andreas Walther* for their great work and contributions to this dissertation via their Diploma, Master and Bachelor thesis.

- my room mates *Stephan Geprägs, Andi Brandlmaier, Hans-Martin Eiter, Jan Götz, Alma Dorantes, Friedrich Wulschner,* and *Prof. Dr. B. S. Chandrasekhar* for the great atmosphere. In particular, I'd like to appreciate the discussions with Chandra which were inspiring and helpful.

- Diploma and Doctoral students of other groups for the many social events we shared. In particular: *Stephan Geprägs, Andi Brandlmaier, Elli Hoffmann, Peter Eder, Friedrich Wulschner, Jan Götz, Max Häberlein,* and *Christoph Zollitsch*

- the technical staff, in particular *Helmut Thies, Robert Müller, Georg Nitschke,* and *Christian Reichlmeier* for their great work. They manufactured many pieces for the new TERS setup and always gave good advice regarding the design of new parts.

- *Emel Dönertas,* and *Ludwig Ossiander* for taking care of financial and organizational problems, even on short notice.

- *Hans, Wolfi, Polster, Zolli, Marc und Max*, my munich role-playing group, for the countless adventures in the realms of Faerûn, Aventurien and Cuba Libre.

- I am deeply grateful to my parents *Karin* and *Wolfgang*, and my brothers *Julian* and *Kilian* for their love, friendship, patience and everlasting support.

- Finally, and most of all, I would like to thank my wife *Tini* for always covering my back, her continuous encouragement, patience and love. I dedicate this thesis to you and our beloved daughter *Cleo*.